Controlled Solid-Vapour CO2 phase transitions in methane rich streams applied to biogas upgrading

Sylvain Haddad

▶ **To cite this version:**

Sylvain Haddad. Controlled Solid-Vapour CO2 phase transitions in methane rich streams applied to biogas upgrading. Chemical and Process Engineering. Université Paris sciences et lettres, 2019. English. NNT : 2019PSLEM069 . tel-03118446

HAL Id: tel-03118446
https://pastel.hal.science/tel-03118446

Submitted on 22 Jan 2021

HAL is a multi-disciplinary open access archive for the deposit and dissemination of scientific research documents, whether they are published or not. The documents may come from teaching and research institutions in France or abroad, or from public or private research centers.

L'archive ouverte pluridisciplinaire **HAL**, est destinée au dépôt et à la diffusion de documents scientifiques de niveau recherche, publiés ou non, émanant des établissements d'enseignement et de recherche français ou étrangers, des laboratoires publics ou privés.

PSL UNIVERSITÉ PARIS

THÈSE DE DOCTORAT
DE L'UNIVERSITÉ PSL

Etude des transitions contrôlées entre phases Solide-Vapeur de CO_2 à partir d'un écoulement contenant du méthane en vue de l'épuration du biogaz.

Controlled Solid-Vapour CO_2 phase transitions in methane rich streams applied to biogas upgrading

Confidentielle

Fin de confidentialité 31 Décembre 2020

Soutenue par

Sylvain HADDAD

Le 17 décembre 2019

Ecole doctorale n° 621

Ingénierie des systèmes, matériaux, mécanique énergétique

Spécialité

Énergétiques et procédés

Composition du jury :

Daniel BROSETA Professeur, Université de Pau	*Président*
Carolina FONT PALMA Senior Lecturer, University of Chester	*Rapporteur*
Isabelle MABILLE Maître de conférences, HDR, Sorbonne Université	*Rapporteur*
Jean-Philippe PASSARELLO Professeur, Université Paris 13	*Examinateur*
Rodrigo RIVERA-TINOCO Chargé de Recherche, MINES ParisTech	*Examinateur*
Chakib BOUALLOU Professeur, MINES ParisTech	*Directeur de thèse*

MINES ParisTech | PSL

Acknowledgements

First, I would like to express my sincere gratitude to my PhD supervisor Dr. Rodrigo Rivera-Tinoco who guided me and mentored me during my 3 years of PhD work. I thank him for his constant encouragement and the time he invested in order to finish this work even when it seemed like an impossible task.

I would like to thank my PhD Director Pr. Chakib Bouallou, his involvement was a major contributor to the completion of this work. I am really grateful for his advices and help especially in the third (and most difficult) year.

I also would like to thank Dr. Maroun Nemer, the director of the CES. He gave me the opportunity to start this PhD and helped me, however indirectly, to finish it too.

I would like to thank the members of the jury Pr. Jean-Philippe PASSARELLO, Dr. Isabelle MABILLE, Dr. Carolina FONT PALMA, Pr. Daniel BROSETA who accepted to invest time for reading this work and providing interesting and constructive feedback which was much appreciated

Also, I extend my thanks to the members of Mines ParisTech CES “Centre Efficacité Energétique des Systèmes”: the PhD students, researchers, trainees and the administrative staff for creating a good working atmosphere. I would like to thank Florent for the advices and guidance in the start of this thesis. I especially thank Rony, Rachelle, Luca, Afif, Samer, Hussein, Joe, Franck, Assaad, Christina, Hala, Boutros… for the discussions we had and the good times we spent together. And a more particular thank you to Haytham and Rami for their support, encouragement, help and time when things were really complicated.

I would like to thank all my friends outside work whom I consider my family in France. A special thanks to Eliane without whom this work would not have been completed. Her constant support and her “being there” got me through the hard times.

Of course, last but not least, I would like to thank all my family in Lebanon especially my parents Milad and Hoda, my sister Sarah and my brother Etienne. They were always there for me for encouragement and support. I am really grateful for their presence in my life.

This thesis is dedicated to my mother Hoda who is currently fighting one of life’s hardest fights. I thought my PhD was difficult to finish but she was my encouragement and my role model on how to surpass any obstacle in life. My problems were diminished by her suffering which she is facing with the highest moral, the strongest heart and the largest smile. Thank you mom and I hope that you are proud and as I always say :” This Too Shall Pass”.

Table of Contents

List of Figures

List of tables

Nomenclature

Symbol	*Description (unit)*
A	*Area (m^2)*
AHR	*Air Humidity Ratio (kg/kg)*
cp	*Specific heat capacity at constant pressure ($J.K^{-1}.kg^{-1}$)*
cv	*Specific heat capacity at constant volume ($J.K^{-1}.kg^{-1}$)*
d	*Diameter (m)*
D	*Mass diffusivity coefficient ($m^2.s^{-1}$)*
D_{AB}	*Mass diffusivity coefficient of component A in B ($m^2.s^{-1}$)*
DCA	*Dynamic contact angle (°)*
Dh	*Hydraulic diameter (m)*
h_c	*Convective heat transfer coefficient ($W.m^{-2}.K^{-1}$)*

h_m	*Mass transfer coefficient ($kg.s^{-1}.m^{-2}$)*
k	*Thermal conductivity ($W.m^{-1}.K^{-1}$)*
L	*Length (m)*
l	*Width (m)*
Le	*Lewis number*
L_{sv}	*Latent heat of sublimation ($J.kg^{-1}$)*
L_{vl}	*Latent heat of vaporisation ($J.kg^{-1}$)*
$\dot{m}$	*Mass flux ($kg.s^{-1}.m^{-2}$)*
Nu	*Nusselt number*
P	*Pressure (Pa)*
Pr	*Prandtl number*
$\dot{q}$	*Heat flux ($W.m^{-2}$)*
$\dot{Q}$	*Heat flow (W)*
Re	*Reynolds number*
RH	*Relative humidity (%)*
Sc	*Schmidt number*
T	*Temperature (K)*
ΔT	*Temperature difference (K)*
t	*Time (s)*
v	*Velocity ($m.s^{-1}$)*
$\dot{V}$	*Flowrate ($m^3.s^{-1}$)*
x,y,z	*Cartesian coordinates*
X_i	*Mass concentration (kg/kg)*
$x_{i/j}$	*Relative mass concentration of component i relative to component j*
y_i	*Molar concentration (mol/mol)*

Greek symbols

Θ_{frost}	*Frost thickness (m)*
α	*Densification rate ($kg.\ s^{-1}.m^{-3}$)*
β	*Porosification rate ($kg.s^{-1}.m^{-3}$)*
γ	*Specific heat capacities ratio*
ε	*Efficiency*
μ	*Dynamic viscosity (Pa.s)*
ρ	*Density ($Kg.m^{-3}$)*

Subscripts

A,B	*Related to component A and B respectively*
avg	*Average*
carac	*Characteristic*
cond	*Conductive (related to conduction)*
Cu	*Cupper*
eff	*Effective*
flue gases	N_2+CO_2
fr	*Frost*
lat	*Latent*
liq	*Liquid*
sat	*Saturation*
s-c	*Solid coolant*
sens	*Sensible*
STP	*Standard temperature and pressure conditions*
surf	*Surface*
tot	*Total*
w	*Related to water*
Θ_{frost}	*Affecting the frost thickness (at the frost surface)*
ρ_{frost}	*Affecting the frost thickness (inside the frost)*

Introduction

As energy demands increase worldwide, fossil originated energy resources are being exploited and the results on Earth's wildlife and climate are devastating. The problem is not only with the amount of energy needed to fulfil global consumption but rather its source. Conventional sources are of fossil origin and produce a large amount of pollutants especially carbon dioxide, a greenhouse gas (GHG). The principal function of GHG is trapping heat in the atmosphere to prevent Earth's icing. However, high emissions of GHGs are the main cause of global warming and climate change.

Globally, carbon dioxide makes up to 75% of the total GHG emissions [1]. According to a study by the International Energy Agency, global CO_2 emissions rose to "a historic high of 33.1 Gt (Giga-tonnes)"[2]. Between 2014 and 2016, CO_2 emissions did not increase even though energy demands did. This was the result of low-carbon processes development and increasing energy efficiency. But from 2016 to 2018, the increase in energy demand could not be met while conserving low carbon dioxide emissions fostering. Between 2010 and 2018, the average increase in CO_2 emissions was by 0.3% for every 1% increase in global economic output.

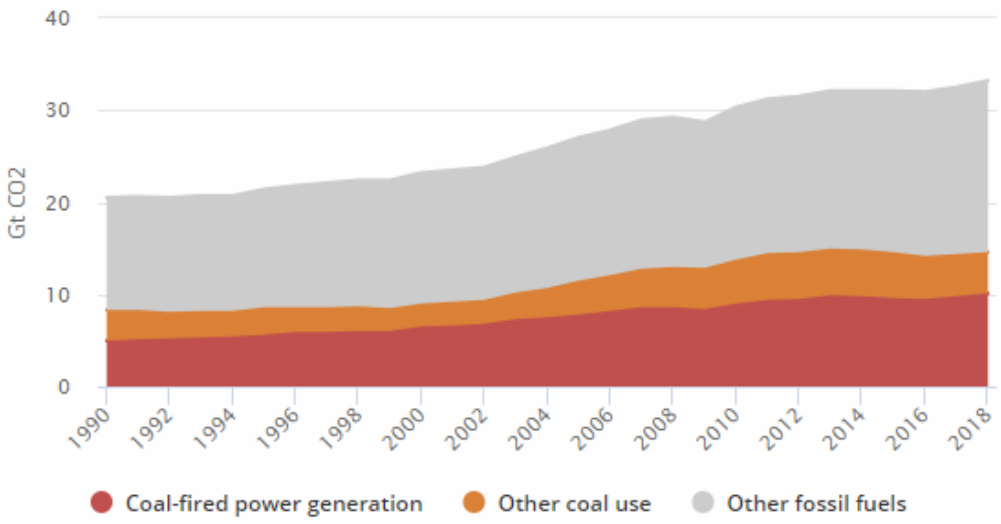

Figure 1: Global energy-related carbon dioxide emissions by source from 1990 to 2018[2]

Limiting CO_2 emissions has become a necessity. The replacement of fossil fuels and coal by renewable clean energies can be a solution to this problem. Solar energy, hydropower, wind energy, biomass and many others are suggested to lower CO_2 emissions and limit the consumption of resources that take millions of years to be formed. Although all these renewable energy sources have their advantages, in this thesis the focus will be on an energy source that limits CO_2 emissions while presenting a high calorific value that can compete with fossil fuels: the biogas.

All organic material that comes from animals or plants is called biomass. Food leftovers, unwanted wood, animal manures… undergo anaerobic digestion to produce biogas. Many constituents are present in the final product and their concentrations depend on the biomass

source. The two main components are methane CH_4 and carbon dioxide CO_2. Methane will be used to produce energy. But in order to use it efficiently and cleanly, it must be separated from the other impurities like N_2, O_2, H_2, H_2S and NH_3, but most importantly CO_2. Many techniques can be used to remove carbon dioxide from biogas and obtain biomethane. One of these techniques is cryogenic separation, which separates components based on their saturation temperatures. This process has a high methane yield and purity. Carbon dioxide separated in this process can be stocked and valorised. However, the main problem with cryogenic separation is high energy intensity for cooling to very low temperatures.

In this thesis, a phenomenon that can be a potential solution to this problem is studied: a new concept for CO_2 removal and cold recovery in multiphase systems. The first part of the concept is cryogenic separation of carbon dioxide from biogas which is an already existing technology. The second part presents the disruptive valorisation of the cold contained in the CO_2 frost by controlled evaporative cooling. The concept will lower, if not eliminate the need for the external cold source that cools down the system allowing the separation of CO_2 from biogas.

This thesis will be divided into five chapters. In the first chapter, a global view of CO_2 removal techniques from biogas is reviewed with the aim to set the relevance of the cryogenic separation. Controlled sublimation is presented as a potential solution for the reduction of energy demands and in the end of the first chapter the new concept for CO_2 cryogenic separation with cold recovery is explained as each of its parts will be developed and well detailed in the rest of the thesis.

In the second chapter, CO_2 frosting is studied. The deposition phenomenon is explained and the model used for predicting frost formation and growth is presented. Very few studies have been carried out on solid CO_2 and CO_2 frost properties which are very important for modelling CO_2 frost deposition. Several assumptions of the model are discussed and the results are compared to experimental data gathered for frosting of CO_2 contained in flue gases on a cold surface.

In the third chapter, the model is applied for the case of CO_2 deposition from biogas. A parametric study is conducted to analyse the effect of several parameters on frost growth and heat transfer. Several heat exchanger geometries are discussed in order to choose the optimal solution for CO_2 removal by solid deposition.

In the fourth chapter, several defrosting methods are reviewed. CO_2 defrosting by controlled sublimation is studied. The model of CO_2 sublimation by cold nitrogen gas is presented. Results are analysed in order to calculate the efficiency of the cold recovery and the possibility of applying it in a whole system of biogas upgrading and biomethane liquefaction.

The fifth chapter mainly discusses the experimental setup constructed for CO_2 deposition and controlled sublimation. The experimental procedure is described in all its details and results obtained from the experiment are analysed and thoroughly discussed. Frost growth and defrosting are observed. The cold recovery by “controlled sublimation” is discussed.

Introduction

Les besoins énergétiques augmentent dans le monde entier, les ressources énergétiques d'origine fossile sont exploitées et les conséquences sur la planète et sur le climat sont dévastatrices. Le problème ne concerne pas seulement la demande d'énergie nécessaire pour satisfaire la consommation mondiale, mais plutôt la source de cette énergie. Les sources conventionnelles sont d'origine fossile et produisent une grande quantité de polluants, en particulier le dioxyde de carbone, un gaz à effet de serre (GES) qui est la cause principale du réchauffement planétaire et du changement climatique.

À l'échelle mondiale, le CO_2 représente jusqu'à 75% des émissions totales de GES [1]. Selon une étude de l'Agence Internationale d'Energie, les émissions mondiales de CO_2 ont atteint «un record historique de 33,1 Gt (Gigatonnes)»[2]. Entre 2014 et 2016, les émissions de CO_2 n'ont pas augmenté grâce au développement de procédés à faible teneur en carbone et d'une efficacité énergétique élevée. Mais de 2016 à 2018, l'augmentation de la demande d'énergie ne pourrait plus être satisfaite tout en limitant les émissions de dioxyde de carbone. Entre 2010 et 2018, l'augmentation moyenne des émissions de CO_2 était de 0,3% pour chaque croissance de 1% de l'économie mondiale.

Limiter les émissions de CO_2 est devenu une nécessité. Le remplacement des combustibles fossiles et du charbon par des énergies propres renouvelables peut être une solution à ce problème. L'énergie solaire, l'hydraulique, l'éolien, la biomasse et bien d'autres solutions sont suggérées pour réduire les émissions de CO_2. Cette thèse se focalise sur une source d'énergie limitant les émissions de CO_2 tout en présentant un pouvoir calorifique élevé pouvant rivaliser avec les combustibles fossiles : le biogaz.

Toute matière organique provenant d'animaux ou de plantes s'appelle biomasse. Les restes de nourriture, les déchets animaux et végétaux… subissent une digestion anaérobique pour produire du biogaz. La composition du produit final dépend de la source de la biomasse. Les deux principaux composants sont le méthane CH_4 et le dioxyde de carbone CO_2. Le méthane sera utilisé pour produire de l'énergie. Mais pour l'utiliser efficacement et proprement, il faut le séparer des autres impuretés telles que N_2, O_2, H_2, H_2S et NH_3, mais surtout le CO_2. De nombreuses techniques peuvent être utilisées pour éliminer le dioxyde de carbone du biogaz et obtenir du biométhane. L'une de ces techniques est la séparation cryogénique, qui sépare les composants selon leurs températures de saturation. Ce processus produit un rendement élevé de méthane de haute pureté. Le dioxyde de carbone séparé au cours de ce processus peut être stocké et valorisé. Cependant, le problème principal de la séparation cryogénique est le besoin énergétique élevé pour le refroidissement à très basse température.

Dans cette thèse, on étudie un phénomène qui peut représenter une solution potentielle à ce problème : un nouveau concept pour l'élimination du CO_2 et la récupération simultanée du froid. La séparation cryogénique du dioxyde de carbone du biogaz est une technologie énergivore. L'originalité concerne la valorisation du froid contenu dans le givre de CO_2 : le refroidissement par sublimation contrôlée. Le concept réduira, voire éliminera la nécessité d'une source de froid externe qui refroidit le système, permettant ainsi de séparer plus de CO_2 du biogaz.

Cette thèse est divisée en cinq chapitres. Dans le premier chapitre, les techniques d'élimination du CO_2 provenant du biogaz sont détaillées dans le but de définir la pertinence de la séparation cryogénique. L'évaporation contrôlée est présentée comme une solution potentielle pour la réduction de l'énergie de refroidissement. À la fin du premier chapitre, le nouveau concept de séparation cryogénique du CO_2 avec récupération du froid est expliqué. Chaque partie est détaillée dans la suite du document.

Dans le deuxième chapitre, le givrage du CO_2 est étudié. Le modèle utilisé pour prédire la formation et la croissance du givre est présenté. Très peu d'études ont été réalisées sur les propriétés du CO_2 solide et du givre de CO_2, qui sont très importantes pour la modélisation des dépôts de givre CO_2. Plusieurs hypothèses du modèle sont discutées et les résultats sont comparés à des données expérimentales de givrage du CO_2 contenu dans les gaz de combustion sur une surface froide.

Dans le troisième chapitre, le modèle s'applique au cas de la séparation du CO_2 contenu dans le biogaz. Une étude de sensibilité est menée afin d'analyser l'effet de plusieurs paramètres sur la croissance du givre et le transfert de chaleur. Plusieurs géométries d'échangeurs de chaleur sont discutées afin de choisir la solution optimale pour l'élimination cryogénique du CO_2.

Dans le quatrième chapitre, les méthodes classiques de dégivrage sont présentées. Le dégivrage du CO_2 par évaporation contrôlée est étudié. Le modèle de sublimation de CO_2 par l'azote froid est présenté. Les résultats sont analysés afin de calculer l'efficacité de la récupération du froid et la possibilité de l'appliquer sur un système d'épuration et de liquéfaction du biogaz.

Le cinquième chapitre traite principalement du banc d'essai permettant d'étudier le givrage du CO_2 et l'évaporation contrôlée. La procédure expérimentale est décrite dans tous ses détails et les résultats de l'expérience sont analysés et discutés. La croissance du givre et le dégivrage sont observés. La récupération du froid par « sublimation contrôlée » est analysée et discutée.

Chapter 1: State of the art on CO_2 removal and evaporative cooling methods

Introduction

The world is facing a problem of supplying and securing the sustainable energy resources needed to cover industrial and domestic energy needs. Energy independence from non-renewable (and polluting) sources and the deployment of recovery technologies for renewable and clean energy is becoming a requirement. In a study carried out by the U.S. Energy Information Administration in 2017[3], it is forecasted that the energy consumption will have increased by 28% worldwide between 2015 and 2040 with fossil fuels as the main energy source. According to Figure 2, fossil fuels contributed to 84% of the total energy in 1990 to about 10% for renewable energy. In 2015, the latter increased to cover 12% of the total energy but the fossil fuels remained at 84% with an increase of 20% in the world energy consumption. In 2040, it is expected that fossil fuels will cover 77% and the contribution of renewable energy will increase to 17%. Although it is clear that renewable and nuclear energy sources are improving in terms of contribution to the world energy consumption, there is still a long way for such sources to cover worldwide energy

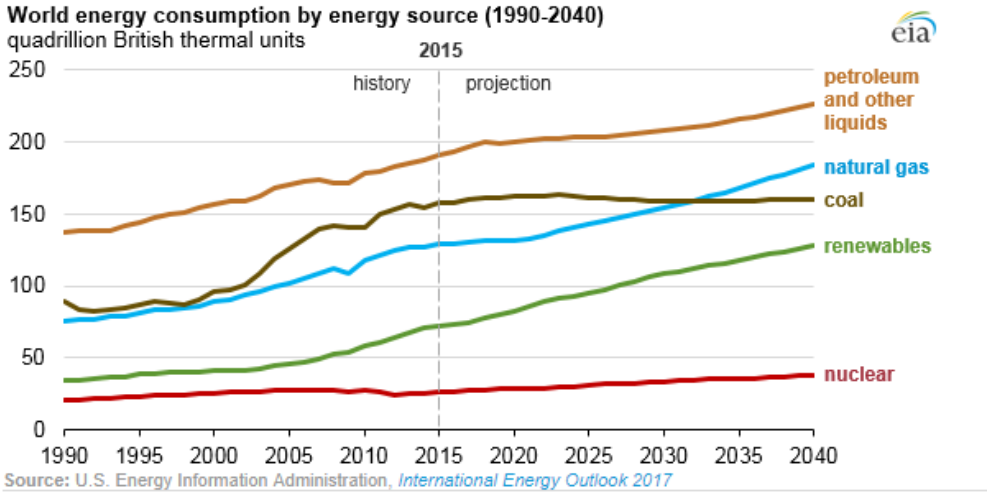

Figure 2: World energy consumption by energy source[3]

Besides limited availability, the problem with fossil originated energy is the impact that it imposes on the environment. They are the main cause of CO_2 emissions which are responsible for the greenhouse effect. This process causes the atmosphere to retain more of the sun's heat than it should thus cause global warming.

Many actions were taken in several countries and by many companies in order to limit CO_2 emissions especially in the power generation sector[3]. First, CO_2 emissions can be limited by increasing the efficiency of the systems for example using heat regeneration in thermodynamic systems, heat integration in power plants and overall research and development in all industrial sectors like automobile, home appliance and others. Although, this can reduce CO_2 emissions it will not be enough especially that energy demand is

constantly increasing worldwide. Nuclear energy can be a solution in some countries since it is a low carbon dioxide emissive energy source; however nuclear waste management remains a problem still besides inherent risks of malfunction of a power plant that can lead to devastating results.

Here lies the importance of substituting fossil fuels by renewable energy sources. Photovoltaic solar power, wind power using wind turbines, hydroelectricity, biomass and other solutions were proposed as alternative energy sources to reduce CO_2 emissions. Within this context, this research work will focus on the renewable version of natural gas, the biomethane, as case study for the advanced upgrading technique by controlled sublimation of solid phase to reduce energy consumption.

1.1 Biogas as a renewable energy

Biogas is one of the solutions to this problem[4]. Biomass for collective or industrial use represents a very important part of energy production as identified by the "Syndicat des énergies renouvelables"[5]. It is estimated that the global bulk of renewable energy by 2020 will be provided by biomass energy, in particular biogas, with a contribution of at least 25%[6]. Thus, biogas energy production from commercial facilities is estimated to double in the next decade from 14.5 GW in 2012 to 29.5 GW in 2022[4]. In 2018, the top ten European countries in terms of biogas production account for 38.9% of world production, followed by China and the United States, which produce 31.25% and 24.73% respectively[7]. In Figure 3[8], the evolution of the biogas market by country from 2012 to 2015 with a projection to 2022 is presented. The demand for biogas should increase continuously in the years to come mainly for environmental reasons. Biogas is produced from organic matter containing CO_2 that was present in the atmosphere unlike fossil fuels which will release and accumulate CO_2 that was underground into the atmosphere causing global warming... Also, in many countries, governments are issuing laws regarding the use of renewable energy for fuel production to promote this industry. In fact, several countries (Sweden, France, Germany, the Netherlands ...) are already producing methane (usable as fuel) from biogas[9] at industrial scale.

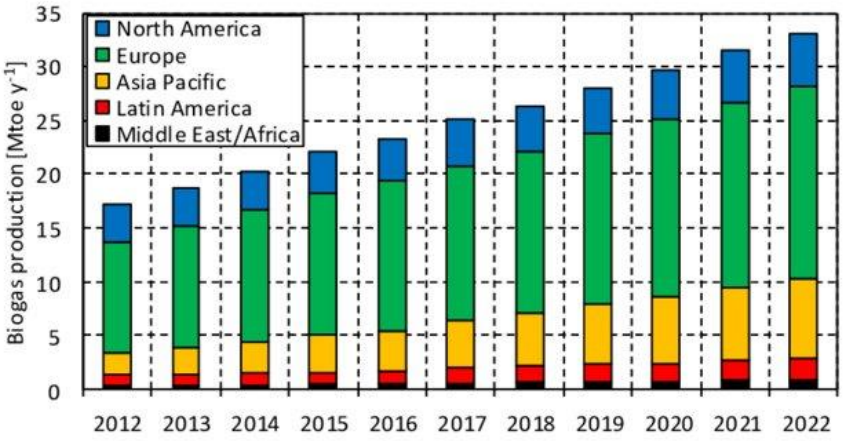

Figure 3: Comparison of the evolution of biogas production in different continents[8]

According to a study carried out by the "Syndicat des énergies renouvelables" (SER) and gas network operators (GRDF, GRTgaz, TIGF)[5], in France the production of biomethane which was authorized in 2011, progressed in one year (2015-2016) by 162% to reach 215 GWh, the

equivalent of a consumption of 18,000 homes. In 2016, biogas production was spread over 550 units, 26 of which produced biomethane (purified biogas) ready for injection into the natural gas network. Even though it seems unlikely to be achieved, the government's objective is to reach 8 TWh of biomethane injected in 2023[10] and a volume between 14 and 22TWh in 2028, thus biogas will contribute between 6 and 8% of the total gas consumption in France[11].

1.1.1 From raw biogas to injection of biomethane into the natural gas grid

The production of biomethane goes through several stages:

1. Collection: Biomethane is produced from organic matter such as food waste, agricultural products, wastewater treatment residues collected and put in a digester or stored in landfills.

2. Methanisation: in a digester the degradable organic matter is transformed into biogas, the solid residues are put apart to become fertilizers (digestate).

3. Biogas upgrading: this is a treatment of biogas before being injected into the network, all the impurities (CO_2, H_2O, N_2 ...) must be removed to obtain almost pure methane at the minimum concentration set by the gas network operator specifications[12].

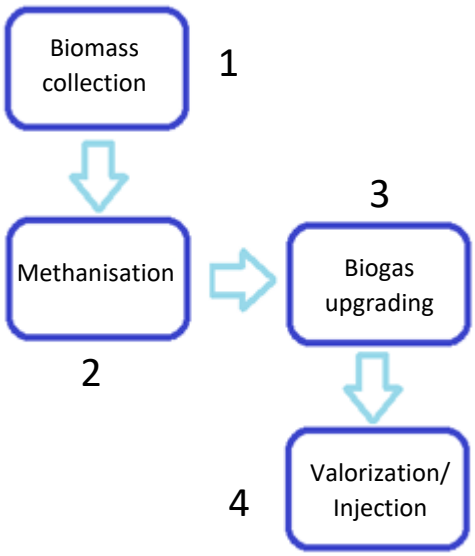

Figure 4: Different steps from collection of biomass to injection of clean energy source

4. Injection: the biomethane is odorised and controlled. Then it is injected into the network or stored for later use in transportation.

Biogas composition can differ depending on the source of organic matter. However, the main components are methane CH_4 and carbon dioxide CO_2. In the biogas upgrading phase CO_2 will be removed in order to obtain clean and usable biomethane. The importance of biogas production is not limited to the disposal of organic waste but extends to a significant valorisation -domestic or industrial - in the thermal and electrical fields[13].

1.1.2 Biogas composition

As it was mentioned before the two main components in biogas are methane CH_4 and carbon dioxide CO_2 but it also contains traces of impurities that should also be treated before using biogas. The gas mixture also contains water vapour and possibly some solid particles [14].

As Table 1 shows, impurities other than CO_2 are much less abundant in the biogas composition. In this thesis, the focus is on removing carbon dioxide from biogas, all the other impurities are considered removed prior to this step. Carbon dioxide is the second largest content compound in biogas after methane, and its removal proves to be the most energy

demanding. Thus, it impacts the energy efficiency of biomethane units and their competitiveness as it will be shown in the following section.

Table 1: Biogas composition from various sources[15]

Component	Agriculture waste	Landfills	Industrial waste
Methane CH_4	50-80	50-80	50-70
Carbon dioxide CO_2	20-50	20-50	30-50
Hydrogen Sulfide H_2S	0.7	0.1	0.8
Hydrogen H_2	0-2	0-5	0-2
Nitrogen N_2	0-1	0-3	0-1
Oxygen O_2	0-1	0-1	0-1
Water vapor H_2O	Saturation	Saturation	Saturation

1.1.3 Methanisation (Anaerobic digestion)

In order to obtain biogas, the biomass must pass through a fermentation process in anaerobic conditions (absence of O_2). In terms of economic and environmental efficiency, anaerobic digestion is better than composting or incineration. It has a more eased energy balance and limits the emission of volatile compounds to the atmosphere, including methane[16]. It also provides the fuel which is the biogas and a digestate that can be used as a fertilizer for crops cultivation. This process can solve the organic waste management problem and decrease GHG concentration the atmosphere[14]. A specific type of bacteria is added to the biomass in a liquid volume to transform the organic waste into methane and carbon dioxide[17][18] and four steps are followed in order to obtain biogas: hydrolysis, acidogenesis, acetogenesis and methanogenesis [19], [20]. Every step requires specific environmental conditions and different types of bacteria:

- In the hydrolysis step, macromolecules are degraded into soluble organic material compounds.
- In the acidogenesis step, the hydrolysed soluble molecules obtained from the first phase are transformed into light acids such as lactic and fatty acids containing 2 to 5 carbon atoms. The composition of the final product depends of the process conditions.
- The acetogenesis step can be performed in parallel to the acidogenesis. Acetogenic reducing bacteria convert alcohols and light acids into carbon dioxide, hydrogen and acetate. H_2S is also obtained in this phase and is an undesirable product that must be removed before the use of biogas. The hydrogen partial pressure must remain low [21] because its increase can inhibit the metabolism of acetogens.
- The final step is the methanisation in which methane is obtained. During this phase, two types of methanogenic bacteria intervene. The acetotropic bacteria is used to reduce acetate to methane and carbon dioxide. Finally, a biogas stream is obtained which needs a certain degree of purification depending on the targeted applications, as well as a digestible that can be used in agriculture.

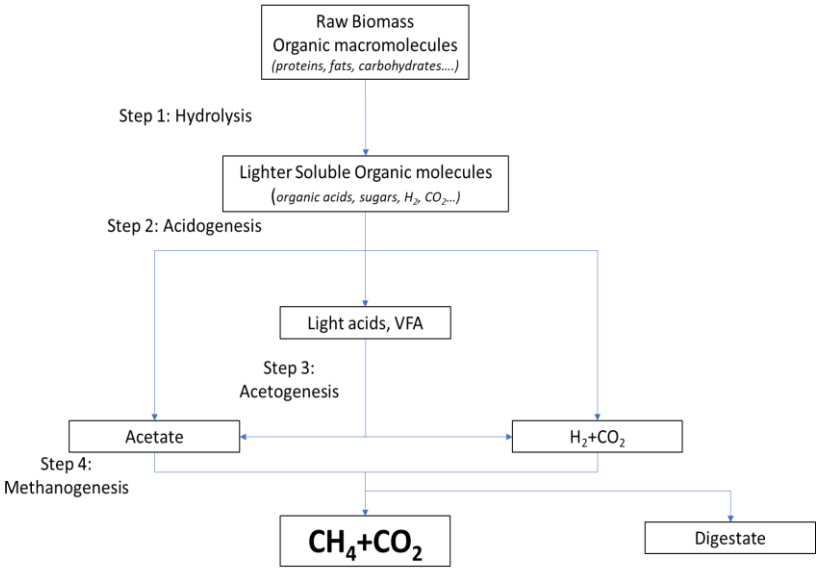

Figure 5: The different stages from biomass to biogas (based on [19], [21]**)**

1.1.4 Biomethane valorisation

The removal of H_2S from biogas enables its use in Combined Heat and Power units (CHP), either engines or turbines, and boilers [22]. If biogas is treated to remove CO_2 in pre-combustion, biomethane is obtained and can be valorised in several ways.

Biomethane can be used in the transport sector in cars and trucks. Vehicles using compressed natural gas (CNG) or liquefied natural gas (LNG) as their fuel contribute to the development of an environmentally friendly transport sector with low GHG emission. Locally produced biomethane can be a solution in countries aiming to reduce their CO_2 emissions resulting from the transport sector. Moreover, biomethane can be injected into the natural gas grid, hence, it can be transported to its use in industry and domestic appliances.

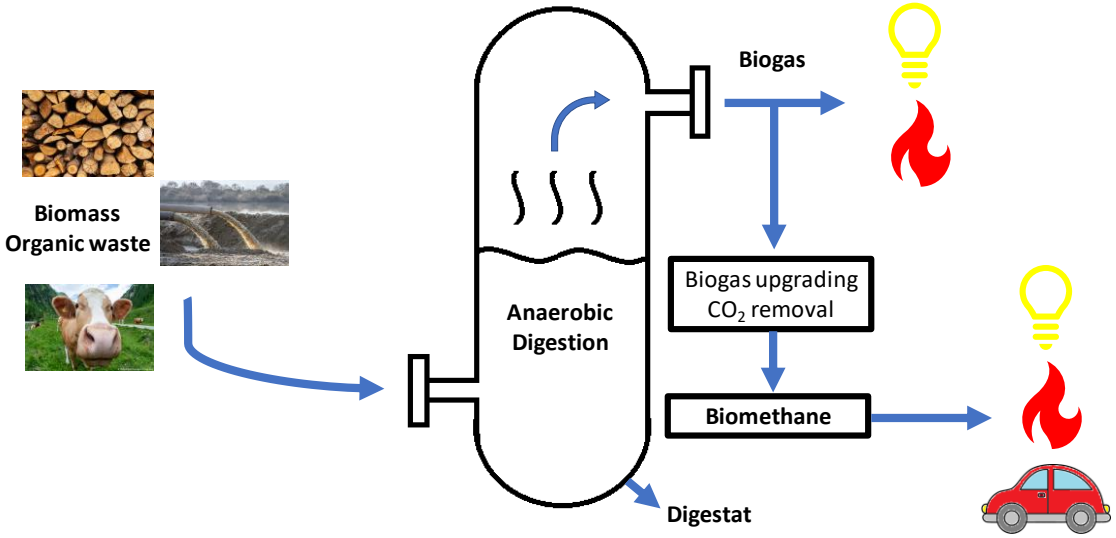

Figure 6: From biowaste to valorisation of biogas and biomethane

In order for biogas to take its place as a lead renewable environmentally friendly energy source and replace the traditional fossil fuel, it must be treated. All its impurities must be removed and most importantly carbon dioxide which is the second major component of biogas after methane. Although CO_2 is not as harmful and corrosive as other impurities, it decreases the calorific value of biogas [23]. Raw biogas has an average calorific value of about 30MJ/kg, its upgrading to biomethane containing 90% CH_4 increases its calorific value to 45MJ/kg [24]. This value is slightly lower to the calorific values of diesel and fuel, 45.6MJ/kg and 46.4MJ/kg respectively[25]. Therefore, in this thesis, the focus will be on CO_2 removal from biogas. Different techniques were designed for biogas upgrading. They will be presented and compared in this chapter.

1.2. Carbon dioxide removal techniques

Carbon dioxide in its pure state is used today in the agriculture in greenhouses, pharmaceutical and food industry. CO_2 is a basic component in chemical industry, it is used to form several compounds of interest. Global CO_2 utilization in industrial processes is estimated at 200 Mt per year, the equivalent of only 0.5% of total CO_2 emissions[26].

Solid CO_2 also known as dry ice, is a refrigerant that sublimates at atmospheric pressure. Its triple point is at P=5.1 bar and T=-56°C. Everything below these conditions will result in a direct passage of CO_2 from its solid phase to its gas phase and vice-versa (see Figure 7).

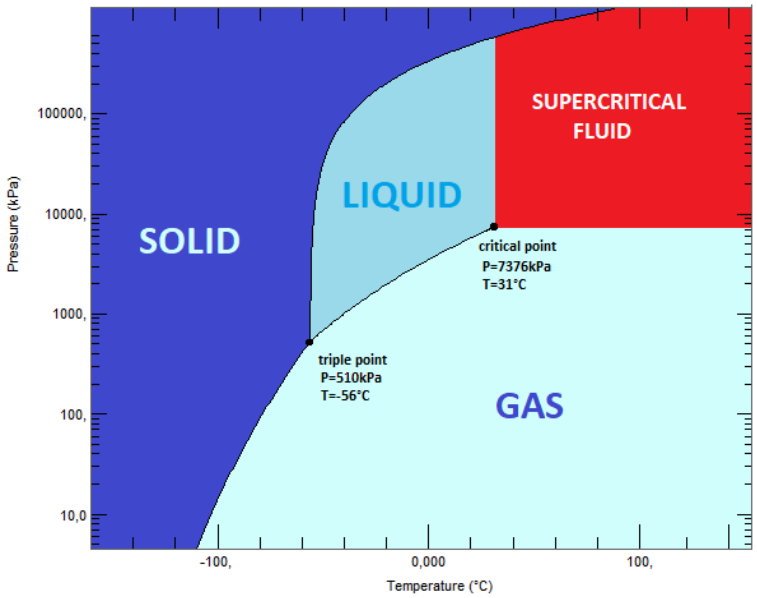

Figure 7: Phase diagram of carbon dioxide (REFPROP)

CO_2 removal technologies are usually classified into three major parts:

- pre-combustion: removal of CO_2 is completed before the combustion of the purified fuel. Biogas is converted via gasification or partial oxidation into a synthetic gas[27]. Syngas is mainly composed of CO and H_2[28]. CO reacts with steam in a water gas shift

reformer to obtain more H_2 and CO_2 [28] which will be removed via several removal techniques that will be discussed later. Generally, CO_2 concentration in pre-combusted fuel is high since it is not yet mixed with an oxidizing agent. This results in a higher driving force for CO_2 separation[30] eliminating compression necessity thus reducing separation cost.

- post-combustion: the fuel containing CO_2 is burned and its energy used. The CO_2 contained in the flue gases resulting from the combustion is then removed. Its advantage is that a post-combustion technology can be added to a pre-existing process.

- oxy-fuel combustion: the product of burning fuel in an oxygen enriched medium is mainly CO_2 and H_2O (water vapor). Nitrogen absence during the combustion eliminates NOx traces and results in a high CO_2 concentration. Similarly to pre-combustion, this makes CO_2 removal easier. The major disadvantage is the high cost of pure oxygen production.

In the following, several techniques for CO_2 removal are presented. They can be used for upgrading biogas in pre-combustion or for CO_2 removal from flue gases in post-combustion. It is important to state that even though the work done in this thesis focuses on CO_2 removal from biogas in pre-combustion, the concept that will be mater proposed can be used in post-combustion and this will be highlighted in chapter 2. The CO_2 removal techniques presented below are mostly considered in a pre-combustion state.

1.2.1. Water Scrubbing

Water scrubbing is a physical absorption based on the different solubilities of the components of a gas mixture in a liquid scrubbing (water). This technique has a 41% share of the total biogas upgrading market and is the most used[31]. It can be used in pre-combusiton since CO_2 is 26 times more soluble in water than CH_4 in water at 25°C [32]. H_2S can also be removed with this technique because its solubility is even higher to that of CO_2, but it is advisable to remove it in a prior step because its dissolving in water renders it corrosive.

The raw biogas is pressurized at around 6-12 bar depending on the process. It is then introduced to the bottom of a column containing a structurally packed bed to increase the gas-liquid mass transfer. As the biogas moves up the column, CO_2 (upon other impurities) is captured by the liquid in the column. Upgraded biogas can be collected and water filled with captured impurities carries on towards a regenerative desorption column. Gases absorbed by water are removed at low pressure so it can be used again.

Recent studies on water scrubbing focus on reducing the quantity of water used and increasing the pressure of the system. In a study by Lantela et al.[33] on a pilot scale project, they studied the effect of pressure, water flow and temperature on the system which operated at high pressure (20-25 bar) and low pH water[13]. They found that the system can reduce halogenated compounds by 99.9% and siloxanes by 99.1%. These impurities are mainly found in biogas produced from landfills and industrial waste [34].

Power consumption in water scrubbers is mainly divided between the gas compression (0.1-0.15 kWh.Nm^{-3} considering a compression to 6-8 bar), water compression (0.05-0.1 kWh.m^{-3}) and water cooling (0.01-0.05 kWh.m^{-3}) therefore a total power need ranging between 0.16-0.3 kWh.Nm^{-3} [35]. Water scrubbers are usually used for treatment of high biogas flowrates because the investment cost decreases from 5500 to 2500€/Nm^3.h^{-1} when going from 100 to 500 Nm^3.h^{-1} CH_4. Also energy consumption decreases from 0.3 kWh.Nm^{-3} at 500 Nm^3.h^{-1} to 0.2 kWhNm^{-3} at 2000 Nm^3.h^{-1} [35].

The amount of water required can be calculated as follows[35] :

$$Q_{water}(m^3.h^{-1}) = Q_{biogas}(kmol.h^{-1})/(He(mol.L^{-1}.atm^{-1}) \times P(atm))$$

With He the Henry's Law constant which quantifies the physical absorption of a gas in a liquid, it corresponds to the amount of gas that dissolves in the liquid at its partial pressure. Water flow rates used for biogas upgrading depend on the operational pressure and they typically range between $0.18 - 0.23\ \mathrm{m^3_{water} Nm^{-3}_{biogas}}$ with water recycling [36].

The main advantage in this process is the simultaneous removal of many impurities like CO_2, H_2S, NH_3…[37] using only water without the need for any additional chemicals. The main disadvantage of the water scrubbing system is the important amount of water needed even with regeneration; in order to avoid accumulation of damaging by-products especially H_2S, 20-200L.h^{-1} of water are constantly purged. A base might be added to increase the pH which decreases due to oxidation of H_2S in raw biogas[38].

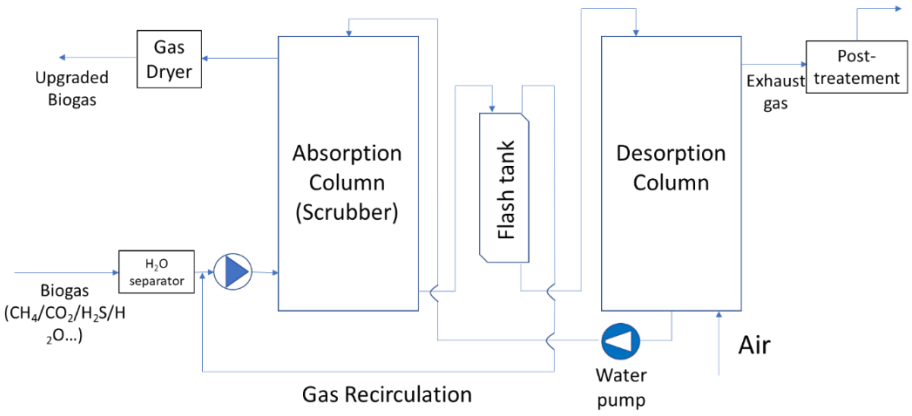

Figure 8: Schematic of water scrubbing process (based on [13] [23])

1.2.2. Chemical absorption using alkaline aqueous solutions

Scrubbing takes place by using a solvent in which acidic gases in the biogas mixture will be separated by chemical reactions. Several types of alkaline chemical compoudns can be used in treating biogas. The most commonly alkali aqueous solutions are (KOH, NaOH…) [39] and alkanolamines (Monoethanolamine (MEA), Methyldiethanolamine (MDEA)[23]. Although chemical absorption by amines was mainly studied for removal of CO_2 from flue gases and natural gas, its extrapolated use for biogas upgrading can be envisaged. In a study by Biswas

et al.[40], they reported that biogas bubbling with 10% of MEA solution reduced CO_2 volume content from 40% to less than 1%. In the chemical absorption process (Figure 9), raw biogas enters an absorption column containing a packed bed (similarly to water scrubbing) where CO_2 is removed by the amine solution. Then amine traces are removed by a water wash scrubber. Upgraded biogas carries on to the outlet while amine is regenerated in a desorption column.

Similarly to the case of water scrubbing, treatment of high biogas flowrates reduce the investment cost per $Nm^3.h^{-1}$ from 3200€/$Nm^3.h^{-1}$ for 600 $Nm^3.h^{-1}$ to 1500€/$Nm^3.h^{-1}$ for 1800 $Nm^3.h^{-1}$ [36]. Chemical absorption can operate at low pressures (1-2 bar in the absorption column [35]), which requires moderate power consumption for biogas compression and solvent pumping (0.12-0.15kWh.Nm^{-3})[41]. However, the solvent used for CO_2 removal needs to be regenerated which occurs at 120-150°C, this requires high energy consumption (0.55 kWh.Nm^{-3}) [35] which might be the major limitation in this upgrading technique[31].

Amine solutions are widely used for CO_2 removal since it has a methane recovery higher than 99%. This is due to the fact that the chemicals will only react to specific gases allowing methane to pass through, unaltered. Advantages of this technique is the ability to operate at low pressure, high CO_2 removal efficiency and high reaction rate compared to water scrubbing[42]. However, since additional chemicals are introduced into the system, they can cause salt precipitation or foaming. Treatment of chemical waste is required. Also, in case of temperature drop, water vapor can cause corrosion of material. But the most important disadvantage is the high energy consumption.

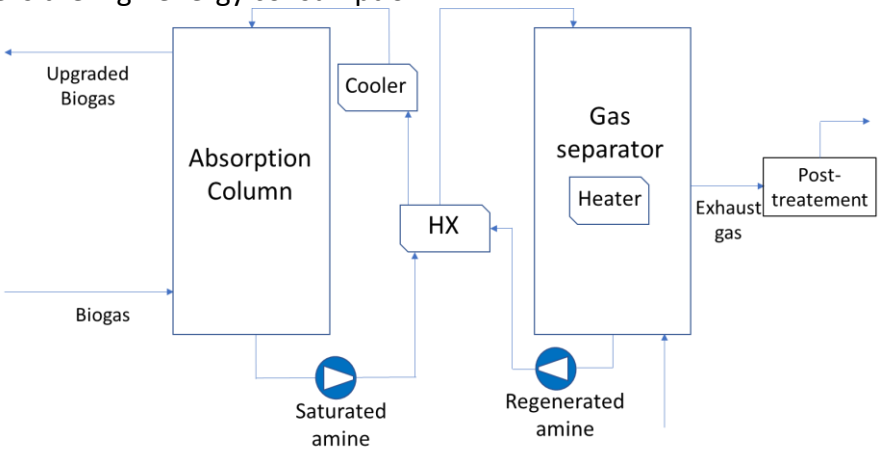

Figure 9: Schematic for chemical absorption process using amines (based on [13], [23]**)**

1.2.3. Membrane separation

When a gas or liquid passes through a solid it is called permeate, hence the term membrane permeation. The separation by a membrane depends on the concentration gradient (pressure difference from every side of the membrane) of the gases contained in a mixture, their mass diffusivity, different molecule size and the membrane's permeability[43]. In newly developed processes of gas liquid adsorption, micro-porous hydrophobic membranes are used. CO_2 is retained in the "liquid membrane" along with other impurities and methane carries on. In a study by Atchariyawut et al.[44], an aqueous NaOH solution was used as the liquid membrane and was compared to water. It was found that captured CO_2 flux was six times higher in the

NaOH solution. Increasing the temperature was more beneficial for NaOH because it increased the mass transfer coefficient while it lowered the solubility of CO_2 in water. Methane recovery was reported to be approximately 100%. If amines are used as liquid membrane, they can be regenerated with heating to release CO_2. The advantage of using a liquid membrane is that it can function at low pressure.

Another type of membrane separation is the high-pressure gas-gas permeation. These systems operate at pressures around 8-10 bar and can even get up to 20 bar; 92-97% methane can be produced[45]. The membranes retain the CH_4 at the inlet side while CO_2 and other impurities pass through it. In order to achieve more purity, several membranes can be added in series to form a multistage process producing CH_4 content more than 96% [13]. This can cause methane losses that can be avoided by recirculating off-gases. Effective CO_2 selective polyvinylamine/polyvinylalcohol blend membranes were studied by Deng et Hagg [46]. They compared four different processes and found a 2-stage cascade with gas recycling to be optimal with a 98% CH_4 purity. In a study by Scholz et al. [47], they stated that high CH_4 purity and yield cannot be achieved with single stage membrane processes. Figure 10 shows a multistage membrane separation process: biogas enters each stage with less CO_2 content in order to obtain the highest CH_4 % possible in the last stage.

The investment cost of membrane technology is estimated around 2500€/$Nm^3.h^{-1}$ for biogas flow rates of 400$Nm^3.h^{-1}$ to 6000€/$Nm^3.h^{-1}$ when reducing the biogas flow to 100$Nm^3.h^{-1}$[36]. For membrane separation, operating cost depends on the cost of biogas compression (0.2-0.38 kWh.Nm^{-3}) [35], the membrane functioning time before need of replacement and the biogas pre-treatment [41]

Membrane permeation requires low maintenance of equipment. Low energy is needed in these processes. However, the membrane cost is high unless low cost membranes are used but this can lead to a low CH_4 yield and purity.

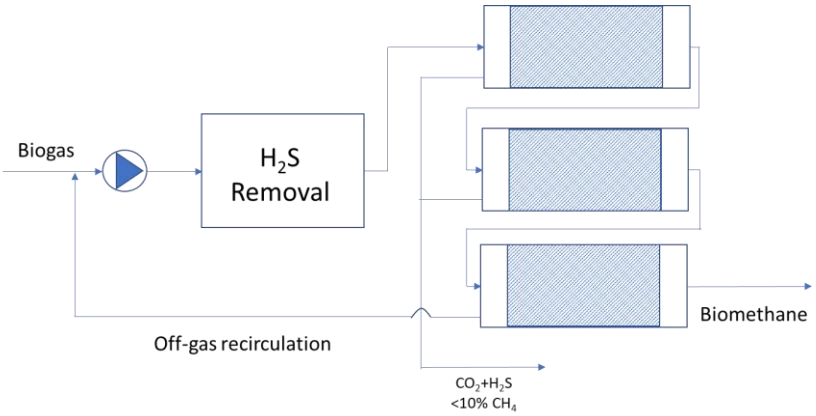

Figure 10: Schematic for membrane separation process (based on [13], [23]**)**

1.2.4. Pressure Swing Adsorption

Pressure Swing Adsorption commonly known as PSA is a process that operates at high pressure and separates gases by their binding forces to an adsorbent. Pressure increase results in more adsorption. Activated carbon and charcoal, or a molecular sieve of zeolite (micro-

porous aluminosilicate) can be used as adsorbent. Their high specific area and porous texture result in a selective separation of gases.

In Figure 11, Biogas is introduced into the adsorption column packed with adsorptive material. Upgraded biogas with high methane content passes through while CO_2 is retained in the column. When adsorbent saturation with CO_2 is attained in a batch operating mode, the packed column is depressurized to almost atmospheric pressure to release CO_2 (by desorption) which is led into off-gas stream. Some impurities should be removed in prior steps because the adsorption by molecular sieves is irreversible[48]. Several columns are required in order for the system to operate efficiently by reducing gas compression energy needs and creating a continuous operation[36].
The PSA investment cost is estimated around 2700€/$Nm^3.h^{-1}$ for a biogas flow of 600$Nm^3.h^{-1}$. It decreases to 1500€/$Nm^3.h^{-1}$ for a higher biogas flowrate of 2000 $Nm^3.h^{-1}$[45]. H_2O removal and biogas compression require around 0.24 to 0.6 $kWh.Nm^{-3}$ [41], [49].
This method leads to upgraded biogas with methane content up to 97% can be obtained [43]. It is an efficient and flexible process that can absorb many impurities from feed gas [50]. The main drawback of PSA is high gas loss because of the desorption phase where pressure is released. Mass transfer zone inside the packed column affects the system's performance directly. This method is the second most used after water scrubbing.

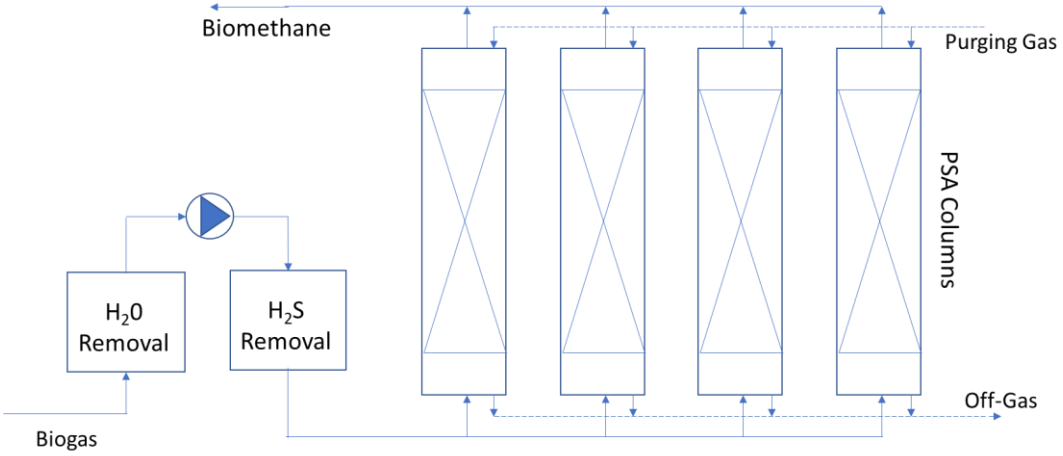

Figure 11: Schematic for pressure swing adsorption process(based on [13] [23]**)**

1.2.5. Cryogenic techniques for removal of CO_2

When a gas mixture is cooled, every component has a different condensation temperature for which it is separated from the mixture. For example, at atmospheric pressure CO_2 frosts directly from its vapor phase at -78°C, meanwhile methane liquifies at -162°C. Several studies have been conducted to improve CO_2 capture technologies. Cryogenics has several advantages: no chemical absorbents used and the process can operate at atmospheric pressure. Pure CH4 (99%) as well as pure CO_2 (98%) can be obtained with low methane losses (<1%). The methane produced is already cold reducing the cooling load needed for liquefaction. The major disadvantage of this process is the expected cooling cost of a cryogenic process which has limited the research done on this subject. Still, several cryogenic separation techniques were developed in an attempt to overcome this problem and reduce energy demands of the cryogenic process.

i. Compression-refrigeration CO_2 separation

When the CO_2 pressure increases, its phase change occurs at a higher temperature (Figure 7). It should be noted that the pressure of carbon dioxide in the mixture is equal to its partial pressure and not the pressure of the stream. Therefore, increasing the pressure of the mixture containing CO_2 increases the temperature at which cooling load is needed to remove it. This method is more suitable for streams with high CO_2 concentration otherwise increasing the partial pressure (compression) of CO_2 will be more costly than cooling it.

Suarsana [52] developed a multistage cryogenic process for CO_2 removal from biogas. The process included several separators at different P-T conditions. A high CO_2 molar concentration (71%) feed was introduced to the system. In every stage the remaining CO_2 would be compressed and cooled to be removed. The best technico-economic case study was with four separators at -15.56°C, -62°C, -90°C, -101°C and 90, 3.45, 3.45, 3.45 bar respectively. The final product contained 8.63% molar concentration of CO_2.
In 2012, Xu et al. [53] proposed a two-stage compression-refrigeration process for CO_2 separation from H_2 and liquefaction. The two-stage compression increased the pressure of the system thus the liquefaction temperature of CO_2. This reduced the cryogenic cooling load needed and the additional compression needed for liquefaction. Xu et al. studied the effect of the CO_2 concentration in the mixture and the pressure of the system on the temperature needed to remove 90% of CO_2. Like it was previously discussed it was found that less cooling is needed at high concentrations and high pressures.
Not many data can be found concerning biogas upgrading using cryogenic processes and it represents about 0.4% of all the biogas upgrading market [54]. Biomethane can provide biomethane with a high purity (99%) and low methane losses (1%) [13]. Its major drawbacks are the necessary removal of impurities like water, H_2S… prior to CO_2 removal to avoid clogging and other operational problems[36]. There's a large uncertainty in the energy needs estimation [35] but it can be approximated between 0.42 and 1 $kWh.Nm^{-3}$ which is high compared to other processes due to the high cooling load needed in these processes[36] . It should be mentioned that biomethane obtained in cryogenic separation is at low temperatures which can facilitate its liquefaction in a later step.

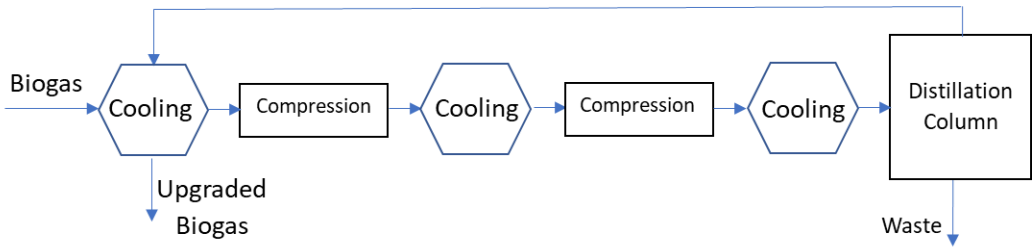

Figure 12: Schematic of cryogenic process by compression-refrigeration(based on [23] [51])

ii. Variable temperature post-combustion cryogenic separation

According to Clodic et al. [55], the only possibility of capturing CO_2 from a mixture at atmospheric pressure is frosting it on a cold surface. He introduced the term "anti-

sublimation" for the direct solidification from the gas phase. The deposition temperature of CO_2 depends on its partial pressure in the mixture. For an initial concentration of 15% of CO_2 in the flue gases which are at atmospheric pressure (CO_2 partial pressure $P_{CO2} = 0.15P_{atm}$), deposition takes place at -99°C. If the CO_2 is cooled to -122°C, the concentration of CO_2 reaches 1% so 93% of the CO_2 present in the mixture would have been captured.
CO_2 frosts on the surface of a heat exchanger for temperatures between -99°C and -122°C depending on its concentration in the mixture. In order to reduce the system losses, the temperature difference between the refrigerant and the frosting temperature must be reduced. Therefore, a refrigerant mixture which evaporates between -125°C and -102°C is selected so an average evaporation temperature of -113.5°C is reached. The CO_2 can then frost at an average temperature of -110°C. A defrosting system makes it possible to recover a part of the latent heat of sublimation/evaporation of the solid CO_2.

To remove the frosted CO_2, a "hot" cooling mixture at -50°C is introduced into the heat exchanger containing the CO_2 frost (exchanger No. 2 in Figure 13). It will be cooled by evaporating the CO_2. The evaporator containing frost is closed, the temperature and the pressure rise to -56°C and 520 kPa respectively (close to the triple point) and liquid CO_2 is recovered using a pump. The frosting/defrosting process is done alternatively between heat exchangers No. 1 and No. 2 (Figure 13). This alternation saves 35% of energy by recovering a part of the cold from the CO_2 frost. Clodic et al. calculated the energy needed for CO_2 capture with the recovery of cold by defrosting and found 1077kJ/kg of CO_2. For the whole system with the liquefaction of CO_2, he found 1224kJ /kg of CO_2.

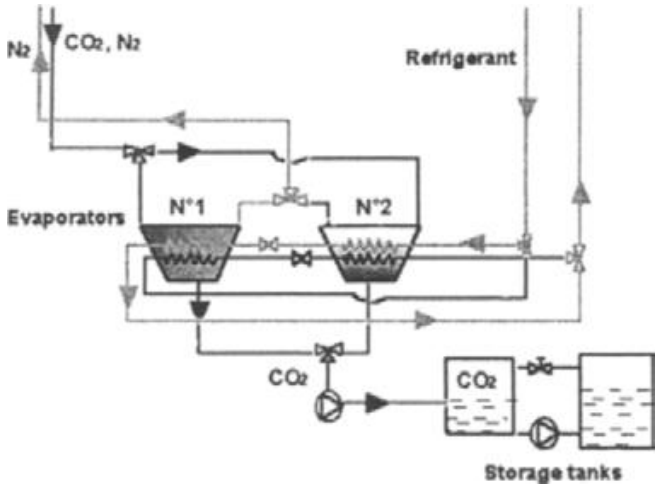

Figure 13: Schematic for CO_2 cryogenic separating from combustion gases using two alternating heat exchangers [55]

iii. Cryogenic separation using packed bed process

Tuinier et al. [56], [57] stated that the cryogenic CO_2 capture process from flue gases developed by Clodic et al.[55] is highly efficient. The CO_2 is frosted on the walls of a heat exchanger then the cold is recovered in a regeneration step at high pressure to obtain liquid CO_2. This cryogenic process showed an improvement in energy consumption by comparing it

to amine absorption. The main disadvantage is that the presence of H_2O in the inflow is not tolerated because the ice can plug the pipes; also the formation of CO_2 on the surface of the heat exchanger limits the exchanges then the efficiency of the system. Finally, it is noted that the temperature cycles in the heat exchangers occurs between -56°C and -120°C approximately, which leads to greater energy consumption in the thermal inertia of the equipment.

To overcome these problems, Tuinier et al. proposed the use of a new concept called "cryogenic packed bed process". The post-combustion flue gases at the inlet pass through a pre-cooled cryogenic packed (Figure 14), which leads to a separation of the CO_2 and H_2O from the rest of the mixture because of the different points of solid and liquid condensation. The flow that enters the bed afterwards will heat it. This flow will be cooled. The H_2O begins to condensate to reach a temperature of equilibrium between the bed and the gas. The water flows in liquid form inside the bed until it exits the system. The bed heats up at its inlet because the temperature of the flue gas is higher than the equilibrium temperature mentioned before. This causes evaporation of the condensed H_2O which in turn passes through the bed (at a slower rate than the liquid phase) to the outlet. The rest of the gas cools down to a second equilibrium temperature, that of the CO_2 which deposits inside the bed. By the same principle as water, the deposition and sublimation of the CO_2 makes it proceed to the exit of the bed. The amount separated depends on the initial cold temperature of the bed. Thus, clogging problems are overcome. When the bed temperature reaches a value at which CO_2 could pass without frost, the bed begins a regeneration phase: Pure CO_2 is introduced to recover the solid CO_2 frosted. The high temperature of the flow introduced at the bed inlet can be used to evaporate water and sublimate CO_2. When all the CO_2 is removed the bed is cooled by an inert gas.

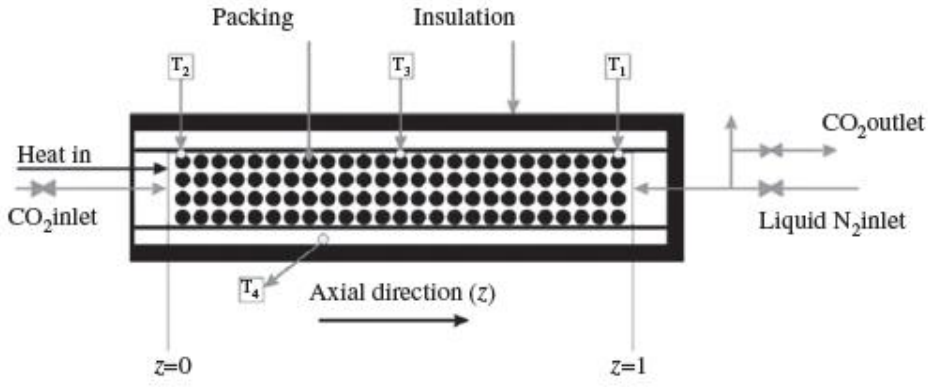

Figure 14: Cryogenic packed beds concept by Tuinier[51]

The initial cold temperature of the bed has a big effect on the amount of CO_2 separated. Tuinier et al. compared between an initial temperature of -120°C and -110°C, recovering respectively 90% and 12% of CO_2. Comparing the energy consumption in this process (1.8MJ /kg of CO_2) with the chemical absorption using amines process (3-4 MJ/kg of CO_2), Tuinier et al. found a significant improvement provided that the bed was cooled (by regasification of the LNG for example). Assuming that the cold source is electric power for compressors in refrigeration systems, the consumption can reach 3.6 MJ/kg without the losses. Tuinier et al.

compared different technologies (Cryogenic separation, amine scrubbing and membrane separation) [58] in terms of installation costs, amount of CO_2 captured, operational costs, etc., showing that membrane separation requires a very high cost of capital ($ 740M) [59] compared to cryogenics ($ 345M) and amine absorption ($ 443M) [60]. However, the operational costs of cryogenic separation in the presence of LNG as cooling means ($126.5/tonne of CO_2) and low pressure vapour amine absorption with solvent separation ($133.4/tonne of CO_2) exceed those of membrane separation ($120.9/tonne of CO_2). Tuinier et al. explained that the choice of technology depends mainly on the availability of utilities.

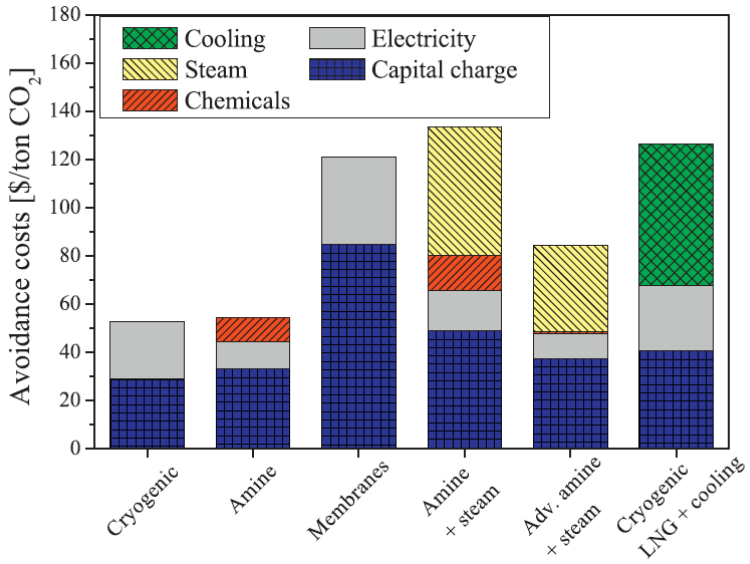

Figure 15: Comparison between the costs of different CO_2 removal technologies[58]

iv. Cryogenic separation by Stirling machines

Song et al. [61] proposed a new post-combustion cryogenic CO_2 capture process using Stirling machines. This cryogenic system has many advantages: high efficiency, high reliability and small size [62]. Water vapour and CO_2 present in the combustion gases were captured at different places in the process over the surface of heat exchangers cooled by Stirling machines. The most important notion in this capture process is that the CO_2 in the flue gases is captured in solid form (without going through the liquid phase). When CO_2 is in contact with the cold surface of the heat exchanger at a temperature below its sublimation temperature, it solidifies and then gets separated from the gas mixture.

The sketch of the cryogenic process based on Stirling Coolers is described in Figure 16. In the process, the feed gas is separated into three streams: condensed water, dry ice (CO_2 frost) and residual gas. In the first Stirling machine, the water in the flue gas condenses in a pre-cooling process by "SC-1" and then the liquid flows through the condensation pipe to the outlet. The other gases flow in the main freezing tower, at atmospheric pressure and cryogenic temperature, the CO_2 gas frosts on the surface of the "SC-2" heat exchanger. It is then stored in the cooled storage column in cryogenic conditions controlled by "SC-3". On the other hand, the residual gas (N_2 and O_2) leaves the system through the vent.

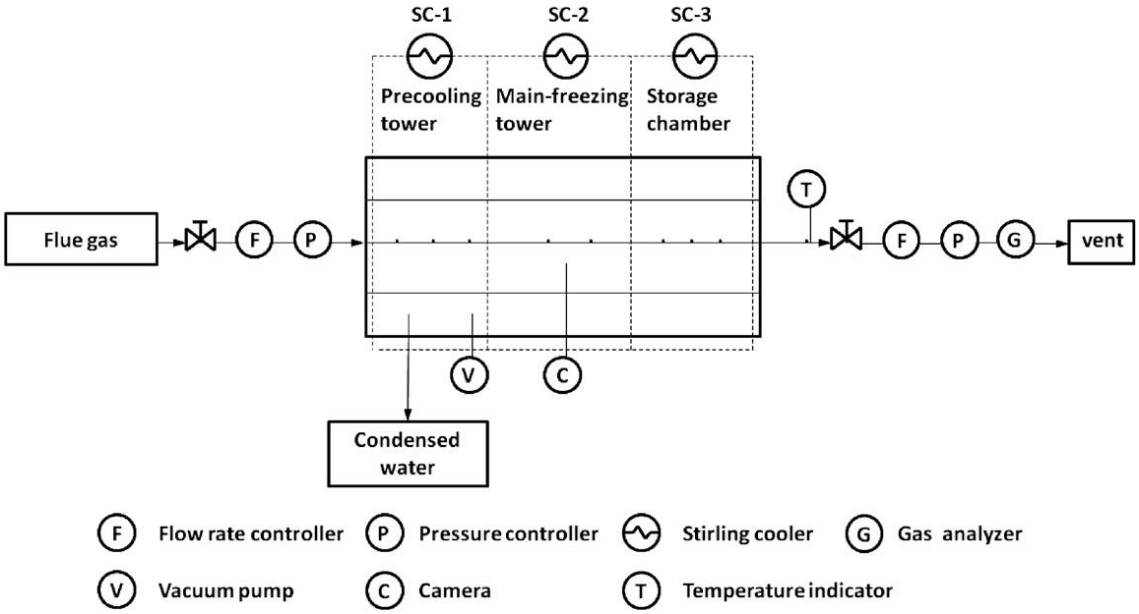

Figure 16: System of cryogenic capture of CO_2 contained in the combustion gases by the Stirling machine[61]

To facilitate the construction of the mathematical model of the system, the following assumptions have been made by Song et al. [61]:

- The deposition process takes place in a quasi-steady state. This hypothesis makes it possible to calculate mass and energy balances for a time step. During this step the properties of flue gases and frost are determined. Then, it is possible to calculate the heat and mass transfer and to monitor the evolution of the system[63].
- The distribution of the frost layer is homogeneous on the cooling surface.
- The conductivity of frost varies only with its density
- No heat transfer by radiation between the gas flow and the frost layer.

These assumptions should be taken into consideration when constructing a frosting model, they can be found in many references in the literature and will be detailed in chapter 2 when the CO_2 deposition model used in this thesis is presented. To calculate the mass flux of frost formed on the cold surface, Song et al. use the analogy between heat and mass transfer that is based on the difference in CO_2 concentration between the gas flow and the cold surface. Instead of using concentration, they used the density because the system is at constant volume.

$$\dot{m}_{co2\_frosted} = h_{m,co2}(\rho_{co2,flue\_gases} - \rho_{co2,frost\_surface}) \quad (1.1)$$

CO_2 is considered an ideal gas and densities are calculated by the ideal gas law under saturation conditions with known P and T conditions. The volume of frost can then be calculated and knowing the exchange surface the thickness can be calculated. Heat transfer in the system can be divided into three major parts: convection between the gas flow and the solid surface, conduction in the frost and a latent heat of CO_2 solid condensation. The convective heat exchange coefficient correlations are chosen according to the geometry of the cold surface and the type of the flow.

Song et al. compared CO_2 removal cost by amines absorption in a power station with cryogenics done in the laboratory. He found that the cost of the kg of CO_2 can be reduced by 0.003$ using cryogenics but with an energy penalty of 1.5 MJ power/kg of CO_2 while the chemical absorption using MEA has a penalty of 1.6 MJ power/kg of CO_2.

Another study was conducted by Jonsson and Westman [64] on the cryogenic separation of CO_2 from biogas using plate heat exchanger. This will be discussed in detail in chapter 3.

1.2.6. Comparison between different biogas upgrading technologies

Table 2 shows the advantages and disadvantages of each CO_2 removal technique as well as the methane yield and purity at the outlet of the pre-combustion treatment. As it was cited before, water scrubbing and membranes have low energy demands but don't give the best results in terms of methane purity and yield. If the main objective is to obtain the highest methane purity then chemical absorption using amines and cryogenic separation are the processes that should be considered. But they both present a common disadvantage: high operating cost. In chemical absorption high energy is needed for solvent regeneration and in cryogenic systems high cooling load is required even though it lowers the biomethane temperature which facilitates its liquefaction.

Removal of CO_2 in pre-combustion gives biomethane with higher calorific value. It can be liquefied and transported. It can be used in transportation. All these options are not present in post-combustion. But the issue remains with the high energy need for cooling. In this thesis a solution to this problem is presented where CO_2 removed from biogas through cryogenic separation is reused to capture more CO_2.

Table 2: Comparison between different biogas upgrading technologies[35], [36], [43], [65]

Biogas upgrading technology	Advantages	Disadvantages	Methane Loss	Methane purity
Water Scrubbing	• CO_2 and H_2S are removed in the same process • Low methane losses, possible regeneration • The technology is established and in use • Energetically efficient	• Bacterial growth might cause clogging • No flexibility of input gas • Possible foaming occurrence • Very high water consumption	<2%	>97%
Chemical Absorption using amines	• High methane purity • Low methane losses • More efficient than water as more CO_2 is dissolved per unit volume of amines than water • Regenerative	• Expensive, heat required for regeneration • Presence of O_2 might cause corrosion and poisoning • Possible foaming and formation of salt participate • High maintenance cost	<0.1%	>99%
Membrane Separation	• Simple process and operation • Low methane losses • H_2S and H_2O are removed simultaneously • No waste from the process	• Necessity of compromise between methane purity and quantity • Requires multi-step configuration for high purity • Low membrane selectivity	~0.5%	>96%
Pressure Swing Adsorption	• High methane purity • CO_2 and H_2S are removed in the same process • Established and developed technology • No waste streams • Tolerant to impurities	• Expensive process and operation • Valves malfunction might cause methane losses • High maintenance cost • Continuous and delicate process control	<3%	~98%
Cryogenic separation	• High methane purity • Pure CO_2 can be stored and reused • Low additional energy for methane liquefaction	• Newly developed process • High energy required for cooling • Expensive operation and investment • Low energy efficiency because of the cooling load	<1%	>99%

1.3. Evaporative cooling

Cryogenics can recover more than 98% of CO_2. In all cryogenic CO_2 capture systems, the same problem limits studies: the cost of cooling. In the system designed by Tuinier et al., part of the cold contained in the solid CO_2 was recovered in the evaporation phase to cool the packed bed. In the system designed by Clodic et al., part of the cold is recovered by evaporating the CO_2 with a refrigerant at -50°C and the frost is sublimated in a closed volume then reaches -56°C with a pressure of 520 kPa to recover liquid CO_2.

Since the percentage of CO_2 valorised in industrial uses is very little compared to the total worldwide CO_2 emissions (0.5%), storing CO_2 seems to be less interesting. On the other hand, what if it was possible to recover all the cold contained in the solid CO_2 separated from biogas (or flue gases) during the cryogenic biogas upgrading with a reduced temperature cycling in the heat exchangers?

The study conducted in this thesis is placed in this context of cryogenic CO_2 separation from biogas in a first step and cold recovery from the CO_2 frosted in a second step. The cold recovery will be achieved by controlled sublimation, a concept that can be found in cooling towers. The principles of controlled evaporation will be explained then its application in the biogas case study will be described.

1.3.1. Evaporative Cooling: General concept

Many cooling systems provide cool air for domestic and industrial use. The efficiency of these systems is defined by its energy consumption and its environmental impact more precisely carbon dioxide emissions to the atmosphere. Conventional evaporative cooling is a simple technique that uses only air and water with no other chemicals nor refrigerants. Also, the compressor in conventional refrigeration cycles is replaced by a fan with a much lower power consumption[66]. As dry hot air welcomes water, its humidity increases as water evaporates due to the heat transfer with the air stream and the “moisture” gradient between the gaseous and liquid streams. The increase of water vapour concentration in the air stream decreases its temperature. The result is a cold stream of air and low energy consumption[67]. Evaporative coolers are more efficient in dry conditions. It is also possible to use evaporative cooling for water regeneration in cooling towers.

There are two types of evaporation cooling: direct and indirect.

i. Direct Evaporation Cooling

Figure 17 shows the concept of direct evaporative cooling. Hot dry air enters a wet channel and is in direct contact with water. Heat transfer occurs from the air stream to the water. Air is cooled down by sensible heat transfer towards the cold water which evaporates by latent heat. Water vapour diffuses in the air stream increasing its water vapour content and decreasing its temperature. The enthalpy of the air stream does not change as its temperature decrease is met by humidity increase[68]. Direct evaporative cooling is a simple process but its disadvantage is possible high humidity in the outlet air which might be undesirable.

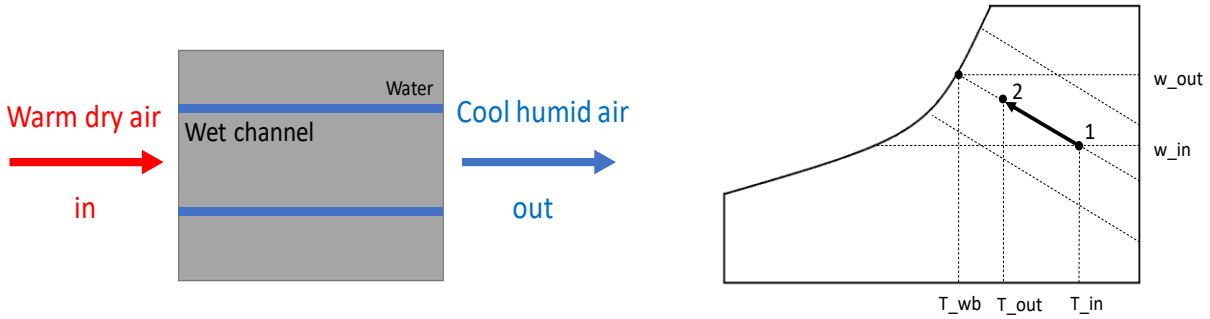

Figure 17: Direct evaporative cooling

ii. Indirect Evaporation Cooling

This concept solves the problem of high humidity content in outlet air by using two inlet air streams. The product air that will be used at the end flows inside a dry channel (Figure 18). It is connected to the wet channel by a heat exchange surface. Another airstream flows through the wet channel like in the case of direct evaporative cooling but with a supplementary sensible heat transfer from the product air flowing in the dry channel. The heat from the two air streams will evaporate the water as they cool down. The humidity of the product air remains the same as it is not in direct contact with water. The air flowing in the wet channel remains at constant enthalpy.

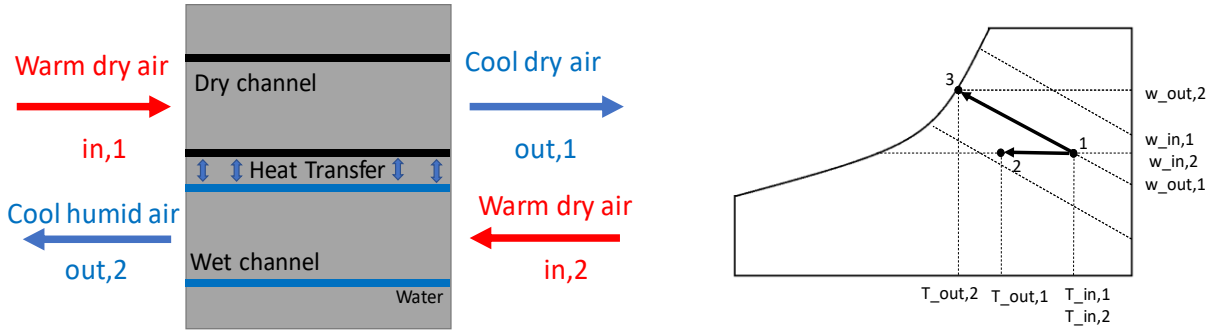

Figure 18: Indirect evaporative cooling

The issue of high humidity in the product air was resolved in this process but its temperature decrease is still limited by the air flowing through the wet channel. It is possible to precool the secondary air stream before it passes in the wet channel like in the Maisotsenko-cycle (Figure 19). This allows further cooling of the product air[69].

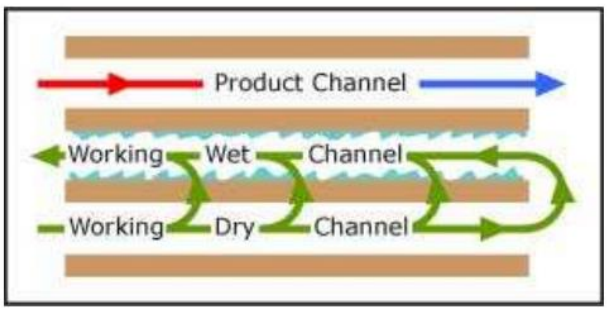

Figure 19: M-cycle principle of heat and mass exchange[69]

1.3.2. Evaporative Cooling in cooling towers

A cooling tower is a heat rejection device. Its main function is to extract residual heat from hot water present in the atmosphere of the tower in order to generate a stream of water at a temperature lower than the ambient[70]. Heat rejection in the cooling tower is specified by convection heat transfer between fine water droplets and the surrounding air, and evaporation of a small portion of water in the moving air[71]. So the process involves both heat and mass transfer. Cooling towers are widely used in most power plants, air conditioning and refrigeration industries, etc.[72].

Mechanical draft cooling towers are widely used in industry for the deep cooling of circulating water[73] . The height of the mechanical draft cooling towers can vary from 2m to 12m. The basic elements of these cooling towers are the shell, the water distribution system, water collection basin and the fan to create an artificial exhaust. In a cooling tower a polydispersed set of droplets is formed by nozzles which spray water. Although in the industry cooling towers with rather wide distribution of droplet rays are used, in most evaporative cooling simulations a droplet volume is considered.

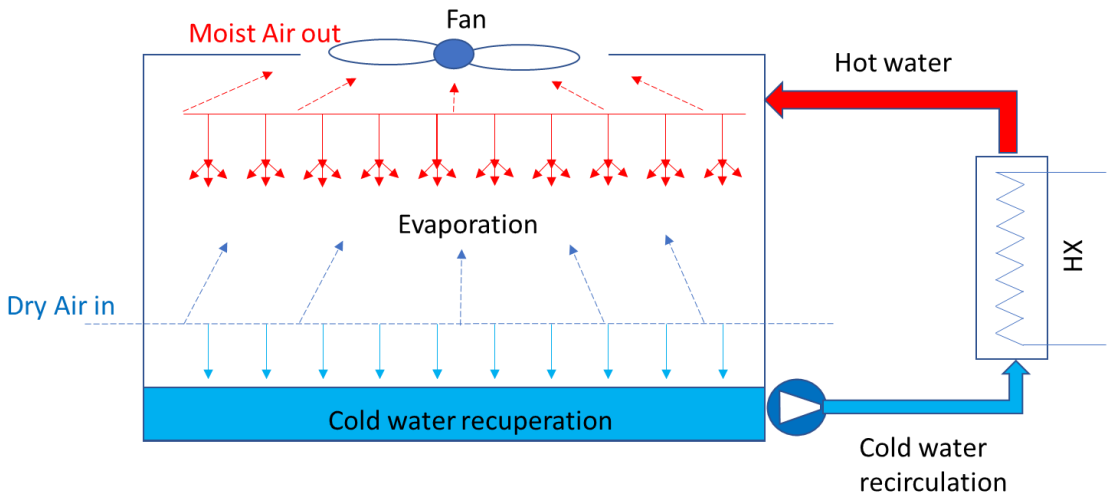

Figure 20: Schematic of a cooling tower operating(based on [74]

The solution of a problem describing two phases moving in opposite directions gives a complete understanding of cooling by evaporating the water droplets. As droplets fall, water comes into contact with the air that is injected in the cooling tower. Air is colder than the hot water stream so water is cooled by convective heat transfer. Also, a part of the water droplet is transferred into the air stream due to water vapour concentration difference between the water droplet and the relative water content in the air. With increasing droplet velocity, the interaction time with colder air is reduced. On the other hand, as the air rises, it is heated and saturated with water vapour. This reduces the intensity of heat transfer and mass droplets during evaporative cooling. In a one-dimensional approximation, the average air speed is considered constant over the height of the section. The airflow velocity is determined by the fan power and its aerodynamic drag. Unlike natural draft cooling towers, where the convection speed depends on the degree of air heating and its degree of water vapour saturation. In a cooling tower, heat

and mass transfers depend on the specific mass flow rates of water and air, as well as the temperature and relative humidity of the air entering the cooling tower, the temperature of the hot water entering the cooling tower, wind speed and atmospheric pressure (73).
Three media of heat and mass transfer are considered in a cooling tower [75]:

- The flow of water that cools
- The air flow whose humidity increases for carrying water vapour from the water surface
- An interstitial film between a water droplet water and air.

The assumptions made are as follows:

- The air coming out of the tower is almost saturated
- The interstitial film is air saturated with moisture at the water temperature
- The number of Lewis is equal to 1
- All the thermal transfer of the liquid is on the air side.

Considering a mass flux of water droplets inside the cooling tower. The energy balance of the water droplets can be described as follows:

$$\dot{q}_w = \dot{m}_w \times c_{p,w} \times \Delta T_w \quad (1.2)$$

where $\dot{m}_w$ is the water droplets mass flux and ΔT_w the water droplets temperature difference between their inlet to the cooling tower in the "hot stream" and their exit through the pump as "cold water recuperated" (see Figure 20).

The energy Q_w is used to heat the air by convective heat transfer Q_{sens}, and to evaporate the water that will be transported by the dry air stream which is the latent heat transfer Q_{lat}.

$$\dot{q}_{sens} = h_c \times (T_{w,surf} - T_{air}) \quad (1.3)$$

where h_c is the coefficient of heat transfer, $T_{w,surf}$ being the temperature of the water droplets surface (the interstitial film) assumed to be equal to the temperature of the water droplets, and T_{air} that of the air.

$$\dot{q}_{lat} = h_m \times (x_{w,surf} - x_{w,air}) \times L_{lv} \quad (1.4)$$

h_m being the coefficient of mass transfer linked with h_c the heat transfer coefficient, $x_{w,surf}$ being the relative saturation humidity of the film and $x_{w,air}$ that of the air. L_{lv} represents the latent heat of vaporization of water.

Therefore, the energy balance of the hot water droplet in contact with the dry air can be summarized by Eq.1.2 and Eq.1.5:

$$\dot{q}_w = h_c \times (T_{w,surf} - T_{air}) + h_{mass} \times (x_{w,surf} - x_{w,air}) \times L_{lv} \quad (1.5)$$

Other simplifications can be made but what is important is that the terms $(T_{w,surf} - T_{air})$ and $(x_{w,surf} - x_{w,air})$ are always positive which means that ΔT_w will always be a positive term so the water will cool down.

1.3.3. Cooling by sublimation

Similarly to evaporative cooling, it is proposed to use the sublimation of a solid to cool a gas flow with a different chemical compound that makes a reduction of partial pressure of the deposit lager. Very few, event non, applications can be found and the concept is not as "famous" as evaporative cooling.

i. Cryogenic-solid cooling system

Gross et al. [76] suggested a system of solid-cooling for applications with small heat transfer in space. The apparatus presented in Figure 21 consists of an insulated container filled with a cryogenic solid (solidified methane, neon, hydrogen, nitrogen), a conduction rod connecting the solid coolant to the device to be cooled and a channel for sublimated solid to be released into the atmosphere.

The system uses the relation between temperature and vapour pressure. For example, if the solid coolant is at $T_{s-c}°K$, its vapour pressure will be $P_{s-c}\ bar$. If the pressure is to remain constant over the solid, its temperature will not change [76]. When the solid coolant is heated by the conduction rod, it is sublimated. The pressure and the temperature increase. If the supplementary vapour is rejected to the atmosphere through the pressure control port, then it is possible to maintain the same temperature $T_{s-c}°K$ in the system. Conductive heat transfer will not decrease and it is possible to maintain the same cooling potential. The temperature of the system depends on the solid coolant and pressure control of the system.

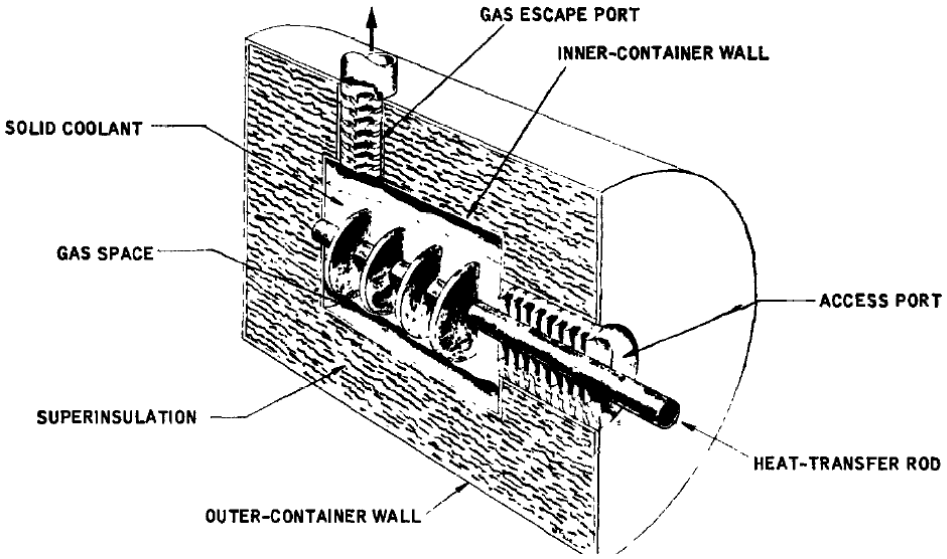

Figure 21: Model of Cryogenic-Solid Cooler[76]

Gross et al. conducted a study to determine the optimal dimensions of such systems depending on the desired temperature and time of operation. Insulation was the major problem especially at the access ports. An experimental study was conducted and the temperature of the conduction rod remained constant as the solid coolant was undergoing sublimation.

ii. Sublimation cooling with dry-ice sprays

As it was mentioned before, cooling systems usually use the liquid vaporization instead of solid sublimation. Coolant liquids are more available and circulate easily unlike solids who cannot be used in a closed circuit system. If the amount of heat given to the liquid coolant is not enough

to vaporize it all, a liquid film will form, reducing further evaporation and cooling performance. This problem can be avoided using the solid coolant. Sublimation spray cooling consists of two stage: the expansion of liquid CO_2 and the heating of solid+gas CO_2. On the CO_2 phase diagram shown in Figure 22, point A is the initial state; the system contains liquid CO_2. Isenthalpic expansion decreases the pressure to get to point B and obtain solid+vapor CO_2. As the cooling spray reaches the hot surface, the solid fraction in the spray decreases and eventually its temperature increases to get to point C. The CO_2 phase diagram was taken from "CO_2 transcritical systems Training Manual"[77].

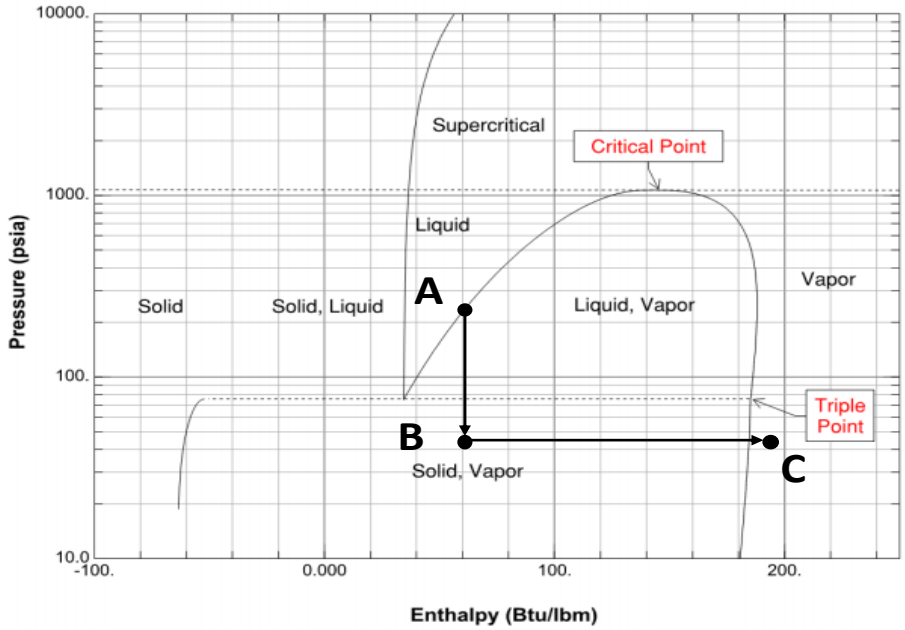

Figure 22: CO_2 phase diagram Pressure vs Enthalpy

In a study by Panão et al. [78] on thermal assessment of sublimation spray cooling using dry-ice, they stated that most applications using dry-ice are for surface cleaning purposes [79] with no usage of the thermal effect of sublimation. They concluded that dry ice particles are an advantage when it comes to cooling applications.

1.4. Discussion and framework for this thesis

1.4.1. A new concept of cryogenic CO_2 separation with cold recovery using controlled sublimation

What is proposed in this thesis is to build a model to simulate controlled sublimation cooling (sublimation of CO_2) in order to reduce the energy needs of cryogenic CO_2 capture processes. The chosen application case for this thesis is the controlled sublimation of frosted carbon dioxide during the purification of biogas. The sublimation heat of the CO_2 frost would be optimally recovered by the controlled sublimation of frost by a third gas. The latter is expected to dramatically reduce the energy consumption of carbon dioxide separation.

The controlled sublimation case is similar to direct evaporative cooling, e.g. the concept of cooling towers. It is also possible to use indirect evaporation cooling in the application presented in this thesis and it will be discussed later in details.

In the concept of controlled evaporation in conventional cooling towers, dry air cools the water by evaporating it, but its temperature is not necessarily equal to the evaporation temperature of water given the driving force of initial moisture content in the dry air and the potential to reach a high content of- water. Hence, by analogy, it is possible to evaporate the CO_2 frost by another fluid that generates a mass transfer driving force (concentration) at frost temperature.

In the particular case study, since the biomethane leaving the heat exchanger after CO_2 separation is already at a very low temperature, the cooling load needed to liquify it is reduced. Liquid nitrogen can be used to accomplish this step. While methane is being liquified by liquid nitrogen, the latter is being vaporized and can be used in a further step for the defrosting of CO_2. Even if the nitrogen gas temperature is inferior to that of the frost, sublimation will occur and cold is expected to be recovered by the controlled sublimation of solid CO_2. In the work carried out in this thesis, the new concept for cryogenic capture and cold recovery can be presented in 2 major parts:

1.4.2. CO_2 frosting

The first part of the concept is the CO_2 deposition on a cold surface and this demands a better understanding of the carbon dioxide frost properties and the phenomena involved. CO_2 frost properties are barely available as the state of the art on frosting shows mainly the case of water vapour contained in moist air. In the literature, no comparable experimental results are found for deposition of CO_2 contained in biogas and very few results of experimental results are found for CO_2 frost deposition from flue gases. In order to validate the model proposed in this work, the case of CO_2 frosting from flue gases will be studied as a first step before applying it into the biogas treatment case study.

In order to apply the study to a process for biogas upgrading, the deposition of CO_2 from biogas over a cold surface (Figure 23) will be studied for different operating parameters and different heat exchanger geometries in order to choose the best conditions for CO_2 cryogenic separation from biogas.

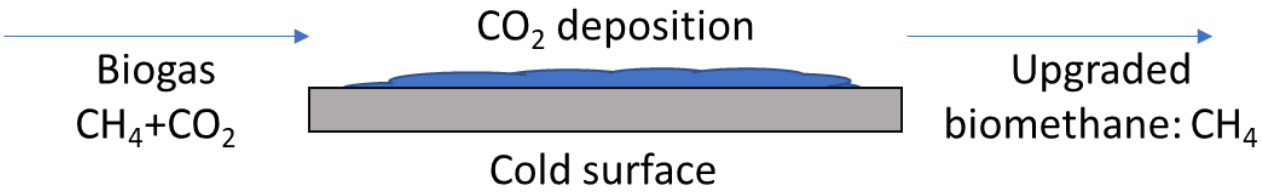

Figure 23: Simplified scheme of biogas cryogenic upgrading by CO_2 deposition

1.4.3. CO_2 controlled sublimation

The second part consists on the novelty added to the cryogenic separation process: the CO_2 controlled sublimation near atmospheric pressure. Upgraded methane exited the heat exchanger where CO_2 frost is contained. A third fluid, preferably at a lower temperature (or equal) than the frost will pass and evaporate CO_2 by concentration difference between the frost surface and the flow (Figure 24). This sublimation will cool the CO_2 frost and eventually the heat exchanger. The now cold heat exchanger can be reused for cryogenic CO_2 removal from biogas

in batch mode. The phenomenon of CO_2 sublimation by controlled sublimation, its limits and optimization are studied.

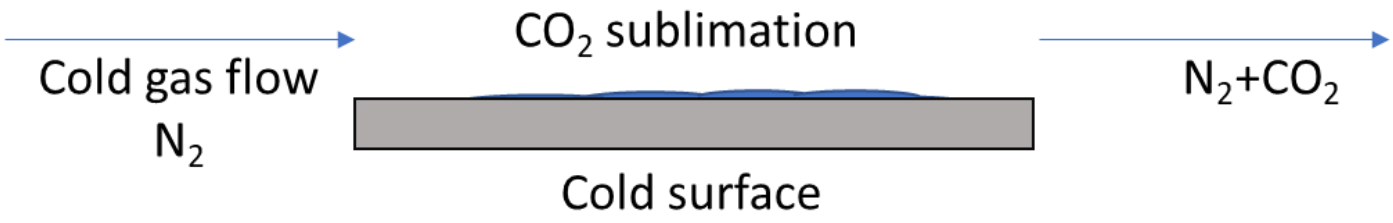

Figure 24: Simplified scheme of solid CO_2 defrosting using a third gas as part of sublimative cooling

As an additional study and as it was mentioned before, the CH_4 resulting from cryogenic sublimation is already at a very low temperature. Its liquefaction is made easier by this fact. Since a cold fluid is needed for CO_2 sublimation, the same fluid can be used for CH_4 liquefaction. In a more global view on the concept, liquid N_2 will be used to liquify upgraded methane, evaporate CO_2 frost and cool down the biogas entering the biomethane upgrading process. In order to optimize the process, alternative frosting and defrosting will be discussed. Also, other configurations can be applied to this concept and will be discussed later in this thesis.

1.4.4. Scientific objectives of this thesis

The main scientific objectives of this thesis can be summarized as follows:

- Understanding the concept of cooling by controlled sublimation and its application.
- Study of CO_2 phase change from solid to vapour and vice-versa, collecting data of the thermophysical properties and modelling the frost formation phenomenon.
- Applying knowledge of the CO_2 deposition phenomenon in a cryogenic biogas upgrading and liquefaction process, and optimization of the system.
- Applying the concept of evaporative cooling on CO_2 frosted from biogas for cold recovery and energy saving by sublimation cooling.
- Validating the work through an experimental procedure.

Chapitre 1: Contexte et état de l'art sur la séparation du CO_2 et le refroidissement par sublimation

Le monde est confronté à un problème d'approvisionnement et de sécurisation des ressources énergétiques durables nécessaires pour couvrir les besoins énergétiques industriels et domestiques. L'indépendance énergétique vis-à-vis des sources non renouvelables (et polluantes) et le déploiement de technologies de récupération des énergies propres et renouvelables deviennent une nécessité. Selon la Figure F1, les combustibles fossiles représentaient 84% de l'énergie totale en 1990 tandis que les énergies renouvelables contribuaient à environ 10%. En 2015, ces dernières ont augmenté pour couvrir 12% de l'énergie totale, mais les combustibles fossiles sont restés à 84% avec une augmentation de 20% de la consommation mondiale d'énergie. En 2040, les combustibles fossiles devraient représenter 77% du total et la part des énergies renouvelables devrait atteindre 17%. Bien que l'énergie renouvelable et l'énergie nucléaire contribuent de plus en plus à la consommation mondiale d'énergie, il reste encore beaucoup à faire pour que ces sources couvrent les besoins mondiaux en énergie.

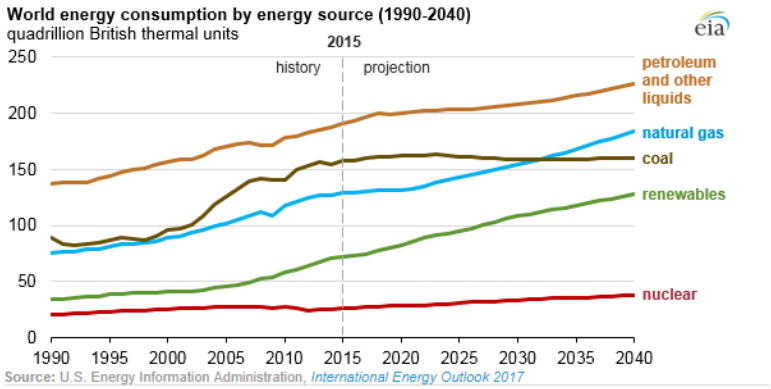

Figure F1: Consommation mondiale d'énergie par source d'énergie [3]

En plus de la disponibilité limitée, le problème de l'énergie d'origine fossile est son impact sur l'environnement. Elle est la cause principale des émissions de CO_2 responsables de l'effet de serre et du réchauffement climatique. D'où l'importance de remplacer les combustibles fossiles par des sources d'énergie renouvelables. L'énergie solaire, l'énergie éolienne, l'hydroélectricité, la biomasse et d'autres solutions ont été proposées comme sources d'énergie alternatives pour réduire les émissions de CO_2. Dans ce contexte, ces travaux de recherche porteront sur la version renouvelable du gaz naturel, le biométhane, en tant que cas d'étude de la technique d'épuration cryogénique suivie par une sublimation contrôlée de la phase solide afin de réduire la consommation d'énergie.

1.1 Le biogaz comme énergie renouvelable

On estimait que la majeure partie des énergies renouvelables sera fournie par la biomasse d'ici 2020, en particulier le biogaz, avec une contribution d'au moins 25%[6]. Ainsi, la production énergétique de biogaz à partir d'installations commerciales devrait doubler en passant de

14,5GW en 2012 à 29,5GW en 2022[4]. La demande de biogaz devrait augmenter de manière continue dans les années à venir, principalement pour des raisons environnementales. Le biogaz est produit à partir de matières organiques contenant du CO_2 présent dans l'atmosphère, contrairement aux combustibles fossiles qui vont libérer dans l'atmosphère le CO_2 qui se trouvait sous terre, entraînant un réchauffement planétaire. Dans plusieurs pays (Suède, France, Allemagne, Pays-Bas ...) du biométhane est produit déjà à l'échelle industrielle (utilisable comme carburant) à partir de biogaz [9]. Une étude réalisée par le Syndicat des énergies renouvelables (SER) et des opérateurs de réseaux de gaz (GRDF, GRTgaz, TIGF)[5], montre qu'en France, la production de biométhane a progressé de 162% en un an (2015-2016) pour atteindre 215GWh. Même si cela semble peu probable, le gouvernement a pour objectif d'atteindre 8TWh de biométhane injecté en 2023[10] et produire entre 14 et 22TWh en 2028, ainsi le biogaz représentera entre 6 et 8% de la consommation totale de gaz en France [11].

1.1.1 Du biogaz brut à l'injection de biométhane dans le réseau de gaz naturel

La production de biométhane passe par plusieurs étapes. Tout d'abord, la biomasse (déchets alimentaires, ordures ménagers organiques, déchets agricoles) est collectée. Ensuite, elle subit une fermentation dans des conditions anaérobiques pour obtenir du biogaz. Le biogaz est épuré et toutes ses impuretés sont éliminées. Le produit final peut ensuite être injecté dans le réseau pour un usage domestique ou industriel.

La composition du biogaz peut varier en fonction de la source de matière organique. Cependant, les principaux composants sont le méthane CH_4 et le dioxyde de carbone CO_2. Au cours de la phase d'épuration du biogaz, le CO_2 sera éliminé afin d'obtenir un biométhane aux spécifications requises en fonction de son utilisation finale. L'importance de la production de biogaz ne se limite pas à l'élimination des déchets organiques mais s'étend à une valorisation en circuit court domestique ou industrielle dans les domaines thermique et électrique[13].

1.1.2 Valorisation du biométhane

En plus de son injection dans le réseau de gaz naturel pour être utilisé dans l'industrie et pour utilisation domestique, le biométhane peut être utilisé dans le secteur des transports pour les voitures et les camions. Les véhicules utilisant du gaz naturel comprimé (GNC) ou du gaz naturel liquéfié (GNL) comme carburant contribuent au développement d'un secteur de transport écologique, propre et émettant peu de GES.

Pour que le biogaz, en tant qu'énergie renouvelable et propre, remplace le combustible fossile traditionnel, il faut le traiter et surtout réduire sa teneur en dioxyde de carbone. Bien que le CO_2 ne soit pas aussi nocif et corrosif que les autres impuretés, il diminue le pouvoir calorifique du biogaz [23]. Le biogaz brut a une valeur calorifique moyenne d'environ 30MJ/kg, son passage au biométhane contenant 90% de CH_4 augmente son pouvoir calorifique à 45MJ/kg [24]. Cette valeur est légèrement inférieure à celles du diesel et l'essence respectivement 45,6MJ/kg et 46,4MJ/kg [25]. Dans cette thèse, l'accent sera mis sur l'élimination du CO_2 du biogaz et comment réduire sa consommation énergétique lorsqu'on considère une épuration cryogénique. Différentes techniques ont été conçues pour valoriser le biogaz. Elles seront présentées et comparées dans ce chapitre.

1.2. Epuration du biogaz et séparation du CO_2

Le dioxyde de carbone à l'état pur est utilisé aujourd'hui dans l'agriculture dans les serres, l'industrie pharmaceutique et l'industrie alimentaire. Le CO_2 est un composant de base dans l'industrie chimique. L'utilisation mondiale de CO_2 dans les procédés industriels est estimée à 200Mt par an, soit l'équivalent de seulement 0,5% des émissions totales de CO_2[26].

Le CO_2 solide, également connu sous le nom de neige ou glace carbonique, est un réfrigérant qui se sublime à la pression atmosphérique. Son point triple est à P=5,1bars et T=-56°C. Tout ce qui se situe en dessous de ces conditions entraînera un passage direct du CO_2 de sa phase solide à sa phase gazeuse et inversement.

Dans la suite, plusieurs techniques d'élimination du CO_2 sont présentées. Il est important de préciser que, même si les travaux de cette thèse portent sur l'élimination du CO_2 présent dans le biogaz en précombustion, le concept proposé ultérieurement peut être utilisé en post-combustion, cela sera souligné au chapitre 2. Les techniques d'élimination du CO_2 présentées sont considérées pour un traitement en précombustion.

1.2.1. Lavage à l'eau (absorption)

Le lavage à l'eau est une absorption physique basée sur les différentes solubilités des composants d'un mélange gazeux dans un liquide (eau) [32]. Le biogaz brut est mis sous pression jusqu'à 'environ 6 à 12 bars. Il est ensuite mis en contact avec de l'eau, à contre-courant, dans une colonne de lavage à garnissage qui assure un transfert de masse gaz-liquide élevé. Pendant que le biogaz traverse la colonne, le CO_2 (ainsi que les autres impuretés) est capté. Le biogaz épuré peut être collecté et l'eau contenant les impuretés continue vers une colonne de désorption régénérative. Le principal avantage de ce processus est l'élimination simultanée de nombreuses impuretés telles que le CO_2, H_2S, NH_3… [37] en utilisant uniquement de l'eau; aussi, la consommation d'énergie est faible dans ce processus. Le principal inconvénient du système de lavage à l'eau est la quantité importante d'eau nécessaire même avec la régénération; pour éviter l'accumulation de sous-produits nocifs, en particulier H_2S, 20 à 200L.h^{-1} d'eau doivent être constamment purgés.

1.2.2. Absorption chimique

L'absorption chimique s'effectue à l'aide d'un solvant dans lequel les gaz acides contenus dans le biogaz seront séparés par des réactions chimiques. Plusieurs types de composés chimiques alcalins peuvent être utilisés dans le traitement de biogaz tels que KOH, NaOH…[39] et les alkanolamines[23]. Dans le procédé d'absorption chimique, le biogaz brut est introduit à une colonne d'absorption à garnissage (de la même manière que le lavage à l'eau) où le CO_2 est éliminé par les amines. Ensuite, les traces d'amines sont éliminées par un lavage à l'eau. Le biogaz épuré sort de la colonne, tandis que les amines passent par une autre colonne où elles sont régénérées (colonne de désorption ou stripper). L'absorption chimique peut fonctionner à basse pression, ce qui nécessite une consommation d'énergie modérée pour la compression du biogaz et le pompage de solvant (0,12-0,15kWh.Nm^{-3})[41]. Cependant, le solvant utilisé pour éliminer le CO_2 se régénère à une température comprise entre 120 et 150°C, ce qui nécessite une consommation d'énergie élevée (0,55 kWh.Nm^{-3})[35] ce qui limite l'utilisation de cette technologie d'épuration du biogaz [31].

1.2.3. Séparation par perméation membranaire

Lorsqu'un gaz ou un liquide passe à travers un solide, il est appelé perméat, d'où le terme perméation membranaire. La séparation par une membrane dépend du gradient de concentration (différence de pression de chaque côté de la membrane) des gaz contenus dans un mélange, leur diffusivité massique, la taille de molécule différente et de la perméabilité de la membrane[43]. Si les amines sont utilisées comme membrane liquide, elles peuvent être régénérées avec chauffage pour libérer du CO_2. Un autre type de séparation membranaire est la perméation gaz-gaz sous haute pression. Ces systèmes fonctionnent à des pressions autour de 8-10 bars et peuvent même atteindre 20 bars; du biométhane contenant 92 à 97% de CH_4 peut être produit [45]. Les membranes retiennent le CH_4 tandis que le CO_2 et d'autres impuretés les traversent. Afin d'obtenir des niveaux de pureté plus élevée, plusieurs membranes peuvent être ajoutées en série pour former un procédé à plusieurs étages produisant du biométhane contenant plus que 96% de CH_4 [13]. Scholz et al. [47] ont démontré qu'une pureté et un rendement élevés simultanés en CH_4 ne peuvent pas être obtenus avec des procédés utilisant une seule membrane. Dans un procédé de séparation membranaire à plusieurs étages : le biogaz entre dans chaque étape avec moins de CO_2 pour obtenir le plus haut pourcentage possible de CH_4 dans la dernière étape. Le coût de fonctionnement dépend de la puissance nécessaire pour la compression du biogaz (0,2-0,38 $kWh.Nm^{-3}$)[35], de la durée de vie de la membrane avant son remplacement et du prétraitement du biogaz[41].

1.2.4. Adsorption (Pressure Swing Adsorption)

Pressure Swing Adsorption (PSA), est un procédé qui fonctionne à haute pression et sépare les gaz selon leurs forces de liaison à un adsorbant. L'augmentation de la pression entraîne une plus grande adsorption. Le charbon actif ou un tamis moléculaire (zéolithes) peuvent être utilisés comme adsorbant. Leur surface spécifique élevée et leur texture poreuse entraînent une séparation sélective des gaz. Le biogaz est introduit dans la colonne d'adsorption garnie de matériau adsorbant. Le biogaz épuré à haute teneur en méthane passe alors que le CO_2 est retenu dans la colonne. Lorsque l'adsorbant devient saturé en CO_2, la colonne à garnissage est dépressurisée à une pression proche de la pression atmosphérique et le CO_2 est libéré (par désorption), il sera ensuite éliminé avec le flux de gaz d'échappement. Certaines impuretés doivent être précédemment éliminées car l'adsorption par les tamis moléculaires est irréversible[48]. Plusieurs colonnes sont nécessaires pour que le système fonctionne efficacement en réduisant les besoins énergétique de compression du gaz et en créant un fonctionnement continu[36]. L'élimination du H_2O et la compression du biogaz nécessitent environ 0,24 tà 0,6 $kWh.Nm^{-3}$ [41], [49]. Cette méthode permet d'obtenir du biométhane contenant jusqu'à 98% de CH_4 [43]. C'est un processus efficace et flexible capable d'éliminer de nombreuses impuretés du gaz d'alimentation [50]. Le principal inconvénient du PSA est la forte perte de gaz due à la phase de désorption au cours de laquelle la pression est libérée.

1.2.5. Séparation cryogénique

Lorsqu'un mélange gazeux est refroidi, chaque composant possède une température de condensation différente à laquelle il sera séparé du mélange. Par exemple, à la pression atmosphérique, le CO_2 se solidifie directement à partir de sa phase vapeur à -78°C, tandis que le méthane se liquéfie à -162°C. La cryogénie présente plusieurs avantages : aucun absorbant chimique n'est utilisé et le procédé peut fonctionner à la pression atmosphérique. Il est possible

d'obtenir du CH_4 pur (99%) ainsi que du CO_2 pur (98%) avec de faibles pertes de méthane (<1%). Le méthane produit est déjà froid, ce qui réduit la puissance de refroidissement nécessaire pour la liquéfaction. L'inconvénient majeur de ce procédé est le coût de refroidissement ; cela a limité les recherches effectuées sur ce sujet. Pourtant, plusieurs techniques de séparation cryogéniques ont été développées pour tenter de surmonter ce problème.

i. Séparation du CO_2 par compression/refroidissement

Lorsque la pression de CO_2 augmente, il passe de sa phase gazeuse au solide à une température plus élevée. Il est important de préciser que la pression de dioxyde de carbone dans le mélange est égale à sa pression partielle et non à la pression totale du flux. Par conséquent, l'augmentation de la pression du mélange contenant du CO_2 diminue la puissance de refroidissement nécessaire pour l'éliminer. Cette méthode est plus adaptée aux flux à forte concentration de CO_2, sinon l'augmentation de la pression partielle (compression) du CO_2 sera plus coûteuse que son refroidissement.

Peu de données sont disponibles concernant l'épuration cryogénique du biogaz qui représente environ 0,4% de tout le marché d'épuration de biogaz[54]. La cryogénie peut fournir du biométhane de haute pureté (99%) et de faibles pertes de méthane (1%) [13]. L'une de ses principaux inconvénients est l'élimination nécessaire d'impuretés telles que l'eau et le H_2S avant d'éliminer le CO_2. Ceci évite tout blocage dans le circuit fluidique et d'autres problèmes opérationnels [36]. Il existe une grande incertitude dans l'estimation des besoins énergétique [35], mais elle peut varier entre 0,42 et 1 $kWh.Nm^{-3}$, ce qui est élevé par rapport à d'autres procédés d'élimination de CO_2. Cette surconsommation est dûe à la puissance de refroidissement élevée dans ces procédés[36]. En revanche, le biométhane obtenu par séparation cryogénique est à basse température, ce qui peut faciliter sa liquéfaction dans une étape ultérieure.

ii. Séparation cryogénique à température variable en post-combustion

D'après Clodic et al. [55], la seule possibilité de séparer le CO_2 d'un mélange à pression atmosphérique est de le givrer sur une surface froide. Il a introduit le terme "anti-sublimation" pour la solidification directe de la phase gazeuse. La température de givrage du CO_2 dépend de sa pression partielle dans le mélange. Pour une concentration initiale de 15% de CO_2 dans les gaz de combustion se trouvant à la pression atmosphérique (pression partielle de CO_2 $P_{CO2} = 0.15P_{atm}$), le dépôt a lieu à -99°C. Si le CO_2 est refroidi à -122°C, la concentration de CO_2 atteint 1%, de sorte que 93% du CO_2 présent dans le mélange aurait été capturé.

Le processus de givrage/dégivrage s'effectue alternativement entre deux échangeurs de chaleur. Pour éliminer le CO_2 givré, un mélange de réfrigérants "chaud" à -50°C est introduit dans l'échangeur de chaleur contenant le givre CO_2. Il sera refroidi par évaporation du CO_2. L'évaporateur contenant du givre est fermé, la température et la pression montent jusqu'à -56°C et 520kPa respectivement (près du point triple) et le CO_2 liquide est récupéré à l'aide d'une pompe. Cette alternance permet d'économiser 35% d'énergie en récupérant une partie du froid du givre CO_2. Clodic et al. ont estimé l'énergie nécessaire pour le captage du CO_2 avec récupération du froid par dégivrage à 1077kJ/kg de CO_2.

iii. Séparation cryogénique par un lit fixe

Tuinier et al. [56], [57] a précisé que le procédé cryogénique de capture de CO_2 développé par Clodic et al.[55] présente une haute efficacité. L'inconvénient principal est que la présence d'H_2O dans le flux entrant n'est pas tolérée car la glace peut boucher les canalisations; aussi la formation de CO_2 sur la surface de l'échangeur limite les échanges et donc l'efficacité du système. Pour surpasser ces problèmes, Tuinier et al. ont proposé l'utilisation de lits fixes. Le flux de gaz post-combustion à l'entrée passe par un lit fixe pré refroidi, cela conduit à une séparation du CO_2 et du H_2O du reste du mélange à cause des différents points de condensation solide et liquide. Le lit est chauffé par le flux entrant. Ce dernier se refroidi, le H_2O se condense. Une température d'équilibre entre le lit et le gaz est atteinte. L'eau sous forme liquide s'écoule dans le lit jusqu'à la sortie. Le lit s'échauffe à son entrée parce que la température du gaz de combustion est supérieure à la température d'équilibre mentionnée avant (entre -110°C et -150°C). Ce qui conduit à l'évaporation du H_2O condensé qui à son tour traverse le lit (à une vitesse plus lente que la phase liquide) vers la sortie. Le reste du gaz se refroidit à une deuxième température d'équilibre, celle de la solidification du CO_2 à sa pression partielle dans les gaz de combustion; le CO_2 est alors solidifié dans le lit. Par le même principe que pour l'eau, la solidification et la sublimation du CO_2 le fait avancer jusqu'à la sortie du lit. La quantité séparée dépend de la température froide initiale du lit. Ainsi, les problèmes de bouchage sont surmontés. Quand on atteint une température du lit à laquelle du CO_2 pourrait passer sans givrer, le lit commence une phase de régénération : on introduit du CO_2 gaz pur pour récupérer le CO_2 solide.

La température froide initiale du lit a un grand effet sur la quantité de CO_2 séparée, Tuinier et al. ont comparé les résultats obtenus pour une température initiale de -120°C et -110°C, on récupère respectivement 90% et 12% du CO_2. En comparant la consommation énergétique dans ce procédé (1,8MJ/kg CO_2) par rapport à celle correspondant au procédé d'absorption aux amines (3-4 MJ/kg CO_2), Tuinier et al. ont trouvé une amélioration importante mais sous condition que le lit soit refroidi (par évaporation du GNL par exemple).

iv. Séparation cryogénique par les machines Stirling

Song et al. [61] ont proposé un captage cryogénique du CO_2 en post-combustion en utilisant des machines Stirling. Ce système cryogénique a beaucoup d'avantages : rendement élevé, grande fiabilité et petite taille [62]. La vapeur d'eau et le CO_2 contenu dans les gaz de combustion ont été capturés à différents positions dans l'échangeur de chaleur refroidi par la machine Stirling. L'avantage principal du processus est que le CO_2 dans les gaz de combustion est capturé sous forme solide (sans passer par la phase liquide). Lorsque le CO_2 est exposé à l'échangeur de chaleur à une température inférieure à sa température de sublimation, il se solidifie et se sépare du mélange gazeux.

Song et al. ont comparé l'absorption aux amines qui a été faite dans une centrale électrique et la cryogénie faite au laboratoire. Ils ont trouvé que le coût du kg CO_2 peut être réduit de 0,003$ en utilisant la cryogénie mais avec une pénalité énergétique de 3,4 $MJ_{electrique}$/kg CO_2 tandis que l'absorption a une pénalité de 2,94$MJ_{thermique}$/kg CO_2.

1.2.6. Comparaison entre différents procédés d'épuration

En comparant les avantages et les inconvénients de chaque méthode de séparation de CO_2, ainsi que leurs pertes de CH_4 et la pureté du biométhane à la sortie, on trouve que le lavage à l'eau et les membranes nécessitent peu d'énergie, mais ne donnent pas les meilleurs résultats en termes de pureté et pertes de méthane. Si l'objectif principal est d'obtenir la plus grande pureté de méthane, l'absorption chimique à l'aide d'amines et la séparation cryogénique sont les procédés à prendre en compte. Mais tous les deux présentent un inconvénient commun: des coûts d'opération élevés liés à leur caractère énergivore. En absorption chimique, une énergie importante est nécessaire pour la régénération du solvant et dans les systèmes cryogéniques, une puissance frigorifique élevée est requise même si elle abaisse la température du biométhane, ce qui facilite sa liquéfaction.

Le problème actuel des procédés cryogéniques reste lié au besoin énergétique élevé de refroidissement. Dans cette thèse, une solution à ce problème est présentée où le froid contenu dans le givre de CO_2 séparé du biogaz par voie cryogénique est récupéré et réutilisé pour capturer plus de CO_2.

1.3. Refroidissement par évaporation

La séparation cryogénique permet la récupération de plus de 98% du CO_2. Dans tous les systèmes de captage cryogéniques de CO_2, le même problème limite les études : le coût du refroidissement. Dans le système conçu par Tuinier et al.[56], une partie du froid contenu dans le CO_2 solide a été récupérée pendant la phase d' sublimation pour refroidir le lit fixe. Dans le système conçu par Clodic et al.[55], une partie du froid est récupérée par sublimation du CO_2 avec un réfrigérant à -50°C et le givre est sublimé dans un volume fermé puis atteint -56°C avec une pression de 520 kPa pour récupérer du CO_2 liquide. Le pourcentage de CO_2 valorisé dans les utilisations industrielles étant très faible par rapport aux émissions totales de CO_2 dans le monde (0,5%) alors le stockage de CO_2 semble moins intéressant. Que se passerait-il s'il était possible de récupérer tout le froid contenu dans le CO_2 solide séparé du biogaz (ou des gaz de combustion) lors de l'épuration cryogénique du biogaz avec un cyclage à température réduite dans les échangeurs de chaleur ?

L'étude menée dans cette thèse est placée dans ce contexte de séparation cryogénique de CO_2 du biogaz dans une première étape et de récupération du froid contenu dans le givre de CO_2 dans une seconde étape. La récupération du froid proposée se base sur le phénomène de sublimation contrôlée, un concept que l'on trouve dans les tours de refroidissement. Les principes de la sublimation contrôlée seront expliqués, puis son application dans le cas du biogaz sera présentée.

1.3.1. Concept général

De nombreux systèmes de refroidissement fournissent de l'air frais pour une utilisation domestique ou industrielle. Le refroidissement par évaporation est une technique simple qui utilise uniquement de l'air et de l'eau, sans autres produits chimiques ni réfrigérants. De plus, le compresseur utilisé dans les cycles de réfrigération conventionnels est remplacé par un ventilateur consommant beaucoup moins d'énergie[66]. Lorsque l'air chaud et sec entre en contact avec de l'eau, cette dernière s'évapore par transfert de chaleur avec le flux d'air et à cause du gradient d'humidité entre les flux gazeux et liquides. Cela augmente l'humidité de l'air

diminuant la température de l'eau. Le résultat est un courant d'eau froid et une faible consommation[67].

1.3.2. Evaporation dans les tours de refroidissement

Une tour de refroidissement est un dispositif de rejet de chaleur qui consiste à extraire la chaleur résiduelle de l'eau chaude de générer un courant d'eau à une température inférieure à la température ambiante[70]. Le rejet de chaleur dans la tour de refroidissement est déterminé par le transfert de chaleur par convection entre de fines gouttelettes d'eau et l'air ambiant et par l'évaporation d'une petite quantité d'eau dans l'air en mouvement[71]. Le processus implique donc à la fois un transfert de chaleur et de masse.
Lorsque les gouttelettes d'eau chutent, l'eau entre en contact avec l'air injecté dans la tour de refroidissement (Figure F2).

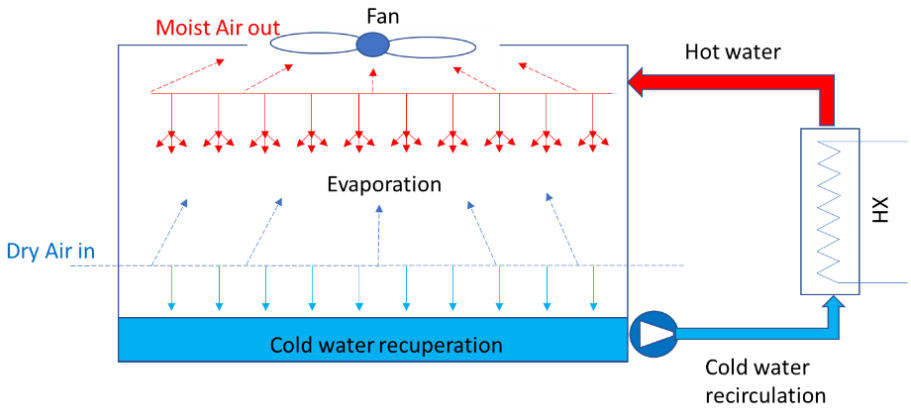

Figure F2: Schéma représentatif d'une tour de refroidissement ([74])

L'air étant sec et en contact avec la surface des gouttes d'eau, l'eau est refroidie à cause du transfert de masse vers l'air. Compte tenu du débit massique de gouttelettes d'eau à l'intérieur de la tour de refroidissement, l'énergie totale est utilisée pour chauffer l'air par transfert de chaleur par convection et pour évaporer l'eau qui sera transportée par le flux d'air sec qui constitue le transfert de chaleur latent. Le bilan énergétique des gouttelettes d'eau peut être décrit par :

$$\dot{m}_w \times c_{p,w} \times \Delta T_w = h_c \times (T_{w,surf} - T_{air}) + h_{mass} \times (x_{w,surf} - x_{w,air}) \times L_{lv} \quad \text{(F.1.1)}$$

Avec $\dot{m}_w$ le flux massique des gouttes d'eau et ΔT_w la différence de température des gouttes d'eau entre l'entrée et la sortie de la tour de refroidissement. $T_{w,surf}$ est la température à la surface des gouttes d'eau dans la tour de refroidissement et T_{air} la température de l'air. $x_{w,surf}$ représente l'humidité relative de saturation à la surface de la goutte et $x_{w,air}$ celle de l'air. L_{lv} représente la chaleur latent de vaporisation de l'eau. Les termes $(T_{w,surf} - T_{air})$ et $(x_{w,surf} - x_{w,air})$ sont toujours positifs ce qui signifie que ΔT_w sera toujours positif et l'eau se refroidit dans la tour.

1.4. Refroidissement par sublimation

Similairement au refroidissement par évaporation, il est possible d'appliquer le concept pour refroidir par sublimation d'un solide. Le concept n'est pas aussi « connu » que le refroidissement par évaporation. Gross et al. [76] ont proposé un système de refroidissement

solide pour les applications spatiales à faible transfert de chaleur. L'appareil est constitué d'un récipient isolé rempli d'un solide cryogénique (liquide ou gaz solidifié), d'une tige de conduction reliant le solide de refroidissement au dispositif à refroidir et d'un canal qui permet l'évacuation de gaz sublimé vers l'atmosphère. Le système utilise la relation entre la température et la pression de vapeur saturante. Par exemple, si le liquide de refroidissement solide est à $T_{s-c}°K$, sa pression de vapeur saturante sera de$P_{s-c}\ bar$. Si la pression doit rester constante au-dessus du solide, sa température ne changera pas[76]. Lorsque le solide de refroidissement est chauffé par la tige de conduction, il est sublimé. La pression et la température augmentent. Si la vapeur supplémentaire est rejetée dans l'atmosphère par l'orifice de régulation de pression, il est alors possible de maintenir la même température $T_{s-c}°K$ dans le système. Le transfert de chaleur par conduction ne diminue pas et il est possible de maintenir le même potentiel de refroidissement. Une étude expérimentale a été menée et la température de l'espace contenant le solide est restée constante alors que le solide de refroidissement était en cours de sublimation.

1.5. Discussion et cadre de travail de cette thèse

1.5.1. Nouveau concept de séparation cryogénique du CO_2 et récupération de froid par sublimation contrôlée

Dans cette thèse on propose de construire un modèle pour simuler le refroidissement par sublimation contrôlée (sublimation du CO_2) afin de réduire les besoins énergétiques des procédés de captage cryogénique de CO_2. Le cas d'application choisi pour cette thèse est la sublimation contrôlée du dioxyde de carbone givré lors de la purification du biogaz. Le froid contenu dans le givre de CO_2 sera récupéré de manière optimale par une sublimation contrôlée du givre par un troisième gaz. Ce dernier devrait réduire considérablement la consommation d'énergie liée à la séparation du dioxyde de carbone. Dans le concept de l'évaporation contrôlée des tours de refroidissement conventionnelles, l'air sec refroidit l'eau en l'évaporant, mais sa température n'est pas nécessairement égale à la température d'évaporation de l'eau. La force motrice d'évaporation devient l'humidité initiale de l'air sec et le potentiel d'atteindre une teneur élevée en vapeur d'eau (température saturante). Ainsi, par analogie, il est possible de sublimer le givre de CO_2 avec un autre fluide générant une force motrice de transfert de masse (concentration) même à la température de givre. Dans l'étude concernant l'épuration cryogénique du biogaz, le biométhane sortant de l'échangeur de chaleur après la séparation du CO_2 est déjà à très basse température, la puissance frigorifique nécessaire pour le liquéfier est réduite. Du N_2 liquide peut être utilisé pour accomplir cette étape. Pendant que le méthane se liquéfie par l'azote liquide, ce dernier est en cours de vaporisation et peut être utilisé dans une étape ultérieure pour le dégivrage du CO_2. Même si la température de l'azote gazeux est inférieure à celle du givre, une sublimation se produira et le froid devrait être récupéré par la sublimation contrôlée du CO_2 solide. Dans le travail effectué dans cette thèse, le nouveau concept de capture cryogénique et de récupération du froid peut être présenté en 2 parties principales :

1.5.2. Givrage de CO_2

La première partie du concept concerne le givrage de CO_2 sur une surface froide, ce qui nécessite une meilleure compréhension des propriétés du givre de dioxyde de carbone et des

phénomènes impliqués. Les propriétés de givre de CO_2 sont à peine disponibles, puisque l'état de l'art concernant le givrage correspond principalement au givrage de la vapeur d'eau contenue dans de l'air humide. Dans la littérature, aucun résultat expérimental comparable n'est disponible pour le givrage du CO_2 contenu dans le biogaz et très peu de résultats expérimentaux sont disponibles dans la littérature ouverte pour le givrage du CO_2 contenu dans les gaz de combustion. Afin de valider le modèle proposé dans ce travail, le cas du givrage au CO_2 à partir de gaz de combustion sera étudié dans un premier temps avant de l'appliquer à l'étude de cas sur le traitement du biogaz. Ensuite, le dépôt de CO_2 de biogaz sur une surface froide sera étudié pour différents paramètres de fonctionnement et différentes géométries d'échangeurs de chaleur afin de choisir les meilleures conditions pour la séparation cryogénique du CO_2 du biogaz.

1.5.3. Sublimation contrôlée du CO_2

La deuxième partie concerne l'apport original au procédé de séparation cryogénique : l'sublimation contrôlée du CO_2 à pression atmosphérique. Après son épuration, le biométhane est liquéfié. Le givre de CO_2 doit être dégivré. Un troisième fluide, de préférence à une température plus basse (ou égale) à celle du givre, rentre en contact direct avec le givre et le sublime par la différence de concentration de CO_2 entre la surface du givre et le flux. Cette sublimation refroidit le givre de CO_2 restant et, éventuellement, refroidira aussi l'échangeur de chaleur qui désormais froid peut être réutilisé pour capter plus de CO_2 du biogaz. Le phénomène de sublimation contrôlée du CO_2, ses limites et son optimisation sont étudiés. Afin d'optimiser le système d'épuration du biogaz dans son ensemble, une alternance entre le givrage et le dégivrage sera discutée. Aussi, d'autres configurations peuvent être appliquées à ce concept et sont discutées plus tard dans cette thèse.

1.5.4. Objectifs scientifiques de la thèse

- Compréhension approfondie du concept de refroidissement par sublimation contrôlée et son application ;
- Etude du changement de phase de CO_2 de l'état solide à l'état vapeur et vice-versa, collecte de données sur les propriétés du givre et la modélisation du phénomène de formation de givre ;
- Application des connaissances au phénomène de givrage de CO_2 dans un procédé d'épuration cryogénique du biogaz suivi de sa liquéfaction et optimisation du système ;
- Application du concept de refroidissement par sublimation contrôlée au CO_2 givré pour la récupération du froid par sublimation ;
- Validation expérimentale.

Chapter 2: Modelling of CO_2 deposition from its gas phase

Introduction

As it was mentioned in chapter 1, the aim of this thesis is to study the solid-vapor CO_2 phase transitions in order to apply it in a cryogenic process for biogas upgrading. In a first step, the CO_2 contained in the biogas will be frosted and deposited on a cold surface thus purifying the biogas to obtain biomethane. This requires knowledge of the procedure involving deposition of CO_2 on a cryogenically cooled surface. In this chapter, the CO_2 frosting phenomena is described and a detailed mathematical model is proposed to study frost growth and heat transfer at the surface and inside the frost layer.

The majority of the work done on frost formation considers water vapour contained in moist air, since this phenomenon is more common. In refrigeration cycles, industrial or domestic, ice could appear under specific operating conditions. Many theoretical and experimental studies can be found in the literature. Some models are based on empirical correlations [80] [81] to predict frost growth but they are limited to certain operating conditions and for specific heat exchanger geometries. Cui et al. [82] developed a CFD model that takes into consideration the nucleation and crystal formation phase which will be discussed later in this chapter. CFD modelling is complex and time costly. The method that is most used to evaluate frost growth is developing a model according to heat and mass transfer equations while considering the frost as a porous medium, hence taking into account the diffusion of the gas phase both in the main passage of flow and inside the solid pores. Na et Webb [83], Lee et al. [84], Le Gall et Grillot [85] and others developed detailed models of water vapour frost growth.

Rare studies concerning the fundamentals of CO_2 deposition on a cold surface can be found in the literature and those found were mainly experimental. In a study by Ogunbameru [86], he compared frost formation of CO_2 contained in flue gases to water vapour contained in moist air. He found that the growth of frost in terms of thickness and mass has a high resemblance. However, the density seemed different. In the case of water icing, the density increased whereas for the case of CO_2 it was decreasing with time; he explains this difference by the presence of a fraction of water vapour in the CO_2-N_2 mixture which could have a concentration lower than that of CO_2 by 200 to 1000 times but may have a significant effect on the frost after its formation.

In a more recent study, Shchelkunov [87] conducted an experiment to observe and monitor the deposition of CO_2 contained in a binary gas mixture (mainly N_2+CO_2) on a cold surface. In his paper, he was able to study the variation of frost thickness, thermal conductivity and density with respect to frosting time. When comparing his results to those found in the literature for frost formation of water vapour (Lee et al. [84], Hermes[80]), a similarity in the frost growth and densification is well observed so it can be assumed that the frosting phenomena of CO_2 contained in a binary gas mixture whether it is biogas or flue gases, can be dealt with similarly to water vapour frosting contained in moist air. Since the only available data found in the literature are for CO_2+N_2 mixtures this case will be considered in this chapter in order to validate

the model and in later chapters the nitrogen will be replaced by methane in order to simulate the case of CO_2 removal from biogas.

2.1. Psychrometry of frost formation

In order to achieve frosting conditions, two criteria should be met: a low temperature and a difference in CO_2 concentrations or dew point. These two are related by a function that can be found in the psychrometric chart (blue curve in Figure 25) that shows phase equilibria.

Consider a N_2/CO_2 mixture at atmospheric pressure $P_{atm} = 1.01325\ bar$ with a concentration ratio $m_{CO2}/m_{N2} = 0.3$ at -95°C. This is point A on the psychrometric in Figure 25. This point represents the inlet flue gases passing over the cold surface. In order to achieve frosting conditions, the mixture should first be cooled down from point A to point B. The enthalpy difference between these two points is the convective sensible heat transfer that will position the mixture in saturation conditions.

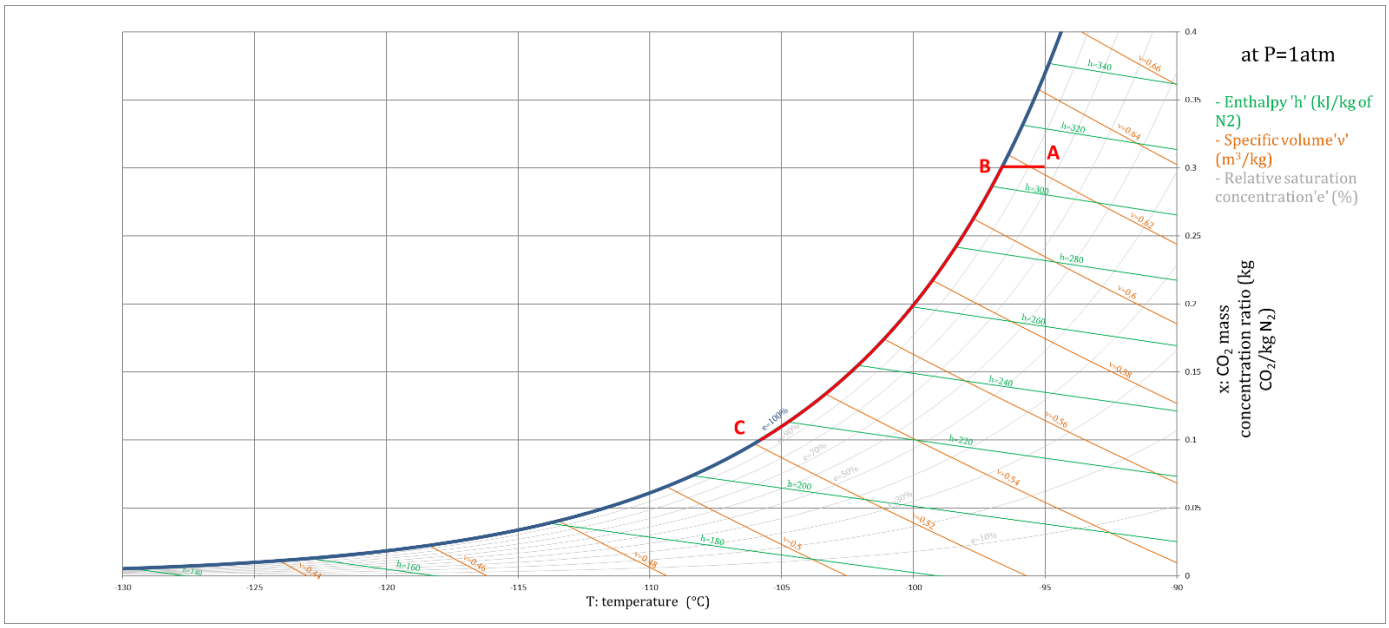

Figure 25: Psychrometric chart for N_2/CO_2 with temperature and concentration evolution in frosting conditions

If at the outlet of the cold surface, a CO_2 relative concentration of 0.1 is required (point C) then the saturation curve is followed from point B to reach the point C. The difference in enthalpy between these two points is mainly represented by the latent heat of solid condensation of CO_2 and a lesser part by the sensible heat of cooling gas and frost. The concentration of CO_2 in the flue gases will therefore decrease due to the deposition of carbon dioxide.

2.2. Frost formation mechanism

The frost formation mechanism can be divided into 3 major parts: the “crystal growth” period, the “frost growth” period and the “fully developed” period[82].

The first moments of frost formation are known as the crystal growth phase or nucleation phase and they are the most complex to simulate and monitor. Crystals will be formed and they will be used as nuclei on which more CO_2 will frost. They are the base of the frost mechanism. This

part is rarely modelled in the literature when studying frost growth because it ends in a very short time so it can be neglected.

The second part is the frost growth period, the flue gases containing the CO_2 gas will come into contact with cold surface, it cools by convection until carbon dioxide reaches its deposition temperature at its partial pressure. The frost begins to form as frost thickness and mass increase. The frost growth increases rapidly at the beginning then it slows down because of the accumulation of the frost layer which forms a thermal resistance layer between the cold surface and the flow of flue gases. The frost formed is porous, the CO_2 passes through it and frosts inside the layer. This simultaneously increases the density and the thickness.

The third part is the fully developed phase in which temperature and concentration equilibrium is achieved at the frost surface limiting or even stopping CO_2 deposition. In this chapter, the model developed will mainly describe the second part because it is the part describing the frost growth evolution with respect to frosting time and the active stage on CO_2 removal from the gas phase.

2.3. CO_2 deposition modelling

The main purpose of the developed deposition model is to predict the mass transfer of CO_2, the variation of the frost thickness θ_{frost} and its density ρ_{frost} by calculating heat and mass transfer during the frost formation and growth phase. The proposed deposition model is presented considering a surface cooled to constant cryogenic temperatures and on which frost is formed (Figure 26). The flue gases pass over the cold surface and cool down. When the temperature of the CO_2 contained in the flue gases reaches the solid condensation temperature of CO_2 with a difference in CO_2 concentration between the gas flow and the surface, frost is formed. As the frost layer increases, the conduction heat transfer is affected mainly by the insulating effect of frost thickness.

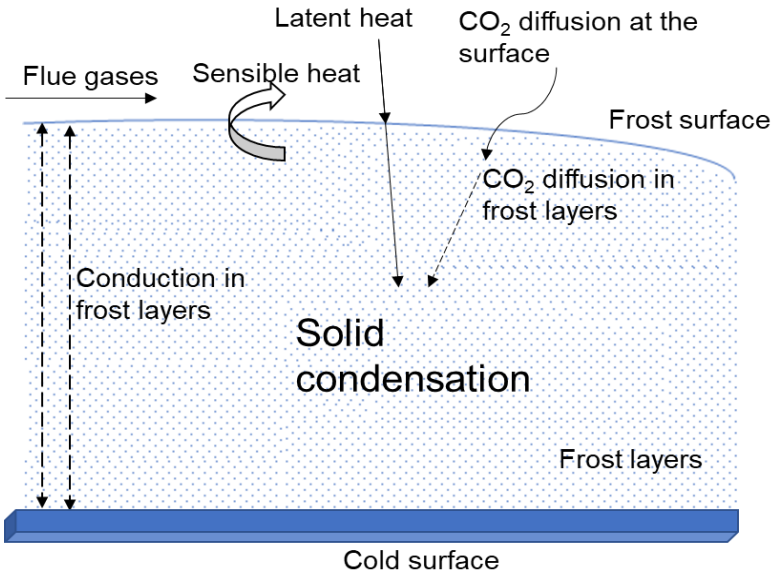

Figure 26: Description of heat and mass transfers during CO_2 deposition

According to Cui et al. [82], two main approaches can be found in the literature for modelling the deposition phenomenon in terms of frost formation and growth. The first approach relies

on empirical equations or experimental correlations [80], [81] , it is usually used for calculation of frost growth parameters, mainly frost thickness and density as function of flow and frost conditions as well as time. Many correlations can be found for the frost thermal conductivity and mass transfer coefficient too. This approach has shown good agreement with the experimental results. However, the problem with this approach is that it focuses mainly on finding the growth parameters in specified known conditions and cannot be generalized for all cases of frost formation [88]. The other problem is the fact that most studies found in literature take the case of water vapour deposition from humid air on a cold surface; therefore, these correlations cannot be used in the case of CO_2 deposition from biogas or flue gases over a cold surface but some of them will be presented in ANNEX A.

Here the second approach presents itself, where generalized equations of heat and mass transfer are used to estimate the frost growth considering the frost as a porous medium [83]–[85], [89]. These models divide the mass flow of deposited frost into two parts: one that deposits at the surface therefore increasing the frost thickness and the other diffuses and deposits inside the frost layer thus increasing its density. Mass and heat diffusion inside the frost layer is considered in all the models found in the literature using this approach. The mass transfer coefficient is found by Lewis analogy with the heat transfer coefficient which will be detailed later. This approach uses general equations but some authors used different hypotheses for the density and the deposition rate; they will be mentioned later in the model and presented with more details in ANNEX B. Since the models considering CO_2 deposition from a binary cold mixture are very limited to a few case studies and most of the work was experimental, the second approach considering the frost as a porous medium with thermal and mass diffusion seems to be more appropriate for the model that will be presented in this study.

2.3.1. Main assumptions

The following general assumptions are widely used in the literature and are taken into account when modelling the CO_2 frost deposition and growth on a cold surface:

- The nucleation phase takes place at the very first few moments of frost formation. Modelling this phase without an initially existing frost layer is complicated and imprecise. Therefore, modelling is carried out considering the pre-existence of a very thin uniform CO_2 frost layer with low density [85]. Initial conditions for the nuclei layer, such as frost density and thickness are required. Several correlations of the frost density have been proposed, depending on the frost surface temperature [90], the porosity [91] or the frost crystal volume fraction [82]. These correlations are either specific to the case of water vapour so cannot be used for the case of CO_2, or they require an initial guess of the porosity which already depends on the frost density. According to a study by Jones and Parker [89], they proposed to take small initialization values for the thickness and density of the frost. They demonstrated that for thickness values close to 0 (~ 10^{-5}) and density values between 8-48 kg/m^3 the results concerning the frost growth phase are not affected. Although the study by Jones and Parker was for the case of water vapour deposition, their assumption will be considered for the model developed in this study. Initial frost thickness is taken as $\theta_{frost,initial} = 2 \times 10^{-5} m$ and $\rho_{frost,initial} = 25\ kg/m^3$. The choice

of initial values was detailed in ANNEX C. Initial frost temperature will be considered equal to that of the cold surface on which frost deposits.

- In a first approach, frost formation modelling is done in 1D: the frost layer develops in the direction normal to the cold surface [92]. In a more thorough study, 2D modelling is considered to take into account the flue gases' temperature and their CO_2 concentration variation as they move along the surface. When the gas flow comes into contact with the cold surface, its temperature will decrease and as CO_2 deposits, its content in the gas flow will decrease.

- The transition between phases is considered solid condensation without any passage through the liquid phase. This is due to the pressure conditions of CO_2 present in the gas mixture which keeps him below its triple point.

- Gas and solid temperatures at the flue gases-frost interface are considered equal.

- The total pressure is considered constant in the volume of biogas / frost. The pressure drops are neglected.

- All the gases in this study (methane, carbon dioxide, nitrogen) are considered ideal gases an operating at atmospheric pressure.

- Radiant heat transfer is neglected.

- The composition of flue gases in nitrogen and carbon dioxide is considered constant at the inlet above the flat cold surface.

- The frost formation reduces the hydraulic diameter of the gas passage over the cold surface, affecting the cross section and the flow velocity. Variations in flow velocity are taken into account in the calculation of the Reynolds number which is used in the calculation of heat and mass transfer coefficients.

2.3.2. Energy and mass balance during deposition

The mass and heat transfer equations considered for water vapour frosting will be used in the case of CO_2 deposition while considering the frost as a porous medium. Figure 27 shows the different heat and mass transfers occurring at the frost surface and inside it as CO_2 deposits over the cold surface. In most of the work found in the literature on water vapour deposition [84] [83], the model is divided into three main parts: the gas flow, the frost surface and the frost.

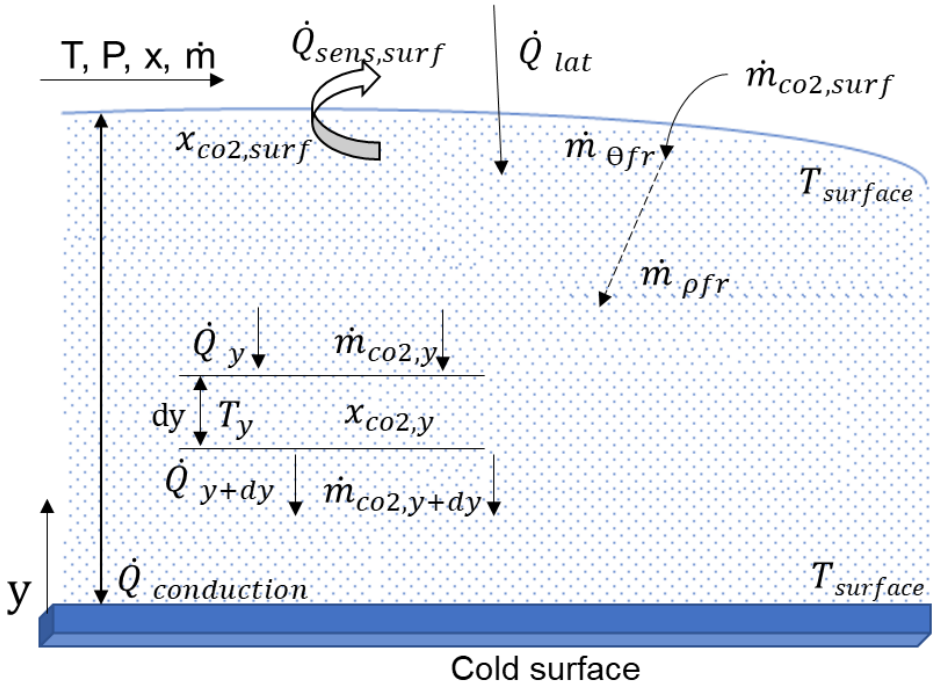

Figure 27: Energy and mass transfer on the surface and inside the frost during deposition

i. The flue gases

The sensible heat exchanged by convection between the flue gases and the cold frost surface is calculated as follows:

$$\dot{q}_{sens} = h_c \times (T_{flue\ gases} - T_{fr,surf}) \quad (2.1)$$

The frost CO_2 mass flow $\dot{m}_{co2,frost}$ from the flue gases to the cold surface can be expressed by the analogy between heat and mass transfers:

$$\dot{m}_{co2,frost} = h_m \times \rho_{flue\ gases} \times (x_{co2/n2} - x_{fr,surf}) \quad (2.2)$$

Thermodynamic equilibrium is considered on the frost surface at the interface between the flue gases and the frost. The CO_2 concentration at the surface is related to the frost surface temperature by means of the equation that describes phase equilibria such as in the psychrometric chart of nitrogen and carbon dioxide. The chart's construction is presented in the ANNEX D.

ii. The frost-bulk interface

On the frost surface, the mass flow of condensed CO_2 is represented by two terms. The first is the mass flux $\dot{m}_{\rho,frost}$ which corresponds to the mass of CO_2 diffused from the surface inside the frost, which increases the frost density; the second $\dot{m}_{\theta,frost}$ corresponds to the condensation of CO_2 on the frost surface which increases its thickness. Thus, the total mass flow of condensed CO_2 can be expressed as follows:

$$\dot{m}_{co2,surf} = \dot{m}_{\rho frost,surf} + \dot{m}_{\theta frost} \quad (2.3)$$

The flow of carbon dioxide that is diffused into the frost is expressed by Fick's law for the diffusion of matter:

$$\dot{m}_{\rho frost,surf}=D_{eff} \times \rho_{flue\ gases} \times (\frac{dx_{flue\ gases}}{dy})_{y=y,surf} \quad (2.4)$$

With $(\frac{dx_{flue\ gases}}{dy})_{y=y,surf}$ is the concentration gradient of CO_2 as y tends to θ_{frost} meaning at the frost surface. D_{eff} is the effective diffusion coefficient of CO_2 in the porous frost layers. It is limited by the porosity of frost. The diffusion resistance will be discussed later.

Knowing the total frosted CO_2 mass flow, it is possible to calculate the CO_2 mass flow rate responsible for the thickness increase $\dot{m}_{\delta fr}$. Frost thickness can then be calculated as follows:

$$\frac{d\theta_{frost}}{dt} = \dot{m}_{\theta frost}/\rho_{frost} \quad (2.5)$$

It should be noted that the density of the frost is not constant. Frost is a porous medium consisting of solid CO_2 and flue gases stream. The frost porosity affects its density which will vary according to the densification rate which consists of solid condensation in the porous frost instead of the surface.

At the frost surface, convective heat transfer occurs at the interface with the flue gases. Latent heat transfer is responsible for the CO_2 deposition. The frost is cooled by conductive heat transfer between the cold surface and the frost surface. The total heat transfer at the frost surface is described by the following equations:

$$\dot{q}_{tot,surf}= \dot{q}_{sens} + \dot{q}_{lat,surf} \quad (2.6)$$

$$\dot{q}_{lat,surf} = \dot{m}_{\theta frost} \times L_{sv} \quad (2.5)$$

$$\dot{q}_{cond,surf}=k_{frost} \times (\frac{dT_{fr}}{dy})_{y=y,surf} \quad (2.7)$$

With $(\frac{dT_{fr}}{dy})_{y=y,surf}$ is the temperature gradient between the frost layers when y tends to θ_{frost}, that is to say on the surface of the frost. k_{frost} is the thermal conductivity of CO_2 frost.

The energy balance at the frost surface is expressed by:

$$\dot{q}_{tot,surf} = \dot{q}_{cond,surf} \quad (2.8)$$

iii. Inside the frost layer

Inside the frost layer, frosted CO_2 mass flow $\dot{m}_{\rho frost}$ is obtained by the law of Fick for the diffusion of matter:

$$\dot{m}_{\rho frost}=D_{eff} \times \rho_{flue\ gases} \cdot \frac{dx}{dy} \quad (2.9)$$

The effective diffusion coefficient D_{eff} is limited by the porosity of the CO_2 frost layer. Since the frost densifies as more frost is formed, a new term called the mass absorption rate (or densification) will be introduced [93], this term calculates the density variation with respect to time inside each layer. This variation can be used to calculate the mass flow of frosted CO_2 inside the frost layer. The frost densification is calculated as follows:

$$\alpha_{co2} = \frac{d\dot{m}_{\rho frost}}{dy} \quad (2.10)$$

Since α_{co2} represents the densification of the frost layer, then the variation of the frost density can be calculated:

$$\frac{d\rho_{frost}}{dt} = \alpha_{co2} \quad (2.11)$$

Inside the frost layer, conductive heat transfer following Fourier's law is expressed as follows:

$$\dot{q}_{cond} = k_{frost} \times \frac{dT_{fr}}{dy} \quad (2.12)$$

One could then find the balance between the conductive heat transfer and the CO_2 condensation rate inside the frost layer:

$$\frac{d\dot{q}_{cond}}{dy} = -\alpha_{co2} \times L_{sv} \quad (2.13)$$

Thermodynamic equilibrium is considered inside the frost layer between the flue gases and the CO_2 frost similarly to the frost surface. Therefore, the temperature of the flue gases and their CO_2 concentration are related by psychrometry.

iv. The cold source

The cold required for CO_2 deposition will be provided by a cold source which can be at constant temperature. Another case is considering the cold source as a heat capacitor with an initial cryogenic temperature. As flue gases pass and deposition occurs, the heat capacitor is heated. The heat flux towards the cold surface is expressed by:

$$\dot{q}_{tot} = m_{cold\ surface} \times c_{p,cold\ surface} \times \frac{dT_{cold\ surface}}{dt} \quad (2.14)$$

Other models of CO_2 deposition can be found in the literature. They are used to calculate the frost formation and growth in terms of heat and mass transfer similarly to the model presented above. In each model a different assumption is taken concerning the density and absorption rate. They are presented in ANNEX B but they will not be considered in this study.

2.4. Density of new frost layer formed

Similarly to the case of the initial density, the density of each layer formed is not the same as the previous one. The main approaches to estimate this entity are:

- As for the case of the initial layer, a very small density is considered as initial value for the new frost layer formed. It will finally make a part of the total frost layer[83].
- Na and Webb also proposed to take the density of the new layer equal to that of the layer on the surface of the frost.
- The density of the new layer can be calculated by a correlation of the literature. This can also be applied for the initial frost density [90].
- The density of the new layer is equal to the average density of the frost layer[89].

If the case of average density is considered in the model (see Hypothesis 1) then the 4th approach is valid. In the model developed in this study the assumption of average density is not considered. The correlation proposed by Hayashi et al. [90] is specific to the case of water vapour. The most logical approach according to Na and Webb is to take a density in the new layer equal to that of the layer on the surface.

2.5. Thermophysical properties

2.5.1. Solid carbon dioxide density

According to a study conducted by Mass and Barnes [94] one can find the evolution of the density of solid CO_2 as a function of temperature as shown in figure 28.

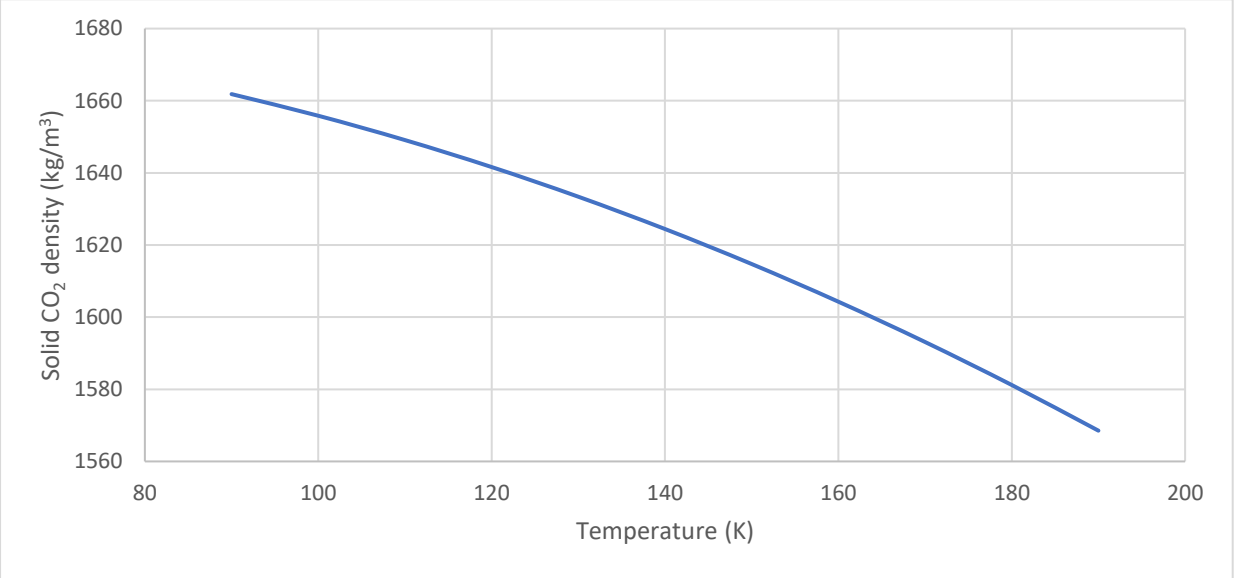

Figure 28: Density of solid CO_2 as a function of temperature

The density (kg/m^3) of the solid CO_2 is then determined as a function of temperature (K) in the range 90 and 191.65 K.

$$\rho_{CO2,solid} = -0.0037T^2 + 0.1029T + 1682.5 \quad (2.15)$$

2.5.2. Thermal conductivity of solid CO_2 and CO_2 frost

Correlations of heat and mass transfer coefficients, as well as thermophysical properties values, can have a major impact on the results. One of the main thermophysical properties is the effective thermal conductivity of frost k_{frost}. This has a direct impact on the frost growth calculations.

Several correlations for frost thermal conductivity can be used depending on the system conditions, in a particular temperature and density range. Most of the correlations found in the literature were applicable to water vapour frost and for temperatures much higher compared to temperatures of CO_2 frosting. In an article by Sumarokov et al.[95] on the thermal conductivity of CO_2 at low temperature, the thermal conductivity of CO_2 in its solid phase was presented in a temperature range of 1.5-36 K with a comparison to the conductivity found by Koloskova and al. The CO_2 used in the frosting was chemically pure (~100%), and liquid helium

was used as a refrigerant. The experimental error does not exceed 10%. Operational temperatures of the CO_2 deposition model developed in this thesis are estimated between 100K and 195K.

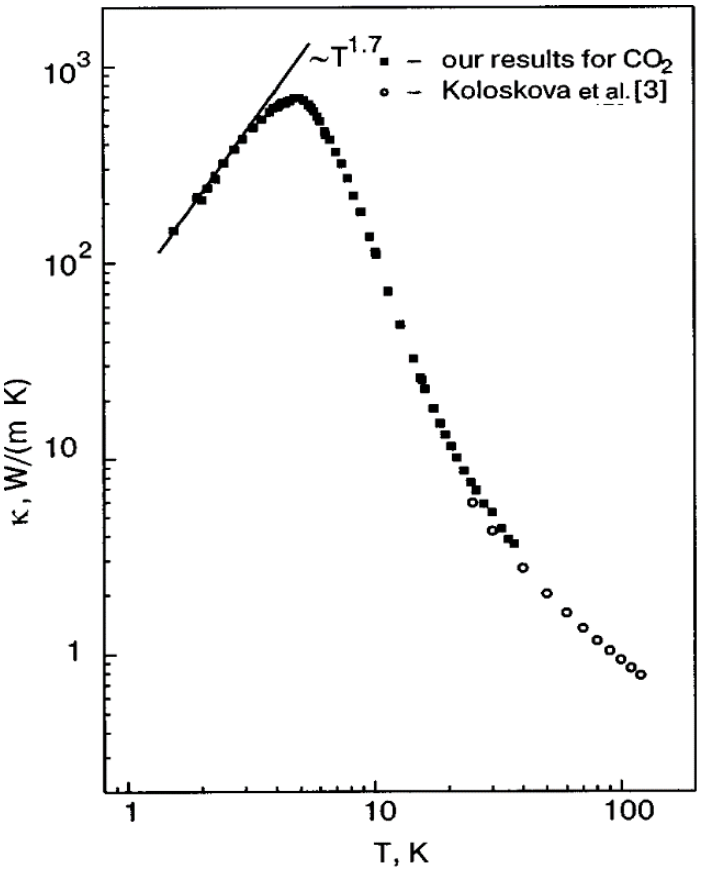

Figure 29: Thermal conductivity of solid carbon dioxide with respect to the temperature (modified from [95]**)**

Figure 29 shows the thermal conductivity of solid CO_2 as a function of temperature. Sumarokov et al. added thermal conductivities from 36K up to 100 K using the results found by Koloskova et al. As stated before, the thermal conductivity sought in this thesis is estimated at a temperature margin between 100K and 195K (CO_2 deposition temperature 1 atm), these values will be found by extrapolating the curve in the graph.

The equation found that links the thermal conductivity of solid CO_2 to temperature is of the form:

$$k_{co2,solid} = e^{a+{}^{b}/_{T}+c\times ln(T)} \qquad (2.16)$$

With a = 2.93503; b = 34.406011; c = -0.723579. The curve can then be plotted for the temperature margin 110-195 K.

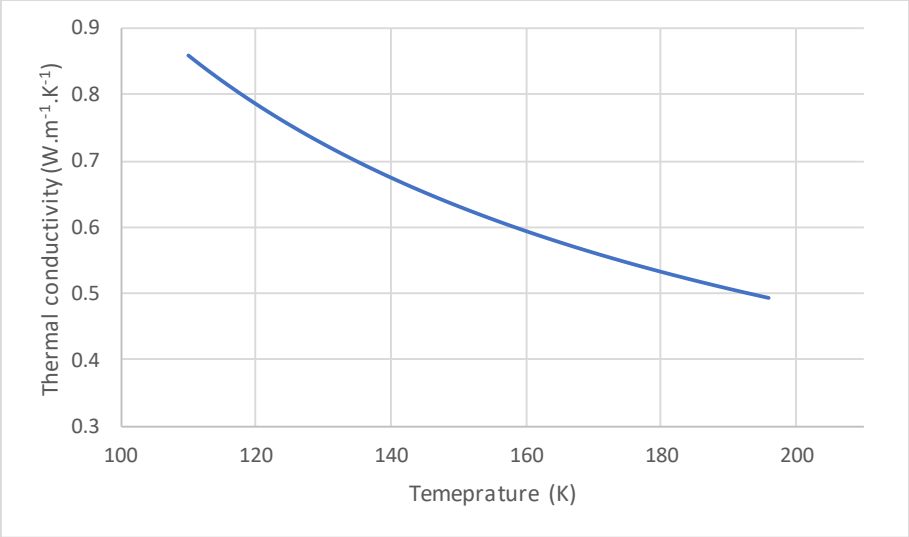

Figure 30: Thermal conductivity of solid carbon dioxide for temperature range between 110K-195K

This relation found is for solid CO_2 when no porosity is present. In the literature, thermal conductivity of frost is found to be dependant of the density of frost, thus its porosity. In order to calculate the effective thermal conductivity of the CO_2 frost, the real geometry of the frost as well as the thermal conductivity of the flue gases at each position along the surface should be known. These calculations are complicated and have no reference in the literature. Therefore, thermal conductivity of CO_2 frost is estimated using the results found in an experiment by Shchelkunov et al [87]. Although the article was written in 1985, it is one of very few studies on CO_2 deposition on a cold surface with experimental data. Using several experimental results found by Shchelkunov et al., the following correlation for effective thermal conductivity of CO_2 frost was estimated:

$$k_{eff} = \frac{0.27 \times \rho_{fr,avg}}{2386.037 - \rho_{fr,avg}} \quad (2.17)$$

In his article "Low-temperature data for carbon dioxide"[96], Azreg-Aïnou presents several properties of CO_2 at low temperature. He has based his work on articles by Giauque and Edgan[97] to find a function that represents the thermal heat capacity of solid CO_2. He also presents a comparison between different correlations for calculating vapour pressure and CO_2 heat of sublimation. In the following sections, the main solid CO_2 properties that will be considered in the model are described.

2.5.3. Diffusion resistance in porous medium

CO_2 frost is considered as a porous medium therefore it is important to add a resistance factor to the diffusion coefficient[85]. The resistance factor μ is function of the frost geometry, mainly frost porosity. Many empirical correlations can be found in the literature based on experiments for the case of water vapour deposition from moist air. In this study, the more general relation proposed by Brian et al. [98] will be used. This relation gives the diffusion resistance coefficient as function of the porosity and the tortuosity. The tortuosity is was estimated between $1.1 \leq \tau \leq 1.3$ for deposited water vapour; the resistance factor is calculated as follows:

$$\mu = \varepsilon / \tau \quad (2.18)$$

Where ε is the porosity of the CO_2 frost, $= \frac{gas\ volume\ in\ frost}{total\ volume\ of\ frost}$.

2.5.4. Heat capacity of solid CO_2

Specific heat capacity is given in literature for several temperature ranges. Based on the work carried out by Giauque et Egan[97], data can be gathered for heat capacity of solid carbon dioxide for the temperature range between 15.25K and 189.78K. Introducing the data found into a a 2D curve equation finder software, the heat capacity of solid carbon dioxide can be expressed as follows:

$$c_{p,co2\ solid}(kJ.(kg.K)^{-1}) = a + b \times r^T + c \times T \quad (2.19)$$

$$a = 0.6687 \qquad b = -1.115 \qquad c = 0.002905 \qquad r = 0.9699$$

Between 163K and 217 K, Maas and Barnes [94] found a correlation between the thermal capacity of solid CO_2 (cal.g^{-1}.K^{-1}) and the temperature (K) based on their experimental results.

$$c_{p,co2\ solid}\ (cal.(g.K)^{-1}) = \ 1.25 \times 10^{-5}T^2 - 2.83 \times 10^{-3}T\ -\ 0.4 \quad (2.20)$$

In Figure 31, the two correlations presented above were plotted in their respective temperature range. The maximum deviation between the two correlations is at $T = 189K$ and is about 7%. In the rest of the study, the correlation based on Giauque and Egan's data[97] was used unless the temperature of the frost surpassed 189K.

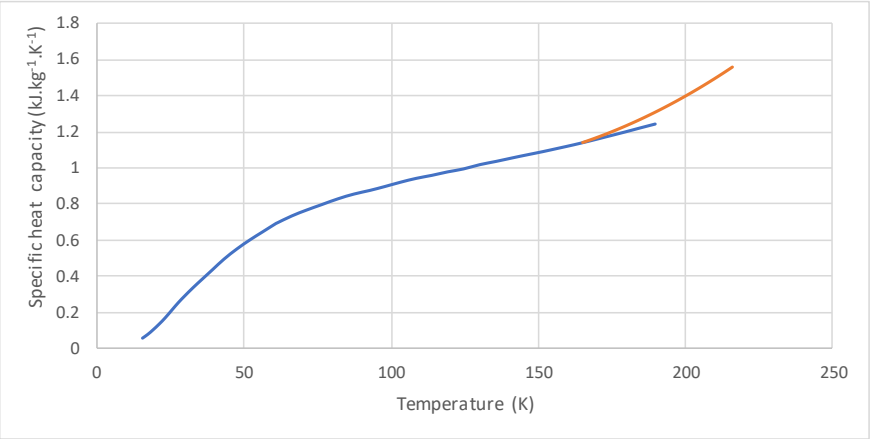

Figure 31: Solid CO_2 specific heat capcity as function of temperature

2.5.5. Enthalpy of CO_2 at cryogenic temperature

The calculation of the enthalpy is carried out with a reference temperature, in this case with $T = 0K$ for which $h_{reference,co2,solid} = -297kJ/kg$[96]. The heat capacity was calculated in the previous part then it is possible to calculate the enthalpy such that:

$$h_{co2,solid}(T) = \int_0^T c_{p,co2\ solid}dT + h_{reference,co2,solid} \quad (2.21)$$

The thermal capacity values are varied by varying the temperature between 0 and 189.8 K with a step of 0.1 K. Enthalpy equation is found to be of the same form as the specific heat capacity:

$$h_{co2,solid}(kJ.(kg)^{-1}) = a + b \times r^T + c \times T \quad (2.22)$$

$a = -407.1$ $b = 112.9$ $c = 1.314$ $r = 0.9875$

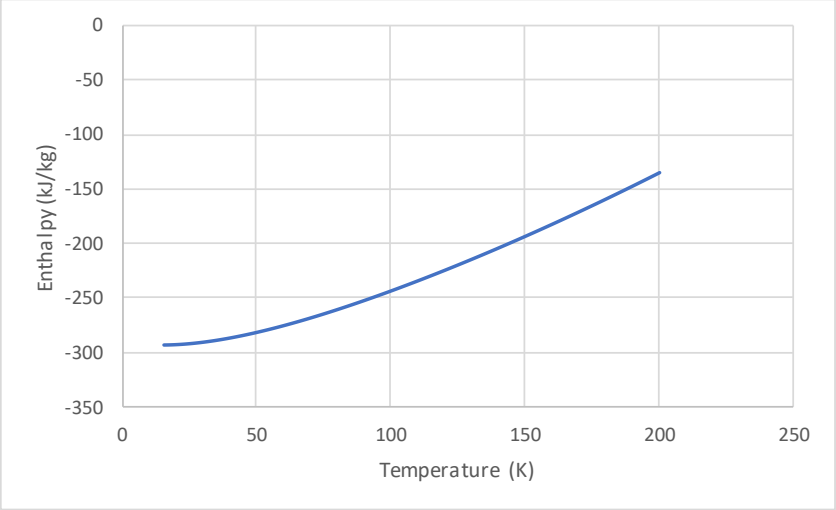

Figure 32: Solid CO_2 enthalpy as function of the temperature

As for the enthalpy of CO_2 in the gaseous state, Azreg-Aïnou[96] proposed an equation of the following form:

$$h_{co2,gas}(cal/mol) = R[(7T/2) - (\theta_r/3)] - T^2[d(a_v/T\,)/dT\,] \quad (2.23)$$

With $R = 1.98724\ cal.mol^{-1}.K^{-1}$. It is important to note that the enthalpy reference is for $T = 0K$. a_v is the four vibrational contributions to the free energy of an idea gas.

$$\theta_r = 0.561\ K;\ a_v\ (cal.mol^{-1}) = 2a_{v1} + a_{v2} + a_{v3} \quad (2.24)$$

$$a_{vi} = RT\ ln[1 - \exp\ (-\theta_{vi}/T)] \quad (2.25)$$

$\theta_{v1} = 954\ K$ $\theta_{v2} = 1890\ K$ $\theta_{v3} = 3360\ K$

2.5.6. Entropy of solid CO_2

As in the case of solid CO_2 enthalpy, entropy is calculated using the thermal capacity of solid CO_2. Also, a reference temperature $T = 0K$ is considered, therefore the reference solid CO_2 entropy is $s_{reference,co2,solid} = -2.1\ kJ/(kg.K)$[96].

$$s_{co2,s}(T) = \int_0^T (c_p/T)dT + s_{reference,co2,solid} \quad (2.26)$$

The heat capacity values are calculated for the temperature between 0 and 189.8 K with a step of 0.1 K. Entropy of solid carbon dioxide as function of the temperature is plotted in Figure 33 and it can be calculated as follows:

$$s_{co2,solid}(kJ/(kg.K)) = \alpha + \frac{\theta \times T^{\vartheta}}{\beta^{\vartheta} + T^{\vartheta}} \quad (2.27)$$

$\alpha = -2.225$ $\theta = 3.435$ $\beta = 198.9$ $\vartheta = 1.316$

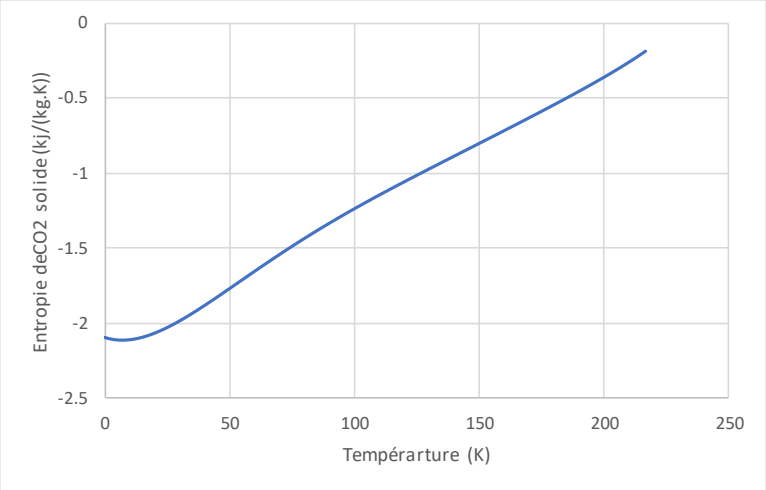

Figure 33: Solid CO_2 entropy as function of the temperature

2.5.7. CO_2 sublimation pressure

The sublimation pressure as a function of temperature is calculated by several results found in the literature for different temperature ranges. In his article, Azreg-Aïnou[96] presented several correlations and compared them for different temperature ranges. The results showed a good agreement between the different equations proposed.

- Giauque and Egan[97]: empirical equation between 154 and 196 K

$$p_{G\&E}(kPa) = \frac{101.325}{760} \times 10\, e^{[(a_1/T)+b_1+c_1T+d_1T^2]} \quad (2.28)$$

$$a_1 = -1354.21 \ln(10) \qquad b_1 = 8.69903 \ln(10)$$

$$c_1 = 0.001588 \ln(10) \qquad d_1 = -4.5107 \times 10^{-6} \ln(10)$$

- Azreg-Aïnou[96] : equation of Antoine between 154.3 and 195.9 K

$$p_A(kPa) = 100 \times \mathrm{e}^{\{\bar{A}_1-[\bar{B}_1/(T+C_1)]\}} \quad (2.29)$$

$$\bar{A}_1 = A_1 \ln(10)\ ;\ \bar{B}_1 = B_1 \ln(10)\ ;\ A_1 = 6.81228\ ;\ B_1 = 1301.679\ ;\ C_1 = -3.494$$

Constants A1, B1 and C1 are estimated by the National Institut of Standards and Technology (NSIT).

Other correlations have been found by Azreg-Ainou[96] for temperatures below 154 K which show that the CO_2 behaves like an ideal gas below this temperature.

- Azreg-Aïnou[96] : correlation for $T > 5K$

$$p_{AA} = C\, T^{5/2} Z_r\, Z_v\, e^{\frac{\Delta h_S - T\, s_{co2,solid} - \Delta h_{S,0} - B(T)p}{RT}} \quad (2.30)$$

$$B(T)p = R l_1 [1 - (\frac{l_2}{T^2})]\, p \quad (2.31)$$

$$l_1(K.kPa^{-1}) = \frac{9\times304.1}{128\times72.8\times101.325} \qquad l_2(K^2) = 6 \times 304.1^2$$

$$C = 7.575 \times 10^5$$

$$Z_{vi} = \frac{1}{1 - e^{-\frac{\theta_{vi}}{T}}} \qquad Z_r = \frac{T + \theta_r/3}{2\,\theta_r} \qquad Z_v = Z_{v1}^2 Z_{v2} Z_{v3}$$

$$\theta_{v1} = 954\ K \qquad \theta_{v2} = 1890\ K \qquad \theta_{v3} = 3360\ K \qquad \theta_r = 0.561\ K$$

$$\Delta h_{s,0} = 6273.4\ cal.mol^{-1} \qquad R = 1.98724\ cal.(K.mol)^{-1}$$

Δh_s is the heat of sublimation and $s_{co2,solid}$ is the entropy of the solid CO_2. $\Delta h_{s,0}$ is the heat of sublimation at T = 0 K. Rewriting previous equations:

$$p_{g,ideal}(kPa) = 10^{-3} \times C\ T^{5/2} Z_r\ Z_v\ e^{\frac{\Delta h_S - T\,s_{co2,solid} - \Delta h_{s,0}}{RT}} \tag{2.32}$$

$$p_{AA}\ (kPa) = \frac{(\frac{101.325}{760}) p_{g,ideal}}{1 + \frac{l_1[1 - (l_2/T^2)] p_{g,ideal}}{T}} \tag{2.33}$$

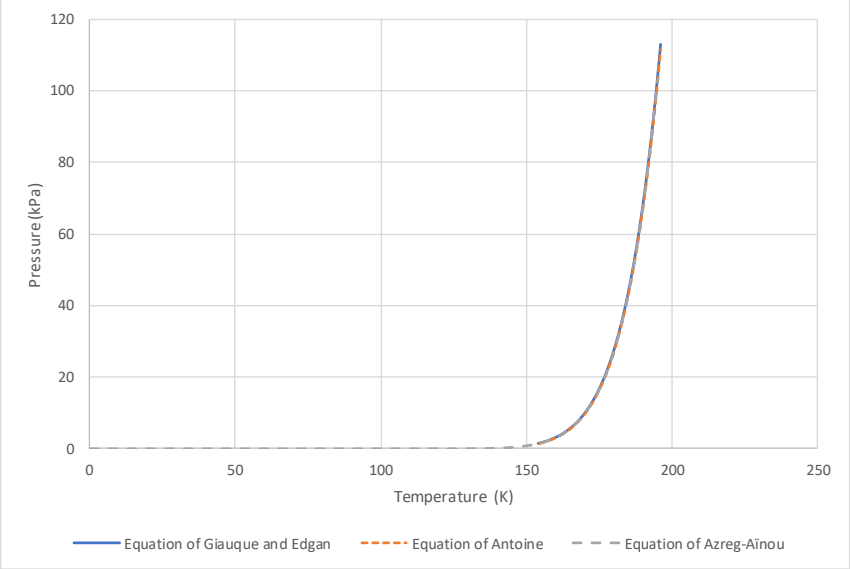

Figure 34: vapour pressure of carbon dioxide as function of the temperature

Figure 34 shows very good agreement between the 3 different correlations and since the Azreg-Aïnou equation (2.35) covers the largest temperature range, it will be used for the rest of the study. The CO_2 sublimation pressure is one of the most important parameters since it gives the relation between the pressure and temperature at CO_2 saturation conditions. The partial pressure of CO_2 in the flue gases (or biogas) changes as deposition occurs, this leads to a change in saturation temperature which should be attained in order for CO_2 to frost on the cold surface.

2.5.8. Sublimation Heat

The curve representing heat of sublimation as a function of temperature can be found in the Azreg-Aïnou article. The equation of this curve is found. Then using values found by Eucken and Donath and presented in an article by Giauque and Egan[97], the curve representing heat sublimation of CO_2 can be plotted as a function of temperature.

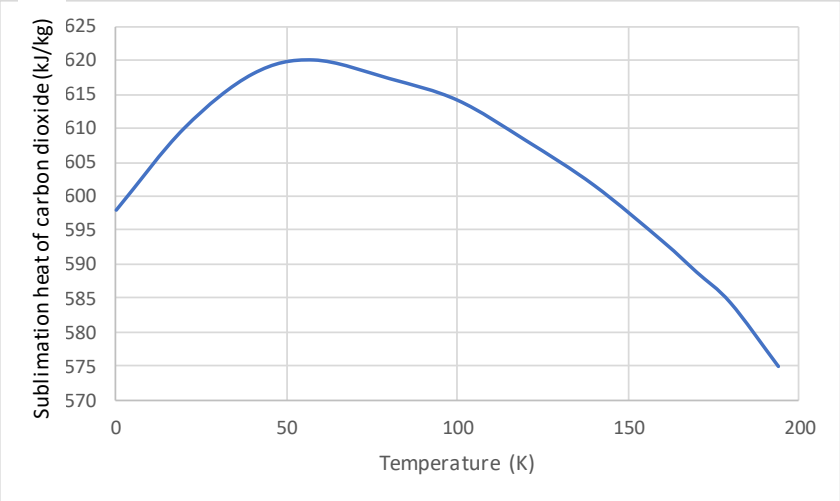

Figure 35: CO_2 sublimation heat as function of the temperature

$$L_{CO2,sv} = -10^{-7}T^4 + 5 \times 10^{-5}T^3 - 0.0111T^2 + 0.8714T + 597.68 \quad (2.34)$$

2.6. Properties of binary gas mixtures

Since this study does not deals with common gas mixture like humid air which is composed of air and water vapour, the thermophysical properties of the flue gases (or the biogas) are not well known nor tabulated. A study was made in order to determine the best correlation to use when calculating these properties. "Properties of gases and liquids" by Poling et al. [99] served as the main reference for this study.

2.6.1. Viscosity and conductivity

Since the heat transfer between the gas mixture containing the CO_2 and the cold surface is carried out by forced convection, the coefficient of heat transfer was calculated (this heat transfer coefficient is considered for calculations of mass transfer by analogy). This requires the values of dynamic viscosity and thermal conduction in the gas flow. The viscosity will be used to calculate the Reynolds number thus knowing if the flow is turbulent or laminar.

Viscosity depends mostly on the interaction of molecules in a system. From the data found in "Properties of gases and liquids" [99], Chapmann-Enskog proposed the most accurate relation for the viscosity derived from the Boltzmann equation in which it was found that the viscosity depends on the attraction and repulsion of the molecules and is principally a function of the temperature. The two increase simultaneously. As for the viscosity of a gas mixture, many methods extended from Chapmann-Enskog kinetic theory were found in the literature. A method was proposed by Wilke (1950) where the dynamic viscosity of a gas mixture is function of mole fractions of each substance, their molar masses and their viscosities as pure substances. In 1958, Mason and Saxena proposed a modification to a formula previously suggested by Wassiljewa (1904) to find the thermal conductivity of a gas mixture so that the relation becomes similar to that of Wilke's viscosity but with thermal conductivities. This relation can be written as:

$$Z_m = \sum_{i=1}^{n} \frac{y_i z_i}{\sum_{j=1}^{n} y_j \emptyset_{ij}} \quad (2.35)$$

Where Z_m is the transport property of the mixture, z is the transport property of each component, y is the molar fraction and $\emptyset$ is a function of η the viscosity and M the molar mass of each component.

$$\emptyset_{ij} = \frac{\left[1+(\eta_i/\eta_j)^{1/2}(M_i/M_j)^{1/4}\right]^2}{\left[8(1+M_i/M_j)\right]^{1/2}} \quad (2.36)$$

The results found by this method will be compared to results extrapolated from REFPROP data in which viscosity and thermal conductivity are modelled by ECS methods (using critical temperature and density), by the friction method or by fluid-specific correlations. These models were coded with extensive comments and tested with several compilers. The calculations of these properties can be performed at a given (T, ρ, x) state. The composition of the mixture is fixed and the corresponding transport property can be found. For example, considering two mixtures of N_2-CO_2 and CH_4-CO_2 with respective molar compositions of 80/20 and 70/30, viscosities and thermal conductivities are estimated as follows:

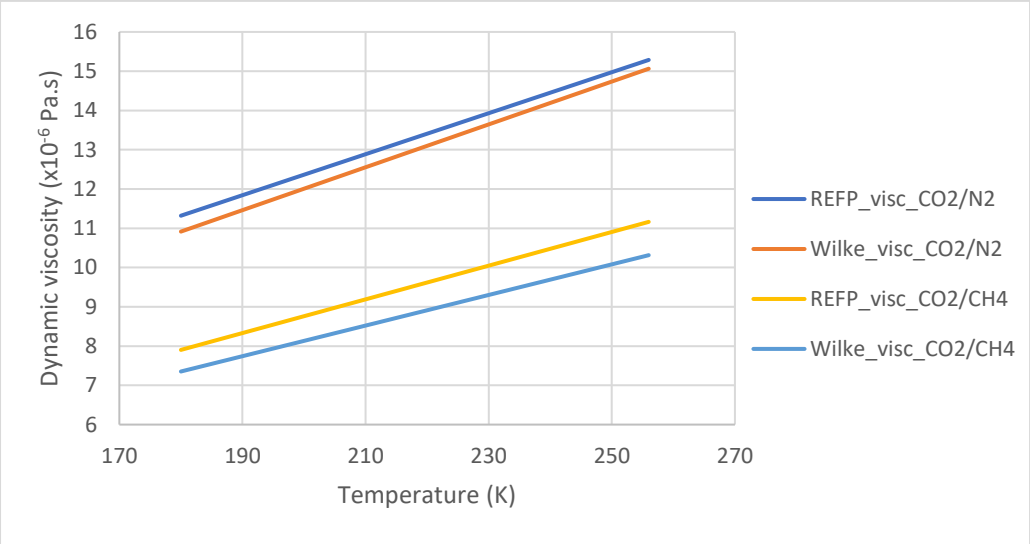

Figure 36: Comparision between viscosities found by the Wilke correlation and the data found in REFPROP

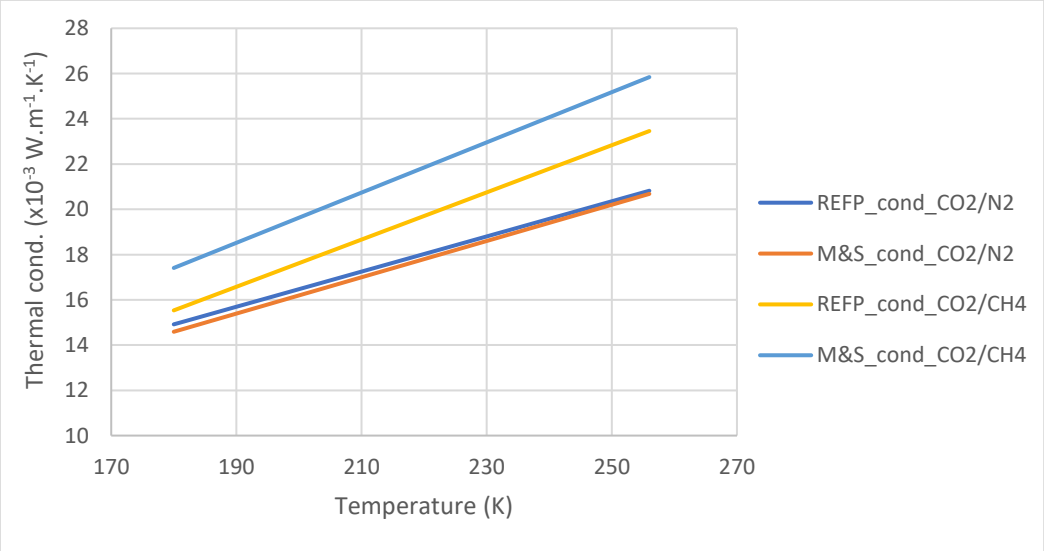

Figure 37: Comparision between thermal conductivities found by the Mason and Saxena correlation and the data found in REFPROP

The difference between Wilke's viscosity and REFPROP for the case of N_2+ CO_2 is less than 10% and for the case of CH_4+CO_2 it reaches 15%. On the other hand, the thermal conductivity shows a difference up to 25% for both cases therefore in the model proposed in this thesis, the data gathered by Wilke for the viscosity and Mason and Saxena for the thermal conductivity will be used. The data gathered from REFPROP can be used, however, only by taking several composition intervals which will reduce the precision of the calculations.

2.6.2. Coefficient of diffusion calculation

In order to calculate the mass flux of frosted CO_2 inside the frost layer, Fick's law of diffusion was used. The diffusion coefficient is a key parameter in order to determine this mass flux of solidified CO_2. In the literature [99], it is possible to find theoretical and empirical prediction of the diffusion coefficient for binary gas systems at low pressure. Chapman and Enskog derived the following equation:

$$D_{AB} = \frac{3}{16}\frac{(4\pi kT/M_{AB})^{1/2}}{n\pi\sigma_{AB}^2\Omega_D} f_D \tag{2.37}$$

Where M_A and M_B are molecular weights in g/mol of components A and B.

$$M_{AB} = 2[(1/M_A) + (1/M_B)]^{-1} \tag{2.38}$$

n is the number density of molecules in the mixture which can be expressed by the ideal-gas law, k is Boltzmann's constant and T is the absolute temperature in K. Ω_D represents the dimensionless collision integral for diffusion which is function of the temperature, it is predicted by the choice of the intermolecular force law between colliding molecules. $\sigma_{AB}$is the characteristic length in Å of the intermolecular force law which depends on the size of each molecule. $f_D$is a correction factor that depends principally of the molecular masses, which is usually taken as a value of 1.

Therefore, the diffusion coefficient of the binary mixture can be written as follows:

$$D_{AB} = \frac{0.00266T^{3/2}}{PM_{AB}^{1/2}\sigma_{AB}^2\Omega_D} \tag{2.39}$$

Where D_{AB} is in cm^2/s and P is the pressure of the mixture in bar. The most important part to be able to use equation is the evaluation of σ_{AB} and Ω_D. Therefore, the Lennard-Jones 12-6 Potential should be used. This entity calculates the intermolecular energy ψ between two molecules to the distance r separating them by the following equation:

$$\psi = 4\varepsilon\left[\left(\frac{\sigma}{r}\right)^{12} - \left(\frac{\sigma}{r}\right)^{6}\right] \tag{2.40}$$

With ε and σ the characteristic Lennard-Jones energy and length respectively. These parameters can be found in the literature for each molecule. In order to find these parameters for the mixture, these simple relations can be used: $\varepsilon_{AB} = (\varepsilon_A\varepsilon_B)^{1/2}$ and $\sigma_{AB} = \frac{\sigma_A+\sigma_B}{2}$. Ω_D, was found to be function of kT/ε. In order to estimate Ω_D, many analytical approximations were proposed (Hattikudur and Thodos 1970; Johnson and Colver 1969; Neufield et al. 1972). The accurate relation of Neufield et al. 1972 is:

$$\Omega_D = \frac{A}{(T^*)^B} + \frac{C}{\exp(DT^*)} + \frac{E}{\exp(FT^*)} + \frac{G}{\exp(HT^*)} \tag{2.41}$$

Where $T^* = kT/\varepsilon_{AB}$; $A = 1.06036$, $B = 0.15610$, $C = 0.19300$, $D = 0.47635$,

$E = 1.03587$, $F = 1.52996$, $G = 1.76474$, $H = 3.89411$. Thus, it is possible to calculate the diffusion coefficient of the CO_2-N_2 or CO_2-CH_4 mixture. It should be noted that viscosity data can be used to determine this property.

As for empirical correlation based on experiment data, many equations were used to estimate the diffusion coefficient of a binary gas mixture at low pressure. Agreement with experimental data was within 5 to 10%. Two methods were the most reliable:

1- Wilke and Lee (1955):

$$D_{AB} = \frac{[3.03-(0.98/M_{AB}^{1/2})](10^{-3})T^{3/2}}{PM_{AB}^{1/2}\sigma_{AB}^2\Omega_D} \quad (2.42)$$

All the parameters are the same as mentioned in the Chapman-Enskog relation. The diffusion coefficient is in cm^2/s. This method uses boiling point temperature and liquid molar volume in order to estimate Ω_D, ε and σ.

2- Fuller et al. (1965, 1966, 1969)

$$D_{AB} = \frac{0.00143T^{1.75}}{PM_{AB}^{1/2}\left[(\sum v)_A^{1/3}+(\sum v)_B^{1/3}\right]^2} \quad (2.43)$$

$\sum v$ is found for each component of the mixture by summing the atomic diffusion volumes found in the literature. The error of these values is estimated to be about 4%. This method is compared with the Chapman-Enskog method to calculate the deviation percentage between the two relations.

Considering two mixtures of CO_2-N_2 and CO_2-CH_4 at P=1 bar.

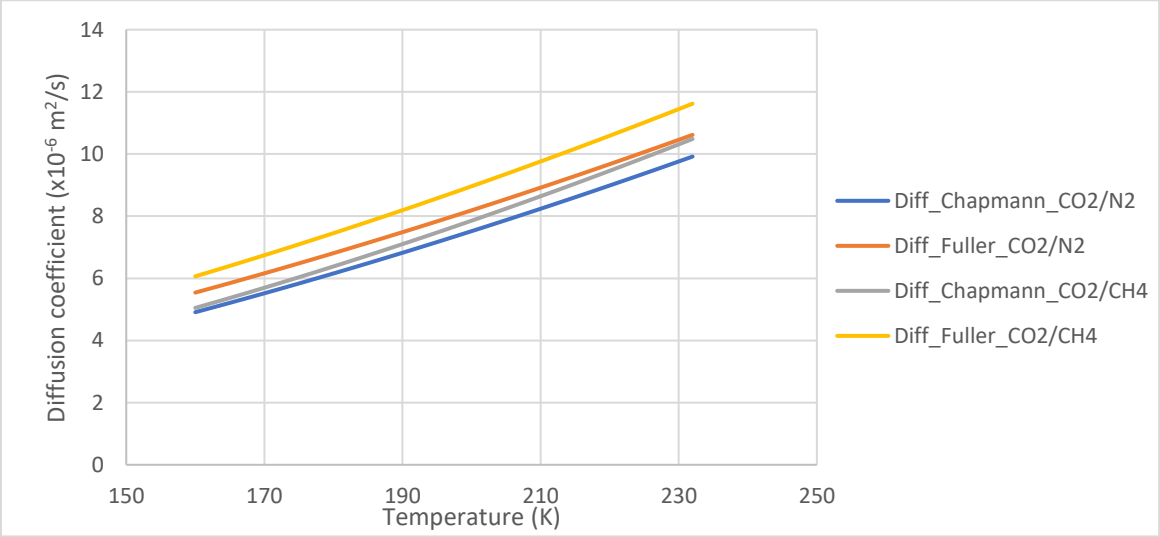

Figure 38: Comparision between diffusion coefficient found by Wilke and Lee (Chapman-Enskog) and that found by Fuller et al.

The temperature and the diffusion coefficient increase simultaneously as predicted from the relations of Chapmann-Enskog ($D \propto T^{1.5}$) and Fuller et al. ($D \propto T^{1.75}$). The percentage error

between the theoretical and the empirical relations decreases with temperature increase. For the CO_2-N_2 mixture the error is 12.8% at T=160K and decreases to 7% at T=232K. As for the CO_2-CH_4 mixture the error ranges from 20% at T=160K to 10% at T=232K. The error is remarkable between the two values therefore it is important to see the effect of the diffusion coefficient on the frost growth and heat transfer. The equation proposed by Fuller et al. will be used and then the effect of the diffusion coefficient on the frost growth will be studied.

2.6.3. Properties of pure components

Equation 2.36 shows that in order to calculate the viscosity and thermal conductivity of the mixture, these properties should be calculated before for each pure component. Using the "Chemical Properties Handbook" by Carl Yaws [100], it is possible to calculate these properties as well as the heat capacities as function of the temperature.

$$\mu_{co2}(\mu P) = 11.811 + 0.4938 \times T - 1.0851 \times 10^{-4} \times T^2 \quad (2.44)$$

$$k_{co2}(W/(m.K)) = -0.012 + 1.0208 \times 10^{-4} \times T - 2.2403 \times 10^{-8} \times T^2 \quad (2.45)$$

$$cp_{co2}(J/(mol.K)) = 27.437 + 0.042315 \times T - 1.9555 \times 10^{-5} \times T^2 + 3.9968 \times 10^{-9} \times T^3 - 2.9872 \times 10^{-13} \times T^4 \quad (2.46)$$

$$\mu_{n2}(\mu P) = 42 + 0.475 \times T - 9.88 \times 10^{-5} \times T^2 \quad (2.47)$$

$$k_{n2}(W/(m.K)) = 0.00309 + 7593 \times 10^{-5} \times T - 1.1014 \times 10^{-8} \times T^2 \quad (2.48)$$

$$cp_{n2}(J/(mol.K)) = 29.342 - 0.0035395 \times T + 1.0076 \times 10^{-5} \times T^2 - 4.3116 \times 10^{-9} \times T^3 + 2.5935 \times 10^{-13} \times T^4 \quad (2.49)$$

2.7. Heat transfer coefficient

The choice of heat transfer coefficient has a major effect on the results of the model because it affects directly the sensible heat transfer by convection as well as the mass transfer coefficient which will estimate the mass flux of CO_2 solid frosted on the cold flat surface. The frost thickness will increase with time increasing the flow velocity. The Reynolds number is proportional to the flow velocity, it is used to estimate the Nusselt number which can be used to find the heat transfer coefficient. In the table below, the correlations closest to the case studied will be compared to decide which fits the model the most. Even though in some cases not all conditions are met concerning the nature of the flow or the presence of frost, the cases cited below will be considered while validating the model to choose the best fit for the rest of this study.

Table 3: Nusselt number correlations for different geometries and flows

Nusselt number correlation	Flow nature and geometry	References
$\boldsymbol{Nu_L = 0.664.Re_L^{1/2}.Pr^{1/3}}$ (2.50)	Laminar flow parallel to a flat plate. Uniform temperature. Re<5.10^5	Yunus A. Cengel [101]
$\boldsymbol{Nu_L = \left(0.037.Re_L^{0.8}\right).Pr^{1/3}}$ (2.51)	Turbulent flow parallel to a flat plate. Uniform temperature. Re≥5.10^5	Yunus A. Cengel [101]
$\boldsymbol{Nu_{Dh} = 0.034.Re_{Dh}^{0.8}}$ (2.52)	Two parallel plates with frost. 6000<Re<50000	Yamakawa [102]
$\boldsymbol{Nu_{Dh} = 0.021.Re_{Dh}^{0.8}.Pr^{0.6}}$ (2.53)	Turbulent flow in a duct over a cold surface with frost	Dientenberger et al. [103]

The Nusselt number is found according to the geometry and the nature of the flow, the heat transfer coefficient of convection can then be calculated as follows:

$$h_{conv} = \frac{Nu \times k_{flue\_gases}}{L_{carac}} \quad (2.54)$$

With k_{flue_gases} the thermal conductivity of the flue gases discussed previously and L_{carac} the characteristic length which is considered as the hydraulic diameter to take into account the frost thickness and its effect on the velocity and eventually the Reynolds number.

2.8. Mass transfer coefficient

The Lewis number creates a link between the heat and the mass transfer coefficients. It represents the ratio of mass to thermal diffusion. The Lewis number can be calculated according to $Le = Sc / Pr$ with Pr the Prandtl number and Sc the Schmidt number. In the case of humid air, most studies consider the Lewis number Le equal to 1. But since the Lewis number depends of the gas properties, it can't be assumed as unity for the case of flue gases (N_2+CO_2) or biogas (CH_4+CO_2). In this study, the Lewis number will be calculated using the thermophysical properties of the flue gases:

$$Le = \frac{k_{flue\_gases}}{D_{flue\_gases} \times \rho_{flue\_gases} \times C_{p,flue\_gases}} \quad (2.55)$$

The relation between mass transfer and heat transfer coefficients can be found in Lee and Ro[92] from Bergman et al.[104]:

$$h_m = h_c/(\rho_{flue\_gases}.c_{p,flue\_gases}.Le^{\frac{2}{3}}) \quad (2.56)$$

2.9. Model validation

Data gathered from literature concerning CO_2 frosting on a cold surface are very few. In 1985, Shchelkunov et al.[87] conducted experiments on a horizontal cold flat plate (5.6cmx5.6cm), a mixture of N_2 and CO_2 at different concentrations, atmospheric pressure, different inlet temperatures and mass flows. Three cases from Shchelkunov's results will be compared with the results obtained from the model developed in this thesis for different heat transfer coefficients. The values that will be compared are the frost thickness and the frost density.

Table 4: Operating conditions for Shchelkunov's different experiments

	$T_{flue\_gases}\ (°C)$	$x_{CO2/N2}\ (kg/kg)$	$v_{flue\_gases}\ (m/s)$	$T_{cold\_surface}\ (°C)$
Case 1	-80	0.0715	3	-128
Case 2	-80	0.0715	0.5	-128
Case 3	-74	0.151046	3	-122

The results below show the importance of the heat transfer coefficient in predicting the evolution of frost formation. In all the cases, frost thickness and frost density seem to increase at a high rate at the beginning of the frost formation then the growth rate decreases; this was discussed before and it results from the thermal resistive layer created by the frost as it grows, which will limit the heat transfer between the cold surface and the flue gases. All the correlations show an under estimation of the thickness and over estimation of the density. Heat transfer coefficient affects the sensible heat transfer directly and the mass of CO_2 frosted through the mass transfer coefficient. Thermal conductivity of the CO_2 frost was correlated from the experimental results done by Shchelkunov et al. It affects mainly the heat transfer by conduction inside the frost layer which will affect the temperature distribution inside the frost layers. Even though the correlation not taking into account the presence of frost on the cold surface shows a very high accordance with Case 2 (Figure 39.a), all the other cases and results show important differences. For all 3 cases the evolution of the frost with respect to the inlet conditions seems to follow the same direction as the experimental data. The correlation of Dietenberger et al. [103] gives the best estimation of frost growth.

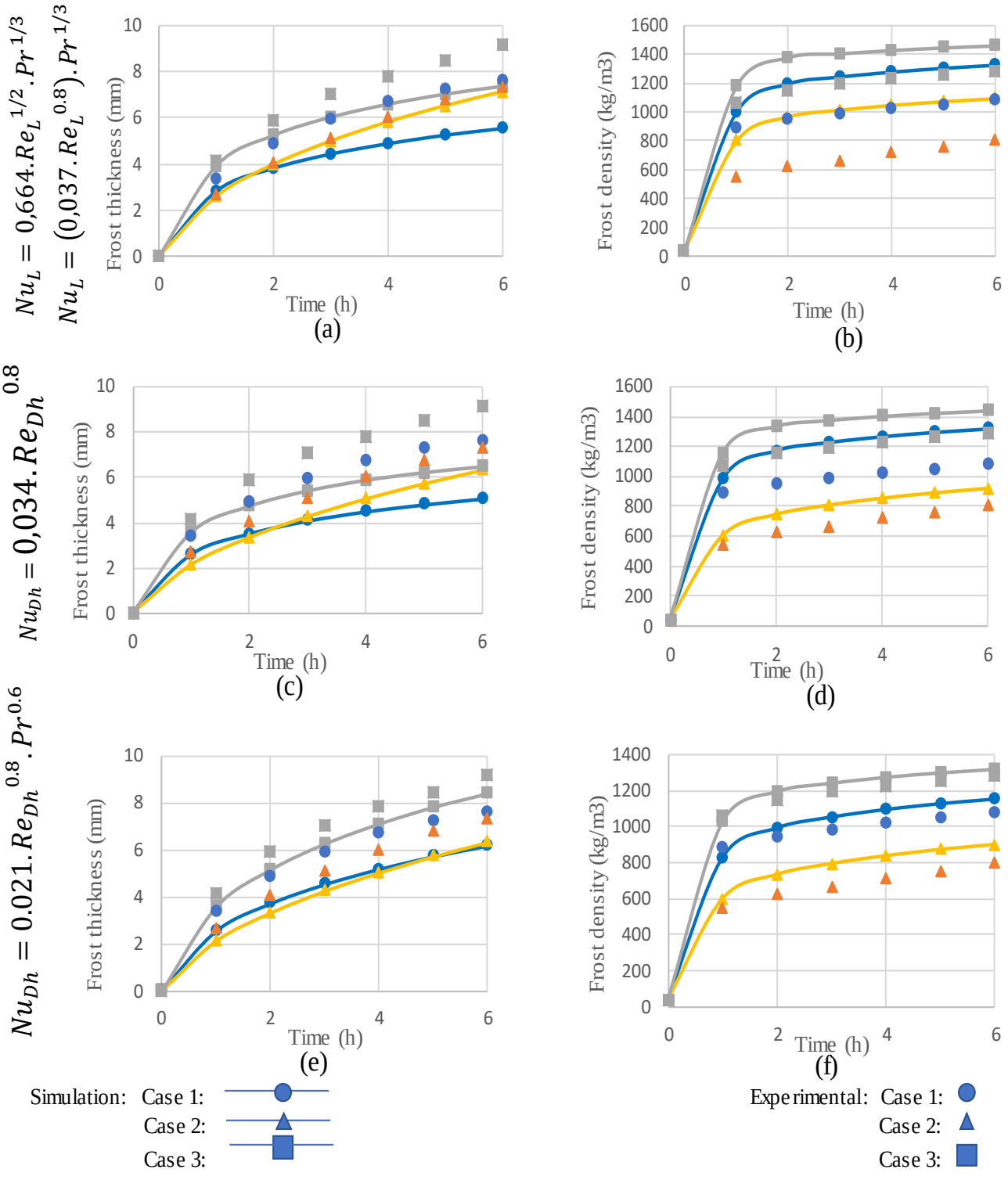

Figure 39: Comparison of frost thickness and density growth experimental data from Schlenjunov and calculations for different heat transfer coefficient equations

Conclusion

In this chapter, the psychrometric relation connecting temperature and relative concentration was explained. The deposition mechanism was detailed and cases from the literature were proposed to better understand this complicated phenomenon. CO_2 frosting on a cold surface was modelled with values for the transport properties from REFPROP or relations found in literature. Simulation results show good agreement when compared to experimental results done by Shchelkunov et al. who conducted experiments of CO_2 frost deposition on a cold surface from a binary mixture of N_2+CO_2. A correlation of the CO_2 frost thermal conductivity was found using the experimental results of Shchelkunov et al. A correlation proposed by Dietenberger et al. was used to define the heat transfer coefficient equation that will be used to calculate the mass transfer coefficient and eventually the mass flow of CO_2 frosted. Results show the importance of taking frost presence when considering the choice of the heat transfer correlation.

One of the objectives of this thesis is to apply the CO_2 phase change knowledge acquired to the biogas upgrading by cryogenics. In chapter 2, a model of CO_2 deposition from a binary mixture over a flat plate was proposed and validated using data from the literature; however the binary mixture was N_2 +CO_2 (flue gases). In chapter 3, the flue gases will be replaced by biogas (CH_4 +CO_2) but keeping the same model. The properties of the flow will be changed accordingly. A sensitivity study will be conducted in order to improve the operating conditions and the deposition phenomenon is detailed even more by studying the frost formation and heat transfers along the cold surface. These steps should be followed in order to obtain the most efficient and accurate results possible of CO_2 separation from biogas before moving to the next step which will be presented in chapter 4: the cold recovery by controlled sublimation.

Chapitre 2: Modélisation du givrage de CO_2 à partir d'une phase gazeuse

Introduction

Ce chapitre décrit les phénomènes de givrage du CO_2 et propose un modèle mathématique détaillé pour étudier la croissance du givre et le transfert de chaleur à la surface et à l'intérieur de la couche de givre.

La majorité des travaux effectués sur la formation de givre considèrent le cas de givrage de vapeur d'eau contenue dans l'air humide, ce phénomène étant plus courant. La méthode la plus utilisée pour évaluer la croissance du givre consiste à élaborer un modèle basé sur les équations de transfert de chaleur et de masse tout en considérant le givre comme un milieu poreux, prenant ainsi en compte la diffusion de la phase gazeuse à la fois à la surface du givre et à l'intérieur des pores du givre. Na et Webb[83], Lee et al. [84], Le Gall et Grillot [85] et d'autres auteurs ont développé des modèles détaillés de la croissance du givre d'eau.

Shchelkunov et al. [87] ony mené une expérience visant à observer et à contrôler le dépôt de CO_2 contenu dans un mélange de gaz binaire (principalement N_2+CO_2) sur une surface froide. Dans son article, il a pu étudier les variations d'épaisseur, de conductivité thermique et de masse volumique du givre en fonction du temps de givrage. En comparant ses résultats avec ceux de la littérature sur la formation du givre à partir de la vapeur d'eau (Lee et al. [84], Hermes[80]), une similarité peut être observée dans la croissance et la densification du givre, alors on pourra supposer que les phénomènes de givrage du CO_2 contenu dans un mélange gazeux binaire, qu'il s'agisse de biogaz ou de gaz de combustion, peuvent être traités de la même manière que le givrage de la vapeur d'eau contenu dans l'air humide. Comme les seules données disponibles dans la littérature concernent les mélanges CO_2+N_2, ce cas sera considéré dans ce chapitre afin de valider le modèle. Dans les chapitres suivants, le N_2 sera remplacé par du CH_4 afin de simuler le cas de l'élimination du CO_2 contenu dans le biogaz.

2.1. Mécanisme de formation du givre

Le mécanisme de formation du givre peut être divisé en 3 phases principales: la première correspond à la «formation des cristaux», la seconde à la « croissance du givre» et la dernière au «développement complet du givre»[82]. Les premiers moments de formation de givre sont appelés phase de croissance cristalline ou phase de nucléation. Ils sont les plus complexes à simuler et sont généralement négligés. Dans cette phase, des cristaux se forment et ils sont utilisés comme base pour plus de givre de CO_2. Pour la phase de croissance du givre, les gaz de combustion contenant le CO_2 vont se refroidir par convection avec la surface froide jusqu'à ce que le CO_2 atteigne sa température de solidification à sa pression partielle. La croissance du givre augmente rapidement au début puis ralentit à cause de l'accumulation de la couche de givre qui forme une résistance thermique entre la surface froide et le flux de gaz de combustion. Le givre formé est poreux, le CO_2 le traverse et givre à l'intérieur de la couche ce qui augmente principalement la masse volumique du givre. La phase de développement complet correspond à l'équilibre entre la température et la concentration est atteint à la surface du givre, ce qui limite, voie arrête le givrage additionnel de CO_2. Dans ce chapitre, le modèle développé décrira

principalement la deuxième phase car il s'agit de la partie décrivant l'évolution de la croissance du givre en fonction du temps de givrage et de l'élimination du CO_2 du flux gazeux.

2.2. Modélisation du givrage de CO_2

L'objectif principal du modèle de givrage développé est de prédire le transfert de masse de CO_2, la variation de l'épaisseur du givre θ_{frost} et sa masse volumique ρ_{frost} en calculant le transfert de chaleur et de masse pendant les phases de formation et de croissance du givre. Le modèle de givrage proposé est présenté en considérant une surface refroidie à une température cryogénique sur laquelle le givre se forme. Lorsque la température du CO_2 dans les gaz de combustion atteint sa température de condensation solide avec une différence de concentration de CO_2 entre le flux de gaz et la surface, du givre se forme. La croissance de la couche de givre affecte la conduction dans le givre par l'effet isolant de l'épaisseur du givre.

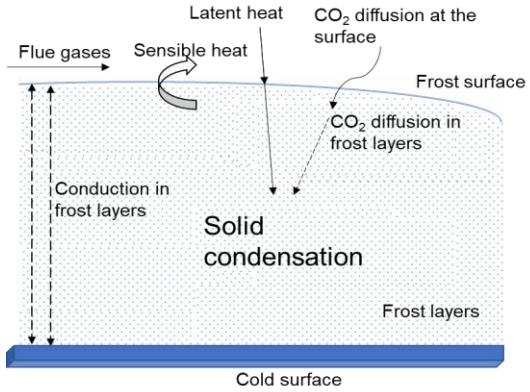

Figure F3: Description des transferts thermiques et massiques lors de la phase de givrage du CO_2

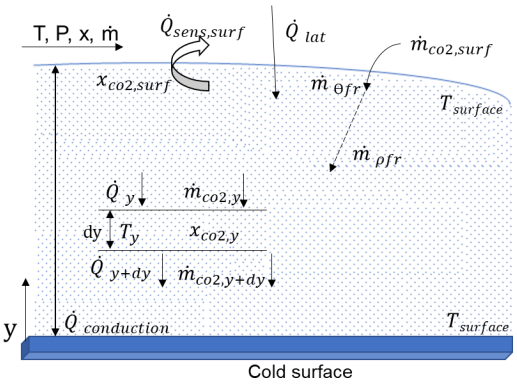

Figure F4: Transfert thermique et massique à la surface et dans la couche de givre

Plusieurs auteurs ont présenté des corrélations de l'épaisseur et la masse volumique du givre en phase de croissance, mais ces corrélations sont limitées à des conditions de température, géométries et au cas de givrage de vapeur d'eau contenu dans l'air humide. L'approche la plus commune pour la modélisation du givrage utilise des équations généralisées du transfert de chaleur et de masse pour estimer la croissance du givre en considérant le givre comme un milieu poreux [82]–[84],[88]. Ces modèles divisent le flux massique de givre formé en deux parties : le givre qui se forme à la surface et qui conduit à l'augmentation de son épaisseur, l'autre se diffusant et se déposant à l'intérieur de la couche de givre, augmentant ainsi sa masse volumique. La diffusion de masse et de chaleur à l'intérieur de la couche de givre est prise en compte dans tous les modèles étudiés dans la littérature utilisant cette approche. Le coefficient de transfert de masse est déterminé par analogie de Lewis avec le coefficient de transfert de chaleur. Étant donné que les modèles prenant en compte les dépôts de CO_2 à partir d'un mélange froid binaire sont très limités à quelques études de cas et que la plupart des travaux étaient expérimentaux, la seconde approche considérant le givre comme un milieu poreux avec diffusion thermique et massique semble plus appropriée pour le modèle présenté dans cette étude.

2.2.1. Hypothèses

Les hypothèses largement utilisées dans la littérature sont prises en compte lors de la modélisation des dépôts de givre et de la croissance de CO_2 sur une surface froide:

- La modélisation de la phase de nucléation sans couche de givre existante est compliquée et imprécise. Par conséquent, on considère une couche préexistante, mince et uniforme de givre de CO_2 avec une faible masse volumique[85].

- La modélisation de la formation de givre est effectuée en 1D: la couche de givre se développe dans la direction normale à la surface froide[92]. Dans une étude plus approfondie, on considère la modélisation en 2D pour prendre en compte la variation de la température des gaz de combustion et leur concentration en CO_2 tout le long de la surface.

- La transition entre les phases est considérée comme une condensation solide sans aucun passage à travers la phase liquide. Ceci est dû aux conditions de pression du CO_2 présent dans le mélange gazeux qui le maintiennent en dessous de son point triple.

- Les températures à l'interface gaz de combustion-givre sont considérées égales.

- Tous les gaz sont considérés comme gaz parfaits à pression atmosphérique.

2.2.2. Bilan énergétique et massique lors du givrage

Les équations de transfert de masse et de chaleur considérées pour le givrage de la vapeur d'eau seront utilisées dans le cas du givrage de CO_2, tout en considérant le givre comme un milieu poreux. La Figure F4 montre les différents transferts de chaleur et de masse se produisant à la surface et à l'intérieur du givre lors du givrage du CO_2 sur la surface froide. Dans la plupart des travaux considérant le givrage de vapeur d'eau[84] [83], le modèle est divisé en trois parties: le flux de gaz (N_2+CO_2) , la surface du givre et la couche de givre.

v. Le flux de gaz de combusiton

On calcule la chaleur sensible par convection entre les gaz de combustion et la surface froide :

$$\dot{q}_{sens} = h_c \times (T_{flue\ gases} - T_{fr,surf}) \quad \text{(F.2.1)}$$

Le flux de CO_2 givré $\dot{m}_{co2,frost}$ à partir des gaz de combustion vers la surface froide peut être calculé par analogie avec le transfert thermique convective :

$$\dot{m}_{co2,frost} = h_m \times \rho_{flue\ gases} \times (x_{co2/n2} - x_{fr,surf}) \quad \text{(F.2.2)}$$

La concentration du CO_2 à la surface est liée à la température par la psychrométrie.

vi. La surface du givre

A la surface du givre, le flux de CO_2 givré est divisé en deux parties principales : $\dot{m}_{\rho,frost}$ qui correspond au flux de CO_2 givré dans la couche de givre et $\dot{m}_{\theta,frost}$ à la surface.

Le flux de CO_2 que diffuse dans le givre est exprimé par la loi de diffusion de Fick:

$$\dot{m}_{\rho frost,surf} = D_{eff} \times \rho_{flue\ gases} \times \left(\frac{dx_{flue\ gases}}{dy}\right)_{y=y,surf} \quad \text{(F.2.3)}$$

$\left(\frac{dx_{flue\ gases}}{dy}\right)_{y=y,surf}$ est le gradient de concentration du CO_2 quand y tends vers θ_{frost}.

Connaissant le débit massique total de CO_2 givré, il est possible de calculer le débit massique de CO_2 responsable de l'augmentation de l'épaisseur $\dot{m}_{\delta fr}$. L'épaisseur du givre est alors calculée par:

$$\frac{d\theta_{frost}}{dt} = \dot{m}_{\theta frost}/\rho_{frost} \quad \text{(F.2.4)}$$

À la surface du givre, un transfert de chaleur par convection a lieu à l'interface avec les gaz de combustion. Le givre est refroidi par conduction entre la surface froide et la surface givrée. Le transfert de chaleur total à la surface du givre est décrit par les équations :

$$\dot{q}_{tot,surf} = \dot{q}_{sens} + \dot{m}_{\theta frost} \times L_{sv} \quad \text{(F.2.5)}$$

$$\dot{q}_{cond,surf} = k_{frost} \times \left(\frac{dT_{fr}}{dy}\right)_{y=y,surf} \quad \text{(F.2.6)}$$

Le bilan énergétique à la surface du givre est exprimé par :

$$\dot{q}_{tot,surf} = \dot{q}_{cond,surf} \quad \text{(F.2.7)}$$

vii. La couche de givre

A l'intérieur de la couche de givre, le flux massique de CO_2 givré $\dot{m}_{\rho frost}$ est calculé suivant la loi de Fick (diffusion de la matière) :

$$\dot{m}_{\rho frost} = D_{eff} \times \rho_{flue\ gases} \cdot \frac{dx}{dy} \quad \text{(F.2.8)}$$

Le coefficient de diffusion massique effectif D_{eff} est limité par la porosité de la couche de givre de CO_2. Etant donné que le givre se densifie au fur et à mesure que du givre se forme, un nouveau terme appelé taux d'absorption massique (ou densification) est introduit[93]. Ce terme permet de calculer la variation de la masse volumique à l'intérieur de chaque couche de givre en fonction du temps. Cette variation peut être utilisée pour calculer le débit massique de CO_2 givré à l'intérieur de la couche de givre. La densification du givre est calculée par:

$$\alpha_{co2} = \frac{d\dot{m}_{\rho frost}}{dy} \quad \text{(F.2.9)}$$

Où α_{co2} représente la densification de la couche de givre, la variation de la masse volumique du givre peut être calculée :

$$\frac{d\rho_{frost}}{dt} = \alpha_{co2} \quad \text{(F.2.10)}$$

Dans la couche de givre, la conduction est calculée suivant la loi de Fourier :

$$\dot{q}_{cond} = k_{frost} \times \frac{dT_{fr}}{dy} \quad \text{(F.2.11)}$$

Il est alors possible de trouver une relation entre la conduction et le terme de densification et la chaleur latente de sublimation du CO_2 L_{sv} :

$$\frac{d\dot{q}_{cond}}{dy} = -\alpha_{co2} \times L_{sv} \quad \text{(F.2.12)}$$

2.2.3. Conductivité thermique du givre de CO_2

Les corrélations des coefficients de transfert de chaleur et de masse, ainsi que les valeurs des propriétés thermophysiques, peuvent avoir un impact majeur sur les résultats. L'une des principales propriétés thermophysiques est la conductivité thermique effective du givre k_{frost} . La plupart des corrélations utilisées dans la littérature sont applicables au givre de vapeur d'eau et non au CO_2.

Dans la littérature, la conductivité thermique du givre dépend de sa masse volumique, donc de sa porosité. Pour calculer la conductivité thermique effective du givre CO_2, il convient de connaître la géométrie réelle du givre ainsi que la conductivité thermique des gaz de combustion à chaque position le long de la surface. Ces calculs sont compliqués et n'ont aucune référence dans la littérature. Par conséquent, la conductivité thermique du givre de CO_2 est estimée à l'aide des résultats expérimentaux de Shchelkunov et al. [87]. Bien que l'article a été écrit en 1985, il s'agit de l'une des très rares études sur le givrage de CO_2 sur une surface froide contenant des données expérimentales. En utilisant plusieurs résultats donnés par Shchelkunov et al., la conductivité thermique effective du givre CO_2 a été estimée par la corrélation suivante :

$$k_{eff} = \frac{0.27 \times \rho_{fr,avg}}{2386.037 - \rho_{fr,avg}} \qquad \text{(F.2.13)}$$

Azreg-Aïnou[96] présente plusieurs propriétés du CO_2 à basse température. Il a basé son travail sur ceux de Giauque et Egan [97] afin d'établir une corrélation pour le calcul de la capacité thermique du CO_2 solide. Il présente également une comparaison entre différentes corrélations permettant de calculer la pression de vapeur saturante et la chaleur de sublimation du CO_2.

2.3. Propriétés des mélanges binaires gazeux

Puisque cette étude ne traite pas de mélanges de gaz tels que l'air humide composé d'air et de vapeur d'eau, les propriétés thermophysiques des gaz de combustion (ou du biogaz) ne sont pas facilement disponibles dans la littérature. Une étude a été réalisée afin de déterminer la meilleure corrélation à utiliser lors du calcul de ces propriétés. "Properties of gases and liquids" par Poling et al. [99] a servi comme référence principale pour cette étude

2.3.1. Viscosité et conductivité thermique

Le transfert de chaleur entre le mélange gazeux contenant le CO_2 et la surface froide étant réalisé par convection forcée, le coefficient de transfert de chaleur doit être calculé (ce coefficient de transfert de chaleur est utilisé pour les calculs de transfert massique). Cela nécessite les valeurs de la viscosité dynamique et de la conduction thermique du gaz. Wilke (1950) a proposé une méthode dans laquelle la viscosité dynamique d'un mélange de gaz est fonction des fractions molaires de chaque substance, de leurs masses molaires et de la viscosité de chaque composant. En 1958, Mason et Saxena[99] ont proposé une modification de la formule précédemment suggérée par Wassiljewa (1904) afin de déterminer la conductivité thermique d'un mélange gazeux de telle sorte que la relation devienne similaire à celle de la viscosité de Wilke, mais avec des conductivités thermiques:

$$Z_m = \sum_{i=1}^{n} \frac{y_i z_i}{\sum_{j=1}^{n} y_j \emptyset_{ij}} \qquad \text{(F.2.14)}$$

Z_m est la viscosité/conductivité du mélange, z est celle de chaque composant, y la fraction molaire et ∅ une fonction de η la viscosité et M la masse molaire de chaque composant.

$$\emptyset_{ij} = \frac{\left[1+(\eta_i/\eta_j)^{1/2}(M_i/M_j)^{1/4}\right]^2}{\left[8(1+M_i/M_j)\right]^{1/2}} \quad \text{(F.2.15)}$$

Les résultats obtenus par cette méthode seront comparés aux résultats extrapolés à partir des données REFPROP V9.0. Les calculs de ces propriétés s'appliquent à un état donné (T, ρ, x). Si la composition du mélange est fixe, la propriété correspondante peut être trouvée.
La différence entre la viscosité de Wilke et REFPROP V9.0 pour le cas de N_2+CO_2 est inférieure à 10% et pour le cas de CH_4+CO_2, elle atteint 15%. Par ailleurs, la conductivité thermique présente une différence pouvant aller jusqu'à 25% dans les deux cas. Par conséquent, dans le modèle proposé dans cette thèse, les données recueillies par Wilke pour la viscosité et celles de Mason et Saxena pour la conductivité thermique seront utilisées. Les données recueillies à partir de REFPROP ne peuvent toutefois être utilisées qu'en prenant plusieurs intervalles de composition ce qui réduit la précision des calculs.

2.3.2. Calcul du coefficient de diffusion

Afin de calculer le flux de masse de CO_2 givré à l'intérieur de la couche de givre, la loi de diffusion de Fick a été utilisée. Le coefficient de diffusion est alors un paramètre clé. Dans la littérature[99], il est possible de trouver une prédiction théorique et empirique du coefficient de diffusion de mélanges de gaz binaires. L'équation théorique de Chapman et Enskog[99] :

$$D_{AB} = \frac{3}{16}\frac{(4\pi kT/M_{AB})^{1/2}}{n\pi\sigma_{AB}^2\Omega_D} f_D \quad \text{(F.2.16)}$$

Concernant la corrélation empirique basée sur les données expérimentales, de nombreuses équations ont été utilisées pour estimer le coefficient de diffusion d'un mélange de gaz binaire à basse pression. L'accord avec les données expérimentales était comprise entre 5 et 10%. Deux méthodes étaient les plus fiables:

3- Wilke and Lee (1955):

$$D_{AB} = \frac{[3.03-(0.98/M_{AB}^{1/2})](10^{-3})T^{3/2}}{PM_{AB}^{1/2}\sigma_{AB}^2\Omega_D} \quad \text{(F.2.17)}$$

Tous les paramètres sont les mêmes que ceux mentionnés dans la relation Chapman-Enskog. Le coefficient de diffusion est en cm^2/s. Cette méthode utilise la température d'ébullition et le volume molaire liquide afin d'estimer Ω_D, ε and σ.

4- Fuller et al. (1965, 1966, 1969)

$$D_{AB} = \frac{0.00143T^{1.75}}{PM_{AB}^{1/2}\left[(\sum v)_A^{1/3}+(\sum v)_B^{1/3}\right]^2} \quad \text{(F.2.18)}$$

$\sum v$ est calculé pour chaque composant du mélange en additionnant les volumes de diffusion atomique utilisés dans la littérature. L'erreur portant sur ces valeurs est estimée à environ 4%. Cette méthode a été comparée à la méthode Chapman-Enskog pour calculer le pourcentage de déviation entre les deux relations. La température et le coefficient de diffusion augmentent simultanément, comme le prédisent les relations de Chapmann-Enskog ($D \propto T^{1.5}$) et de Fuller et al. ($D \propto T^{1.75}$). Le % d'erreur entre les relations théoriques et empiriques diminue avec l'augmentation de la température. Pour le mélange CO_2-N_2, l'erreur est de 12,8% à T=160 K et

diminue à 7% à T=232 K. En ce qui concerne le mélange CO_2-CH_4, l'erreur passe de 20% à T=160K à 10% à T=232K. L'équation proposée par Fuller et al. sera utilisé dans la suite.

2.4. Coefficient de transfert thermique

Le choix du coefficient de transfert de chaleur a un effet majeur sur les résultats du modèle car il affecte directement le transfert de chaleur par convection, ainsi que le coefficient de transfert de masse qui permet d'estimer le flux massique de CO_2 solide givré sur la surface froide. L'épaisseur de givre augmente avec le temps, ce qui augmente la vitesse d'écoulement du fluide restant à cause du diamètre hydraulique réduit. Le nombre de Reynolds est proportionnel à la vitesse d'écoulement, il est utilisé pour estimer le nombre de Nusselt qui est utilisé pour trouver le coefficient de transfert thermique. Les corrélations les plus proches du cas étudié sont comparées pour déterminer laquelle correspond le mieux au modèle. Le nombre de Nusselt est déterminé en fonction de la géométrie et de la nature de l'écoulement; le coefficient de transfert thermique convectif peut alors être calculé par:

$$h_{conv} = \frac{Nu \times k_{flue\_gases}}{L_{carac}} \quad \text{(F.2.19)}$$

2.5. Coefficient de transfert massique

Le nombre de Lewis relie les coefficients de transfert thermique et massique. Il représente le rapport entre la diffusion massique à la diffusion thermique. Le nombre de Lewis est calculé en utilisant les propriétés thermophysiques des gaz de combustion:

$$Le = \frac{k_{flue\_gases}}{D_{flue\_gases} \times \rho_{flue\_gases} \times C_{p,flue\_gases}} \quad \text{(F.2.20)}$$

La relation entre les coefficient de transfert massique et thermique est issue de l'article de Lee et Ro[92] se basant sur Bergman et al.[104]:

$$h_m = h_c / (\rho_{flue\_gases} . c_{p,flue\_gases} . Le^{\frac{2}{3}}) \quad \text{(F.2.21)}$$

2.6. Validation du modèle

Les données disponibles dans la littérature concernant le givrage au CO_2 sur une surface froide sont très rares. En 1985, Shchelkunov et al.[87] ont mené des expériences sur une plaque horizontale à des températures cryogéniques, un mélange de N_2+CO_2 à différentes concentrations, différentes températures d'entrée et débits massiques. Trois cas tirés des résultats de Shchelkunov et al. sont comparés aux résultats obtenus par le modèle développé dans cette thèse pour différents coefficients de transfert de chaleur. Les valeurs comparées sont l'épaisseur et la masse volumique du givre.

Les résultats de la Figure F5 montrent l'importance du coefficient de transfert de chaleur dans la prédiction de l'évolution de la formation de givre. Dans tous les cas, l'épaisseur et la masse volumique du givre semblent augmenter fortement au début de la formation de givre, puis le taux de croissance diminue à cause de la résistance thermique créée par la couche de givre entre la surface froide et le flux gazeux à la surface du givre. Toutes les corrélations montrent une sous-estimation de l'épaisseur et une surestimation de la masse volumique. Le coefficient de transfert de chaleur présente une influence directe sur le transfert de chaleur par convection entre le gaz et la surface froide et le coefficient de transfert de masse présente un impact sur la masse de CO_2

givré. Dans les trois cas, l'évolution du givre par rapport aux conditions d'entrée semble suivre la même tendance que les données expérimentales. La corrélation de Dietenberger et al. [103] (Figure F5, (e) et (f)) donne la meilleure estimation de la croissance du givre.

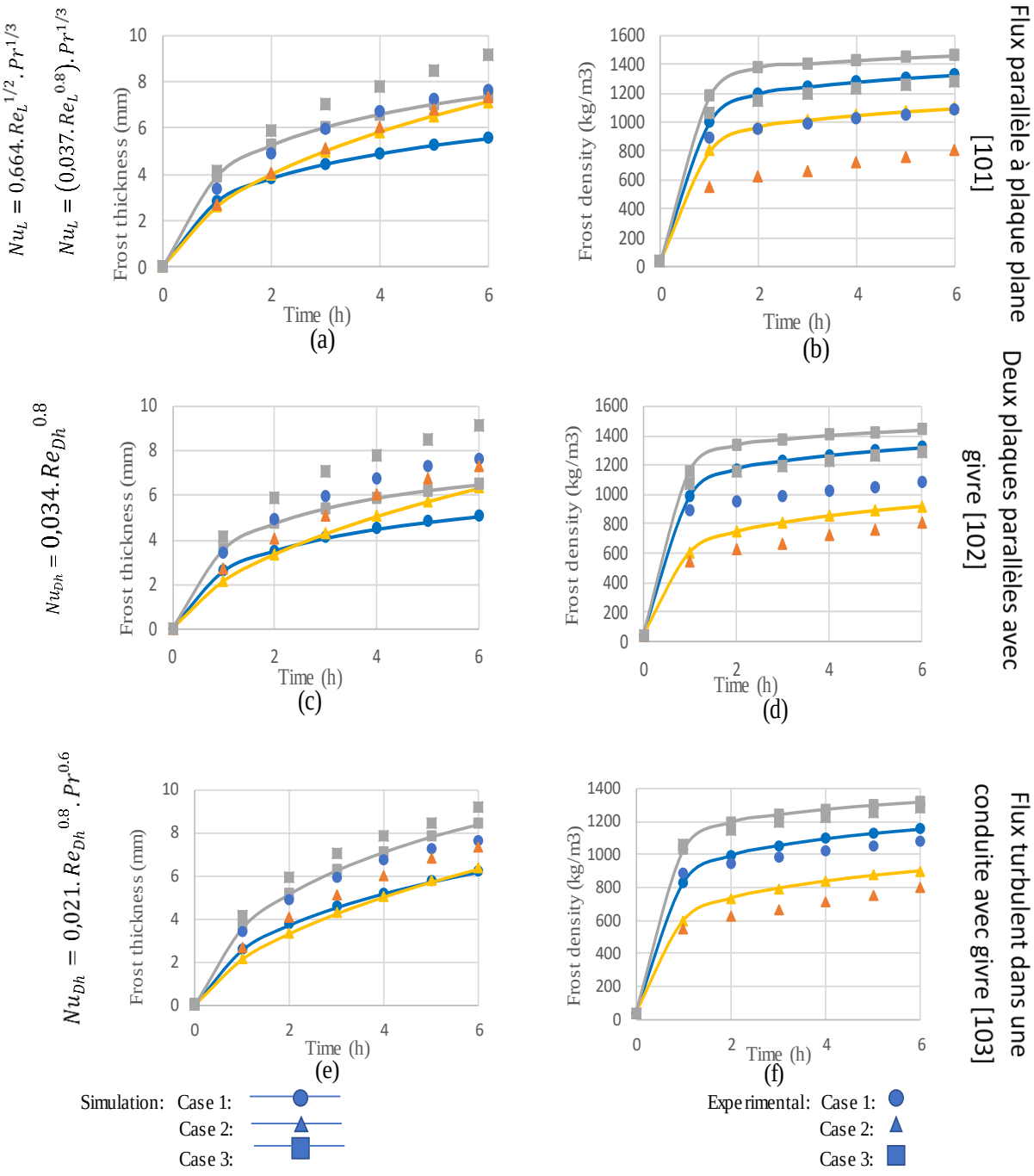

Figure F5: Comparaison des résultats obtenus sur la croissance du givre aux données expérimentales de Schlenkunov et al. pour différentes coefficients de transfert thermique

Conclusion

Dans ce chapitre, le mécanisme de givrage a été détaillé et des cas de la littérature ont été présentés pour mieux comprendre ce phénomène compliqué. Le givrage du CO_2 sur une surface froide a été modélisé et les résultats de la simulation montrent un bon accord par rapport aux résultats expérimentaux de Shchelkunov et al.[87] sur le givrage du CO_2 contenu dans un mélange binaire de N_2+CO_2 sur une surface froide. Une corrélation de la conductivité thermique du givre CO_2 a été déterminée en utilisant les résultats expérimentaux de Shchelkunov et al.[87]. Une corrélation proposée par Dietenberger et al.[103] a été utilisé pour définir l'équation du coefficient de transfert thermique qui servira à calculer le coefficient de transfert massique et, éventuellement, le débit massique de CO_2 givré. Les résultats montrent l'importance de la présence de givre lorsqu'on considère le choix de la corrélation de transfert de chaleur. L'un des objectifs de cette thèse est d'appliquer les connaissances acquises en changement de phase du CO_2 à l'épuration du biogaz par la cryogénie. Au chapitre 2, un modèle de givrage du CO_2 contenu dans un mélange binaire de N_2+CO_2 a été étudié et validé. Au chapitre 3, les gaz de combustion seront remplacés par du biogaz tout en conservant le même modèle. Une étude de sensibilité sera réalisée afin d'améliorer les conditions de fonctionnement. Le phénomène de givrage est encore détaillé par l'étude de la formation de givre et des transferts de chaleur sur la surface froide. Ces étapes doivent être suivies avant de passer à la dernière étape présentée au chapitre 4: la récupération du froid par sublimation contrôlée.

Chapter 3: CO_2 deposition - cryogenic removal from biogas

Introduction

Cryogenic upgrading of biogas implies the removal of carbon dioxide at very low temperatures. The saturation temperature of CO_2 increases as its partial pressure in biogas increases. In this thesis, the focus is mainly on removing carbon dioxide by deposition (physical transition from gas to solid state) at low pressure and the recovery of energy at low temperature in order to reduce the energy intensity of cryogenic deposition of CO_2. In chapter 2, the mass and energy equations governing the frost formation and growth phenomenon were presented. The same model can be applied for the case of CO_2 removal from biogas.

What matters the most in removing CO_2 from biogas is the purity of the biomethane obtained. The biogas mass flow rate, its temperature and the CO_2 concentration in biogas are all parameters that should be studied in order to optimize the carbon dioxide removal process. Also, the geometry of the heat exchanger has a major effect on the heat transfer hence the quantity of CO_2 removed per meter squared by deposition.

In this chapter, the Solid-Gas phase equilibrium between CH_4 and CO_2 is presented. It is followed by a sensitivity study of CO_2 deposition on a flat plate for different initial conditions. In order to optimize the heat and mass transfer, different geometries of the heat exchanger are studied. The whole process including CO_2 removal and biomethane liquefaction was constructed using ASPEN HYSYS® taking into account all the mass flows and heat transfers in the system except the frost formation part which will be calculated in Dymola (ANNEX E). Different configurations of the heat exchanger are compared: first it is considered as a thermal inertia cooled down to a very low temperature by the nitrogen used to liquefy the biomethane. The temperature of the heat exchanger increases as CO_2 deposits. The other case considers a normal heat exchanger with two flows, the hot side being the biogas and the cold side being the nitrogen that will be used to previously liquefy the biomethane.

3.1. Phase equilibria

The model used for the study of CO_2 frost formation and growth by cryogenic removal from a mixture of CO_2 + N_2 can be applied to the case of CO_2 cryogenic removal from biogas. The modifications to the model mainly concern the fluid, flue gases should be replaced by biogas hence nitrogen is replaced by methane. The equations of viscosity and thermal conductivity for the binary mixture remain the same. The properties of methane can be found in "Chemical Properties Handbook" by Carl Yaws[100]:

$$\mu_{ch4}(\mu P) = 3.844 + 0.40112 \times T - 1.4303 \times 10^{-4} \times T^2 \quad (3.1)$$

$$\lambda_{ch4}(W/(m.K)) = -0.00935 + 1.4028 \times 10^{-4} \times T - 3.318 \times 10^{-8} \times T^2 \quad (3.2)$$

$$cp_{ch4}(J/(mol.K)) = 34.942 - 0.039957 \times T + 1.9184 \times 10^{-4} \times T^2 - 1.5303 \times 10^{-7} \times T^3 - 3.9321 \times 10^{-12} \times T^4 \quad (3.3)$$

Similarly to the case of CO_2 deposition from a binary mixture of nitrogen and carbon dioxide, the equilibrium at the interface between the gas and solid phases of CO_2 is considered and graphically shown as a psychrometric chart in Figure 40. The steps to building this chart are presented in ANNEX D.

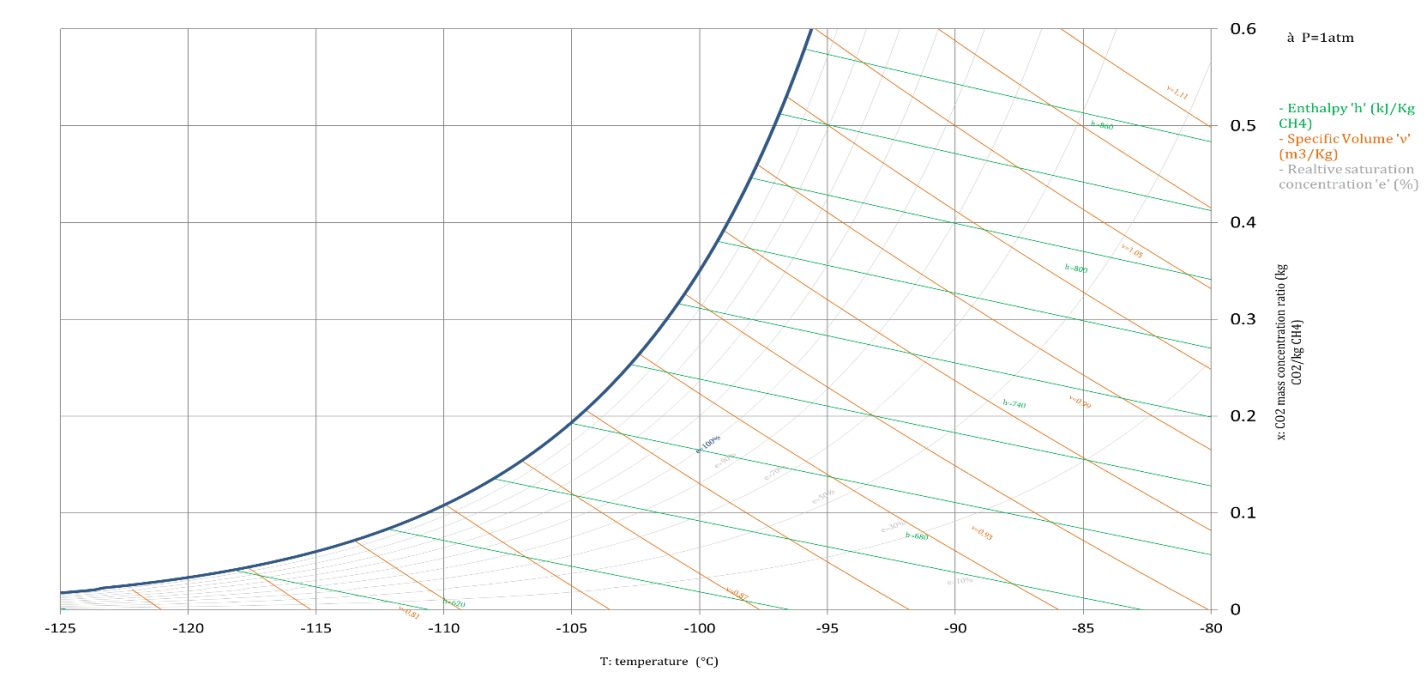

Figure 40: Psychrometric chart for CH_4/CO_2 with temperature and concentration evolution in frosting conditions

3.2. CO_2 separation from biogas

A sensitivity study was conducted for the parameters that could have the greatest effect on the heat and mass transfer. From this parametric study, it will be possible to give better initial operating conditions for the whole process and targeting lower the energy consumption.

3.2.1. Sensitivity study of CO_2 deposition from biogas and frost growth

In this part a sensitivity study is conducted to understand the effect of inlet conditions and plate temperature on the frost thickness and density evolution during the frosting process as well as heat transfer. Biogas (CH_4-CO_2) passes over a cold plate (30cmx15cm) and CO_2 frosts on its surface. Different CO_2 concentrations, inlet biogas temperatures and plate temperatures are studied, and frost growth compared as well as heat transfer distribution between the frost surface and inside the frost layer. It should be noted that the system operates at atmospheric pressure.

i. Flat plate at constant temperature

Table 5 shows the different values of biogas inlet temperature, CO_2 mass concentration in biogas and cold surface temperature considered for the sensitivity study.

Table 5: Operating conditions for sensitivity study cases

	$T_{biogas}\ (°C)$	$X_{co2/biogas}\ (kg/kg)$	$T_{cold\_plate}\ (°C)$
Case 1	-80	0.6;0.5;0.4	-128
Case 2	-80	0.5	-138; -128; -118
Case 3	-85; -80; -75	0.5	-128

In part (a) of Figures 41-43-45 shown below, frost thickness will be compared for the three different values given to the parameter studied in each case and in part (b) density will be compared. Curves with dashes represent the first value given to the parameter being changed in the sensitivity study, dotted curves are for the second value and continuous lines are for the third value of the parameter being varied. In Figures 42-44-46, in part (c), total latent heat will be compared to sensible heat and in part (d) latent heat at the surface will be compared with the latent heat inside the frost layer which represents the quantity of CO_2 frosted. Similarly to frost thickness and density, curves with dashes are for the first value of the parameter being varied in the sensitivity study, dotted curves are for the second value and continuous lines are for the third value of the parameter being changed.

Case 1: Different CO_2 mass concentrations

Varying the CO_2 concentration in the biogas affects mainly the total mass flux of CO_2 frosted and the mass flux of CO_2 frosted inside the frost layers but less than the total mass of frosted CO_2. The difference between these two values gives the mass flux of CO_2 frosted at the surface (Eq. 2.3) which will increase for a higher concentration (20% above the reference concentration) increasing with it the frost thickness by about 13.5% as shown in Figure 41a. Heat exchange

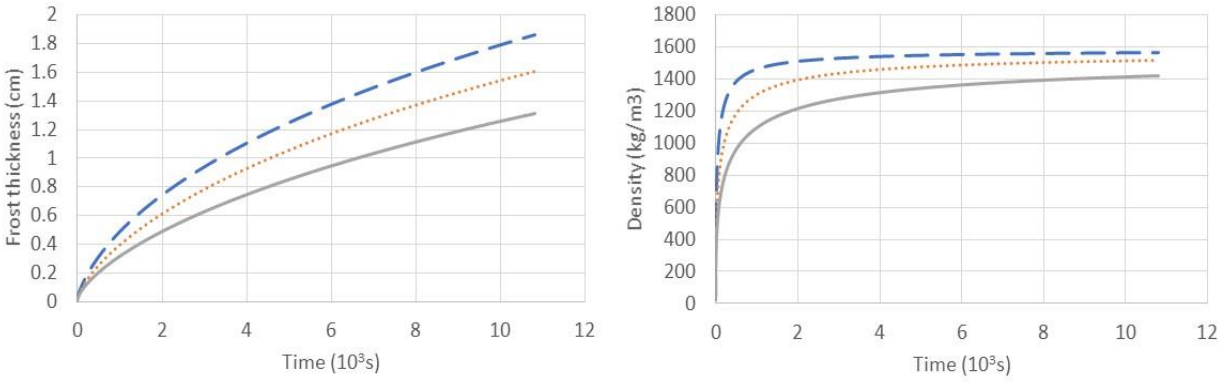

(a) (b)

Figure 41: CO_2 frost growth for different mass conc.: (a) frost thickness, (b) frost density

surface is considered constant in this study. The frost density is calculated using the mass absorption rate α which is function of the mass flow rate of CO_2 frosted inside frost layers and it

increases in a non-uniform rate for a higher CO_2 concentration as shown in Figure 41b. Although an increase in the frost density reduces the thickness growth, the effect of a higher concentration on the mass flow of CO_2 frosted is more important. Frost growth creates a thermal resistance between the plate and the biogas containing the CO_2 as mentioned before, therefore the frost thickness and density both have lower increase slopes as more frost is formed on the plate.

Sensible heat flow is affected by the surface and the temperature gradient between the frost temperature and the biogas. Moreover, the modelling results are affected by the equations considered for the heat transfer coefficients. The heat exchange surface is the same since the same plate is used for all simulations, the temperature gradient is also the same; which means that the change in sensible heat is due to the transfer coefficient, more precisely the viscosity and the thermal conductivity of the biogas which depend on the mixture's composition. Table 6 shows how more CO_2 in the biogas will decrease the thermal conductivity and increase the viscosity resulting in a lower Reynolds number, so the sensible heat transfer will decrease for a higher concentration in CO_2 since the heat transfer coefficient decreased while other parts of the convective heat equation remain constant.

Table 6: Variation of the convective heat transfer coefficient for differnet biogas composition

$\%CO_2$	$\%CH_4$	Dynamic viscosity (µPa.s)	Thermal conductivity (mW/(m.K))	Density (kg/m^3)	Velocity (m/s)	Reynolds	Nusselt	h_c ($W.m^{-2}.K^{-1}$)
0.4	0.6	7.72	19.736	1.37	1.54	13721	37.497	14.807
0.5	0.5	7.825	19.282	1.498	1.41	13537	37.09	14.305
0.6	0.4	7.999	18.514	1.654	1.28	13243	36.447	13.495

As for the total latent heat, it is the product of the heat of sublimation and the mass flow of CO_2 frosted which depends on the concentration difference between the biogas flow and the frost surface, and the mass transfer.

Latent heat indicates the quantity of CO_2 frosted since the heat of sublimation is relatively constant as function of the temperature. Frosting occurs on the surface and inside the frost layer. Although it is not clear in the Figure 42d but in the first few seconds of the frosting, latent heat on the surface is almost zero because the mass flow rate of CO_2 frost at the surface is driven by the rate of thickness increase. This heat transfer varies from almost 0 to a sudden high value due to the start of frost formation which is highest at the beginning as was discussed in the model compared with Shchelkunov. As for latent heat transfer inside the frost, it starts at high values but decreases to get to almost null values. This is due to the densification of the frost layer; it decreases with time so latent heat inside the frost will decrease. Higher CO_2 concentrations result in better transfer at the surface since the concentration gradient is higher.

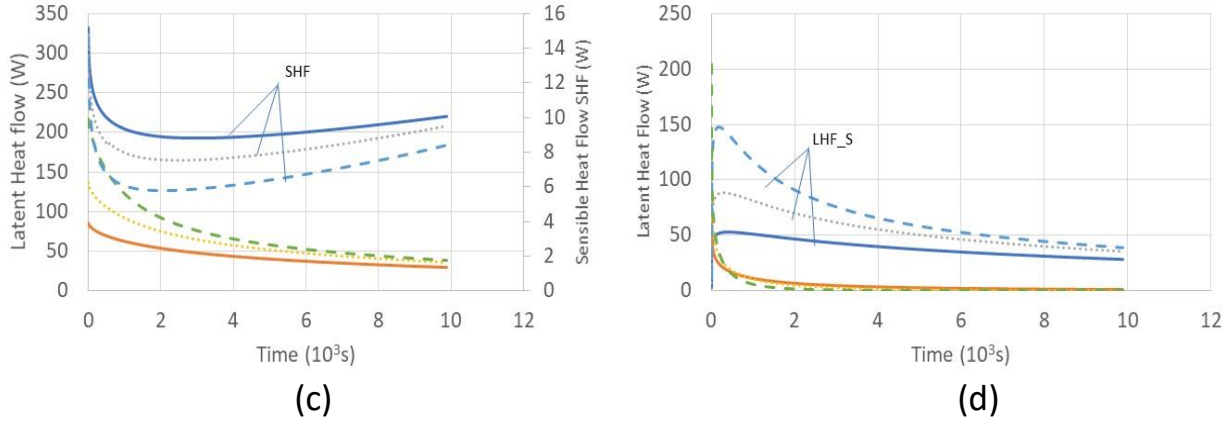

Figure 42: Heat flow for different CO_2 concentrations: (c) total latent heat flow and sensible heat flow, (d) latent heat flow on the surface and inside frost

<u>Case 2</u>: Different plate temperatures

Lower plate temperatures decrease the temperature at the frost surface. This decreases the concentration of CO_2 saturation vapour increasing the CO_2 concentration difference which will increase the total mass flow of CO_2 frosted. This will result in higher values for the frost thickness as shown in Figure 43a. For a decrease of surface temperature by 7.5%, the frost thickness increases by about 11%. As for the density, it decreases for lower plate temperatures because lower temperatures in the frost result in lower saturation vapour concentration in CO_2 inside the frost layers. This will reduce the amount of CO_2 frosting inside the frost layer thus reducing the density.

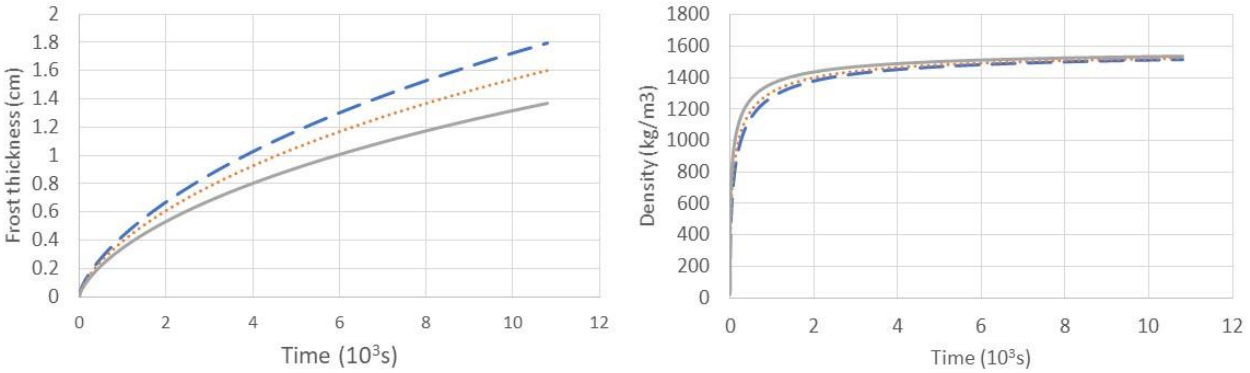

Figure 43: CO_2 frost growth for different plate temperatures: (a) frost thickness, (b) frost density

The variation of sensible and latent heat at the surface and in the frost layer as CO_2 deposits were discussed previously. The convective heat transfer has a negligible impact on the overall heat transfer since the temperature gradient is dominated by the small surface; nevertheless, for a decrease by 7.5% in cold surface temperature, sensible heat flow increases by an average of about 8.7%. Therefore, lower plate temperatures will increase the sensible heat flow but less than 1W. The same applies for latent heat, lower plate temperatures increase the latent

heat transfer at the surface of the frost but not inside the frost since lower temperatures lead to less CO_2 vapour pressure thus less CO_2 concentration which decreases mass transfer from the flow inside the frost layer; this was further proved in Figure 43.b showing the frost density. The increase of the temperature gradient creates a bigger CO_2 concentration gradient between the flow and the frost leading to an increase in the total latent heat.

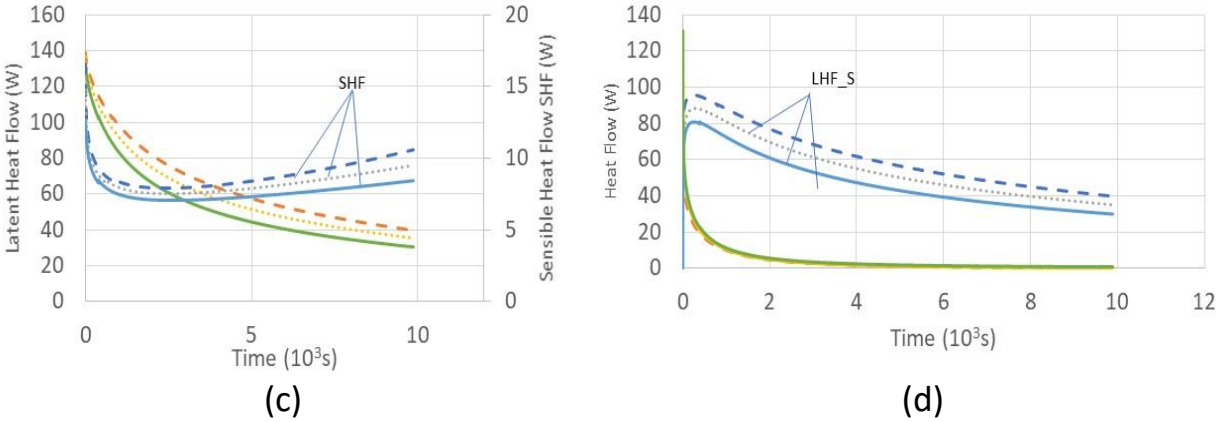

Figure 44: Heat flow for different plate temperatures: (c) total latent heat flow and sensible heat flow, (d) latent heat flow on the surface and inside frost

<u>Case 3:</u> Different biogas inlet temperatures

As for the change in inlet temperature, there is no direct effect on the CO_2 concentration difference at the surface nor in the frost layers, therefore no remarkable change in frost thickness (Figure 45a) and density (Figure 45b) can be seen. Frost thickness increases slightly for lower inlet temperatures because the convective sensible heat decrease has more effect compared to the decrease of conduction heat transfer in the frost layers. The conclusion that can be drawn is that since the mass of CO_2 frosted at the surface will increase, then the thickness will increase too, even if not more than 3%, at the frost surface.

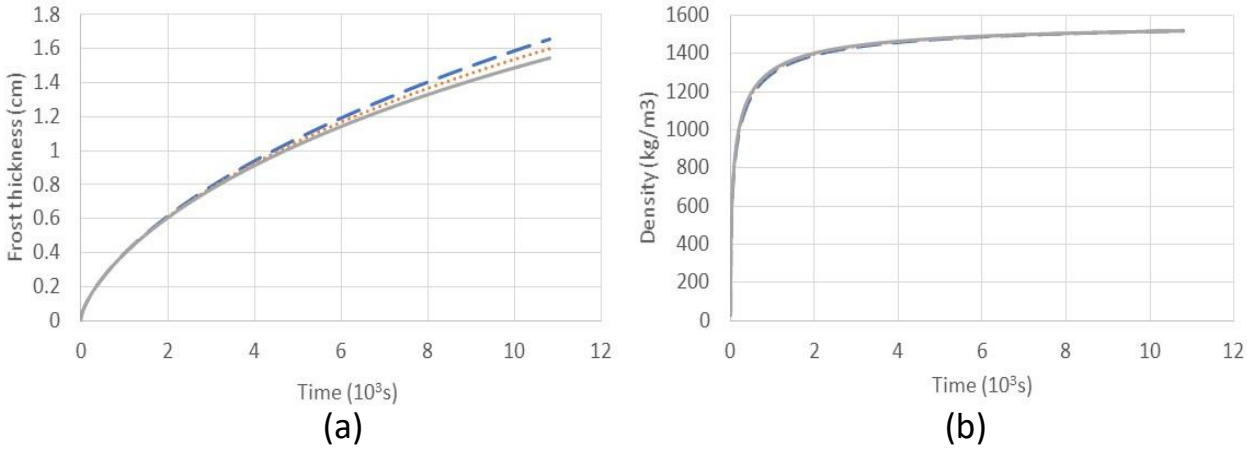

Figure 45: CO_2 frost growth for different biogas inlet temperatures: (a) frost thickness, (b) frost density

As for the change in inlet temperature, sensible heat will surely change since the temperature gradient has changed but in the same time, transport properties changed too so the heat transfer coefficient will be affected accordingly. Higher temperatures will reduce the frosted CO_2 mass flow rate onto the cold surface. It is clear that the biogas temperature has a very minor effect on latent heat flow. At the frost surface and inside the frost layer, latent heat is almost the same for all inlet temperature values. Since the plate is at a very cold temperature compared to the saturation temperature of CO_2, then reaching deposition conditions is easy as long as there is a concentration gradient between the biogas and the frost surface.

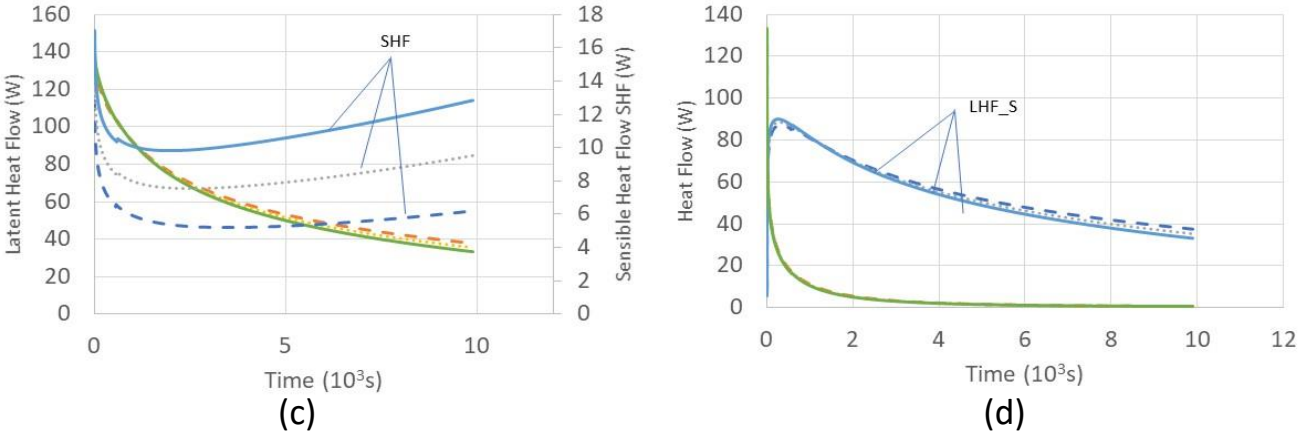

Figure 46: Heat flow for different biogas inlet temperatures: (c) total latent heat flow and sensible heat flow, (d) latent heat flow on the surface and inside frost

ii. Plate considered as heat capacitor with initial low temperature

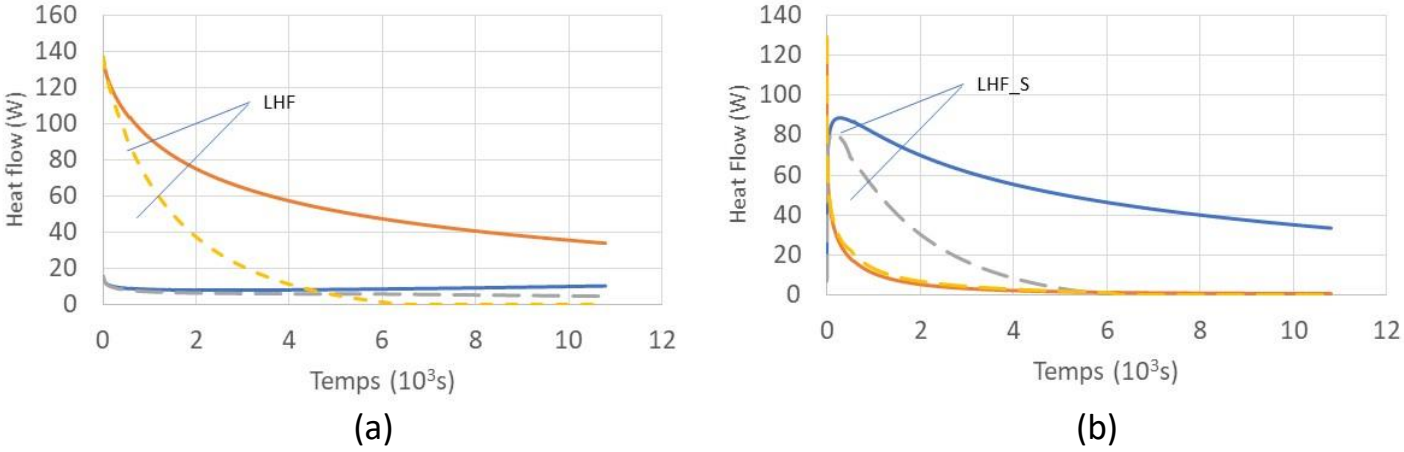

Figure 47: Heat flow for diff. plate config.: (a) total latent heat flow and sensible heat flow, (b) latent heat flow on the surface and inside frost

In this case, the plate is not at a constant temperature, it is considered as a heat capacitor. Results for heat transfer will be compared with the case of a plate at constant temperature with $T_{biogas} = -80°C$, $X_{co2/biogas} = 0.5$ and $T_{plate} = -128°C$. In the Fig.47, dashed points

indicate the plate as a heat capacitor and the continuous line represent the values for the plate at constant temperature.

When the plate is not at constant temperature, it will heat up as CO_2 frosts over it and transfers calories to the plate. This temperature increase will reduce the temperature gradient in the frost layer. This is why sensible heat is decreasing constantly unlike the case of constant temperature in which sensible heat reaches a certain value and stops changing. This temperature is achieved when frost surface temperature is equally heated and cooled by the flow of biogas and the cold plate respectively; when this temperature is reached, frosting mass flow tends to 0. A similar phenomenon is observed in the latent heat transfer: the decrease in temperature gradient results in a lower concentration difference between frost layers which limits the frosting reducing latent heat to a null value.

Conclusion of the sensitivity study

A higher CO_2 concentration in the biogas increased the heat transfer since the concentration gradient had increased. However, concentration usually depends on the biogas source as it was mentioned in chapter 1, and there is hence no manner to control it. Although an increase in the CO_2 concentration might mean more deposited CO_2 and more heat transfer, the CO_2 concentration at the outlet of the heat exchanger should be the criteria and will be discussed later in this chapter.

Decreasing the plate temperature might be better for CO_2 capture but the energy cost of cooling it might be higher than its improvement of the frost formation process. An optimization study must be done in order to find an optimum for this temperature. What is crucial is having a temperature below the deposition temperature of CO_2 at very low concentrations depending on the specifications set for the methane at the outlet of the heat exchanger. For example, if 5% of CO_2 molar concentration is allowed in the biomethane, this means 12.6% of CO_2 mass concentration. Using the psychrometric chart in Figure 40, it can be found that the surface temperature should always be less than ~-108°C.

As for the biogas inlet temperature, it should not be less than the saturation temperature of CO_2 otherwise the latter will deposit prior to its entry to the heat exchanger causing clogging and other disturbances in the system. If a cold source is available then the biogas flow must be cooled to a temperature just above the saturation temperature i.e. the lowest temperature before deposition, for optimal heat transfer as it is shown Case 3 of the sensitivity study.

3.2.2. Composition driven frost formation

The most relevant criteria of biogas upgrading is the methane purity after CO_2 removal. According to the GRDF “Gaz Réseau Distribution France”, the molar concentration of CO_2 in biomethane should not surpass 2.5% after upgrading. This number will be the criterion for choosing the best geometry of heat exchanger.

“Flat plate” and “tube” are the two simple geometries that will be compared. First a small biogas flow will be considered before scaling up to industrial production level. When comparing the two geometries in the case of a fluid flow, it is clear that the tube configuration is much

simpler to manage the fluid circulation. A large plate might require many gas injectors in order to ensure a uniform mass flow over it whereas this problem is not encountered with tubes. Also, unlike flat plates, tubes can be bent to fit in small volumes without any alterations to the flow rate and just a small increase in pressure drop depending on the flow velocity and the friction factor.

When it comes to numerical resolution, the main difference between the two geometries is the heat transfer coefficient correlation which affects the mass transfer coefficient. These coefficients are directly related to the sensible heat transfer and the mass of CO_2 deposited respectively. The same mass flowrate and heat exchange surface will be considered for both cases. Also, all the initial conditions will be identical. Both cold surfaces will be at the same initial cryogenic temperature. The CH_4 molar concentration at the outlet of each heat exchanger will be the criteria upon which the better geometry will be chosen.

Figure 48 shows the biogas flow and the different views of frost formation for the flat plate and tube configurations.

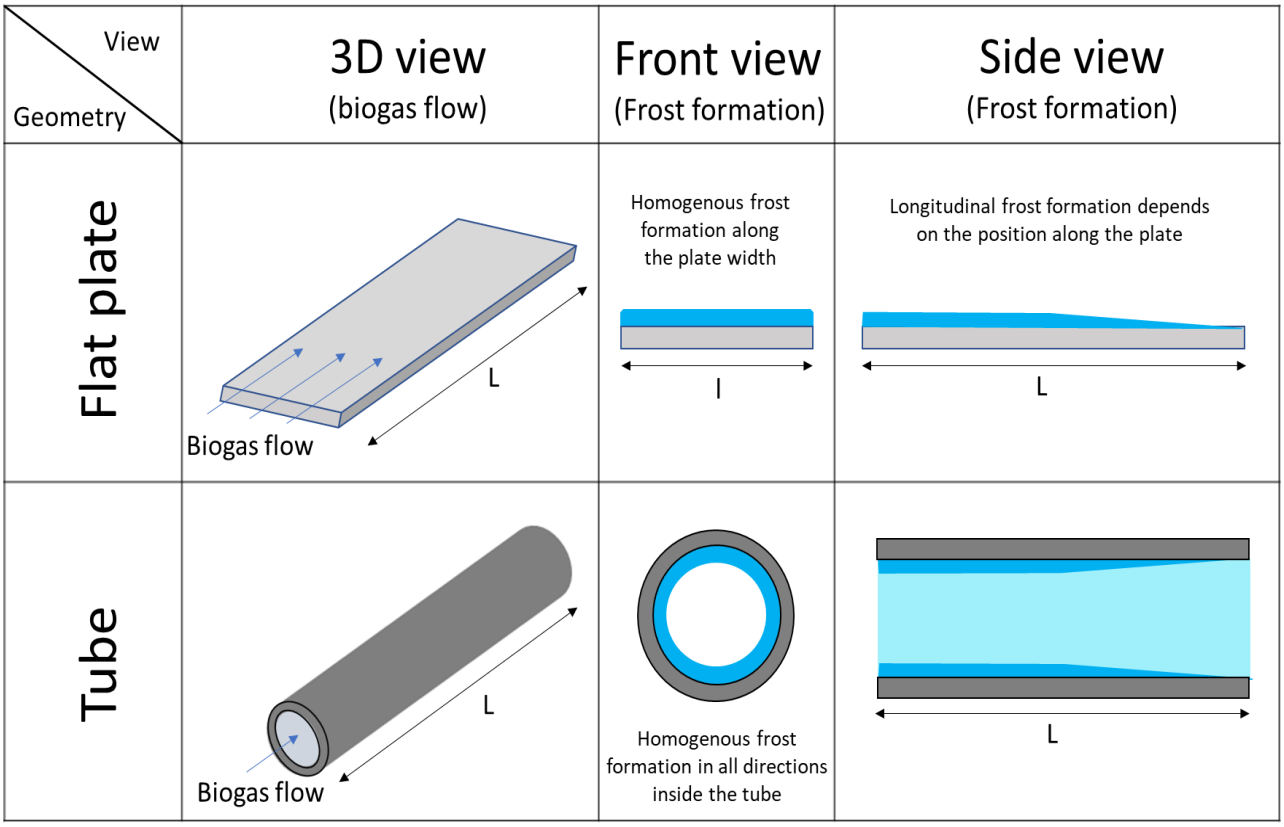

Figure 48: Biogas flow and frost formation visualisation for different heat exchanger geometries

As it was stated before, the molar concentration of CO_2 in biogas is usually between 20-50%. Three cases will be compared in the lower margins of this concentration. Typical biogas upgrading plants generate around 250 Nm^3/h of biomethane. The plate and tube heat exchanger configurations will be compared for different CO_2 molar concentration and upgraded biomethane outlet flowrate, which will affect the biogas inlet mass flowrate. Each initial condition will be varied while fixing the other according to this table.

Table 7: Different inlet biogas conditions for comparison between different heat exchanger geometries

CO_2 molar concentration (%)	Biomethane outlet flowrate (Nm^3/h)
26	200
	250
	300
20	250
26	
35	

In order to obtain a biomethane flowrate of 250 Nm^3/h at the outlet of the heat exchanger after upgrading, preliminary calculations show the need of a huge exchange surface. It is certainly not practical in real life to use one huge tube or plate; instead a number of tubes is used and the flow is equally divided in all of them. Here lies the simplicity of the tube configuration when distributing the flows.

In order to calculate the mass flowrate in each tube, the total mass flowrate of biogas should be calculated. Considering a biomethane outlet of $\dot{V}_{ch4,outlet} = 250\ Nm^3/h$, the density of CH_4 in NTP conditions is $\rho_{ch4,STP} = 0.71786\ kg/Nm^3$. The total mass flow rate of biomethane can be calculated as follows $\dot{m}_{ch4,total}(kg/s) = \dot{V}_{ch4,outlet} \times \rho_{ch4,STP}/3600$. Considering a CO_2 molar concentration in the biogas of $y_{co2} = 26\%$, its mass concentration can be calculated $X_{co2} = (y_{co2} \times 44)/((1 - y_{co2}) \times 16 + y_{co2} \times 44)$. Then the total mass flowrate of biogas $\dot{m}_{biogas,total} = \dot{m}_{ch4,total}/(1 - X_{co2})$. The number of tubes is then chosen depending on the diameter of each tube to maintain a turbulent flow in every tube. This will enhance heat and mass transfer and a better CH_4 purity at the outlet can be obtained. In this case, the number of tubes $N_{tubes} = 240$. The biogas mass flowrate in each tube is obtained by simply dividing the total mass flow rate by the number of tubes: $\dot{m}_{biogas,tube} = \dot{m}_{biogas,total}/N_{tubes}$.

The tube and the plate are considered as heat capacities which will be of equal value for both cases. They are considered as thin bodies ($Biot < 0.1$). Choosing a material with high thermal conductivity favours the homogeneity of the tube temperature in its thickness. Copper tubes have a high heat capacity and a high thermal conductivity $k_{Cu} = 430\ W.(m^{-1}.K^{-1})$ around $-120°C$. They have the same heat exchange surface and the same biogas inlet mass flow. Parameters are fixed for each geometry in a way to ensure these conditions are met.

The reference case for comparison between the plate and the tube are found in Table 7. The choice of the tube's inner diameter was made by balancing the heat exchange surface and the flow velocity which affects the heat transfer coefficient (via the Reynolds number); this will be detailed later. As it was stated in the sensitivity study conducted on the flat plate temperature earlier in this chapter, a lower temperature favours CO_2 deposition but the defrosting phase will take more time and cold recovery will be limited. This point will be further discussed and in details in chapter 4. The biogas inlet temperature was also discussed in the sensitivity study done previously; the conclusion was that the inlet temperature does not have a major impact

on the deposition but mainly on convective sensible heat transfer. It should not be lower than the saturation temperature of CO_2 at its concentration in biogas. A security margin must be kept to prevent frosting before entering the heat exchanger.

Table 8: Reference case for comparison between the plate and the tube geometry

Tubes	N_{tubes}	240
	$d_{tube,in}(m)$	0.02
	$T_{tube,initial}(°C)$	-120
Inlet flow	y_{co2}	0.26
	$\dot{m}_{biogas,tube}(kg/s)$ $(\dot{V}_{ch4,outlet} = 250\ Nm^3/h)$	3.323×10^{-4}
	$T_{biogas,inlet}(°C)$	$-85°$
Material properties	$\rho_{Cu}(kg/m^3)$	8933
	$Cp_{Cu}(J.(kg^{-1}.K^{-1}))$	385

In the following part, a comparison between different geometries, CO_2 concentration in the inlet biogas and biogas flowrate are compared. The case studies considered can be found in Table 8. The legends in the figures will state the geometry, CO_2 molar concentration in the inlet biogas and the biogas flowrate respectively.

i. Case 1: comparison between plate and tube for different CO_2 concentration

In the sensitivity study performed at the beginning of this chapter, higher CO_2 concentration showed a higher deposition but it was stated that this does not necessarily mean a higher methane purity at the outlet.

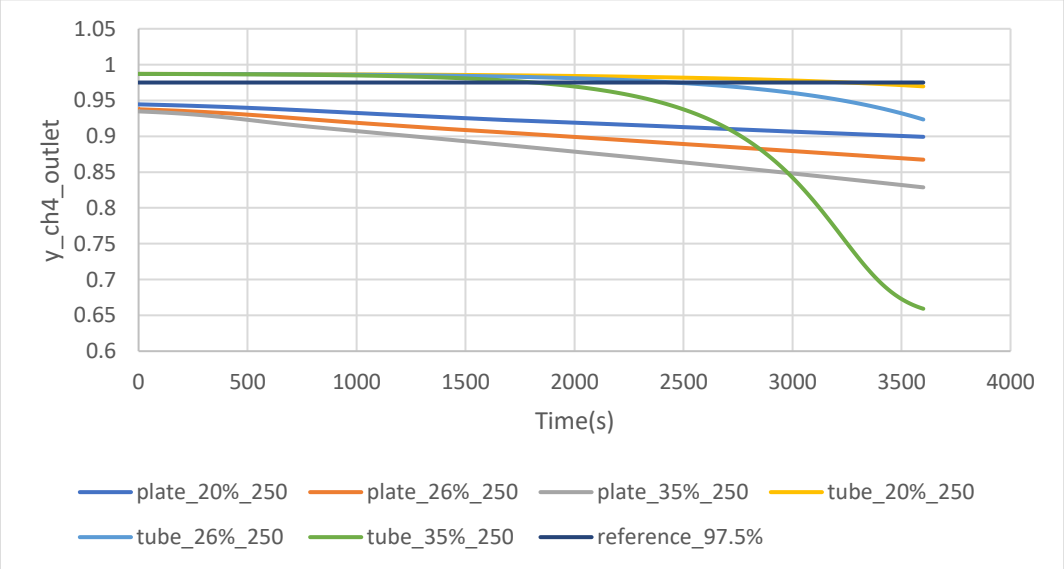

Figure 49: Outlet CH_4 concentration for different inlet CO_2 concentration and different geometries

Figure 49 shows how for the same biogas inlet flow rate, lower CO_2 concentrations yield to a higher CH_4 purity and as frost accumulates the decrease of CH_4 outlet concentration is observed. For the rest of this study, an initial CO_2 molar concentration in biogas $y_{co2} = 26\%$ will be considered (orange and clear blue lines) not to take the most optimistic case (20% (dark blue and yellow lines)) and at the same time having a longer frosting time which will be useful in the defrosting part which will be discussed in chapter 4.

As frosting time increases, the rate of outlet CH_4 concentration decreases at slower rate for the plate compared to the tube. At time $t = 2950s$, CH_4 concentration is higher for the plate than the tube for $y_{co2} = 35\%$ (grey and green lines respectively). The CH_4 concentration curves for tube geometry seem to decrease at a higher rate than the plates. This is due to the change of the effective heat transfer area. Comparing the overall results of the tube and plate configurations, the curves show higher methane purity in tubes. Plates with same heat exchange surface are unable to satisfy the specifications on methane content of $y_{ch4} > 97.5\%$.

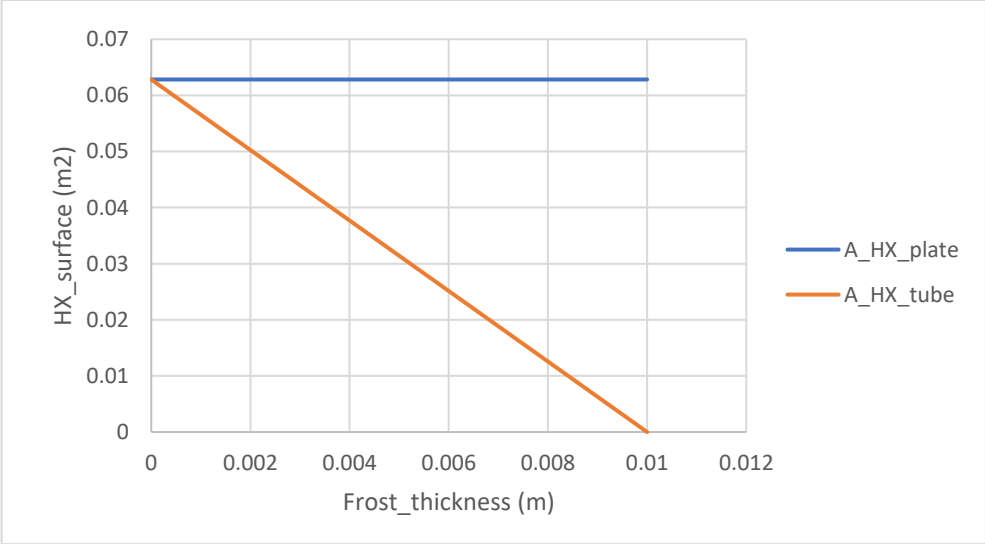

Figure 50: Effective heat exchange surface for plate and tube with frost deposition

Figure 50 shows the variation of the effective heat transfer area as frost accumulates. It should be noted that since frost deposits on the whole inner tube surface, it reduces the tube diameter by $2 \times the\ frost\ thickness$. In the plate configuration, as frost accumulates the heat exchange surface remains the same unlike the tube where the heat transfer area is highly reduced. The main reason that the tube has a higher CH_4 outlet concentration is the higher values of the heat transfer coefficient. The effect of the tube's heat exchange surface decrease takes place when its impact surpasses that of the heat transfer coefficient which will be discussed in case 3.

ii. Case 2: comparison between plate and tube for different biogas inlet mass flowrate

Similarly to the case with different inlet CO_2 concentrations, the tube configuration has a higher CH_4 concentration yield at the outlet when compared to the plate. Figure 51 shows that at a certain amount of time, when enough frost has frosted and the heat exchange surface in the tube is reduced enough, the CH_4 concentration at the outlet considering the plate configuration (lines dark blue, orange and grey) will surpass that of the tube configuration (lines yellow, clear blue and green). Higher biogas flowrates contain more CO_2. They yield in lower CH_4

concentrations at the HX outlet. Frost deposits faster in high flowrates therefore the thermal barrier created by its accumulation grows faster and less CO_2 can further be deposited.

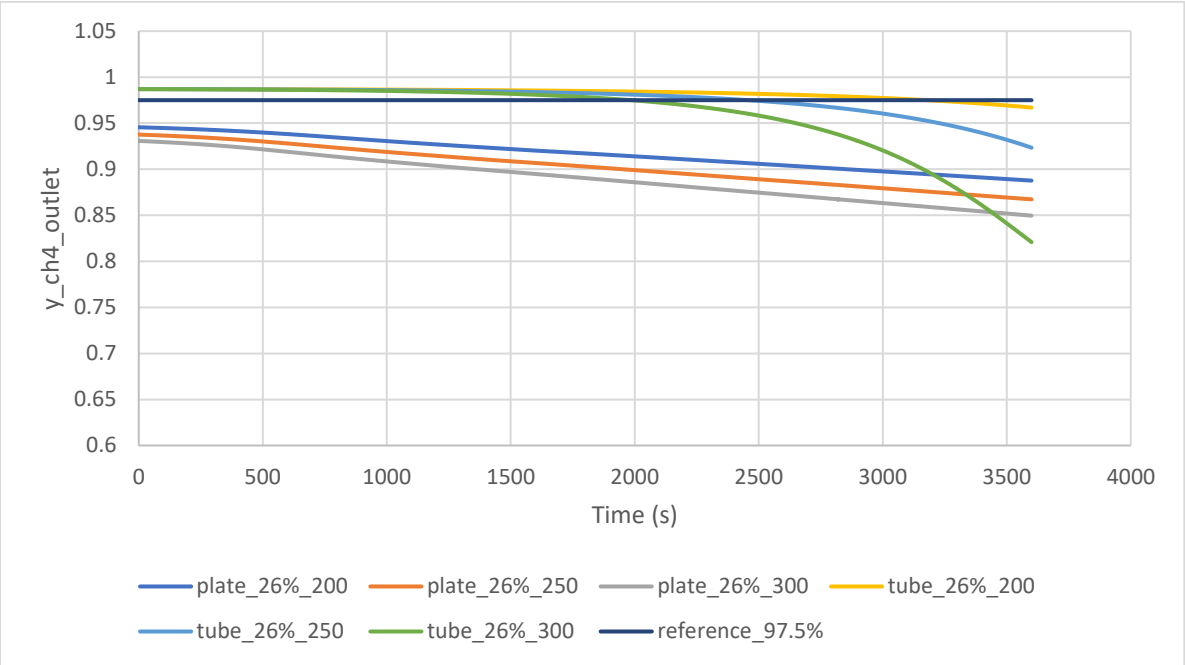

Figure 51: Outlet CH4 concentration for different inlet biogas flow and different geometries

iii. Case 3: comparison of the tube HX for different inner tube diameters

Varying the inner diameter of the tube, the heat transfer surface A_{tube} and the flow passage section S_{tube} are the two main entities that are affected.

$$A_{tube} = \pi \times d_{tube} \times L \quad (3.4)$$

$$S_{tube} = \pi \times \frac{{d_{tube}}^2}{4} \quad (3.5)$$

Reviewing the deposition model presented in chapter 2, all the heat and mass transfers are function of the heat exchange area A_{tube} which is proportional to the tube diameter d_{tube}. Considering the same flow rate, varying S_{tube} will affect the flow velocity hence the Reynolds number and the heat transfer coefficient.

$$v = \frac{\dot{m}}{(\rho \times S_{tube})} = \frac{\dot{m}}{(\rho \times (\pi \times \frac{{d_{tube}}^2}{4}))} \quad (3.6)$$

$$Re = \frac{\rho \times v \times d_{tube}}{\mu} = \frac{\rho \times \dot{m} \times d_{tube}}{\mu \times (\rho \times (\pi \times \frac{{d_{tube}}^2}{4}))} = \frac{4 \times \dot{m}}{\mu \times \pi \times d_{tube}} \quad (3.7)$$

$Nu \sim Re^{0.8}$ therefore $Nu \sim (1/{d_{tube}}^{0.8})$ (3.8)

$h_c \sim Nu/d_{tube}$ therefore $h_c \sim (1/{d_{tube}}^{1.8})$ (3.9)

The mass transfer coefficient h_m is proportional to the heat transfer coefficient h_c. Convective sensible heat transfer $\dot{q}_{sens}$ from Eq. 2.1 and the CO_2 deposition flowrate $\dot{m}_{frost}$ from Eq. 2.2

are function of h_c and A_{tube}. Latent heat flow $\dot{q}_{lat}$ is also function of $\dot{m}_{co2,frost}$ (Eq. 2.5), therefore the total heat and mass transfers are function of $A_{tube} \times h_c \sim (1/{d_{tube}}^{0.8})$. Therefore, smaller diameters increase the deposition rate but as frost accumulates, the heat transfer surface decreases more rapidly for smaller diameters and they could even get clogged. In Figure 52, three tube diameters are being compared.

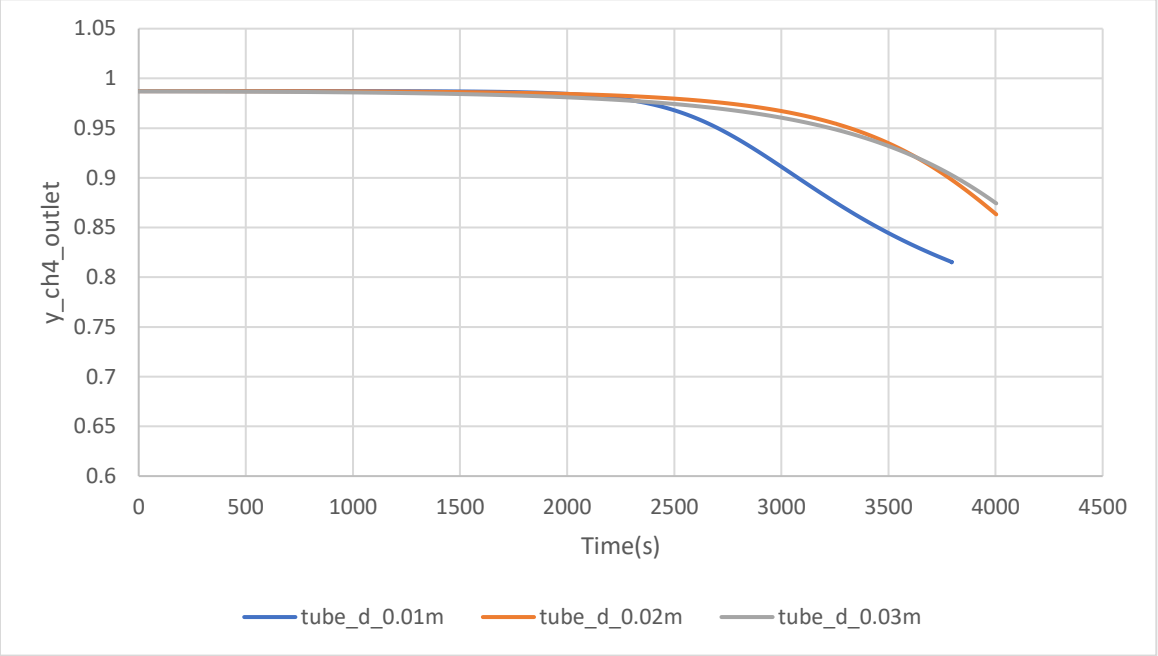

Figure 52: Outlet CH4 concentration for different tube diameters

As it was predicted in the explanation above, Figure 52 shows a higher CH_4 purity for smaller diameters but as frost accumulates, CH_4 concentration decreases earlier for small diameters.

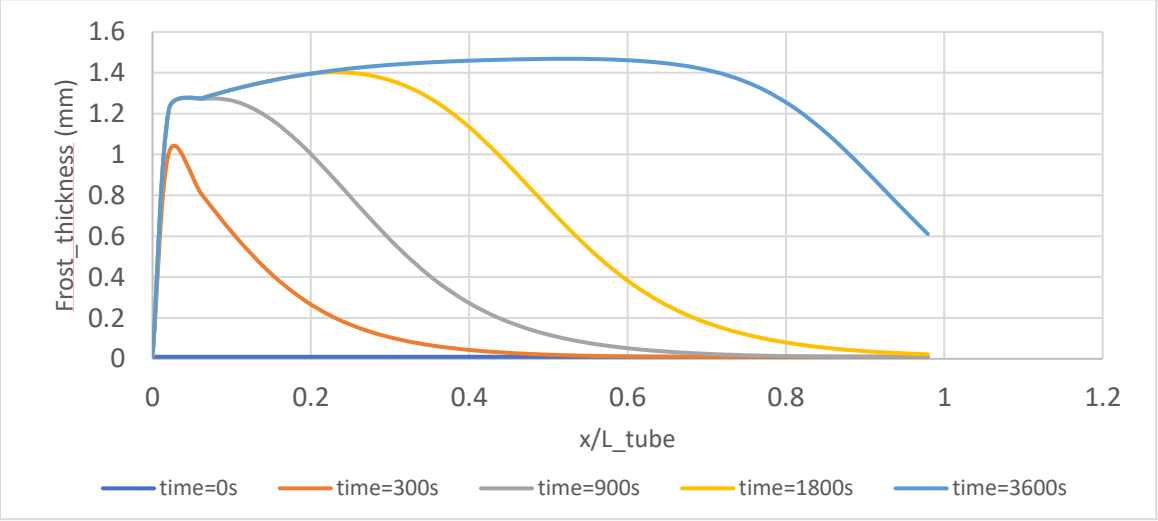

Figure 53: Evolution of frost thickness along the tube of diameter d_tube=0.02 considering one unit length

Figure 53 shows the evolution of frost thickness along the tube considering one unit length. Frost is not homogenous along the surface in the beginning. It forms in the shape of a dome. The orange, grey and yellow lines in Figure 53 show that the frost is much thicker in the first half of the plate until t=1800s. At each time interval, the head of the dome becomes less sharp and is pushed further away from the x=0 position of the tube. As biogas passes inside the tube,

CO_2 deposits and CO_2 concentration in biogas decreases limiting the frost formation along the rest of the tube. As frost accumulates, it creates a thermal resistance in the part closest to the tube inlet and therefore deposition in this part becomes limited. Also, the temperature of the heat capacity starts to rise in this part. Frost starts to accumulate along the part of the tube that is closer to its outlet (blue line).

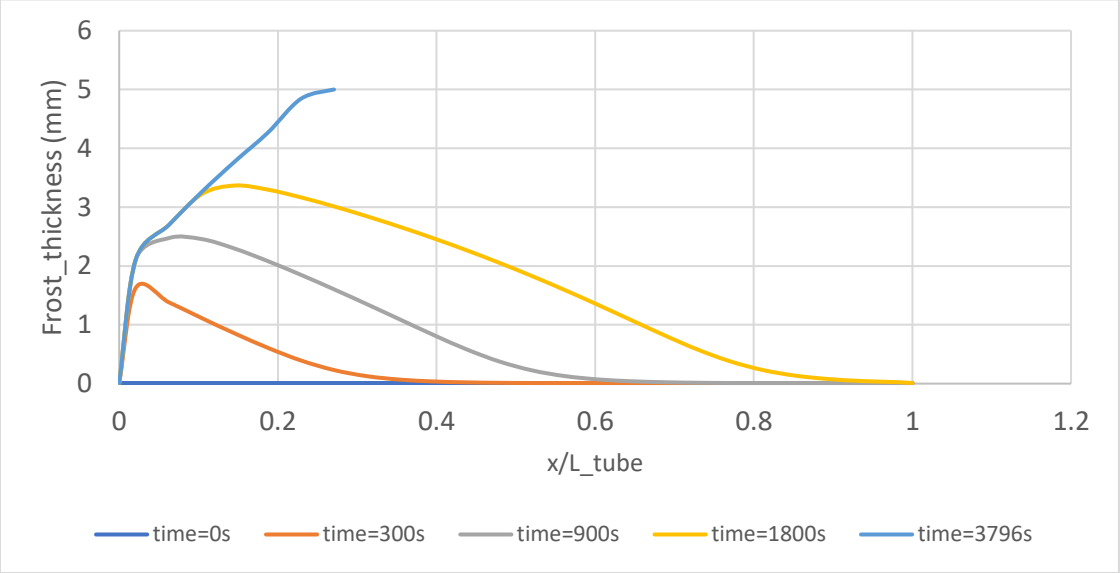

Figure 54: Evolution of frost thickness along the tube of diamter d_tube=0.01m

In Figure 54, at time $t = 3796s$, frost thickness reaches $0.005m$ in the tube having a diameter of $0.01m$ at a distance $x = 2.16L\ m$ from the inlet. Therefore, the tube gets clogged; the flow into the tube is stopped and the simulation doesn't carry on. The difference in CH_4 purity at the outlet of the tubes having diameters of 0.01m and 0.02 m is lower than 0.1%for the first 2010s but it presents a difference of about 0.5% compared with the tube of diameter 0.03m. When the tube diameter goes above $0.03m$, the flow becomes laminar and this decreases heat and mass transfer. Further optimization of the tube diameter can be done but for the rest of this study a tube diameter of $d_{in,tube} = 0.02m$ will be considered since smaller diameters showed possibilities of early clogging in the tube and bigger diameters showed a lower methane purity at the outlet.

iv. Case 4: comparison of the tube HX for different initial temperatures

The initial temperature of the heat capacitor (plate or tube) has a major effect on the CH_4 outlet concentration. As biogas passes inside the tube, CO_2 deposits and its concentration in biogas decreases. Lower CO_2 concentrations require lower temperatures to deposit therefore decreasing the temperature will allow CO_2 deposition in advanced positions in the tube where its concentration is low. Hence the CH_4 outlet concentration will increase for tubes with lower initial temperatures. Also, the faster the heat capacitor heats up and reaches the saturation temperature of the CO_2, less deposition will occur. The shape of the curve for $T = -105°C$ is caused by an increase in tube surface temperature to the point where almost no CO_2 is frosted

and $y_{ch4} = 74\%$ at the tube outlet.

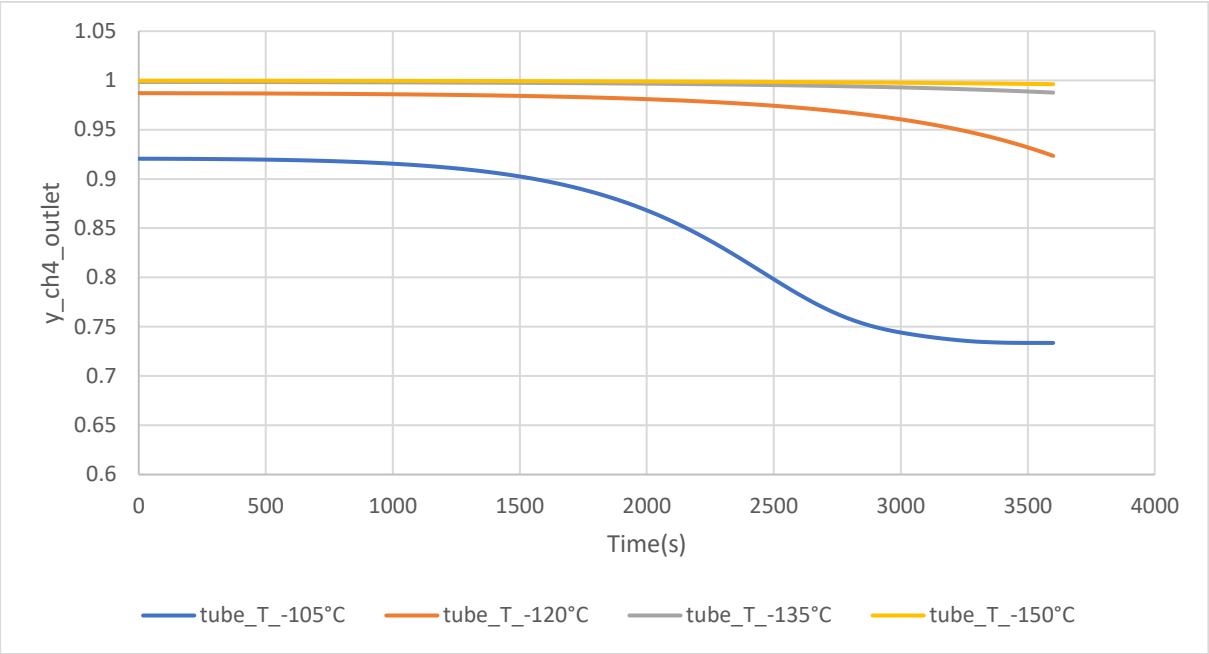

Figure 55: Outlet CH4 concentration for different intial tube temperature

As shown in Figure 55, lower initial temperatures seem to be better in every way when upgrading biogas but the heat capacitors (plate or tube) will require more cooling load and the more importantly, they have a negative effect on the defrosting phase. The effect of the surface temperature will be thoroughly detailed in chapter 4, concentrating on how lower temperatures can sometimes become problematic when defrosting especially when the objective of the defrost is recovering the cold stored in the CO_2 frost. For the rest of this study the initial cold surface temperature will be taken as $T_{surface} = -120°C$ but the effect of lower temperatures on defrosting will be discussed in chapter 4.

3.3. Frost formation and growth along the tube length

As biogas flows along the tube, its temperature decreases due to convective heat transfer with the cold surface and CO_2 deposition on the cold surface causes change in the biogas composition. These changes in the gas flow conditions will affect heat and mass transfer along the tube length.

3.3.1. Frosted CO_2 mass flux

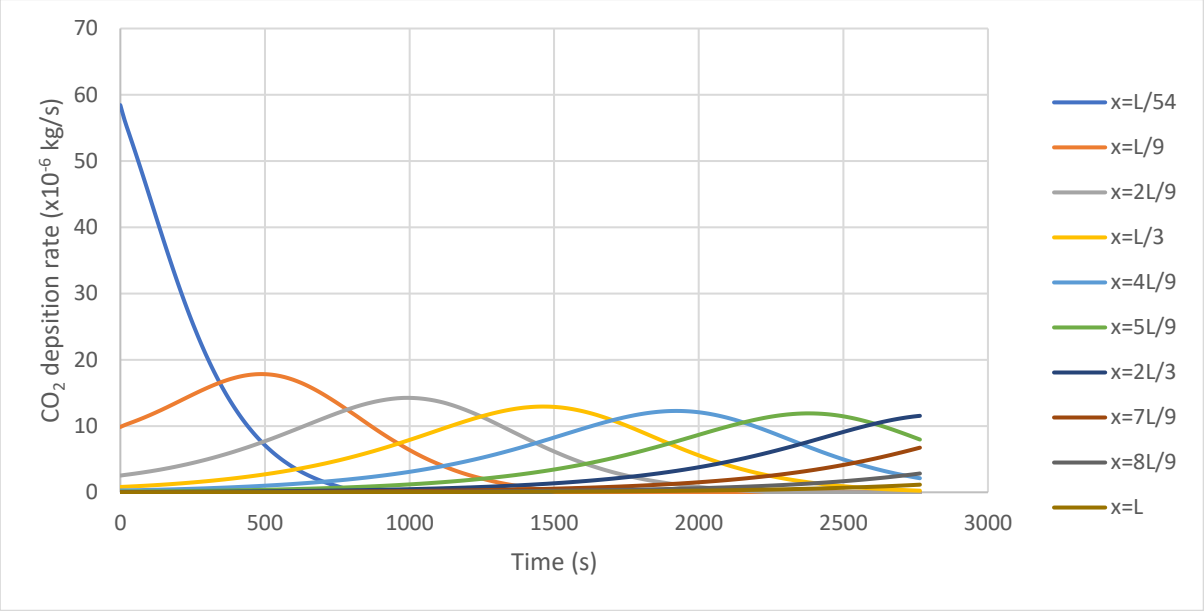

Figure 56: CO_2 deposition rate for different positions along the tube during CO_2 deposition

When the biogas flow containing CO_2 comes into contact with the cold surface, its temperature decreases as it heats up the surface. When the saturation temperature of CO_2 at its partial pressure in biogas is reached, deposition occurs. This will decrease CO_2 concentration in the biogas flow as it continues its flow inside the tube, leading to a decrease in deposition rate. This explains the delay of frost formation in positions further from the inlet show in Figure 56, for example at x=L/3 (yellow line), the peak of frost formation is reached at 1450s. Going to a further position from the inlet to x=5L/9, the peak is reached at 2370s but the difference in amplitude between these two curves is about 7.5%.

At first, CO_2 concentration gradient is high near the inlet but as frost accumulates, it creates a thermal resistance between the cold surface and the biogas flow. Also, the cold surface heats up due to convective heat transfer with the biogas and latent heat for CO_2 deposition. This also reduces the deposition rate. This explains the quick decrease of deposited CO_2 mass flux at $x = L/54$.

As frost accumulates and less CO_2 deposits near the inlet, the concentration gradient becomes higher for positions further from the inlet inducing higher deposition rates. In positions close to the tube outlet, deposition doesn't occur at first since biogas temperature had decreased compared to the inlet temperature and CO_2 concentration gradient tends to zero. Excluding the first position, the curves of frosted CO_2 mass flux show the same shape of a "bell curve" but shifted by a time interval caused by frost accumulation and change in CO_2 concentration gradient in previous positions.

3.3.2. Frost thickness

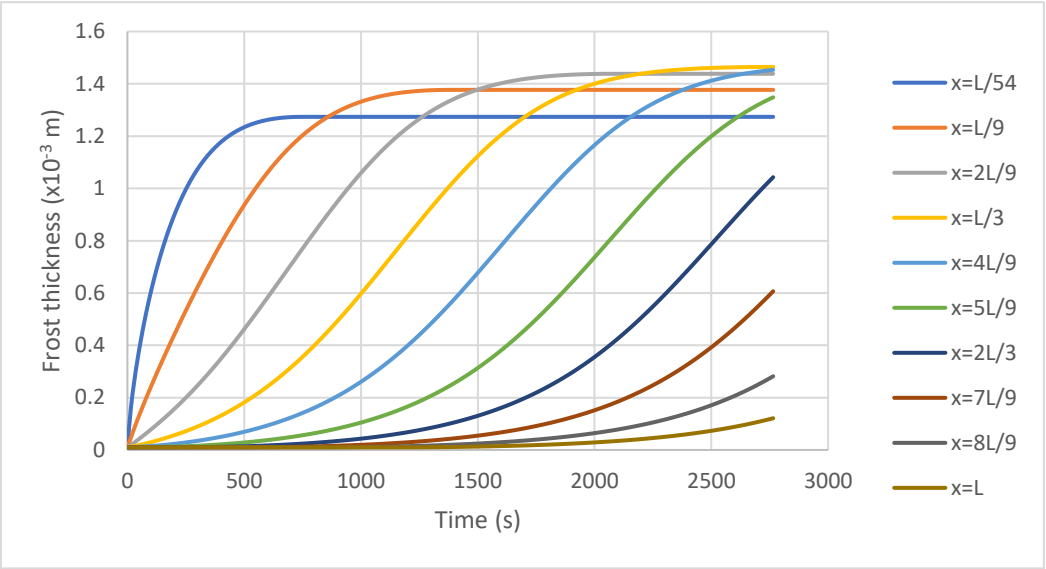

Figure 57: Frost thickness for different positions along the tube during CO_2 deposition

Frost thickness will increase in accord with the CO_2 deposition rate. A delay of frost thickness increase is seen for positions further from the tube inlet and the rate of thickness increase starts low and gets higher as less frost deposits in previous positions. A temperature and CO_2 concentration gradient equilibrium are reached at the interface biogas flow/frost surface. When this equilibrium is reached, deposition stops at this position where frost thickness remains constant at its maximum value. The equilibrium temperature of the cold surface in positions further from the inlet don't increase as much as the previous positions (shown in Figure 60) leading to higher deposition potential therefore higher final thickness value.

3.3.3. Frost mass

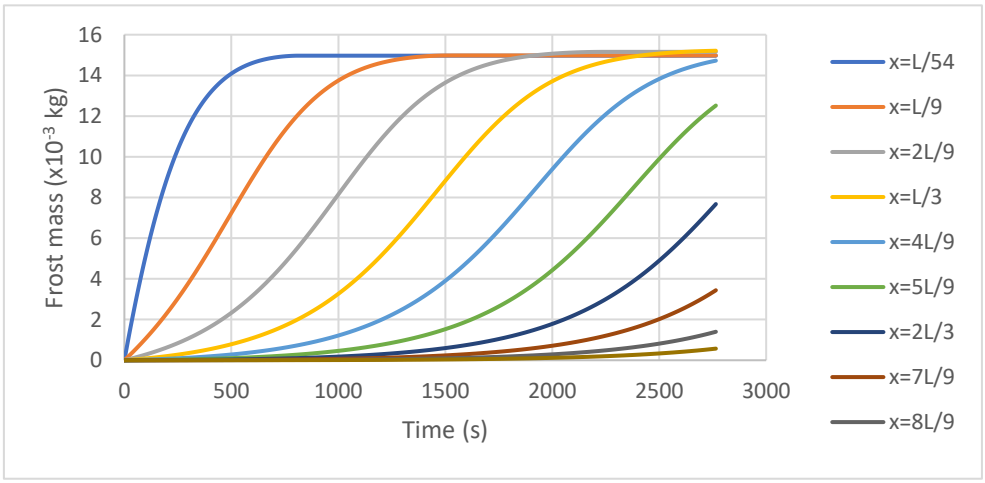

Figure 58: Frost mass for different positions along the tube during CO_2 deposition

The curves showing CO_2 frost mass accumulation are directly related to the deposition rate in every position throughout the tube. They change similarly to the frost thickness with the exception that all frost formed increases the mass but only frosting at the surface increases the thickness (see Eq.2.4 and Eq. 2.5).

3.3.4. Total heat flux

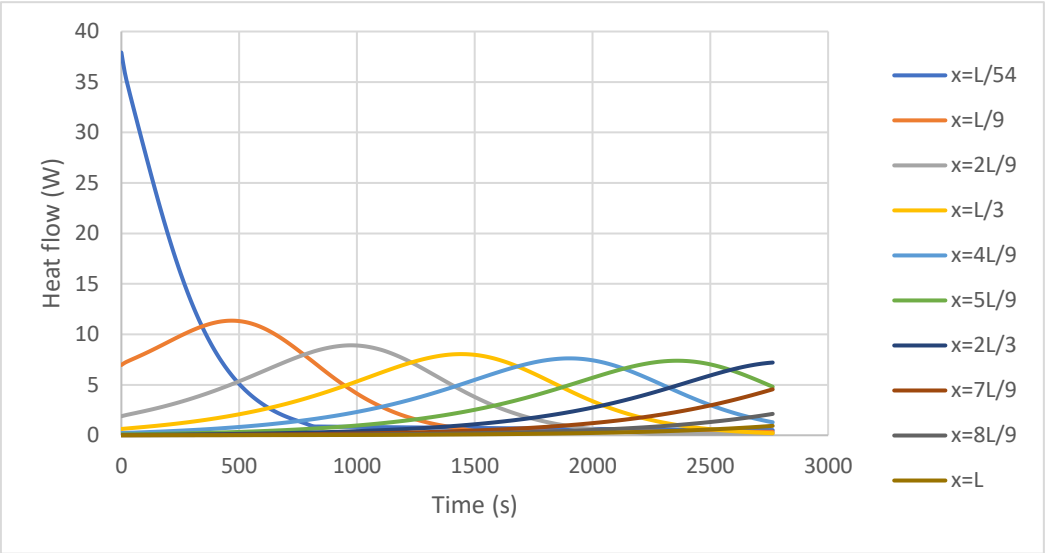

Figure 59: Total heat flux for different positions along the tube during CO_2 deposition

Total heat flux is divided into 2 parts: convective and latent heat flux. As shown in Figures 42, 44 and 46, latent heat has more impact than convective heat and it is function of the deposition rate. Therefore, the curves have the same shape and time interval between different positions throughout the tube as the deposition rate. The amplitude of the latent heat transfer slightly decreases between two consecutive positions (similarly to the deposition rate). Figure 59 shows that after the heat flow reaches its maximum it starts to decrease to an almost null value. This is due to the frost growth that creates a thermal barrier limiting deposition rate therefore latent heat flow. Also, as the temperature of the cold surface increases, convective heat transfer decreases.

3.3.5. Temperature of the tube

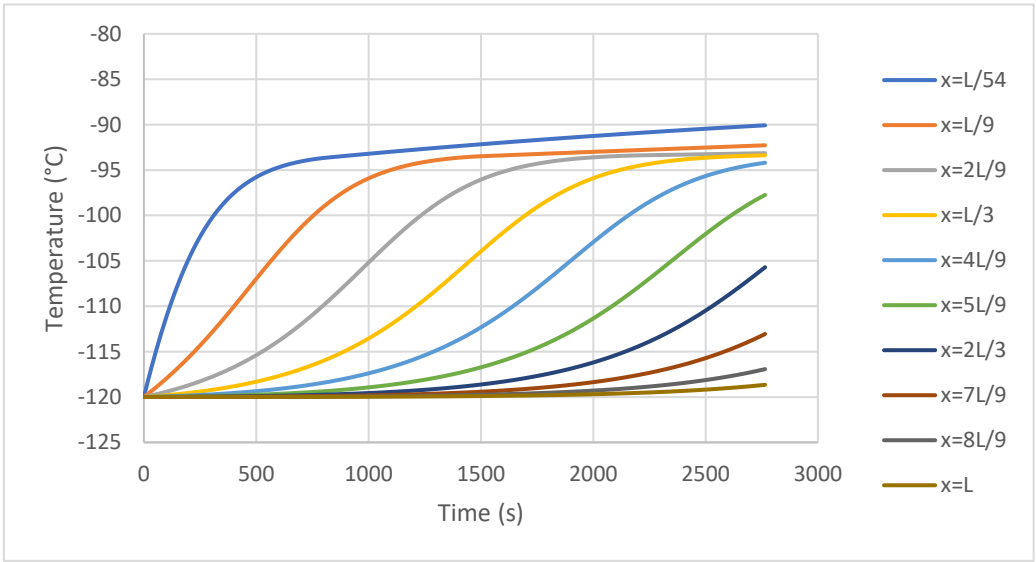

Figure 60: Tube temperature for different positions along the tube during CO_2 deposition

As it was stated before, the tube temperature increases due to convective heat transfer with the biogas flow and latent heat of CO_2 deposition. Although the temperature increase resembles the frost thickness behaviour, for positions further from the inlet, the final equilibrium temperature was lower. Actually, this higher temperature gradient between the biogas flow and the cold surface results in a higher total CO_2 deposition and leads to a higher frost thickness.

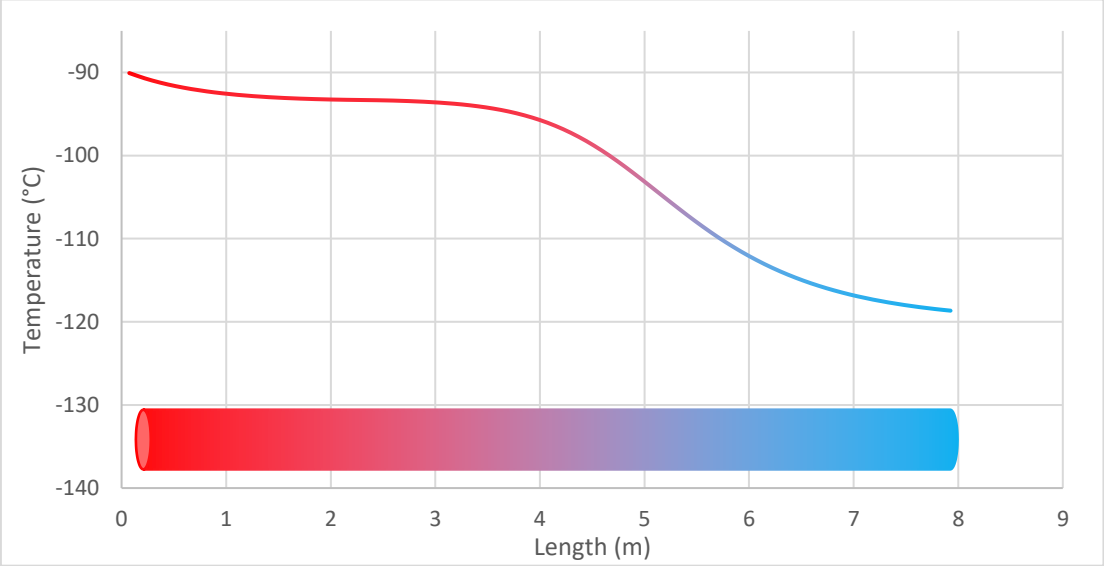

Figure 61: Tube temperature at the end of CO_2 deposition phase at time t=2674s for different positions along the tube

Within the aim of upgrading biogas to biomethane, the concentration of CO_2 in the outlet flow should not exceed 2.5%. This is the condition at which the simulation is stopped at time t=2764s. If the simulation time was higher, the final tube temperature gradient between the inlet and the outlet would have been lower.

For the frost formation stage, the temperature of the tube at the end of the frosting phase is shown in Figure 61. It decreases for positions further from the biogas inlet as stated before and this temperature will be used as initial condition for the defrost part. Hence, the target of the thesis being the recovery of cold stored in the CO_2 solid phase, all modelling of such action will consider as initial conditions the last conditions shown in the tube (or plate) for the deposition phase.

3.4. Comparison with results from the literature

Jonsson and Westman conducted experiments on CO_2 frosting using plate heat exchanger for cryogenic biogas upgrading [64]. Although their HX geometry and inlet conditions are different of what was proposed in this chapter, when comparing the experimental results of temperature and heat flow evolution along the plate, a fit can be found with the simulation results presented above.

In the plate exchanger, temperature sensors were distributed along the plate length (Figure 62). The hot stream of biogas containing CO_2 gets cooled down by a refrigerant. When the temperature of CO_2 deposition is reached, CO_2 frost starts forming.

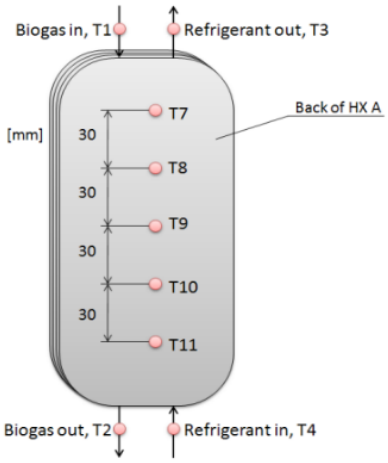

Figure 62: Thermocouple placement in HX [64]

In the experimental test, the HX is not at the same temperature at t=0s which was the case in the model presented in this thesis. At T11 the temperatures of the biogas and the refrigerant are at their lowest contrary to T7. In the simulation, the heat exchanger is considered a cold heat capacity, in the experiment it is a cold stream cooling the biogas to reach the CO_2 deposition temperature. Nevertheless, the temperature and heat flow curves along the cold surface should present the same variations on time.

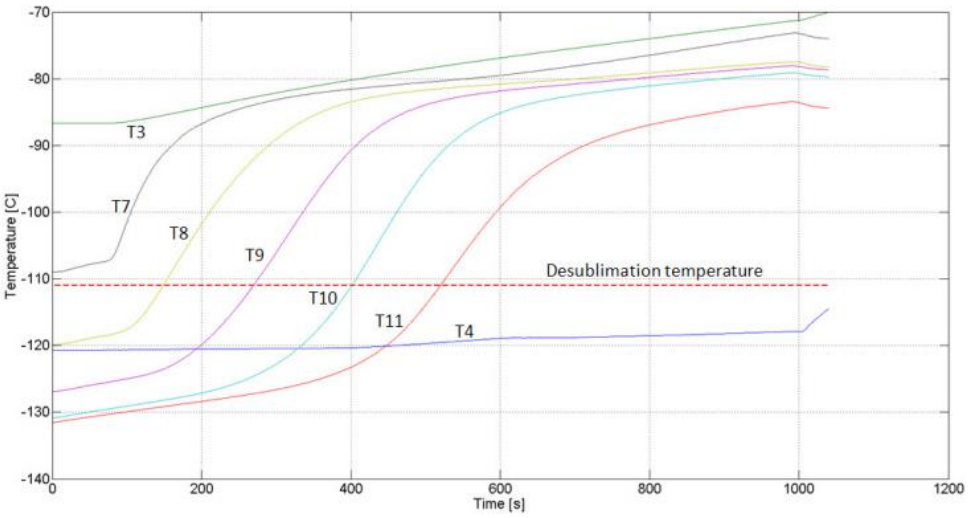

Figure 63: HX temperature distribution [64]

Figure 63 shows the evolution of the HX temperature as deposition occurs. Comparing the results obtained with Figure 60, a high similarity can be found between the curves showing the temperature variations for different positions along the HX. The temperature increase starts slowly and increases when getting closer to the deposition temperature. When the latter is reached, the HX temperature continues increasing to reach an almost constant temperature close to the one of the biogas inlet stream (at infinite time).

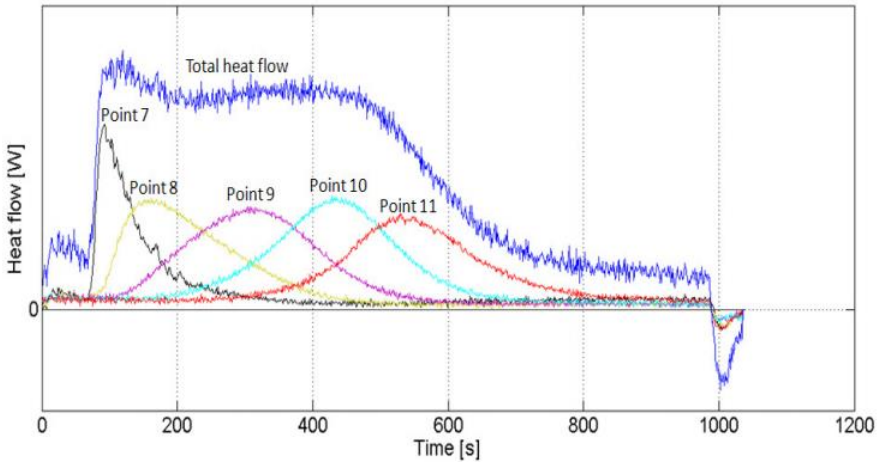

Figure 64: HX heat flow along the plate[64]

Comparing Figure 64 with results obtained in Figure 59, a similar time delay can be found between two consecutive temperature probe positions. The experimental heat flow curve also has a "bell curve" shape.

Song et al. conducted experiments on CO_2 deposition over a Stirling cooler cold head [105]. The frost thickness and density evolution along the cold surface was simulated. As is the case in Figure 53, Figure 65 shows how the frost accumulates nearer to the gas flow inlet and its thickness rapidly increases during the first seconds of operation. The frost creates a thermal barrier between the flow and the cold surface and the deposition rate decreases near the inlet, fostering then the deposition further away from the gas flow inlet.

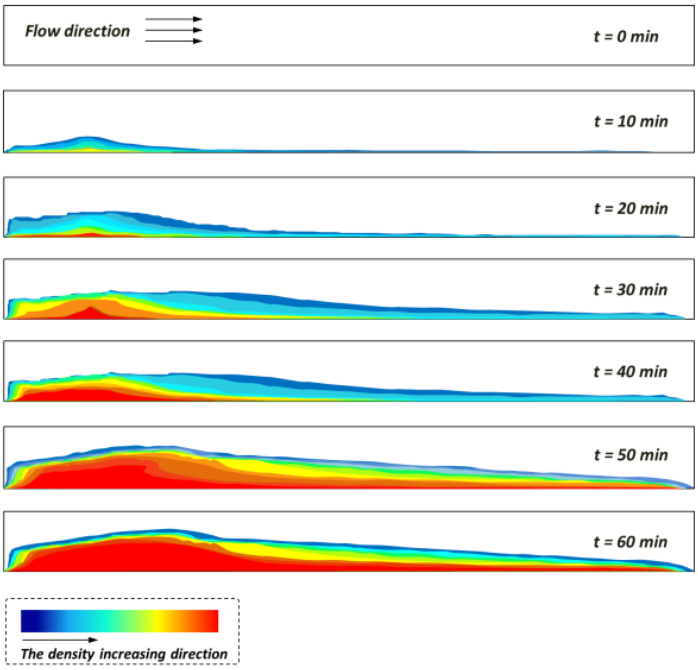

Figure 65: The growth process of the CO_2 frost layer on the cold head of the heat exchanger [105]

As previously mentioned, although the geometry and initial conditions of the systems differ, the frost formation and heat transfer variation present an agreement between the data found in the literature and the simulation results obtained in this thesis.

3.5. CO_2 deposition inside the frost layer

The CO_2 frosted inside the frost layer increases its density and limits heat transfer with the cold surface which reduces the CO_2 deposition rate. The temperature and density variation inside the frost layer was studied at a position x=L/2 from the biogas flow inlet (at the middle of the tube) as it might represent the average frost growth and heat transfer along the tube. Frost deposition at all the positions along the tube presents the same behaviour. As it is shown in Figure 66, going in the y direction (normal to the cold surface - Θ_{frost}), the frost temperature decreases since it is subjected to convective heating from the biogas flow and the thermal resistance of CO_2 frost prevents the cold from arriving to the frost surface. Heat flows by conduction inside the frost layer and the temperature of each layer can be calculated using Eq. 2.12.

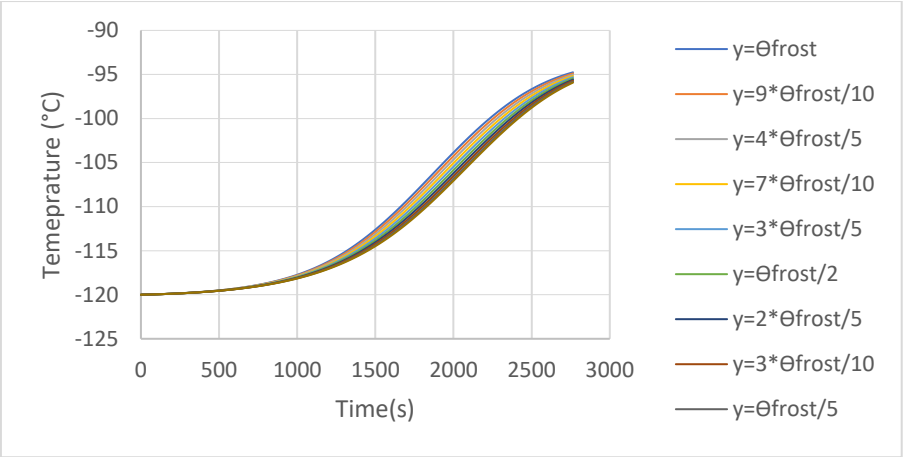

Figure 66: Temperature of the frost layer at different positions along the frost thickness at x = L/2

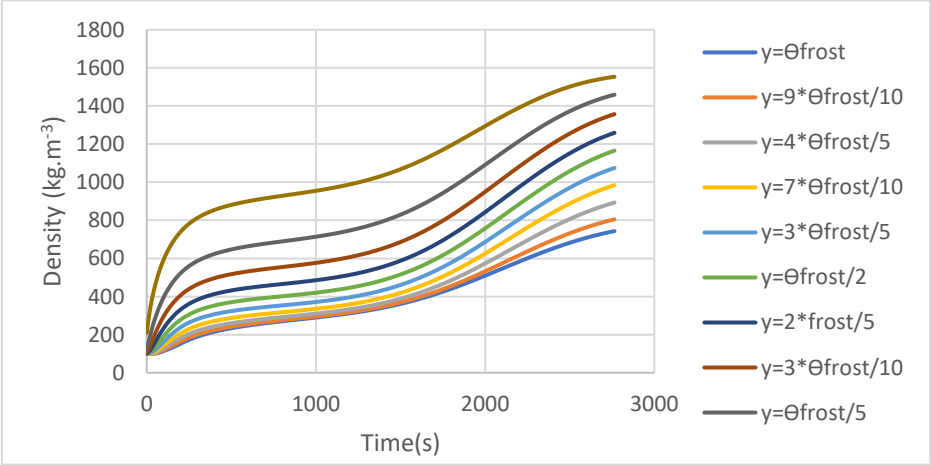

Figure 67: Density of the frost layer at different positions along the frost thickness at x = L/2

Density of the solid CO_2 depends on its temperature (Figure 28), hence, the density of the frost near the cold surface is higher than that at the interface between the frost surface and the gas flow as shown in Figure 67. This is also due to the CO_2 diffusion inside the frost layers and the densification rate presented in Eq.2.10. Figure 65 showing CO_2 deposition on the Stirling cooler head also shows higher frost densities near the cold surface.

3.6. Scale-up of CO_2 solid-formation heat exchanger

3.6.1. Case study of biogas treatment and biomethane liquefaction unit

i. Process description

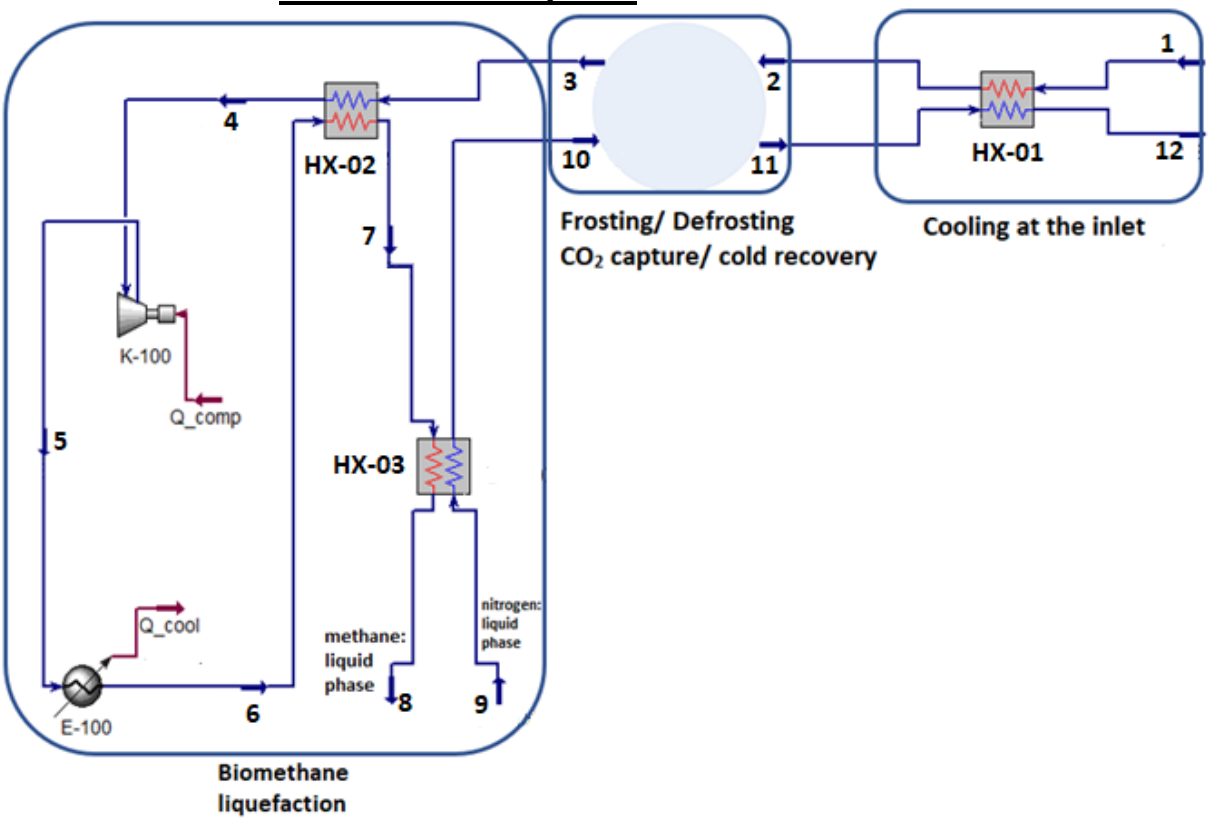

Figure 68: Proposed biogas upgrading and biomethane liquefaction process

Figure 68 describes the system of purification and liquefaction of biogas. This flowsheet was developed and studied with the software AspenTech HYSYS® V8.8 using the Peng-Robinson thermodynamic model since all our gases are real and non-polar. The concentration, temperature and pressure of the inlets and outlets of every heat exchanger can either be calculated or given by the user according to the operating conditions to be considered for a steady state regime.

The initial inlet stream of biogas (Stream 1) composed of methane and carbon dioxide that must be removed in order to obtain pure biomethane, is finally liquefied by nitrogen at cryogenic temperature (Stream 8). It should be noted that the frosting/defrosting heat exchanger is in fact composed by 2 HX that operate alternatively in frosting and defrosting mode (Figure 69).

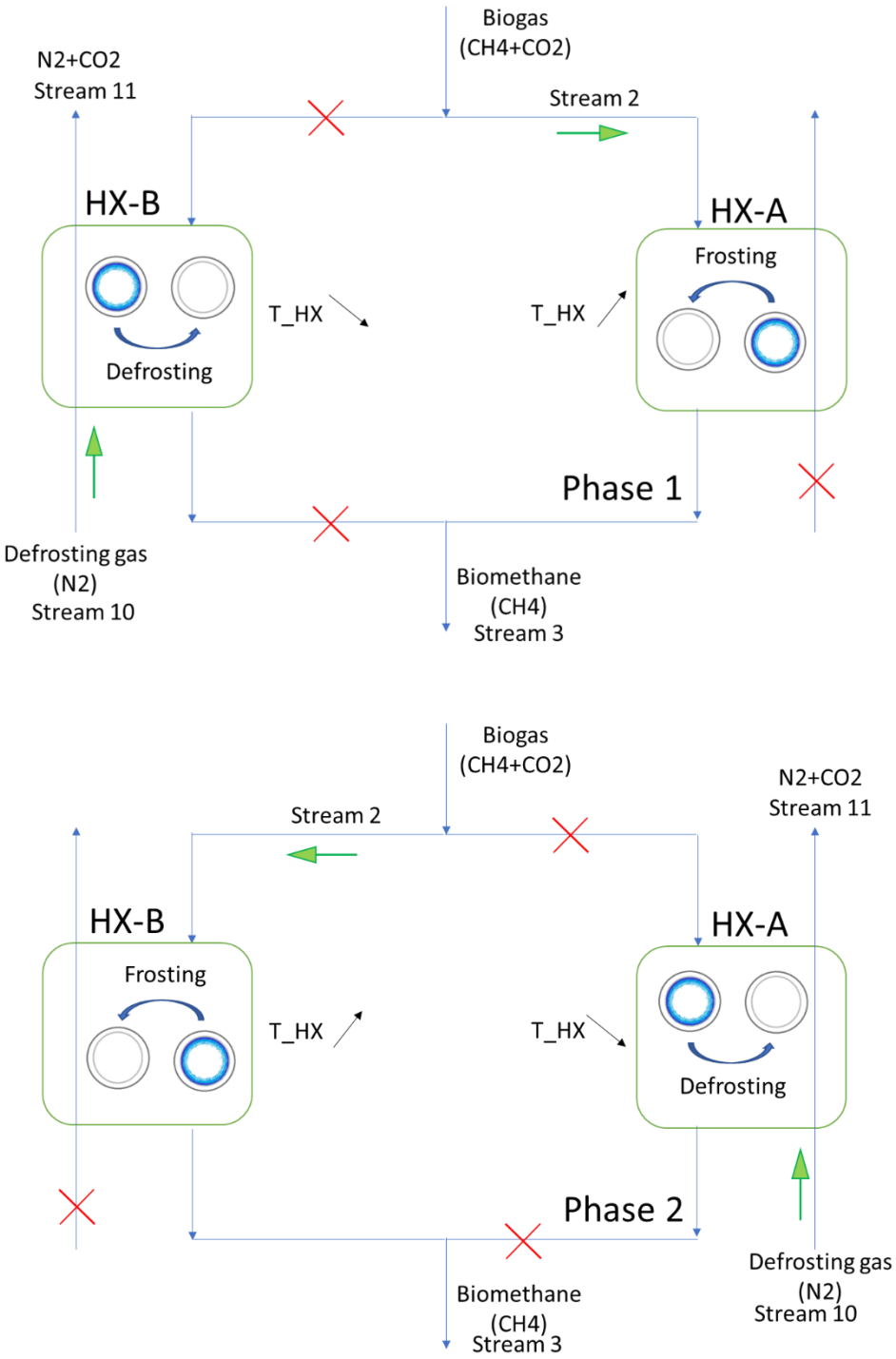

Figure 69: Alternating of CO_2 deposition and defrosting in the 2 HX of the process

In “Phase 1”, biogas passes through HX-A (Stream 2) while biogas injection into HX-B is interrupted. Both heat exchangers are precooled to cryogenic conditions. As frost accumulates, the heat exchanger temperature T_HX-A increases. Upgraded biogas leaves the heat exchanger with a very low percentage of CO_2 and mostly methane (>97.5%) through Stream 3.

In “Phase 2”, the same process described in “Phase 1” takes place but in HX-B. Meanwhile, a gaseous stream (Stream 10) of N_2 passes through HX-A which contains the CO_2 frost from

“Phase 1”. HX-A’s temperature had increased due to frosting. Defrosting by controlled sublimation will decrease its temperature.

It is now possible to go back to “Phase 1”, HX-A is back to cryogenic conditions and it is possible for CO_2 to deposit inside it. HX-B which contains CO_2 frost undergoes controlled sublimation by a stream of N_2 and is cooled. The challenge on the cold recovery proposed in this thesis is finding the exact mass flowrate and temperature of the N_2 stream for which:

- the heat exchanger undergoing defrosting returns to its initial cryogenic conditions in order to repeat the biogas upgrading step with the same result and without using any external utilities.
- frosting is stopped when the molar concentration of the CO_2 contained in biomethane following the frosting phase exceeds 2.5%. In order to optimize the whole system of frosting/defrosting and cold recovery, without wasting time waiting for one phase to end in order to begin the other, it is preferable that time interval needed to achieve complete CO_2 defrosting to be equal to the time spent on frosting.
- the same N_2 stream used for CO_2 defrosting will be used, in a previous step, to liquefy biomethane. The compression + cooling step from Figure 68 should bring biomethane in the right conditions for its liquefaction with the cold energy available in the liquid N_2 flow (out of the scope of this work).

The flow of nitrogen (Stream 9) is also considered an input. These two flows (Stream 1,2,3,4,5,6,7,8 and Stream 9,10,11,12) are counter-current so to better understand the system, it will be divided into three parts:

• Cooling biogas at the entrance:

In this part, the biogas (CH_4 and CO_2) is supposed to have already been purified of anything other than methane and carbon dioxide (H_2S, VOCs...). It will be cooled by the mixture of nitrogen and carbon dioxide arriving from the defrosting stage. This part can be considered as optimization of the biogas inlet temperature for a better entry to the next step as it was discussed before.

• Icing / Defrosting:

The purification of biogas is performed in this part, the model is developed in Dymola instead of ASPEN HYSYS® because it is more complicated to simulate solid phase deposition in dynamic mode in the latter. When all the Dymola results are obtained, they are integrated into Aspen HYSYS® via Excel VB. The frosting part was well detailed in chapter 2, and the defrosting part will be detailed in chapter 4. The models developed and the simulation run aim to predict the temperature, flowrate and composition of the biogas at the outlet of the HX after CO_2 removal. This will allow the optimization of the rest of the system leading to biomethane liquefaction.

• Liquefaction of biomethane:

After the upgrading step of biogas, gaseous biomethane will be obtained. From an economic point of view, it is much more profitable to transport methane in liquid form to the distributor if the availability of gas network infrastructure is limited. Nitrogen is used to liquify biomethane.

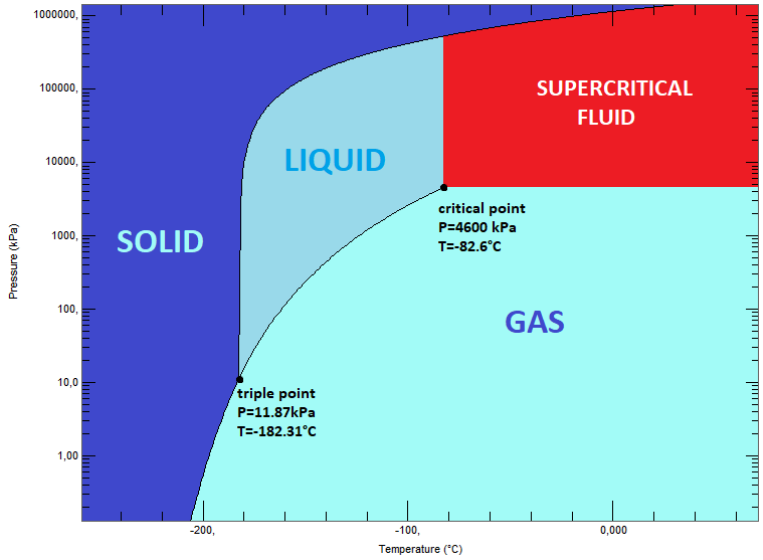

Figure 70: Phase diagram of methane

Referring to the phase diagram in Figure 70, to go from the gaseous state to the liquid it is necessary to lower the temperature or increase the pressure. At $16\ bar$ the methane can be liquefied at $-120°C$ instead of $-160°C$ at $1\ bar$.

After the purification, the upgraded methane (Stream 3) leaves at a very low temperature. It will then be warmed by the same flow of methane that underwent compression (Stream 6). Heating the flow eases the choice of compressors, even though it represents an energy penalty regarding the compression work. A temperature of about $200°C$ is reached with a pressure of $16\ bar$ (and lower temperature is reached if the compression takes place in a multi-stage cooled compression system). At the compressor outlet, the methane (Stream 5) is cooled to ambient temperature using a heat exchanger with the atmosphere. The methane (Stream 6) will be further cooled by the flow exiting the frosting/defrosting equipment (Stream 3). Finally, the liquefaction phase of methane is reached.

ii. Flow and energy calculations

As it was mentioned before, methane at high pressure will require less cooling load in order to be liquified. However, higher liquefaction pressures will need compression power increase which leads to cost increase. Since the compressed biomethane is being cooled with the ambient, the high temperature resulting from compression is not an issue. On the other hand, as liquid nitrogen is used for liquefying methane, the decrease in the cooling load needed will require a smaller flow of nitrogen which can affect the defrosting phase negatively as it will be discussed later.

At the outlet of the HX where the frosting takes place, the mass flowrate of biomethane, its composition and temperature are obtained. Methane molar concentration should be greater than 97.5%, which means that some CO_2 leftovers are still present. Hence, particular attention should be paid the liquefaction step (out of scope) as solidification of remaining CO_2 might cause problems with clogging.

Knowing the state of each flow it will be possible to calculate all the mass flows and temperatures required to complete the system and obtain liquid methane.

- Stream 3: this flow is at the outlet of the HX where frosting takes place. The mass flow rate $\dot{m}_{biomethane,3}$ and composition ($X_{ch4,3}, X_{co2,3}$) depend on the quantity of CO_2 frosted. The results will be obtained by the model developed in Dymola and will be introduced as input into ASPEN HYSYS® (Figures 71 and 72).

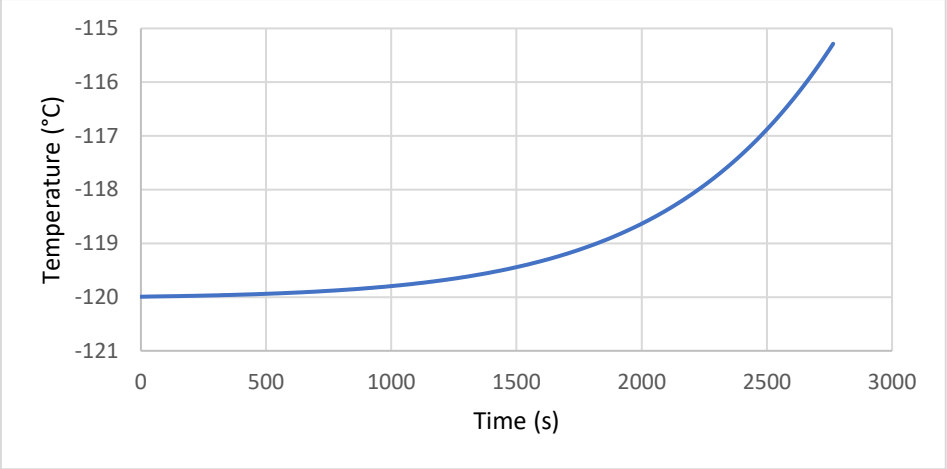

Figure 71: Biomethane outlet temperature calculated in Dymola

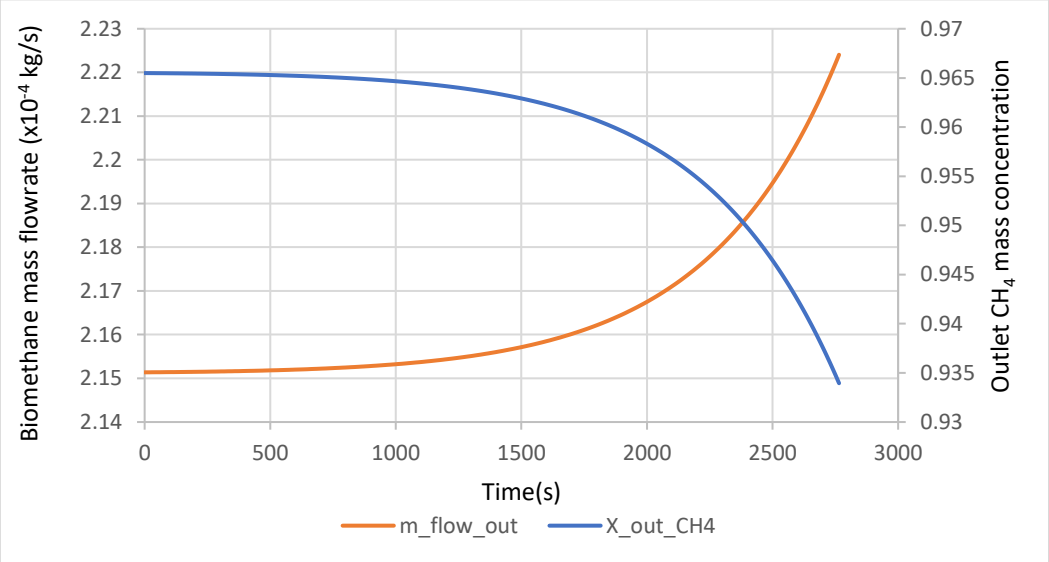

Figure 72: Outlet biomethane mass flowrate and methane mass concentration calculated in Dymola

- Stream 4: the temperature of the cold stream at the outlet of HX-02 depends on the conditions of the hot stream which depend on the compression ratio and the cooling with the atmosphere.
- Stream 5: compression of the methane flow increases its temperature, but it facilitates its liquefaction.
- Stream 6: in order to reduce the cooling load needed during the liquefaction, the hot methane flow is cooled via a heat exchanger with the atmosphere.
- Stream 7: the methane flow is further cooled by Stream 3.
- Stream 8: methane leaves the HX-03 where it gets cooled down to its saturation temperature at the given pressure. It is then liquefied.
- Stream 9: this flow is liquid nitrogen that will serve as cold source for the methane liquefaction.

- Stream 10: depending on the mass flowrate of liquid nitrogen introduced to HX-03, nitrogen will either leave totally in vapour form or as a two-phase flow (liquid/vapor). This outlet temperature affects the defrost phase as it will be discussed in chapter 4.
- Stream 11: the state of the N_2+CO_2 at the outlet of the heat exchanger in defrosting phase will be calculated using the code in Dymola based on the model developed in chapter 4. This flow will serve as cold stream to decrease the biogas temperature at the inlet of the frosting heat exchanger.
- Stream 12: the N_2+CO_2 stream is rejected into the atmosphere after cooling the biogas.

Calculation for each component

As it is shown in Figure 68, the system is divided into two major streams: the biogas which will be upgraded and its carbon dioxide removed and the nitrogen which serves as cold source for biomethane liquefaction and defrosting gas. Mass flow rate and mixture composition remains the same except at the outlets of the HX where frosting and defrosting take place.

- HX-01: in this heat exchanger, biogas is cooled by the nitrogen carrying the sublimated CO_2 from the defrosting phase.

$$\dot{m}_{biogas,1} = \dot{m}_{biogas,2} \quad (3.10)$$

$$\dot{m}_{n2+co2,11} = \dot{m}_{n2+co2,12} \quad (3.11)$$

$$\dot{m}_{biogas,1} \times (h_{biogas,2} - h_{biogas,1}) = \dot{m}_{n2+co2,11} \times (h_{n2+co2,11} - h_{co2+n2,12}) \quad (3.12)$$

Which can also be written as follows:

$$\dot{m}_{biogas,1} \times (cp_{biogas,2} \times T_{biogas,2} - cp_{biogas,1} \times T_{biogas,1}) = \dot{m}_{n2+co2,11}(cp_{n2+co2,11} \times T_{n2+co2,11} - cp_{n2+co2,12} \times T_{n2+co2,12}) \quad (3.13)$$

$T_{biogas,2}$ which will be fixed at -85°C, a temperature slightly above the saturation temperature of CO_2 at its partial pressure in biogas thus optimizing the CO_2 removal cryogenic process. $T_{n2+co2,11}$ will depend on the initial flow of liquid N_2 considering the biomethane liquefaction and the defrosting phase.

- Frosting/Defrosting HX: phase change occurs in this part; in 2 alternatively functioning heat exchangers, the mass flowrate and compositions of the flows entering and exiting the heat exchanger(s) will not remain constant.

  1- The part concerning the frosting of CO_2 contained in biogas:

$$\dot{m}_{biogas,2} = \dot{m}_{ch4,3} + \dot{m}_{co2,3} + \dot{m}_{co2,frost} \quad (3.14)$$

$\dot{m}_{co2,3}$ is added in order to consider the small percentage of CO_2 that doesn't deposit and remains in the biomethane. $\dot{m}_{co2,frost}$ is the mass flowrate of CO_2 frosted on the surface of the heat exchanger. This value is calculated in Dymola using the model presented in chapter 2. The amount of methane does not change since phase change only occurs for the carbon dioxide.

$$\dot{m}_{ch4,2} = \dot{m}_{biogas,2} \times X_{ch4,2} \quad (3.15)$$

$$\dot{m}_{ch4,3} = \dot{m}_{ch4,2} \quad (3.16)$$

$$\dot{m}_{co2,2} = \dot{m}_{biogas,2} \times X_{co2,2} \quad (3.17)$$

$$\dot{m}_{co2,3} = \dot{m}_{co2,2} - \dot{m}_{co2,frost} \quad (3.18)$$

$$X_{co2,3} = \dot{m}_{co2,3}/(\dot{m}_{ch4,3} + \dot{m}_{co2,3}) \quad (3.19)$$

The temperature of the biomethane at the outlet is calculated in Dymola and presented in Figure 71.

2- The part concerning the defrosting of CO_2 with a N_2 flow:

$$\dot{m}_{n2+co2,11} = \dot{m}_{n2} + \dot{m}_{co2,defrost} \quad (3.20)$$

$\dot{m}_{co2,defrost}$ is the mass flowrate of CO_2 that is sublimated from the heat exchanger following the passage of the N_2 flow. This value is calculated in Dymola using the model presented in chapter 4.

$$X_{co2,11} = \dot{m}_{co2,defrost}/(\dot{m}_{n2} + \dot{m}_{co2,defrost}) \quad (3.21)$$

The temperature of the binary mixture N_2+CO_2 at the outlet of the defrosting heat exchanger will also be calculated in Dymola.

- HX-02: in this heat exchanger the cold stream exiting the frosting phase cools down the compressed methane prior to its liquefaction. All mass flowrates are equal since no matter is added nor removed.

  $T_{biomethane,3}$ is found in Dymola, $T_{biomethane,6}$ is at the outlet of the heat exchanger releasing heat to the atmosphere therefore it is equal to ambient temperature. $T_{biomethane,7}$ is the temperature of the biomethane right before its liquefaction. It affects the flowrate of N_2 needed to achieve this step. Also, $T_{biomethane,4}$ is a result that can be found using Eq.2.24; this temperature can limit the compression rate which causes a temperature rise thus going above the critical point of methane. Using Apen HYSYS, it is possible to make sure that all the temperatures are in the acceptable range.

  $$\dot{m}_{biomethane,3} = \dot{m}_{biomethane,4} = \dot{m}_{biomethane,6} = \dot{m}_{biomethane,7} \quad (3.22)$$

  $$\dot{m}_{biomethane,3} \times \left(h_{biomethane,4} - h_{biomethane,3}\right) = \dot{m}_{biomethane,6} \times (h_{biomethane,6} - h_{biomethane,7}) \quad (3.23)$$

  Which can also be written as follows:

  $$\dot{m}_{biomethane,3} \times \left(cp_{biomethane,4} \times T_{biomethane,4} - cp_{biomethane,3} \times T_{biomethane,3}\right) = \dot{m}_{biomethane,6} \times (cp_{biomethane,6} \times T_{biomethane,6} - cp_{biomethane,7} \times T_{biomethane,7}) \quad (3.24)$$

- K-100: the compressor increases the pressure of the biomethane to facilitate its liquefaction. The pressure increase will depend on the liquid N_2 flow available for the liquefaction phase and later the defrosting phase covering all the criteria mentioned before concerning the defrosting time and the frosting/ defrosting heat exchanger final temperature. Knowing the pressure ratio and the isentropic efficiency $\varepsilon_{iseentropic}$ of the

compressor, it is possible to calculate the temperature $T_{biomethane,5}$ at the outlet of the compressor by using gamma the ratio of specific heats [106].

$$\gamma = \frac{cp}{cv} \tag{3.25}$$

$$T_{biomethane,5} = T_{biomethane,4} + \frac{\left(T_{biomethane,4} \times \left(\frac{P_{biomethane,4}}{P_{biomethane,5}}\right)^{\gamma-1/\gamma}\right) - 1}{\varepsilon_{iseentropic}} \tag{3.26}$$

- E-100: this heat exchanger rejects heat to the atmosphere to decrease the biomethane temperature to ambient temperature following the equation below:

$$\dot{Q}_{cool} = \dot{m}_{biomethane,5} \times \left(cp_{biomethane,5} \times T_{biomethane,5} - cp_{biomethane,6} \times T_{biomethane,6}\right) \tag{3.27}$$

- HX-03: in this heat exchanger biomethane liquefaction takes place. Two flows pass through HX: pressurized biomethane and liquid nitrogen. Biomethane which will be cooled in HX-02 undergoes liquefaction as liquid N_2 evaporates. Depending on the pressure of biomethane, its inlet temperature and the mass flowrate of the liquid N_2 introduced several scenarios are presented:
    1- N_2 is not enough and not all biomethane is liquefied. This option is not acceptable since all biomethane should be liquefied for transportation.
    2- N_2 is more than enough, all biomethane is liquefied but N_2 at the outlet of HX-03 is a two-phase flow at -196°C. If N_2 is not heated before entering the defrosting HX, its extremely low temperature and liquid fraction will limit CO_2 defrosting as it is shown in the psychrometric chart in Figure 25. Also, sensible heat from the N_2 flow towards the CO_2 frost will reduce the latter's temperature thus increasing the defrosting time.
    3- All biomethane is liquified as all N_2 evaporates. In order to achieve complete defrosting in a specific time interval, the mass flowrate of liquid N_2 and its temperature at the outlet of HX-03 are the two criteria that should be optimized.

The small traces of CO_2 remaining in the biomethane might undergo deposition during the liquefaction phase. This might slightly affect the heat exchange. In the following, these traces will be considered as an error that can be compensated with a little surplus of liquid N_2.

Biomethane passes through 3 phases:

1- **Precooling**: $\dot{Q}_{biomethane,precooling} = \dot{m}_{biomethane,7} \times \left(cp_{biomethane,7} \times T_{biomethane,7} - cp_{biomethane,gas,sat} \times T_{biomethane,gas,sat}\right)$ (3.28)

2- **Liquefaction**:
$\dot{Q}_{biomethane,liquefaction} = \dot{m}_{biomethane,7} \times L_{vl,biomethane}$ (3.29)
With $L_{vl,biomethane}$ the latent heat of liquefaction of methane at its given pressure.

3- **Postcooling**: $\dot{Q}_{biomethane,postcooling} = \dot{m}_{biomethane,8} \times \left(cp_{biomethane,liq,sat} \times T_{biomethane,liq,sat} - cp_{biomethane,8} \times T_{biomethane,8}\right)$ (3.30)

It should be noted that $cp_{biomethane,8}$ is for liquid biomethane.

Nitrogen passes through two phases:

1- **Vaporization**: $\dot{Q}_{n2,vaporization} = \dot{m}_{n2} \times L_{vl,n2}$ (3.31)
With $L_{vl,n2}$ the latent heat of vaporization of nitrogen.

2- **Postheating**: $\dot{Q}_{n2,postheating} = \dot{m}_{n2} \times \left(cp_{n2,10} \times T_{n2,10} - cp_{n2,gas,sat} \times T_{n2,sat}\right)$ (3.32)
It should be noted that $cp_{n2,10}$ is for nitrogen gas.

Energy balance gives:

$$\dot{Q}_{biomethane,precooling} + \dot{Q}_{biomethane,liquefaction} + \dot{Q}_{biomethane,postcooling} = \dot{Q}_{n2,vaporization} + \dot{Q}_{n2,postheating} \quad (3.33)$$

Postheating of nitrogen N_2 will depend on its mass flowrate and they will both define the defrosting process. The mass flowrate will depend on the temperature and pressure of biomethane entering HX-03. All these entities are connected through the set of equations presented in this part of this chapter. All the results concerning the frosting and the defrosting phases are obtained using Dymola and are implemented into ASPEN HYSYS® which takes into account all the equations presented for each component and connects them together.

3.6.2. Using an intermediate vapour-compression cycle

So far, the heat exchanger used for CO_2 removal was considered as a heat capacity at a starting cryogenic temperature. Another option for CO_2 removal from biogas and cold recovery by controlled sublimation is using an intermediate vapour-compression cycle (Figure 73).

In “Phase 1”, the coolant circulating in the vapour-compression cycle will serve as cold source in HX-A where biogas upgrading occurs and CO_2 deposits. The coolant enters in liquid form and evaporates in HX-A. Then it passes through a compressor where its pressure and temperature increase. As the coolant passes through the defrosting HX-B, its temperature decrease and it partially liquefies before passing through the expansion valve returning to its initial condition. When the CH_4 concentration in the biomethane at the outlet of HX-A goes below 97.5%, “Phase 2” is initiated. The same principle as “Phase 1” remains but the heat exchangers are reversed.

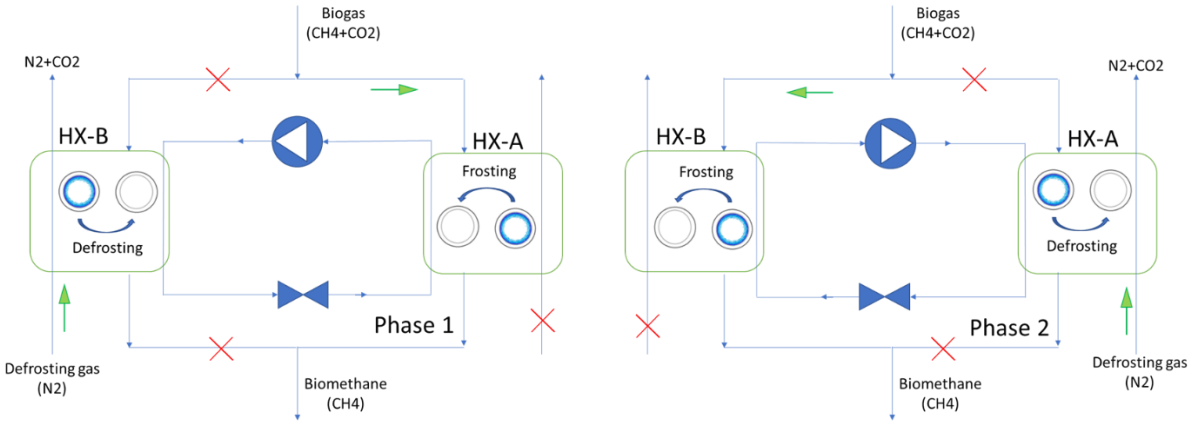

Figure 73: Alternating CO_2 frosting/defrosting system using an intermediate fluid in a vapour-compression cycle

The added cycle increases the cost but it will make possible to better manipulate the CO_2 frosting and defrosting by changing the conditions of the circulating fluid instead of just operating with a heat capacity with fixed parameters.

This case will not be studied in this thesis, but it is interesting as a perspective and it may present some optimization to the existing system. Many configurations can be proposed for this application of frosting/defrosting.

Conclusion

A sensitivity study was led on CO_2 frosting from biogas, and results show that for higher CO_2 concentrations, frost grows faster and more in terms of thickness and density. When the plate temperature was reduced, thickness increased because of the decrease of CO_2 saturation vapour concentration at the frost surface but density decreased because of CO_2 concentration decrease in the frost layer. Also, the increase of the biogas inlet temperature will reduce slightly the frost thickness while almost not affecting the density.

On the other hand, results for CO_2 frosting from biogas showed how higher relative concentrations of CO_2 increase heat transfer especially at the interface between the frost and the gas flow. Plate temperature has a “more constant variation” effect on heat transfer than CO_2 concentration and inlet temperature has an opposite effect than the concentration. Considering a plate as a heat capacitor and not at constant temperature results in a quick decrease of sensible and latent heat either on the surface or in the frost caused by the plate’s temperature increase as it frosts the CO_2.

A comparison between the plate and the tube configuration for CO_2 deposition showed that the tube presents a better configuration in terms of accessibility and heat transfer for a given time but for longer frosting periods the plate is the better choice since its heat exchange surface remains constant during CO_2 deposition . A condition on CH_4 outlet concentration is fixed and the CO_2 frost formation along the tube was studied and compared with the literature for validation. The results show that frost deposition presents a certain delay along the tube; this is caused by the concentration gradient decrease as frost deposits at earlier positions in the tube.

A whole system of biogas upgrading and biomethane liquefaction was presented and all its components and flow calculations were detailed. The process uses two heat exchangers operating simultaneously and alternatively as frosting and defrosting heat exchangers. The N_2 flow that will be used for biomethane liquefaction will be later used for “controlled sublimation” and cold recovery.

Chapitre 3: Givrage de CO_2 - séparation cryogénique du biogaz

Introduction

L'épuration cryogénique du biogaz implique l'élimination du dioxyde de carbone à très basse température. La température de saturation du CO_2 augmente quand sa pression partielle dans le biogaz augmente. Dans cette thèse, on se concentre sur l'élimination du CO_2 par condensation solide à basse pression et sur la récupération d'énergie à basse température afin de réduire la puissance frigorifique nécessaire à l'élimination cryogénique du CO_2 contenu dans le biogaz. Les équations de masse et d'énergie régissant le phénomène de formation et de croissance du givre présentées dans le chapitre 2, peuvent être appliquées dans le cas de l'élimination du CO_2 contenu dans le biogaz.

Ce qui compte le plus dans l'élimination du CO_2 du biogaz, c'est la pureté du biométhane obtenu. Le débit massique du biogaz, sa température et sa concentration en CO_2 sont des paramètres à étudier pour optimiser le procédé d'élimination du CO_2. Aussi, la géométrie de l'échangeur de chaleur a un effet majeur sur le transfert de chaleur et donc la quantité de CO_2 éliminée par mètre carré.

Dans ce chapitre, on présente d'abord une étude de sensibilité sur le givrage de CO_2 sur une plaque plate pour différentes conditions initiales. Afin d'optimiser le transfert de chaleur et de masse, différentes géométries de l'échangeur de chaleur sont étudiées. Le système complet, comprenant l'élimination du CO_2 et la liquéfaction du biométhane, a été construit avec ASPEN HYSYS® en tenant compte de tous les flux massiques et transferts thermiques dans le système, à l'exception de la partie formation de givre qui sera calculée dans Dymola. L'échangeur de chaleur sera considéré comme une inertie thermique refroidie à très basse température par l'azote utilisé pour liquéfier le biométhane. La température de l'échangeur de chaleur augmente pendant la phase d'épuration par givrage du CO_2.

3.1. Etude de sensibilité : givrage de CO_2 du biogaz

Dans cette partie, une étude de sensibilité est menée pour comprendre l'effet des conditions d'entrée et de la température de la plaque sur l'épaisseur du givre, sa masse volumique et les transferts de chaleur pendant la phase de givrage. Le biogaz (CH_4-CO_2) passe au-dessus d'une plaque froide et le CO_2 givre à sa surface. Différentes concentrations de CO_2, températures d'entrée du biogaz et de plaque sont étudiées, la croissance du givre ainsi que les transferts de chaleur à la surface et à l'intérieur de la couche de givre. Les courbes avec des tirets représentent la première valeur donnée au paramètre étudié, les courbes en pointillés pour la deuxième valeur et les lignes continues pour la troisième valeur.

i. Plaque plane à température constante

Cas 1: Variation de la concentration massique de CO_2 $(X_{co2/biogas}\ (kg/kg) = 0{,}6; 0{,}5; 0{,}4)$

La variation de la concentration de CO_2 dans le biogaz affecte principalement le flux de masse total de CO_2 givré et le flux de masse de CO_2 dépoli à l'intérieur des couches de givre, mais moins que la masse totale. La différence entre ces deux valeurs donne le flux de masse de CO_2 givré à la surface qui augmente pour une concentration plus élevée (20% au-dessus de la concentration

de référence), augmentant ainsi l'épaisseur du givre d'environ 13,5%, comme le montre la Figure F6.a.

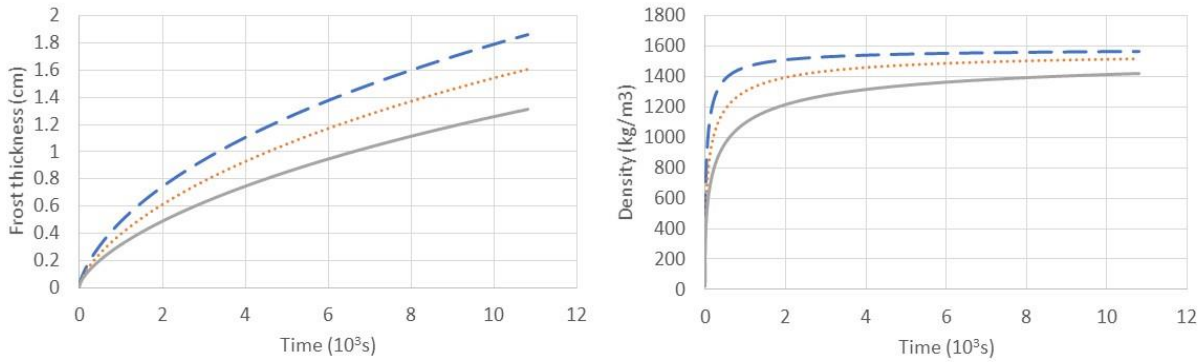

Figure F6: Croissance du givre de CO_2 pour différentes conc. mass.: (a) épaisseur du givre, (b) masse volumique du givre

La masse volumique du givre est calculée à l'aide du taux d'absorption massique α, qui est fonction du débit massique du CO_2 qui givre dans la couche de givre. La masse volumique augmente rapidement pour une concentration de CO_2 supérieure (Figure F6.b.)

La surface d'échange de chaleur et le gradient de température sont constants, ce qui signifie que la variation de la chaleur sensible est due au coefficient de transfert de chaleur, plus précisément à la viscosité et à la conductivité thermique du biogaz, qui dépendent de la composition du mélange.

La chaleur latente totale est le produit de la chaleur latente de sublimation et du flux massique de CO_2 givré qui dépend de la différence de concentration de CO_2 dans le flux de biogaz et à la surface du givre, ainsi que du transfert de masse. La chaleur latente indique la quantité de CO_2 givré puisque la chaleur latente de sublimation est relativement constante en fonction de la température. Le givrage se produit à la surface et à l'intérieur de la couche de givre. Sur la figure F7.d, pendant les premières secondes du givrage, la chaleur latente à la surface est presque nulle car le débit massique de givre CO_2 à la surface est déterminé par le taux d'augmentation d'épaisseur. Quant à la chaleur latente à l'intérieur du givre, elle commence à des valeurs élevées, mais diminue pour atteindre des valeurs presque nulles. Ceci est dû à la diminution de la densification de la couche de givre.

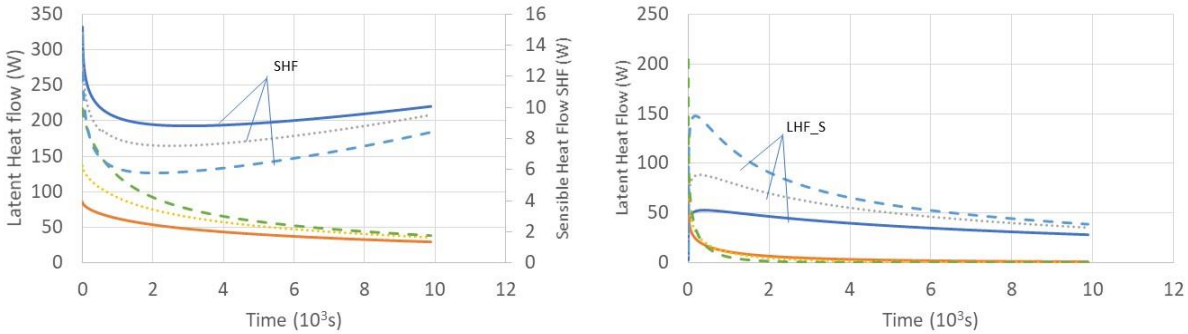

Figure F7 : Puissances échangées pour différentes concentrations de CO_2 correspondant à: (c) chaleur latente totale et chaleur sensible, (d) chaleur latente à la surface et à l'intérieur du givre

Une concentration plus élevée de CO_2 dans le biogaz augmente le transfert de chaleur puisque le gradient de concentration augmente. Cependant, la concentration dépend de la source de

biogaz, comme indiqué au chapitre 1, et il n'y a donc aucun moyen de la contrôler.

<u>Cas 2</u>: Variation de la température de plaque $(T_{cold\_plate}\ (°C) = -138; -128; -118)$

La forme des courbes représentant la croissance du givre et le transfert de chaleur est similaire à celle obtenue pour les différentes concentrations. Les plaques à plus basse température diminuent la température à la surface du givre ce qui diminue la concentration de vapeur saturante de CO_2, ce qui augmente la différence de concentration en CO_2 et donc le débit massique total de CO_2 givré. Ce comportement se traduit par des valeurs plus élevées pour l'épaisseur du givre : pour une diminution de la température de surface de 7,5%, l'épaisseur de givre augmente d'environ 11%. La masse volumique diminue lorsque la température de la plaque est plus basse, ce qui se traduit par la réduction de la concentration de vapeur de saturation en CO_2 dans les couches de givre. La quantité de CO_2 givré dans la couche de givre ainsi que la masse volumique sont réduites.
Les variations de la chaleur sensible et latente à la surface et dans la couche de givre ont été détaillées précédemment. Le transfert de chaleur par convection a un impact négligeable sur le transfert de chaleur global car le gradient de température est dominé par la petite surface; néanmoins, pour une diminution de 7,5% de la température de la surface froide, le flux de chaleur sensible augmente en moyenne d'environ 8,7%. Le même s'applique à la chaleur latente, les températures de plaque plus basses augmentent les flux de la chaleur latente à la surface du givre, mais pas à l'intérieur du givre, car les températures plus basses réduisent la pression de vapeur saturante du CO_2; la diminution de la concentration en CO_2 va diminuer le givrage à l'intérieur de la couche de givre. L'augmentation du gradient de température crée un plus grand gradient de concentration de CO_2 entre le flux et le givre, ce qui augmente le flux de chaleur latente totale. Diminuer la température de la plaque pourrait être préférable pour le captage du CO_2, mais le coût énergétique de son refroidissement pourrait être supérieur à celui de l'amélioration du processus de formation de givre. L'important est d'avoir une température inférieure à la température de givrage du CO_2 à sa pression partielle dans le mélange.

<u>Cas 3:</u> Variation de la température d'entrée du biogaz $(T_{biogas}\ (°C) = -85; -80; -75)$

La forme des courbes représentant la croissance du givre et le transfert de chaleur est similaire à celle observée pour les différentes concentrations. Le changement de température d'entrée n'a pas d'effet direct sur la différence de concentration de CO_2 en surface ni dans les couches de givre, aucun changement remarquable de l'épaisseur et de la masse volumique du givre n'est constaté. L'épaisseur du givre augmente légèrement pour une plus basse température d'entrée, car la diminution de la chaleur sensible par convection a plus d'effet par rapport à la diminution du transfert de chaleur par conduction dans les couches de givre. Par conséquent, la masse de CO_2 givré à la surface augmente, l'épaisseur augmente également mais juste d'à peu près 3%.
Le changement de température d'entrée entraine une variation du flux de la chaleur sensible sûrement puisque le gradient de température varie mais, au même temps, les propriétés du biogaz varient également, de sorte que le coefficient de transfert de chaleur sera affecté. Des températures plus élevées réduiront le débit massique de CO_2 givré sur la surface froide. La

température du biogaz a un effet très mineur sur le flux de chaleur latente. Étant donné que la plaque est à une température très froide comparée à la température de saturation en CO_2, il est facile d'atteindre les conditions de givrage tant qu'il existe un gradient de concentration entre le biogaz et la surface du givre.

La température d'entrée du biogaz ne doit pas être inférieure à la température de saturation du CO_2, sinon ce dernier se solidifie avant son entrée dans l'échangeur, ce qui entraîne un encrassement et d'autres perturbations du système.

ii. Plaque comme inertie avec température cryogénique initiale

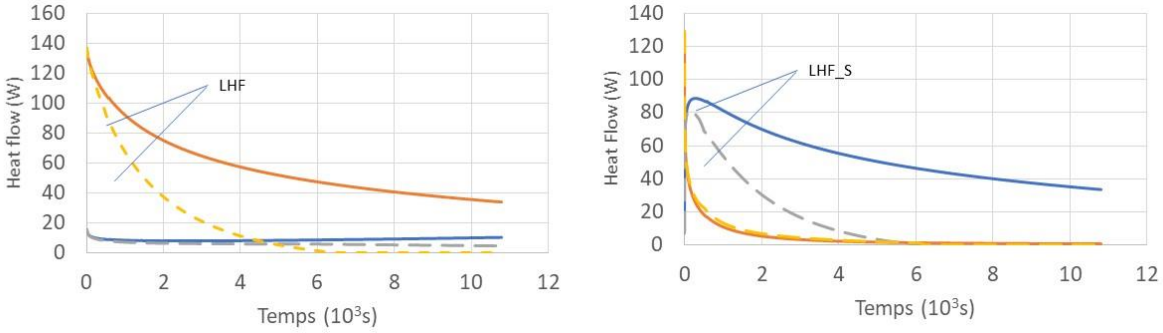

(a) (b)

Figure F8: Puissance echangées pour différentes configurations de la plaque correpondant à : (a) chaleur latente totale et chaleur sensible, (b) chaleur latente à la surface et à l'intérieur du givre

Dans ce cas, la plaque n'est pas à une température constante, elle est considérée comme une inertie thermique. Les résultats du transfert de chaleur sont comparés au cas d'une plaque à température constante avec $T_{biogas} = -80°C$, $X_{co2/biogas} = 0{,}5$ et $T_{plate} = -128°C$. Dans la figure F8, les tirés indiquent la plaque en configuration d'inertie thermique et les lignes continues représentent les valeurs de la plaque à température constante.

Lorsque la plaque n'est pas à température constante, elle se réchauffe sous l'effet du givrage du CO_2. Cette augmentation de température réduit le gradient de température dans la couche de givre. Alors la chaleur sensible diminue constamment contrairement au cas de la température constante dans laquelle la chaleur sensible atteint une certaine valeur et cesse de varier. Cette température est atteinte lorsque la température de surface du givre est chauffée et refroidie de manière identique par le flux de biogaz et la plaque froide respectivement; lorsque cette température est atteinte, le débit massique de givrage tend vers 0. Un phénomène similaire est observé pour le flux de chaleur latente : la diminution du gradient de température entraîne une différence de concentration plus faible entre les couches de givre, ce qui limite le givrage réduisant à zéro la chaleur latente.

3.2. Givrage conditionné par le %CH_4 à la sortie

Le critère le plus pertinent durant l'épuration du biogaz est la pureté du méthane après l'élimination du CO_2. Selon GRDF «Gaz Réseau Distribution France», la concentration molaire du CO_2 dans le biométhane ne devrait pas dépasser 2,5% après l'épuration. Ce critère sera utilisé pour choisir la meilleure géométrie de l'échangeur thermique. La «plaque» et le «tube» sont les deux géométries simples qui seront comparées. Lorsque l'on compare les deux

géométries en termes de logistiques d'écoulement de fluide, il est clair que la configuration du tube est beaucoup plus simple pour gérer la circulation du fluide. Une grande plaque peut nécessiter de nombreux injecteurs afin d'assurer un écoulement de masse uniforme. De plus, contrairement aux plaques planes, les tubes peuvent être coudés pour s'insérer dans de petits volumes avec une faible pénalité pour les pertes de charge en fonction de la vitesse d'écoulement et du facteur de frottement.

En ce qui concerne la modélisation numérique, la différence principale entre les deux géométries est la corrélation du coefficient de transfert thermique qui affecte le coefficient de transfert massique. Ces coefficients sont directement liés à la chaleur sensible et à la masse de CO_2 givré, respectivement. Le même débit massique et la même surface d'échange seront considérés pour les deux cas. De plus, toutes les conditions initiales seront identiques. Les deux surfaces froides seront initialement à une température cryogénique. Comme indiqué précédemment, la concentration molaire du CO_2 dans le biogaz est généralement comprise entre 20 et 50%. Les unités classiques de valorisation du biogaz génèrent environ 250 Nm^3/h de biométhane. Dans la partie suivante, une comparaison entre différentes géométries, différentes concentrations de CO_2 dans le biogaz à l'entrée et un débit différent de biogaz est effectuée. Les légendes de la figure indique respectivement la géométrie, la concentration molaire du biogaz en CO_2 et le débit de biogaz.

i. Cas 1: Comparaison entre plaque et tube pour différentes concentrations de CO_2 dans le biogaz à l'entrée

L'étude de sensibilité réalisée montre qu'une concentration plus élevée en CO_2 aboutit à plus de givrage, mais pas nécessairement à une pureté plus élevée du méthane à la sortie.

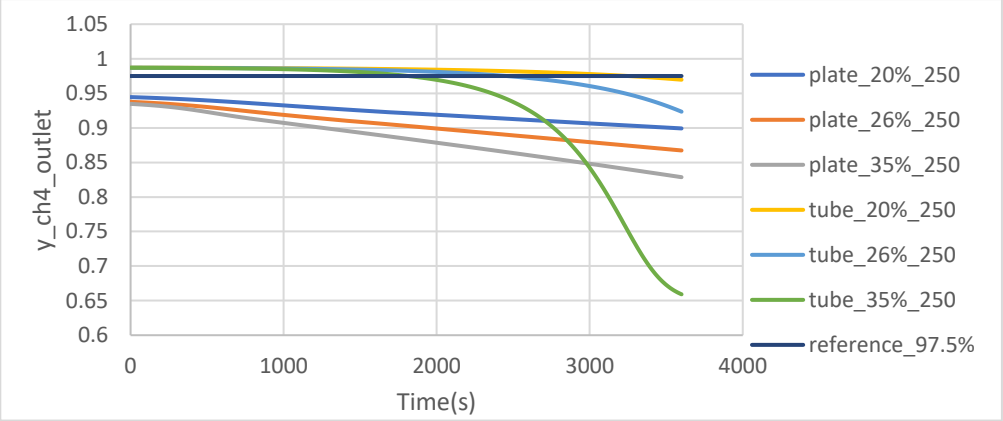

Figure F9: Concentration en CH_4 à la sortie du HX pour diff. concentrations de CO_2 en entrée et diff. géométries

La figure F9 montre comment, pour le même débit de biogaz, la diminution de la concentration en CO_2 conduit à une pureté supérieure de CH_4 et que l'accumulation du givre diminue la concentration en CH_4 à la sortie. Pour la suite de cette étude, on considère une concentration molaire initiale de CO_2 dans le biogaz de $y_{co2} = 26\%$ (lignes orange et bleu clair) pour ne pas prendre le cas le plus optimiste (20% (lignes bleu foncé et jaune)) et en même temps avoir un temps de givrage plus long qui sera utile pour la sublimation qui sera abordée au chapitre 4.

L'augmentation de la couche de givre diminue la concentration de CH_4, mais elle présente un effet moins important pour la plaque que pour le tube. Au temps t = 2950s, la concentration de CH_4 est plus élevée pour la plaque que pour le tube pour $y_{co2} = 35\%$ (lignes grises et vertes

respectivement). Les courbes de concentration en CH_4 pour la géométrie du tube semblent diminuer plus rapidement que celles relatives aux plaques. Cela est dû au changement de la surface effective d'échange. Les courbes montrent une plus grande pureté de méthane pour les tubes que pour les plaques qui, ayant la même surface d'échange ne peuvent pas satisfaire les spécifications relatives à la teneur en CH_4 de $y_{ch4} > 97.5\%$.
Il faut noter que, puisque le givre se dépose sur toute la surface intérieur du tube, il réduit le diamètre du tube de $2 \times épaisseur\ du\ givre$. Dans la configuration de plaque, L'accumulation du givre n'affecte pas la surface d'échange de chaleur contrairement au tube où la surface de transfert de chaleur est fortement réduite. La raison principale pour laquelle le tube a une concentration de CH_4 plus élevée à la sortie est qu'il possède les valeurs les plus élevées du coefficient de transfert de chaleur. L'effet de la diminution de la surface d'échange du tube par rapport au coefficient de transfert de chaleur sera discuté dans le cas 3.

ii. Cas 2: Comparaison entre plaque et tube pour différents débits de biogaz à l'entrée

La figure F10 montre que lorsque suffisamment de givre est formé et que la surface d'échange de chaleur dans le tube est suffisamment réduite, la concentration de CH_4 à la sortie de la plaque (lignes bleu foncé, orange et gris) dépasse celle du tube (lignes jaunes, bleu clair et vert). Les débits de biogaz plus élevés contiennent plus de CO_2 et donnent de plus faibles concentrations de CH4 à la sortie de l'échangeur. La couche de givre accroit plus rapidement pour les débits élevés; par conséquent, la résistance thermique créée par son accumulation augmente plus rapidement et moins de CO_2 pourra être givré.

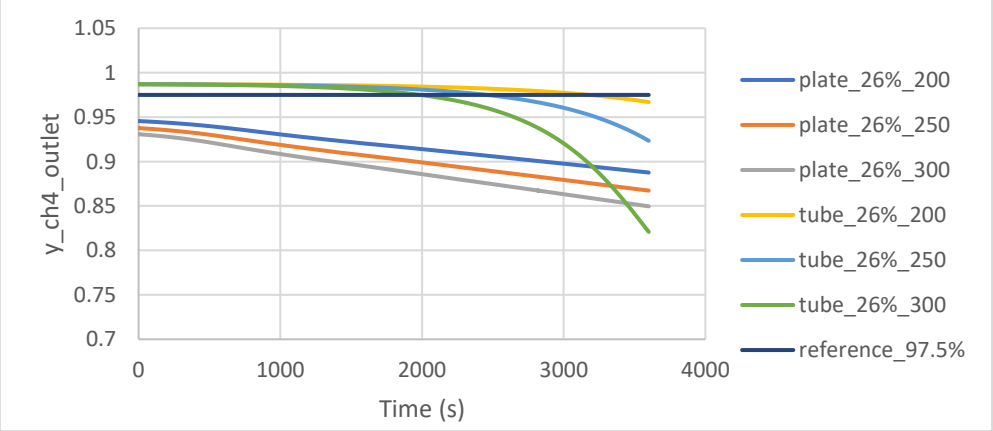

Figure F10: Concentration en CH_4 la sortie du HX pour différents débits de biogaz à l'entrée et différentes géométries

iii. Cas 3: Comparaison pour différents diamètres internes des tubes de l'échangeur

En modifiant le diamètre intérieur du tube, la surface de transfert de chaleur A_{tube} et la section de passage d'écoulement S_{tube} sont les deux principaux paramètres concernés.
En examinant le modèle de givrage présenté au chapitre 2, tous les transferts de chaleur et de masse sont fonction de la surface d'échange de chaleur A_{tube} qui est proportionnelle au diamètre du tube d_{tube}. Le débit est constant à l'entrée, la variation de S_{tube} affecte la vitesse d'écoulement, le nombre de Reynolds et le coefficient de transfert de chaleur. Le coefficient de transfert massique h_m est proportionnel au coefficient de transfert thermique h_c. La chaleur sensible par convection $\dot{q}_{sens}$ de Eq. F.2.1 et le flux de CO_2 givré $\dot{m}_{frost}$ de Eq. F.2.2 sont fonction

de h_c et A_{tube}. La chaleur latent $\dot{q}_{lat}$ est également fonction de $\dot{m}_{co2,frost}$, ainsi tous les transferts de chaleur et de masse sont fonction de $A_{tube} \times h_c \sim (1/{d_{tube}}^{0.8})$. Par conséquent, les diamètres les plus faibles augmentent le taux de givrage, mais l'accumulation plus rapide du givre conduit à une diminution plus rapide de la surface d'échange pour les diamètres les plus faibles qui peuvent se boucher. Sur la figure F11, les résultats pour trois diamètres de tube sont comparés.

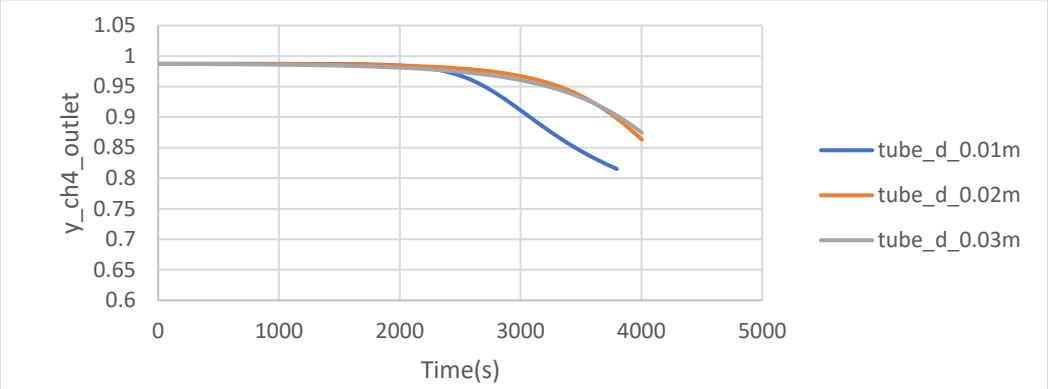

Figure F11: Concnetration en CH_4 à la sortie pour diffénrets diamètres de tube

La figure F11 montre une pureté de CH_4 plus élevée pour les diamètres les plus faibles, mais à fur et à mesure que le givre s'accumule, la concentration en CH_4 diminue plus tôt pour les faibles diamètres en raison du bouchage du tube.

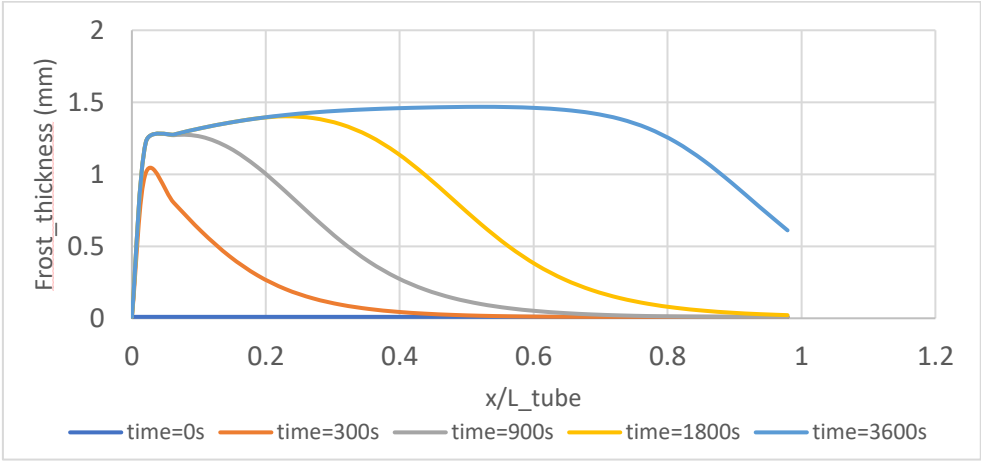

Figure F12: Evolution de l'épaisseur de givre le long du tube de diamètre d_tube=0.02 considérant une unité de longueur

La figure F12 montre l'évolution de l'épaisseur de givre le long du tube en considérant une unité de longueur. Initialement le givre n'est pas homogène sur la surface. Les lignes oranges, grises et jaunes de la figure F12 montrent que le givre est beaucoup plus épais dans la première moitié de la plaque jusqu'à t = 1800s. A chaque intervalle de temps, la tête du dôme devient moins nette et plus éloignée de la position x=0 du tube. Lorsque le biogaz passe à l'intérieur du tube, le CO_2 commence à givrer et la concentration du biogaz en CO_2 diminue, limitant ainsi la formation de givre sur le reste du tube. De plus, la température de la capacité thermique commence à augmenter dans cette partie du tube. Le givre commence alors à s'accumuler le long de la partie du tube la plus proche de sa sortie (ligne bleue).

iv. Case 4: comparison pour différentes temperatures intiales des tubes de l'échangeur

La température initiale de l'inertie thermique (tube ou plaque) affecte la concentration du CH_4 en sortie de l'échangeur. Le biogaz traverse le tube et le CO_2 se solidifie sur la surface froide diminuant ainsi sa concentration dans le biogaz. Des concentrations plus basses de CO_2 requiert une température plus basse pour changer de phase, alors une température de tube initiale plus basse permet le givrage à des positions loin de l'entrée du biogaz où la concentration en CO_2 ait trop diminué. Le réchauffement rapide de l'inertie diminue la quantité de CO_2 givré dessus. Dans la Figure F13, la diminution jusqu'une concentration de CH_4 constante à la sortie (courbe bleue à T=-105°C) est due à l'augmentation de la température au point où le CO_2 ne givre plus dans le tube et $y_{ch4} = 74\%$ à la sortie de l'échangeur.

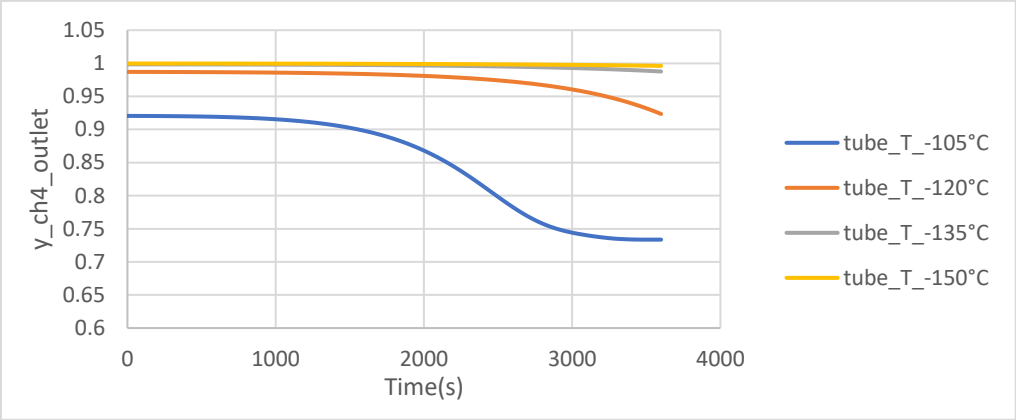

Figure F13: Concentration en CH_4 à la sortie des tubes de l'échangeur iipour différentes températures intiales

3.3. Formation du givre dans la longueur du tube

3.3.1. Taux de givrage de CO_2 givré

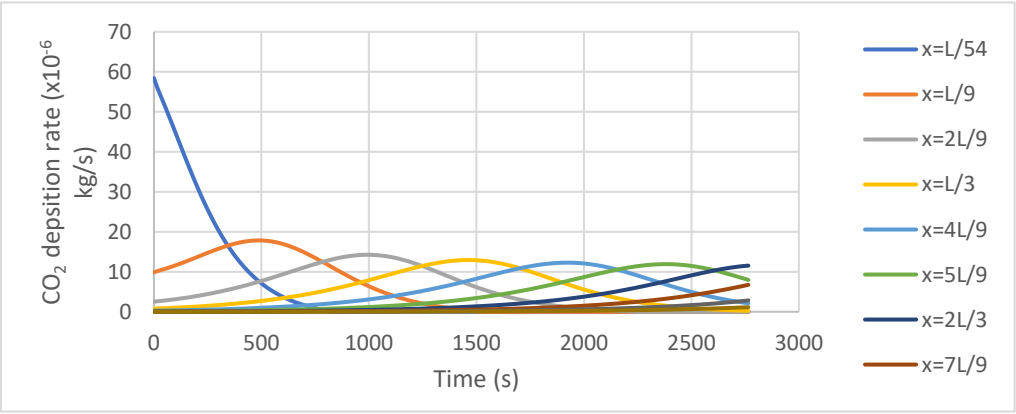

Figure F14: Taux de givrage de CO_2 le long du tube lors de la phase de givrage

Lorsque le flux de biogaz contenant du CO_2 entre en contact avec la surface froide, sa température diminue au fur et à mesure qu'il chauffe la surface. Lorsque la température de saturation du CO_2 à sa pression partielle dans le biogaz est atteinte, un dépôt se produit. Ce qui réduit la concentration de CO_2 dans le flux de biogaz pour le reste du tube, entraînant une diminution du taux de dépôt. Ce qui explique le retard de formation du givre dans les positions plus éloignées de l'entrée (Figure F14), par exemple à x=L/3 (ligne jaune), le pic de formation

de givre est atteint à 1450s. En passant à une autre position de l'entrée à x=5L/9, le pic est atteint à 2370s, la différence d'amplitude entre ces deux courbes est d'environ 7,5%.
Au fur et à mesure que le givre s'accumule et que moins de CO_2 se dépose près de l'entrée, le gradient de concentration devient plus élevé pour les positions les plus éloignées de l'entrée, augmentant alors le taux de givrage à ces positions. Au début, les dépôts ne se produisent pas près de la sortie du tube, car la température du biogaz a diminué par rapport à la température d'entrée et le gradient de concentration en CO_2 tend vers zéro. A l'exception de la courbe de la première position, les courbes de débits de CO_2 givré présentent la même forme « en dôme », mais sont décalées d'un intervalle de temps causé par l'accumulation de givre et la modification du gradient de concentration de CO_2 dans les positions précédentes.

3.3.2. Epaisseur du givre

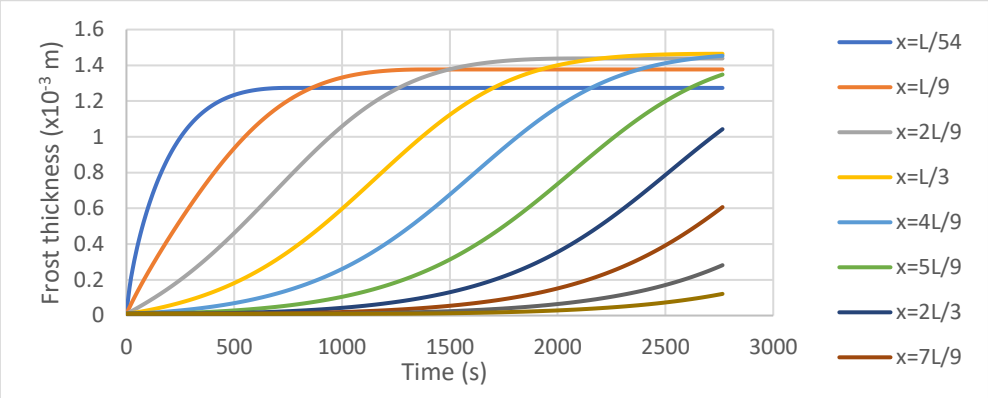

Figure F15: Epasseur du givre de CO_2 pour différentes positions le long du tube lors de la phase de givrage

L'épaisseur de givre augmente en fonction du taux de givrage de CO_2. On observe un retard d'augmentation de l'épaisseur du givre pour les positions les plus éloignées de l'entrée du tube. Le taux d'augmentation de l'épaisseur commence faible et s'accroît lorsque moins de givre se forme aux positions précédentes. Un équilibre de gradient de température et de concentration de CO_2 est atteint au niveau de l'interface flux de biogaz/surface du givre. Lorsque cet équilibre est atteint, le givrage s'arrête à cette position et l'épaisseur de givre y reste constante à sa valeur maximale.

3.3.3. Flux total de chaleur

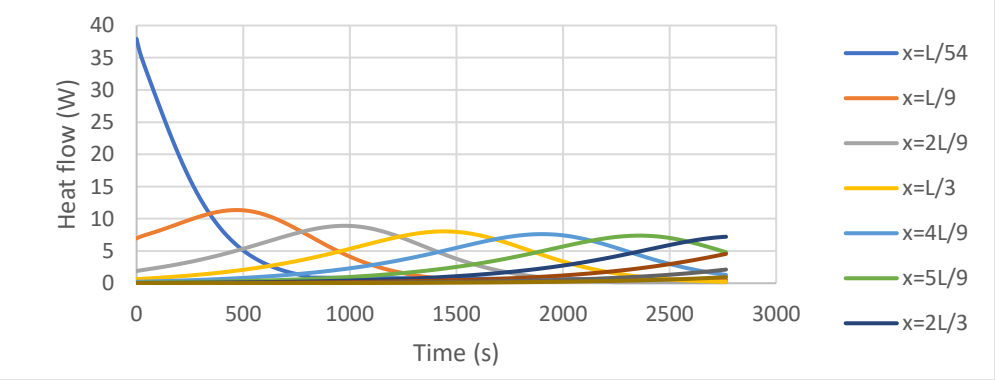

Figure F16: Flux total de chaleur pour différentes positions le long du tube lors de la phase de givrage

Le flux thermique total est divisé en 2 parties: flux thermique sensible et latent. Comme mentionné précédemment, la chaleur latente a plus d'impact que la chaleur sensible et est fonction du taux de givrage. Par conséquent, les courbes ont la même forme et le même intervalle de temps entre différentes positions dans le tube que le taux de givrage. L'amplitude du transfert de chaleur latente diminue légèrement entre deux positions consécutives (de la même manière que le taux de givrage). La figure F16 montre qu'après que le flux thermique ait atteint son maximum, il commence à diminuer jusqu'à atteindre une valeur presque nulle, ce qui est dû à la croissance du givre qui crée une barrière thermique limitant le taux de givrage et donc le flux de chaleur latente.

3.3.4. Température du tube

La température du tube augmente en raison du transfert de chaleur par convection avec le flux de biogaz et la chaleur latente du dépôt de CO_2.

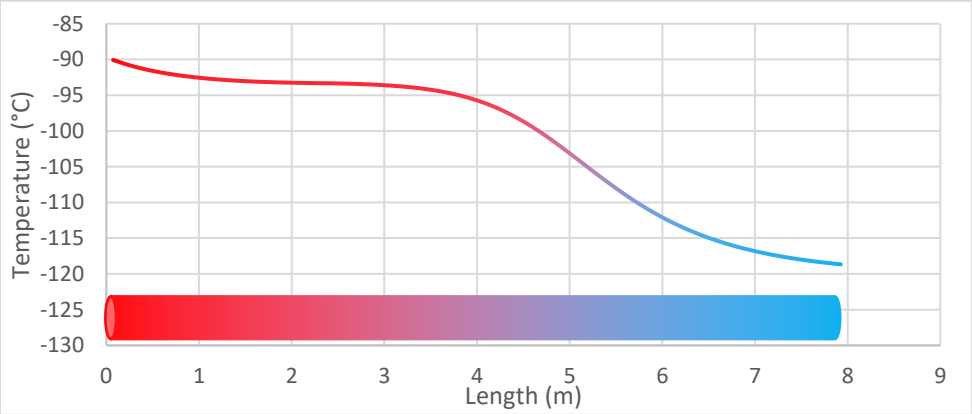

Figure F17: Température du tube à la fin du givrage de CO_2 à t=2674s

Dans le but d'épurer le biogaz et pour obtenir le biométhane, la concentration de CO_2 dans le flux de sortie ne devrait pas dépasser 2,5%. C'est la condition à laquelle la simulation est arrêtée à l'instant t = 2764s. Si le temps de simulation était plus long, le gradient de température final du tube entre l'entrée et la sortie aurait été plus faible. La température du tube à la fin de la phase de formation de givre est illustrée dans la Figure F17. Elle diminue pour les positions les plus éloignées de l'entrée de biogaz et cette température sera utilisée comme condition initiale pour la partie de dégivrage.

3.4. Cas d'étude: Epuration de biogaz et liquefaction de biomethane

i. Description du procédé

La Figure F18 décrit le système d'épuration et de liquéfaction du biogaz. Ce schéma a été développé et étudié sur AspenTech HYSYS V8.8. La concentration, la température et la pression des entrées et des sorties de chaque échangeur de chaleur peuvent être calculées ou indiquées par l'utilisateur en fonction des conditions de fonctionnement à prendre en compte en régime permanent. Il convient de noter que l'échangeur thermique pour givrage/dégivrage est en fait composé de deux échangeurs de chaleur fonctionnant alternativement en mode givrage et dégivrage (Figure F19).

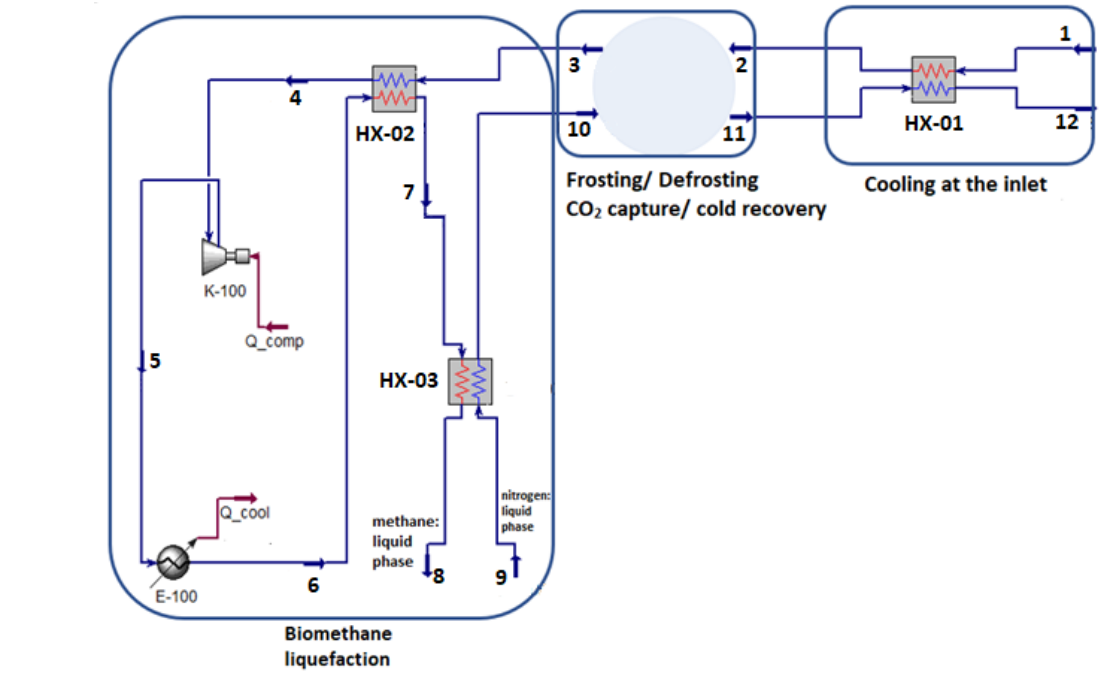

Figure F18: Le procédé proposé pour épuratoin et liquéfaction du biogaz

En «Phase 1», le biogaz passe par HX-A (Stream 2) tandis que l'injection de biogaz dans HX-B est interrompue. Les deux échangeurs de chaleur sont pré-refroidis aux conditions cryogéniques. Au fur et à mesure que le givre s'accumule, la température de l'échangeur thermique T_HX-A augmente. Le biogaz épuré quitte l'échangeur de chaleur avec un très faible pourcentage de CO_2 et principalement de méthane (> 97,5%) via « Stream 3 ». En «Phase 2», le même processus décrit dans la «Phase 1» a lieu, mais dans HX-B. Pendant ce temps, un flux gazeux (Stream 10) de N_2 passe à travers HX-A qui contient le givre CO_2 de «Phase 1». La température du HX-A augmente en raison du givrage. Le dégivrage par sublimation contrôlée diminue sa température.

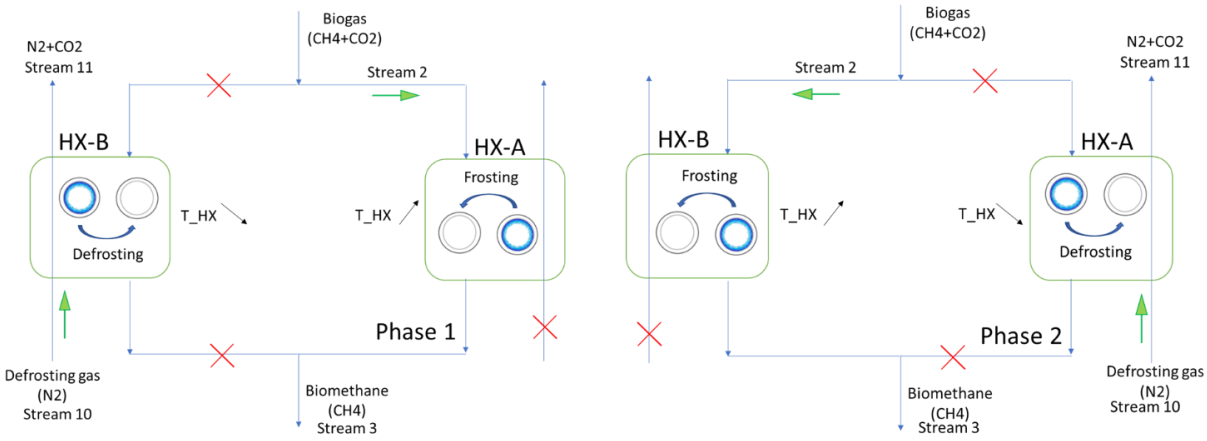

Figure F19: Alternance givrage/ dégivrage de CO_2dans les 2 HX du procédé

Revenant à la « Phase 1», HX-A est de retour aux conditions cryogéniques et il est possible de le réutiliser pour le givrage du CO_2. Le HX-B qui contient du givre de CO_2 subit une sublimation contrôlée par un flux de N_2 et sera refroidi. Le défi dans la récupération du froid proposé dans cette thèse est de trouver le débit massique exact et la température du flux de N_2 pour lesquels :

- l'échangeur de chaleur en mode dégivrage doit retrouver ses conditions cryogéniques initiales afin de répéter l'étape d'épuration du biogaz avec le même résultat et sans utiliser une source de refroidissement externe.
- le givrage est arrêté lorsque la concentration molaire en CO_2 contenu dans le biométhane à la sortie de la phase de givrage dépasse 2,5%. Afin d'optimiser l'ensemble du système de givrage/dégivrage et de récupération du froid, sans perdre de temps à attendre la fin d'une phase pour commencer l'autre, il est préférable que l'intervalle de temps nécessaire pour dégivrer complètement le CO_2 soit égal au temps de givrage.
- le même flux d'azote utilisé pour le dégivrage au CO_2 sera utilisé, dans une étape précédente, pour liquéfier le biométhane. L'étape compression + refroidissement de la Figure F18 devrait amener le biométhane jusqu'aux bonnes conditions pour sa liquéfaction avec l'énergie froide disponible dans le flux de N_2.

Le flux d'azote liquide (Stream 9) est aussi considéré comme donnée fixée par l'utilisateur. Les 2 flux (Stream 1,2,3,4,5,6,7,8 et Stream 9,10,11,12) sont à contre-courant; pour mieux comprendre le fonctionnement du système, il est divisé en trois parties :

• Pré-refroidissement du biogaz à l'entrée :

Dans cette partie, le biogaz (CH_4 et CO_2) est supposé déjà purifié de toute autre impureté que le méthane et du dioxyde de carbone (H_2S, COV ...). Il est refroidi par le mélange d'azote et de dioxyde de carbone provenant de l'étape de dégivrage. Cette partie peut être considérée comme une optimisation de la température d'entrée du biogaz.

• Givrage/Dégivrage:

La purification du biogaz est effectuée dans cette partie, le modèle est développé dans Dymola au lieu de ASPEN HYSYS® car il est plus compliqué de simuler un dépôt en phase solide en mode dynamique dans ce dernier. Lorsque tous les résultats Dymola sont obtenus, ils sont intégrés à Aspen HYSYS® via Excel VB. La partie relative au givrage a été bien détaillée au chapitre 2 et la partie portant sur le dégivrage sera détaillée au chapitre 4. Les modèles développés et la simulation ont pour objectif de prédire les conditions du biogaz à la sortie du HX après élimination du CO_2. Cela permettra d'optimiser le reste du système et de conduire à la liquéfaction du biométhane

• Liquéfaction du biométhane:

Après l'étape d'épuration du biogaz, du biométhane gazeux est obtenu. D'un point de vue économique, il est beaucoup plus rentable de transporter du méthane liquide chez le distributeur si la disponibilité des infrastructures du réseau de gaz est limitée. L'azote est utilisé pour liquéfier le biométhane.
Après la purification, le biométhane propre (Stream 3) est à très basse température. Il sera ensuite réchauffé par le même flux de méthane qui aurait subi une compression (Stream 6). Le chauffage du flux facilite le choix des compresseurs, même si cela représente une pénalité énergétique par rapport au travail de compression. Une température d'environ 200°C est atteinte avec une pression de 16 bars (une température plus basse est atteinte si la compression a lieu dans un système de compression + refroidissement à plusieurs étages). À la

sortie du compresseur, le méthane (Stream 5) est refroidi à température ambiante dans un échangeur de chaleur avec l'atmosphère. Le méthane (Stream 6) est davantage refroidi par le flux sortant du HX de givrage/dégivrage (Stream 3). Enfin, la phase de liquéfaction du méthane est atteinte.

ii. Calcul des débits massiques et thermiques

Comme on a mentionné précédemment, le méthane à haute pression nécessitera moins de puissance frigorifique pour être liquéfié. Cependant, les pressions de liquéfaction plus élevées nécessiteront une augmentation de la puissance de compression et, par conséquent, une augmentation des coûts. Puisque le biométhane comprimé est refroidi avec l'air ambiant, la température élevée résultant de la compression n'est pas un problème. D'autre part, comme l'azote liquide est utilisé pour liquéfier le méthane, la diminution de la puissance frigorifique nécessaire pour la liquéfaction nécessite un débit d'azote plus faible, ce qui peut affecter négativement la phase de dégivrage, comme nous le verrons plus tard. À la sortie du HX en givrage, on obtient le débit massique de biométhane, sa composition et sa température. La concentration molaire en méthane doit être supérieure à 97,5%, ce qui signifie que certains résidus de CO_2 sont encore présents. Il faut donc accorder une attention particulière à l'étape de la liquéfaction (hors cette étude) car la solidification du CO_2 restant pourrait causer des problèmes d'obstruction et blocage des tuyaux.

Calcul de chaque composant

Comme le montre Figure F18, le système est divisé en plusieurs flux: le biogaz qui subit l'épuration et l'azote qui agit comme source froide nécessaire à la liquéfaction du biométhane et dégivrage du CO_2. Le débit massique et la composition du mélange restent les mêmes, sauf aux sorties du HX de givrage et dégivrage.

- HX-01: dans cet échangeur de chaleur, le biogaz est refroidi par l'azote transportant le CO_2 sublimé issu de la phase de dégivrage. $T_{biogas,2}$ est fixé à -85°C, une température légèrement supérieure à la température de saturation du CO_2 à sa pression partielle dans le biogaz. $T_{n2+co2,11}$ dépend du débit initial de N_2 liquide compte tenu de la liquéfaction du biométhane et de la phase de dégivrage
- Echangeur givrage/dégivrage: le changement de phase se produit dans deux échangeurs de chaleur fonctionnant alternativement, le débit massique et la composition des flux entrant et sortant de cet échangeur de chaleur ne restent pas constants.

3- La partie concernant le givrage du CO_2 contenu dans le biogaz:

$$\dot{m}_{biogas,2}=\dot{m}_{ch4,3}+\dot{m}_{co2,3}+\dot{m}_{co2,frost} \quad \text{(F.3.1)}$$

4- La partie concernant le dégivrage du CO_2 par un flux de N_2:

$$\dot{m}_{n2+co2,11}=\dot{m}_{n2}+\dot{m}_{co2,defrost} \quad \text{(F.3.2)}$$

$\dot{m}_{co2,defrost}$ est le débit massique de CO_2 sublimé de l'échangeur de chaleur après le passage du flux de N_2. Le calcul de ce terme est effectué dans Dymola en utilisant le modèle du chapitre 4.

- HX-02: dans cet échangeur de chaleur, le courant froid sortant de la phase de givrage refroidit le méthane comprimé avant sa liquéfaction. Tous les débits massiques sont égaux car aucune matière n'est ajoutée ou retirée. $T_{biomethane,3}$ est calculée sur Dymola, $T_{biomethane,6}$ est la température à la sortie de l'échangeur de chaleur libérant de la chaleur vers l'atmosphère, elle est donc égale à la température ambiante. $T_{biomethane,7}$ est la température du biométhane juste avant sa liquéfaction. Elle affecte le débit de N_2 nécessaire pour réaliser cette étape.
- K-100: le compresseur augmente la pression du biométhane pour faciliter sa liquéfaction. L'augmentation de la pression dépend du débit de N_2 liquide disponible pour la phase de liquéfaction, puis pour la phase de dégivrage couvrant ainsi tous les critères mentionnés précédemment en ce qui concerne le temps de dégivrage et la température finale de l'échangeur de chaleur de givrage/dégivrage.
- E-100: cet échangeur de chaleur rejette la chaleur vers l'atmosphère pour réduire la température du biométhane comprimé jusqu'à la température ambiante.
- HX-03: dans cet échangeur de chaleur, le biométhane est liquéfié. Deux flux traversent HX-03: biométhane sous pression et azote liquide. Le biométhane qui est refroidi dans le HX-02 subit une liquéfaction pendant que le N_2 liquide s'évapore.

Conclusion

Une étude de sensibilité a été menée sur le givrage du CO_2 contenu dans le biogaz et les résultats montrent que, pour des concentrations de CO_2 plus élevées, la croissance du givre est plus rapide en épaisseur et en masse volumique. Lorsque la température de la plaque a été réduite, l'épaisseur a augmenté en raison de la diminution de la concentration de vapeur de saturation en CO_2 à la surface du givre, mais la masse volumique a diminué en raison de la diminution de la concentration en CO_2 dans la couche de givre. En outre, l'augmentation de la température d'entrée du biogaz réduit légèrement l'épaisseur de givre sans presque affecter la masse volumique. D'autre part, les résultats concernant le givrage du CO_2 à partir de biogaz ont montré comment des concentrations en CO_2 plus élevées augmentaient le transfert de chaleur, en particulier à l'interface entre givre/biogaz. La température de la plaque et la température d'entrée ont moins d'effet sur le transfert de chaleur que la concentration de CO_2.

Une comparaison entre la configuration de la plaque et celle du tube lors du givrage de CO_2 a montré que le tube présente une meilleure configuration en termes d'accessibilité et de transfert de chaleur pour un temps donné, mais que pour des périodes de givrage plus importantes, la plaque est le meilleur choix car sa surface d'échange reste constante. La formation de givre de CO_2 en longueur du tube a été étudiée en fixant la concentration de CH_4 en sortie. Les résultats montrent que les dépôts de givre présentent un certain retard aux positions plus loin de l'entrée.

Un système d'épuration de biogaz et de liquéfaction de biométhane a été présenté et tous ses composants et ses calculs de débit ont été détaillés. Le procédé utilise deux échangeurs de chaleur fonctionnant simultanément et alternativement en givrage et dégivrage. Le flux de N_2 qui est utilisé pour la liquéfaction du biométhane sera ultérieurement utilisé pour la « sublimation contrôlée» et la récupération du froid.

Chapter 4: Controlled sublimation CO_2 frost and cold recovery

Introduction

Many defrosting methods can be found in the literature. However, unlike the frosting phenomenon, not many defrosting models were developed even for the case of water ice. Usually it is not very interesting to study the defrosting process as much as getting rid of the solid deposit which usually affects the system negatively. In most defrosting studies, the focus is mainly on the heat needed to defrost. Also, most of the defrosting techniques heat the surface where frost is formed, which renders impossible the recovery of cold.

One of the objectives of this thesis is the study of CO_2 phase changes from gas to solid and vice-versa. In chapter 2, the deposition of CO_2 contained in a binary mixture (N_2 +CO_2) over a cold surface was studied and modelled. In chapter 3, a sensitivity study of the deposition of CO_2 from biogas was conducted. In this chapter, solid to gas phase change of CO_2 will be studied and modelled. Contrary to typical defrosting methods, the CO_2 will be sublimated by controlled sublimation whilst coming into contact with a cold third gas. As it was explained in chapter 1, this method allows the recovery of the cold stored in the CO_2 deposit in order to use it for upgrading more biogas in a semi-batch mode. Results of CO_2 defrosting and cold recovery will be presented and are integrated in the whole process of biogas upgrading and liquefaction in order to calculate the efficiency increase by adding the controlled sublimation of CO_2 to the process.

4.1. Defrosting methods

The cryogenic removal of CO_2 results in a heat exchanger containing solid CO_2 frost that must be removed. As it was mentioned in Chapter 1, CO_2 frost will be removed by introducing a tertiary cold gas that will defrost CO_2 while cooling the system by the same concept as evaporative cooling. In order to assess the relevance of the controlled sublimation, it is interesting to know what other options of defrosting are available in order to compare them with what was suggested. Most of the defrosting techniques were conceived for defrosting ice formed in domestic and industrial refrigeration applications. Since the working pressure in the evaporator of conventional refrigeration cycle is usually above the atmospheric pressure, ice is not sublimated but rather melted and drained or evaporated.

A detailed mathematical model for defrosting a multi-row tubes and fins evaporator was constructed by Dopazo et al. [107]. They separated the defrosting phenomenon into six stages: preheating, tube frost melting, fin frost melting, air presence, tube-fin water film, dry heating. They used the model to study the effect of the refrigerant inlet temperature and mass flow rate. As the inlet temperature increases, the energy delivered by the refrigerant and the defrost time increase too until the temperature reaches a certain value (295°C in the case of Dopazo et al.) at which the energy and defrosting time start decreasing. For increasing mass flow rate, energy delivered from the refrigerant and defrosting time both decreases.

Refrigeration cycles that operate at temperatures below water's freezing temperature (0°C) might experience frost formation on the tubes and fins of the evaporator. The performance of the system degrades as frost accumulates on the heat exchanger surface [108], it acts as an insulator between the refrigerant circulating and the environment from which heat will be removed. Therefore, a solution must be found in order to remove the frost from the heat exchanging surface. Three main defrosting methods are used: the on-off defrosting, electrical defrosting and gas defrost [109]. These will be discussed later. Other methods include the use of desiccants as dehumidifiers which consume less energy than conventional methods; they increase the system efficiency by reducing the water vapour concentration in the system.

The two main challenges in the defrosting cycles are defining the optimal defrosting time with respect to power consumption and the heat passed on to the refrigerant during the defrosting phase [110].

4.1.1. On-Off defrost

The on-off cycle (Figure 74) is as simple as its name. When frost accumulates and needs to be removed, the refrigeration system is turned off and no more refrigerant enter the evaporator. When all the frost melts, the system is turned back on. The evaporator might be at a temperature below 0°C but the air in the refrigerated space is usually at a higher temperature. The latter keeps on circulating in the evaporator, heating it up as it passes. Infiltration of outside air into the refrigerated space also rises the temperature thus accelerating the defrosting time. A time clock can be used to start and stop the defrosting cycle. When the clock is activated, the compressor is cycled off and the liquid line solenoid valve is activated to prevent the circulation of the refrigerant into the evaporator. This method is more suited for defrosting in medium temperatures and not very low temperatures. If the air present in the refrigerated medium is at a temperature below water's freezing point, defrosting takes much longer depending on the infiltrated air. The advantage of the on-off cycle is its simplicity and no additional power is needed to defrost. It is also possible to replace the time clock by a manual actuator.

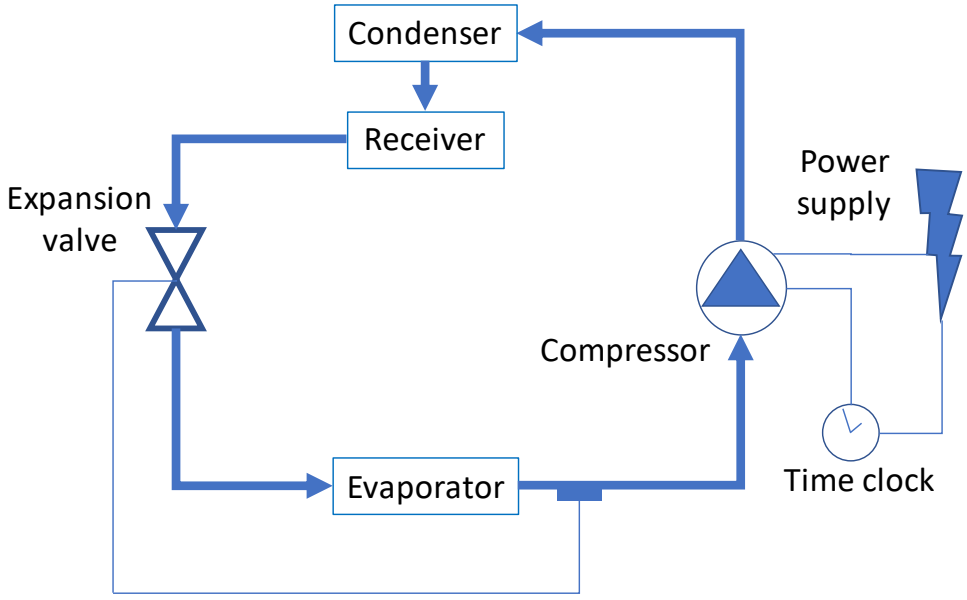

Figure 74: Timed on-off defrost cycle (based on [111])

4.1.2. Electric defrost

Electric defrost (Figure 75) can be used in medium and low temperature application. Electrical resistance heating rods are embedded in the evaporators and when frost accumulation surpasses the limit, an electrical current pass through the resistive heater. The added heat source rises the temperature of the heat exchanger which induces defrosting. When defrosting starts, three things happen:

- the liquid line solenoid valve closes which prevents the passage of more refrigerant flow into the evaporator
- power is supplied to the electrical resistance which starts to heat raising the temperature of the evaporator
- no more power is supplied to the fans in the evaporator. Circulating air might transport heat thus reducing the amount given to the frost.

The power is cut off the heaters after a certain defrosting time or when a certain temperature of the system is achieved. A time interval is given for the melted frost to circulate into a drain pan. Electric defrosting is also a simple defrosting method: electrical is supplied, heat is created, the frost melts. It presents a shorter time of defrosting than on-off cycle but it requires an outside energy source. Another disadvantage for this type of defrosting is the cost of the heating equipment and its setup.

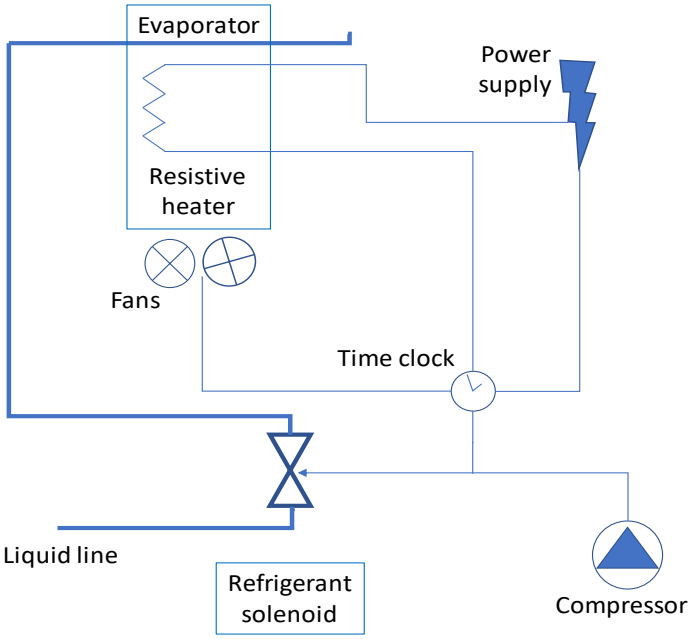

Figure 75: Electric defrost cycle (based on [111])

4.1.3. Gas defrost

This method is the most used for defrosting in industrial refrigeration systems[112]. Gas defrost uses the heat contained in the discharge vapour from the compressor to accomplish defrosting. No more refrigerant pass through the evaporator as a portion (or the totality) of the hot vapour is redirected into the evaporator to melt the frost. The air present in the refrigerated medium is heated and could cause major temperature fluctuations decreasing the system's efficiency [107].

Using a single evaporator is one of the drawbacks when using the gas defrost method because any meaningful load on the compressor will be eliminated [113]. Either a false load must be added to the compressor or the defrosting time must be extremely shortened. No refrigerant can pass through the evaporator because it acts like a condenser so no refrigeration can take place. Several configurations can be used for gas defrost:

- Three pipe: in this method, a bypass connects the compressor discharge to the evaporator's inlet. In the defrost cycle, the hot gas will pass through this bypass into the cold evaporator. The hot gas condenses on the evaporator surface and its heat melts the frost. A reservoir is required for the liquid otherwise it will enter the compressor. The refrigerant in liquid form cannot enter the compressor and the refrigeration cycle cannot continue.
  Figure 76 shows the defrosting cycle as described by Reindl et al. [109]. The solenoid valve is closed in order to prevent the refrigerant from entering the evaporator. A time delay is given for the remaining refrigerant liquid to evaporate before opening the hot gas valve. A hot gas stream at high pressure and high temperature first passes through the drain pan which will serve for draining the frost melt. As hot gas passes through the coil of the evaporator, frost melts and the hot gas condenses by losing its latent heat. The pressure of the refrigerant in the coil increases until the control valve opens allowing the refrigerant to exit the evaporator.

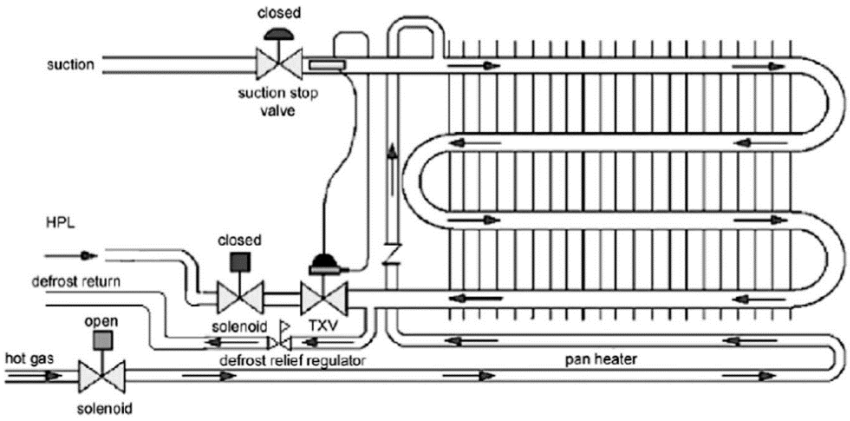

Figure 76: An evaporator in a hot-gas three pipe defrost process [109]

A modification of the "Three pipe" method is the Kramer Thermobank in which the high temperature discharge vapour limited availability is solved. In a single evaporator, the liquid resulting from the condensation and the melting should all be evaporated if refrigeration cycle is to be resumed. A heat exchanger containing static glycol is used as a heat source to vaporize the liquid from the evaporator before it re-enters the compressor thus resuming the refrigeration cycle.

- Reverse cycle - Hot gas: a reversed refrigeration cycle acts like a heat pump. In any direct expansion refrigeration system, the condenser provides the liquid refrigerant. Using the reverse cycle for defrosting requires a four-way reversing valve (Figure 77).This component allows the refrigerant flow to be reversed when defrost starts. The vapour

discharged from the compressor circulates backwards through the evaporator. The frost will evaporate as the hot gas condenses. The liquid resulting from the frost and the water vapour condensation passes through an expansion apparatus and is vaporized. Continuing in the reverse cycle, the vapour passes backwards into the condenser and returns to the compressor at low pressure to close the reverse cycle.

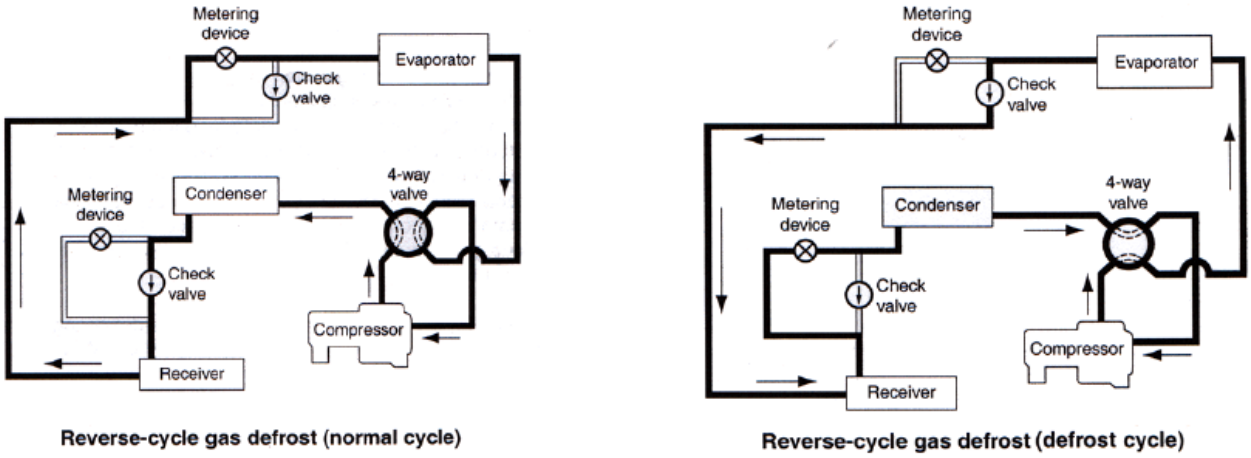

Figure 77: Reverse cycle gas defrost in refrigeration and defrosting cycle[111]

Gas defrost is more expensive to install than electric or on-off cycle but its efficiency and COP are higher because the hot gases passes through the whole channel unlike the resistive heat which is concentrated at the location of the heaters. A comparative study was led by Cho et al. [108] between the performances of an on-off cycle and a hot gas bypass defrosting system. The comparison was applied on a cycle with three evaporators. The temperature of the evaporator remained constant in the case of hot gas defrosting unlike on-off cycling where temperature fluctuated (Figure 78.a). Also, Cho et al. found that the defrosting time for hot gas cycles is much less than that of on-off cycle (Figure 78.b).

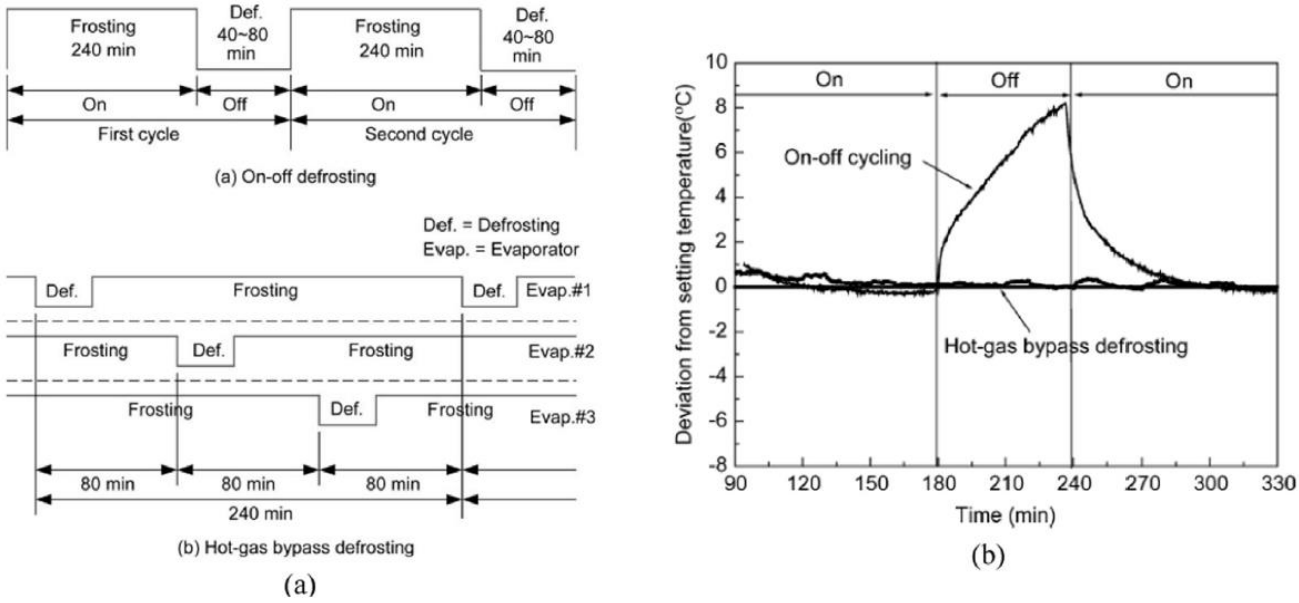

Figure 78: Comparison between on-off cycle and hot gas defrost cycle, a) comparison of frosting/defrosting time[108], b) comparison of cycle temeprature vs time[108]

4.2. Sublimation models

When moist air comes into contact with the cold surface of a heat exchanger, at a temperature below 0°C, water vapour contained in the air will deposit. It is necessary to remove the frost otherwise the efficiency of the heat exchanger will degrade. Usual defrost methods melt the frost and drain the liquid or evaporate it. Since most of the frosting cases were applied to water vapour, considering defrosting by sublimation was less interesting since the pressure must be below atmospheric.

One of the applications of sublimation in real life situations is freeze-drying. This process is used for dehydration of a frozen product, by sublimation at low temperature and low pressure. It is usually used for drying bioproducts particularly food. At low temperatures, no liquid water is present in the product and if the moisture is removed by sublimation then no liquid will form during dehydration. This puts a stop on deterioration and microbiological reactions resulting in a final product of the highest quality without altering its shape and structure [114].

Lin [115] studied the sublimation of uniformly distributed frozen moisture in a porous rigid solid. The solid is put under very low pressure conditions in such a way that the only pressure acting on it is the vapour pressure of the moisture. This is considered as the environment pressure of the system which will remain constant. Similarly to the concept of cryogenic solid-cooling described in chapter 1, the sublimation process takes place at constant temperature which corresponds to the constant vapour pressure of the moisture.
In his study, Lin considered the vapour as an ideal gas. The porous body is initially below the sublimation temperature and the frozen moisture is uniformly distributed. He divided the body into two parts: the frozen region below the sublimation front where there is no moisture movement, and the vapour region above the sublimation front where heat and mass transfer occur. An important parameter in Lin's model was the Luikov number Lu [116] which calculates the ratio of moisture mass diffusivity to thermal diffusivity of the vapour region. The increase in the value of Lu means more moisture can diffuse from the phase interface therefore less concentration gradient is needed to induce sublimation.

Inaba and Imai conducted a study on the sublimation of a horizontal frost layer under forced convection and radiant heat [117]. In typical frost melting methods like the ones mentioned above, refrigeration cycle must be stopped because of liquid presence, thus lowering the efficiency of the system. On the other hand, if defrost is carried on by sublimation, no liquid material appears. In order to sublimate the frost, the heat energy provided must keep the system at a temperature below the triple point. The thermal conductivity of a frost layer is low resulting in a high thermal resistance; therefore, heating the frost from below is not very effective if the objective is sublimating it.
Inaba and Imai conducted an experiment on a horizontal flat plate with a pre-existing frost layer. The frost layer is of equal thickness and distribution over the plate. They compared several radiant heat intensities for the same defrosting time. They showed how the frost thickness decreases as it sublimates. At high radiant heat, the frost melts (Figure 79).

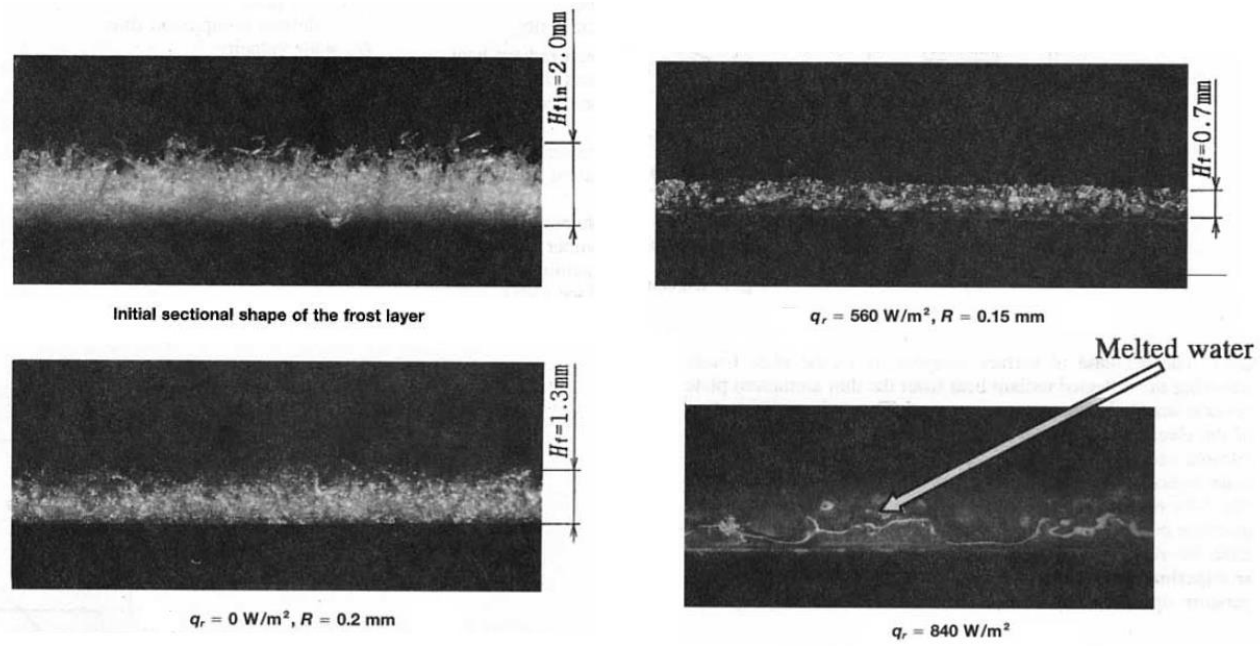

Figure 79: Frost sublimaton evolution for different radiant heat intensities[117]

Sublimation of snow

Unlike evaporation, not many real-life situations include sublimation. One of them, is the sublimation of snow in the poles by the winds flowing. When ice particles present on the snow surface are transported by strong winds, they undergo sublimation and are diffused into the wind if it is not saturated in water vapour [118]. The water vapour concentration in the air is equivalent to its partial pressure. When the water vapour concentration in the air is lower than that at the snow surface, sublimation occurs.

Schmidt (1991) assumed that an equilibrium exists between the latent, convective and radiative heat transfer to a snow particle and the convective transport and diffusion of the water vapour particles in the air stream. A sublimation model based on thermodynamic equilibrium can then be developed. The mass rate of sublimation depends on the water vapour concentration gradient between the snow surface and the air. Some authors use density gradient instead of concentration [119] but since the same control volume is assumed, the two entities are equal.

Pomeroy et al. formulated the rate of water vapour sublimated into air dm/dt considering a circular ice particle of radius R. The mass flow rate is function of the density gradient (or concentration) of water vapour contained in air and at the particle's surface, the diffusivity of water in air D and the Sherwood number Sh to take into account the turbulent transfer of water vapour.

$$\frac{dm}{dt} = 2.\pi.R.D.Sh.(\rho_{w,air} - \rho_{w,part\_surf}) \quad (4.1)$$

Pomeroy et al. also stated that the sublimation rate requires a certain energy that is provided by convective heating as follows:

$$Lsv.\frac{dm}{dt} = 2.\pi.R.k_{air}.Nu.(T_{air} - T_{part\_surf}) \quad (4.2)$$

Where Lsv is the latent heat of sublimation, R is the radius as previously stated, k_{air} is the thermal conductivity of air, the Nusselt number Nu takes into account the heat transfer turbulence in the system. The temperature gradient is between the air and the ice particle's surface.

Looking back at the formulas presented in the deposition model in Chapter 2, a certain resemblance is observed. Temperature and concentration gradients are the main driving forces for solid-vapor phase transition, whether it is water vapour or carbon dioxide.

4.3. CO_2 defrosting model

Cryogenic removal of CO_2 from biogas results in a cold solid deposit that must be removed for further frosting on the cold surface. Many options are available: turning off the system or heating the other side of the surface where CO_2 has deposited using an electric resistance or a hot fluid. If the volume containing the CO_2 frost is sealed, its pressure increases and it will be possible to obtain liquid carbon dioxide. The frost can also be sublimated and expelled from the system as exhaust gas.

Another option of defrosting presents itself in what can be called "controlled sublimation". It follows the same principle as controlled sublimation that was discussed in chapter 1, but instead of having a liquid that is being vaporized, a solid deposit is being sublimated. This is not a common physical phenomenon at atmospheric pressure but this is one of the characteristics of CO_2 (Figure 7). Controlled sublimation requires an outside gas that will come into contact with the frost. If the defrosting gas is hot, its sensible heat will increase the frost's temperature to the point of sublimation. This will remove the CO_2 frost and will cool the defrosting gas but the CO_2 is no longer pure to be reused. Also, the final HX temperature will not be cold enough to be reused for further cryogenic removal of CO_2 from biogas.

One of the major relevant points about defrosting using controlled sublimation is that the gas used to defrost can be colder than the frost and still sublimate it. As the cold defrosting gas passes through the control volume containing the frost, the CO_2 vapour pressure will diffuse in it and get transported to the outlet of the heat exchanger. The CO_2 frost must recover the loss of vapour pressure and will sublimate allowing more CO_2 vapour to be diffused into the defrosting gas and get removed from the heat exchanger. The CO_2 concentration gradient between the frost surface and incoming defrosting gas becomes the driving force that will sublimate the CO_2 frost. No cold from the CO_2 will be wasted as sensible heat towards the passing gas. As the CO_2 sublimates, it will require a heat source to maintain its saturation pressure at its surface temperature. Therefore, the CO_2 frost as well as the surface over which it deposited will cool down, thus recovering the cold that was stored in the CO_2 frost.

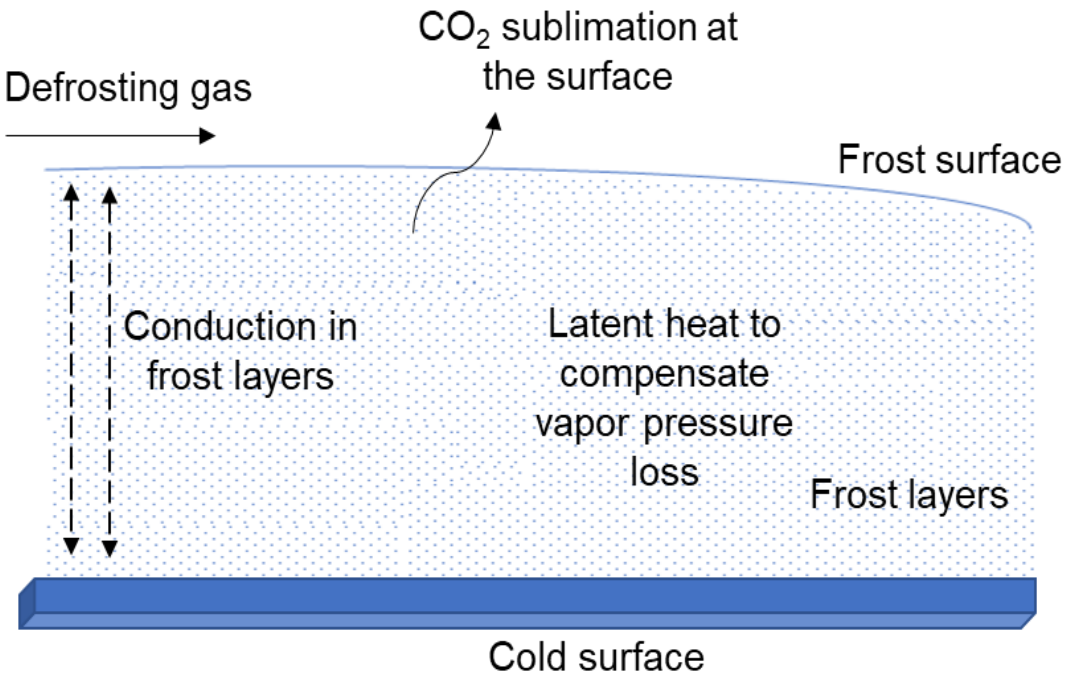

Figure 80: Description of heat and mass transfers during CO_2 deposition

Reviewing the simulation results for CO_2 deposition either from a binary mixture either with nitrogen or methane, it is clear that the density of the CO_2 frost doesn't reach the density of solid CO_2 which means that the frost presents a certain level of porosity. First, the defrosting model will be presented considering the frost as porous medium similarly to the case of frosting. But since the CO_2 frost layer will get colder as it evaporates, its density will increase and it will become a solid block with no pores. If the porosity of the frost layer was low enough it can be assumed from the beginning that the CO_2 is completely solid (rather than a porous medium). This assumption reduces the complexity of the problem as it shall be later explained.

4.3.1. Defrosting inside the frost layer

The equations governing the defrosting phenomenon by introducing a third gas are similar to those of the deposition model with some changes in the direction of mass and heat flows. Figure 81 shows the heat and mass transfers from the frost layer towards the defrosting gas, it is very similar to Figure 27 describing the frosting of CO_2 but the arrows are reversed meaning that the CO_2 defrosted leaves the solid mass into the passing defrosting gas. Heat transfer by conduction inside the frost layers goes from the layers closest to the cold surface to the layer closest to the interface with the gas flow. Heat is transferred to compensate the saturation vapour pressure loss by sublimating more solid CO_2.

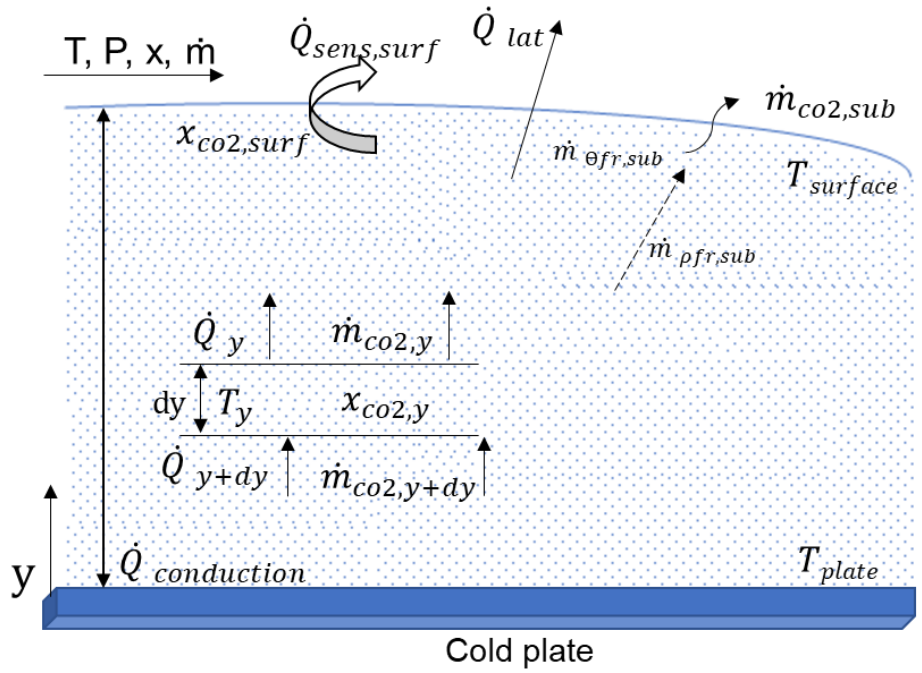

Figure 81: Energy and mass balance on the surface and inside the frost during controlled sublimation

As it was mentioned before, if the temperature of the defrosting gas is high, sensible heat transfer from the gas to the frost might sublimate the latter without recovering the cold stored in the frost layer. On the other hand, if the temperature of the defrosting gas is too low, sensible heat from the frost to the gas will lower the temperature of the CO_2 frost layer. The temperature decrease of the frost layer decreases the saturation vapour concentration at the frost surface, therefore reducing the concentration gradient which is the driving force of the controlled sublimation. Mass transfer from the frost layer towards the gas will decrease, which increases the defrosting time. The optimal temperature for the defrosting gas is to be equal, or close, to that of the frost surface.

Similarly to the case of deposition of CO_2 discussed in chapter 2, the model divides the system into 3 parts: the defrosting gas, the frost-bulk interface, inside the frost layer and cold recovery. Since nitrogen will be used to liquefy the biomethane obtained from the frosting phase, it can be used as the defrosting gas since it will also be at a temperature lower than that of the frost.

4.3.2. Main assumptions

The main assumptions considered in the modelling of defrosting are very similar to those used for the deposition model:

- The initial conditions will be equivalent to the final conditions of the deposition model. A stop point for the frosting simulation is considered, it can depend on the purity of methane obtained from the frosting phase; this point will be discussed when presenting the results.

- Only the phenomenon of sublimation is considered. CO_2 does not pass through a liquid phase, it goes directly from solid to gas since the system operates at atmospheric pressure.

- All gases are considered ideal gases.

- The gas and solid temperature at the defrosting gas-frost interface is considered equal.

- The total pressure is considered constant in the volume of nitrogen / frost; pressure drop is neglected.

- The sublimation of the frost changes the height of the hydraulic diameter. This makes vary the Reynolds number (heat and mass transfer).

i. The defrosting gas

Since the temperature of the CO_2 frost will decrease, the temperature of the defrosting gas should be lower than that of the frost. The aim is to reduce sensible heat transfer as much as possible. It is possible that the convective heat transfer between the frost surface and the defrosting gas reverses signs when the frost surface becomes cooler than the defrosting gas due to the frost sublimation. The sensible heat exchanged by convection between the flue gases and the frost surface over the exchange surface is calculated as follows:

$$\dot{q}_{sens} = h_c \times (T_{fr,surf} - T_{defrosting\ gas}) \quad (4.3)$$

The sublimated CO_2 mass flow from the frost layer towards the defrosting gas $\dot{m}_{co2,sub}$ can be expressed by the analogy between heat and mass transfers:

$$\dot{m}_{co2,sub} = -h_m \times \rho_{defrosting\ gas} \times (x_{fr,surf} - x_{n2/co2}) \quad (4.4)$$

The interface between the defrosting gas (N_2) and the frost surface is considered at thermodynamic equilibrium. The frost surface temperature and the CO_2 concentration are related by psychrometry (Figure 25).

ii. The frost-bulk interface

Similarly to deposition, since the frost layer is considered a porous medium, the mass flow of sublimated CO_2 is represented by two terms. The first $\dot{m}_{\rho,frost}$ takes into consideration sublimation inside the frost layer. The second $\dot{m}_{\theta,frost}$ corresponds to the surface sublimation. These are the same terms used in the frosting model because they affect the frost the same way. The total mass flow of sublimated CO_2 is expressed as follows:

$$\dot{m}_{co2,sub} = \dot{m}_{\rho frost,surf} + \dot{m}_{\theta frost} \quad (4.5)$$

The equations for these two mass flows are the same to those used in the deposition model but the direction of the flux is reversed. The concentration gradient will be negative when going from the frost-gas interface into the frost layers. All the mass flows are negative since CO_2 is being sublimated.

At the frost surface, even if the aim is to eliminate it but convective heat transfer occurs at the interface with the flue gases. Latent heat transfer is responsible for the CO_2 sublimation. As CO_2 evaporates at the surface, the frost is cooled because it is being used as a heat source to compensate the vapour pressure loss. The surface of the heat exchanger will be cooled by conduction inside the frost layers. The total heat transfer at the frost surface is described by the following equations:

$$\dot{q}_{tot,surf} = \dot{q}_{sens} + \dot{q}_{lat,surf} \quad (4.6)$$

$$\dot{q}_{lat,surf} = \dot{m}_{\theta frost} \times L_{sv} \quad (4.7)$$

$$\dot{q}_{cond,surf} = k_{frost} \times \left(\frac{dT_{fr}}{dy}\right)_{y=y,surf} \quad (4.8)$$

The energy balance at the frost surface is expressed by:

$$\dot{q}_{tot,surf} = \dot{q}_{cond,surf} \quad (4.9)$$

iii. Inside the frost layer

Inside the frost layer, sublimated CO_2 mass flow $\dot{m}_{\rho frost}$ is also obtained by Fick's law for the diffusion of matter. But unlike the deposition model, the term $\frac{dx}{dy}$ will be positive when going towards the frost surface:

$$\dot{m}_{\rho frost} = -D_{eff} \times \rho_{defrosting\ gas} . \frac{dx}{dy} \quad (4.10)$$

The frost densification will be a negative term since frost will be sublimated inside the frost layers. It can be expressed as a term of porosification β_{co2}. It is calculated as follows:

$$\beta_{co2} = -\frac{d\dot{m}_{\rho frost}}{dy} \quad (4.11)$$

The variation of the frost density can then be calculated since β_{co2} represents the porosification of the frost layer:

$$\frac{d\rho_{frost}}{dt} = \beta_{co2} \quad (4.12)$$

Using Fourier's law, the conductive heat transfer inside the frost layer can be calculated as follows:

$$\dot{q}_{cond} = k_{frost} \times \frac{dT_{fr}}{dy} \quad (4.13)$$

The balance between the conductive heat transfer and the CO_2 sublimation rate inside the frost layer can be written as follows:

$$\frac{d\dot{q}_{cond}}{dy} = -\beta_{co2} \times L_{sv} \quad (4.14)$$

Similarly to the frost surface, thermodynamic equilibrium between the defrosting gas and the CO_2 frost is considered inside the frost layer.

iv. Cold recovery

As CO_2 sublimates, the solid phase and metal (plate or tube) temperature decreases. The surface upon which frost is formed will be cooled by conduction through the frost layer. This temperature decrease can be used to recover the cold that was stored in the CO_2 frost. A hot gas can be introduced to the heat exchanger without coming into direct contact with the CO_2 frost; the hot gas might lower the efficiency of the heat recovery since it will heat the frost layer but it might speed up defrosting time which is a crucial criteria when defrosting. Another option is leaving the heat exchanger as a heat capacitor as it was done previously in

chapter 3. If the heat exchanger is used as a heat capacitor, its temperature will increase in the deposition phase then it will decrease theoretically to its same initial temperature after complete defrosting. As the heat exchanger surface cools, it becomes harder to sublimate since the CO_2 saturation vapour concentration decreases. As the defrosting gas passes and sublimation occurs, the frost and the heat capacitor are cooled. The heat flux from the heat capacitor towards the frost layer is expressed as follows:

$$\dot{q} = -m_{heat\ capacitor} \times c_{heat\ capacitor} \times \frac{dT_{heat\ capacitor}}{dt} \quad (4.15)$$

4.3.3. Defrosting at the surface

When solid CO_2 is formed, it presents a porous texture. If the CO_2 is solidified from its liquid form or at very low temperatures, it becomes a solid with no pores. The defrosting gas will not be able to pass through the frost, and the sublimation will only occur at the surface since no heat nor CO_2 diffusion into N_2 will occur except at the surface. As for the model, the main difference when adding this assumption is that the mass flow of sublimated CO_2 will not be divided into 2 parts. Sublimation only occurs at the frost surface. The frost layers are all considered as complete solids with no pores. All equations used in the part "inside the frost layer" will not be used and no porosification term exists. Heat transfers will remain the same. This assumption might be used if and only if the porosity of the frost layer during the deposition phase is low. Nevertheless, this is a conservative assumption, as porosity fosters sublimation as heat exchange surface increases with porosity, roughness and tortuosity of solid.

4.4. Controlled sublimation results

A N_2 gas flow is introduced in counter-current to the HX where CO_2 frost had deposited. The initial conditions of the CO_2 frost are the final values found in chapter 3 in figures 57, 58, 66, 67. In this part, a reference N_2 flow will be introduced with $\dot{m}_{n2} = 1.66 \times 10^{-3} kg/s\ (per\ tube)$ and $T_{in,n2} = -120°C$. A sensitivity study will be conducted for optimizing the defrosting phase. The initial conditions of the defrosting phase are the final conditions of the frosting phase at time t=2764s.

Figure 82 shows the frost thickness decrease as the CO_2 frost sublimates. The position x is still considered 0 at the inlet of the biogas similarly to chapter 3; x=L is the position at the N_2 inlet. As it was shown before in Figure 57, the frost accumulates heterogeneously along the tube. At x=L, the least amount of frost is formed and the temperature is the lowest. On the other hand, at positions near the N_2 outlet, more frost has been accumulated and the temperature is the highest (see Figure 61). As the N_2 flows inside the tube, it will be exposed to convective heat transfer from the frost. The inlet temperature of the N_2 is lower than the temperature of the frost at any position in the tube. Therefore, the N_2 flow will heat up as it flows along the tube. Since the final objective of the defrost is to return the tube to its initial conditions to launch a second frosting phase, a part of its temperature decrease will be provided by convection with the cold N_2 flow. The quantity of CO_2 sublimated depends on the frost temperature and the CO_2 partial pressure difference between the frost and the N_2 flow. As more CO_2 is diffused into the N_2 flow, less sublimation should occur. However, since the N_2 is heated and the CO_2 frost is

at a higher temperature at positions further from the N_2 inlet sublimation still occurs at these positions at time t=0s.

4.4.1. Frost thickness and mass decrease

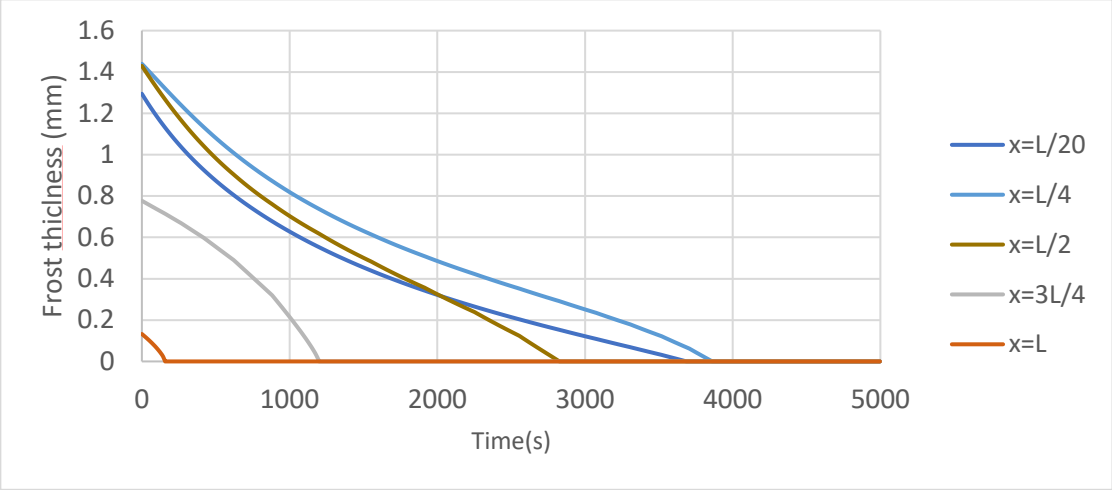

Figure 82: Frost thickness for different positions along the tube during CO_2 defrosting

Figure 82 shows different shapes of frost thickness decrease. At the middle of the tube, frost decrease is close to being linear, closer to the N_2 inlet it becomes convex and closer to the N_2 outlet it becomes more concave. These different rates of sublimation are caused by many factors:

- As the frost cools down, its vapour pressure decreases which leads to a decrease in sublimation rate. The frost still sublimates but in lower quantities.
- The initial density inside the frost layers affects its sublimation rate. The frost density near x=L are low which results in a faster sublimation since more N_2 can be diffused into the frost.

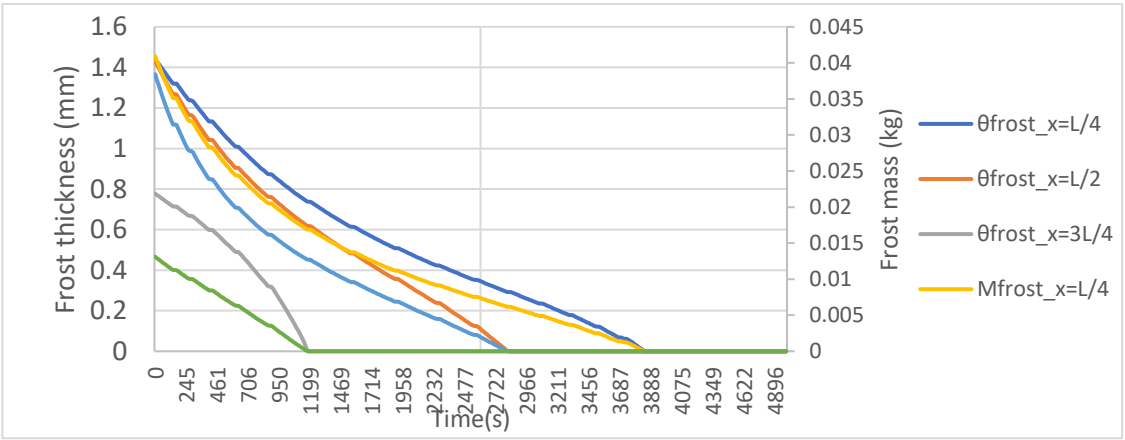

Figure 83: Frost thickness and mass decrease for different positions along the tube during CO_2 defosting

Figure 83 shows how the frost mass and thickness decrease and the different time intervals for complete defrosting at different positions. As it was previously mentioned, the initial conditions of the defrosting phase in terms of frost thickness and mass as well as the density and

temperature of the frost layers are the final conditions of the frosting phase at time t=2764s. The most important part in these graphs is knowing the defrosting time. N_2 flows until all the frost is sublimated. In this case, defrosting time is t=3885s.

4.4.2. HX temperature decrease

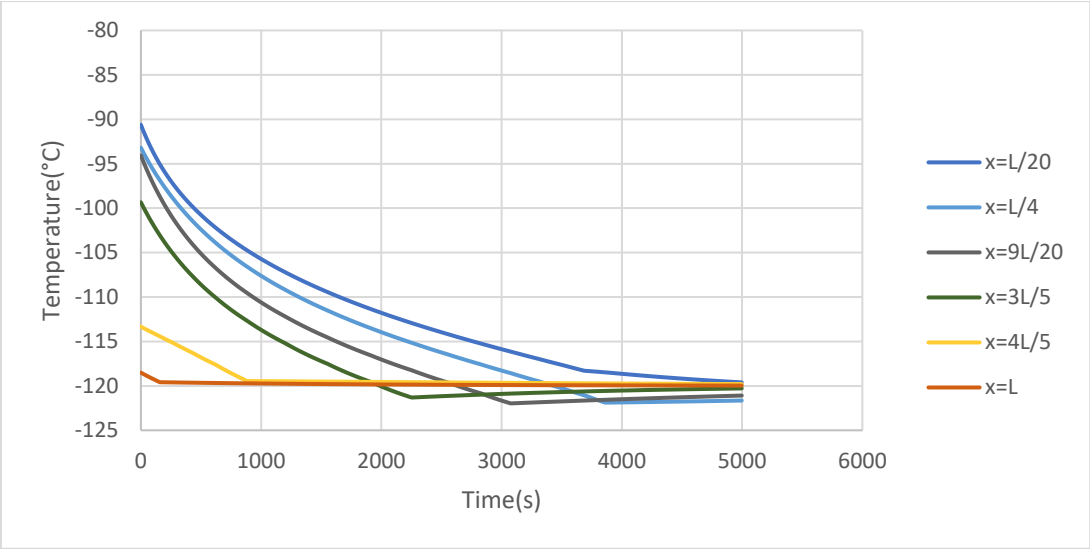

Figure 84: Tube temperature for different positions along the tube during CO2 defrosting

Figure 84 shows the decrease of the tube temperature as defrosting occurs. Convective heat transfer with N_2 will cool down the tube but going beneath the inlet temperature of N_2 is not possible by simple convection. Another phenomenon is put to effect: "the controlled sublimation".

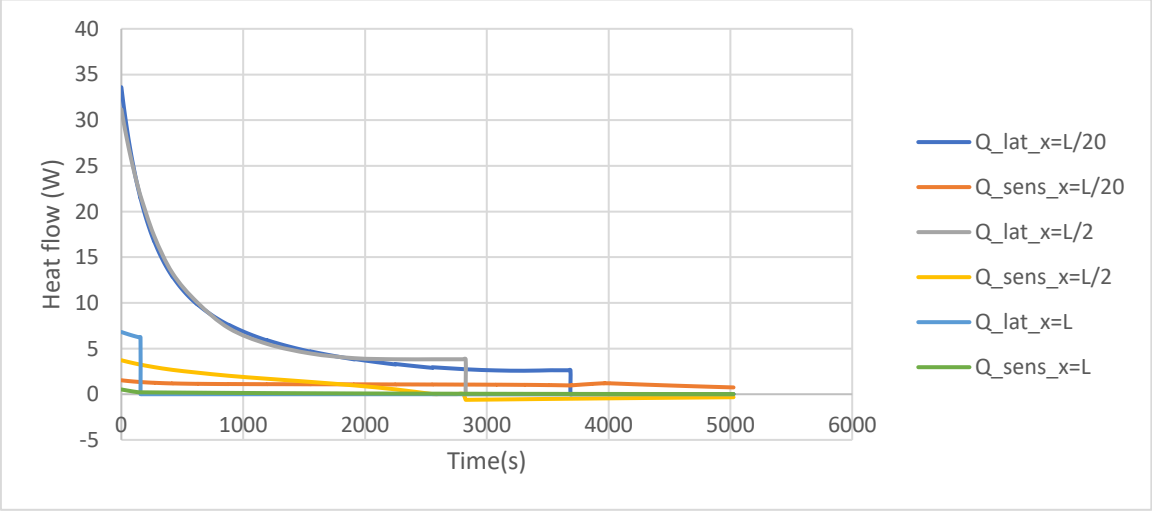

Figure 85: Latent and sensible heat flows at different positions along the tube during CO_2 defrosting

Figure 85 shows the latent and sensible heat flows at the beginning, the middle and the end of the tube. Convection between the "frost+tube" and the N_2 flow is represented by the sensible heat flow. Latent heat is the heat taken from the "frost+tube" for CO_2 sublimation. The results show that the latent heat is responsible for more than 90% of the total heat flow in the system. Since the convective heat transfer is not enough to cover the CO_2 sublimation heat

requirement, temperature decrease of solid phase and plate/tube must be the result of the defrosting. The concentration gradient between the CO_2 frost and the N_2 flow prompts the frost sublimation.

As the frost sublimates by pressure difference between its surface and the N_2 flow, it requires a heat source to cover this pressure loss. In this case, the heat source is the tube that will cool down to temperatures below -120°C, which is its initial temperature before the deposition phase started. A temperature gradient exists between the two extremities of the tube but it is about 3.5°C with the high temperature being at -118.5°C and the low temperature at -121.97°C. In order to optimize the whole defrosting phase, a sensitivity study will be conducted.

4.4.3. Sensitivity study

The sensitivity study aims to better understand the effect of the N_2 mass flowrate and inlet temperature on the defrosting of CO_2. Two results are to be optimized:

- The defrosting time: as it was stated before, ideally the defrosting time should be equal to the frosting time. If the defrosting time is shorter then it will give time for the HX temperature to homogenise which is not a problem. If the defrosting time is higher than that of the frosting, then the latter should be put on hold and methane production should be stopped waiting for the CO_2 frost to be totally sublimated and the HX back to its initial cryogenic temperature, ready for the frosting phase.

- The final tube temperature: since it will not be possible to obtain the exact same temperature in all the tube, the objective is to obtain the least temperature gradient and an average temperature close to the tube's initial temperature for the frosting phase, in this case -120°C.

As the inlet temperature of the N_2 flow increases, the defrost time decreases as more convective heat transfer is involved. When all the frost near the N_2 inlet is sublimated, only convective transfer remains, for high N_2 inlet temperatures the temperature gradient will increase as well as the average temperature in the tube. Even for the highest temperatures, it is still possible to go under the initial temperature of the tube due to cold recovery by controlled sublimation. Nevertheless, the defrosting time remains the main issue and is still very high compared to the frosting time which is t=2764s.

When the mass flowrate of N_2 is increased while fixing the inlet temperature to -120°C, the defrosting time decreases. Since the N_2 flow is at -120°C, it is not possible to heat the frost by convection with the gas flow. The high N_2 flow will result in higher values of heat and mass transfer coefficients, but the impact is greater on the latent heat since it represents the major part of the total heat flow. The temperature gradient in the tube is between 1-2°C and the average and minimal temperatures are close to -120°C.

Table 9: Defrost time and tube temperature for different N_2 mass flowrates and inlet temperatures

Mass flow rate per tube (x10^{-3} kg/s)	Temperature(°C)	Defrost time (s)	Temperature gradient(°C) $(T_{x=0} - T_{x=L})$	Minimal temperature(°C)	Average temperature(°C)
1.667	-100	3666	-14.877	-120.1	-114.267
	-110	3820.1	-6.83	-120.88	-117.301
	-120	4010.9	1.287	-121.93	-120.585
	-130	4258.5	9.46	-128.76	-124.219
	-140	4641	17.63	-137.944	-128.445
0.8333	-120	7127.5	1.573	-121.76	-120.491
1.25		5068.6	1.4	-121.85	-120.542
1.667		4010.9	1.287	-121.93	-120.585
2.083		3332.3	1.2110	-122.02	-120.614
2.5		2870.6	1.14	122.1	-120.631

Although increasing the temperature seems an illogical solution if the HX temperature is to be kept as homogenous as possible, the increase in N_2 flow might present a higher cost than heating a low flow of N_2. In order to properly evaluate the best solution, the defrosting results should be integrated in the whole process presented in Figure 68. High N_2 flows might present a problem if they are meant to liquefy the methane prior to their entry to the defrosting HX. In the next part, a study will be conducted to find the optimal inlet conditions of nitrogen for biomethane liquefaction and complete defrosting. Modifications might be needed to cover all requirements for a successful CO_2 sublimation, cold recovery and biomethane liquefaction in the required time delay.

4.5. Defrosting step in biomethane process

As mentioned before, the N_2 used for CO_2 defrosting and cold recovery will be used to liquefy biomethane in a previous step. In Figure 68, the flows and the components of the process were presented and their equations detailed. The inlet conditions of biomethane to HX-03 the heat exchanger where biomethane liquefies are specified by the compressor and HX-02. The compressor will increase the biomethane pressure thus increasing its saturation temperature, reducing the cold needed for its liquefaction. In HX-02 the biomethane coming from the outlet of the frosting HX will be heated by the same biomethane that was compressed and cooled to ambient temperature (see Figure 68 and the explanation in section 3.6.1.ii.). Decreasing the biomethane temperature before its liquefaction will reduce the sensible heat needed for its cooling to the saturation temperature.

In this study, the final total (in all the tubes) outlet flowrate of biomethane gas is of $\dot{V}_{ch4,outlet} = 250\ Nm^3/h$ which is equivalent to $\dot{m}_{ch4,total} = 179.4\ kg/h$. As shown in Figure 72, a small amount of CO_2 remains present in the outlet biomethane. An average CO_2 mass is added to the $\dot{m}_{ch4,total}$ in Aspen HYSYS® because it will use a part of the cold present in the N_2 flow (Stream 9).

Considering biomethane at the inlet of HX-03 at $P = 15bar$ and $T = -20°C$, the total liquid N_2 flow required for its liquefaction is $\dot{m}_{n2} = 552\ kg/h = 0.000638kg/s\ (per\ tube)$ if the outlet temperatures of biomethane and N_2 are respectively fixed at $T_{biomethane,8} = -170°C$ and $T_{n2\_gas,10} = -120°C$. The defrosting phase should be completed in t=2764s, the deposition time. According to Table 9, the gas N_2 flowrate required for defrosting in this time interval at -120°C is about $\dot{m}_{n2} = 0.0025kg/s\ (per\ tube) = 2160\ kg/h$ which is four times higher than what is required for biomethane liquefaction. If the N_2 flow enters at a higher temperature, it slightly reduces the defrosting time but will increase the tube's final temperature

4.5.1. Modifications and optimization of the process

In the case studied, the final outlet gas biomethane flowrate is fixed at $\dot{V}_{ch4,outlet} = 250\ Nm^3/h$, and the inlet CO_2 concentration is $y_{co2} = 26\%$. In the case presented, cold recovery by controlled sublimation is possible but if it is constrained by the defrosting time condition, it requires high N_2 flowrates which will affect the biomethane liquefaction. The process might need some additional components or it might perform more efficiently for different inlet biogas conditions. In the next part, the concept of cold recovery is applied to different cases of biomethane flows, the addition of new components is proposed and other solutions are presented. This will be put as perspectives for the optimization of the system.

i- Direct modifications to the flow conditions in HX-03

Biomethane is compressed and cooled before entering HX-03 where it is liquefied. If biomethane is not compressed, it will need a higher cooling load to liquefy therefore a higher liquid N_2 flow which can decrease the defrosting time.

Fixing the biomethane inlet (Stream 7) and outlet (Stream 8) flows in the biomethane liquefaction heat exchanger HX-03, the liquid N_2 flow (Stream 9) if calculated for different inlet biomethane pressures.

$T_{biomethane,7} = -20°C,\ T_{biomethane,8} = -170°C,\ \dot{m}_{ch4,total} = 179.4\ kg/h$

N_2 enters HX-03 in its liquid form at atmospheric pressure $T_{n2\_liq,9} = -196°C$. For now, the N_2 inlet temperature to the defrosting HX will be set at $T_{n2\_gas,10} = -120°C$.

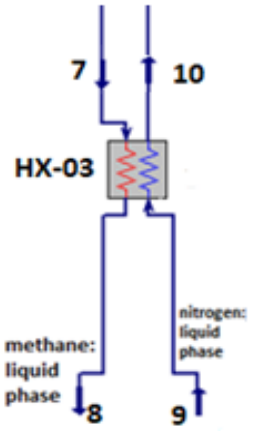

Figure 86: heat exchanger for biomethane liquefaction

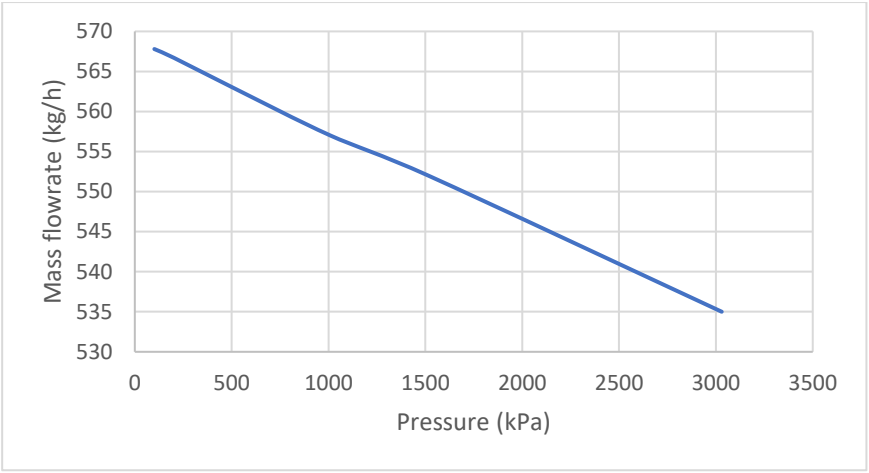

Figure 87: Liquid N_2 flow required for biomethane liquefaction at different pressures

Figure 87 shows that the liquefaction at higher pressure of biomethane indeed requires a smaller amount of liquid N_2. If the biomethane is kept at atmospheric pressure, the power consumption of the compressor can be avoided. $\dot{m}_{n2\_liq} = 567.8\, kg/h$ is required for liquefaction of the total biomethane at atmospheric pressure. In one tube, $\dot{m}_{n2\_gas} = 0.000657\, kg/s$ which will defrost CO_2 in more than 7200s according to Table 9. Therefore, the N_2 flow required to the liquefaction of biomethane is still lower than what is needed for defrosting on time.

A heat exchanger with the atmosphere can be added at the outlet of the N_2 flow from HX-03. In order to go to -120°C, the N_2 flow will be heated by an air stream instead of the liquefying biomethane. In the most optimistic case, $T_{n2\_gas,10} = -196°C$. Combining this case with a non-cooled biomethane pressurized to 30bar, the inlet liquid N_2 flow becomes $\dot{m}_{n2\_liq} = 1120\, kg/h$ which is almost half the required flowrate.

It can be concluded that changing the conditions of the flows at the inlet and the outlet of the heat exchanger where biomethane liquefaction occurs, is not enough to increase the N_2 inlet flow and it increases the cost by adding a heat exchanger and increasing the compressor consumption.

ii- Frosting stage set on hold

The simplest solution that can be presented is delaying the frosting phase until all the CO_2 defrosted. This solution can work for any inlet biogas flow conditions and it doesn't require the addition of any external flow or heat source. This solution might be simple but methane production must be stopped until the defrosting is complete. This is practically impossible at industrial scale.

4.5.2. Lower CO_2 concentration

In this study, the CO_2 molar concentration in inlet biogas was fixed at 26%. Figure 49 shows that biogas containing lower CO_2 concentrations has a longer frosting time before reaching $y_{ch4} < 97.5\%$ at the outlet of the frosting heat exchanger. The outlet CH_4 concentration should not go below this value. For a CO_2 concentration of $y_{co2} = 26\%$ in the inlet biogas, the system of

frosting and defrosting (by controlled sublimation) in two different heat exchangers but in the same time interval was limited by the N_2 flow that was used for biomethane liquefaction. In the following, a study on lower CO_2 concentrations in the inlet biogas is conducted.

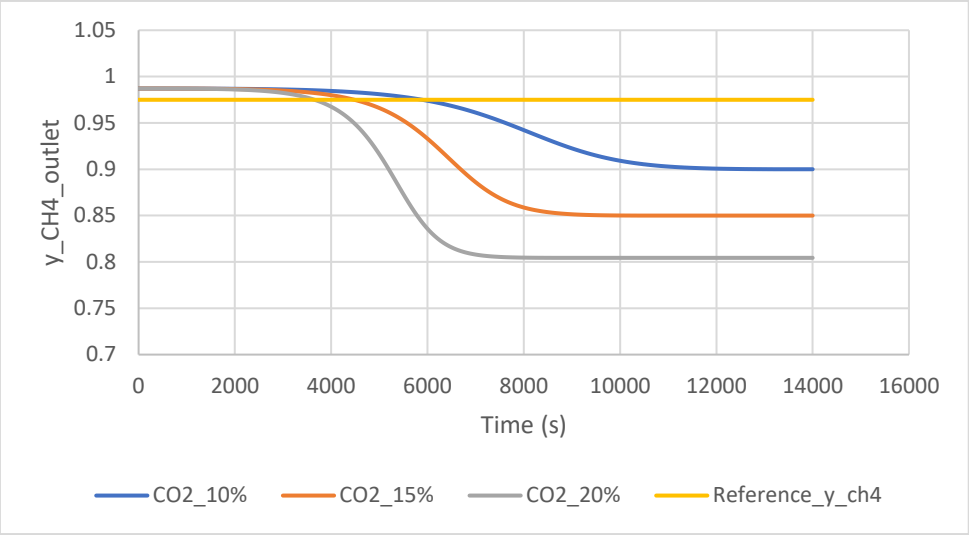

Figure 88: Outlet CH_4 concentration for different CO_2 concentrations in inlet biogas flow

Figure 88 shows the CH_4 concentration in the biomethane flow at the outlet of the heat exchanger where CO_2 deposition takes place. Indeed, lower CO_2 concentrations in the inlet biogas results in a longer frosting time before reaching the $y_{ch4} < 97.5\%$ condition. As more CO_2 frost deposits, the tube temperature increases and the CO_2 concentration gradient between the biogas flow and the frost decreases to the point where no further deposition occurs. This explains the constant outlet CH_4 concentration in the curves presented in Figure 88. Figure 89 shows the total accumulated mass of CO_2 frost along the tube. Although the frosting time at lower CO_2 concentrations is longer but the amount of frost is lower. Therefore, the defrosting time will be shorter even for lower N_2 flows.

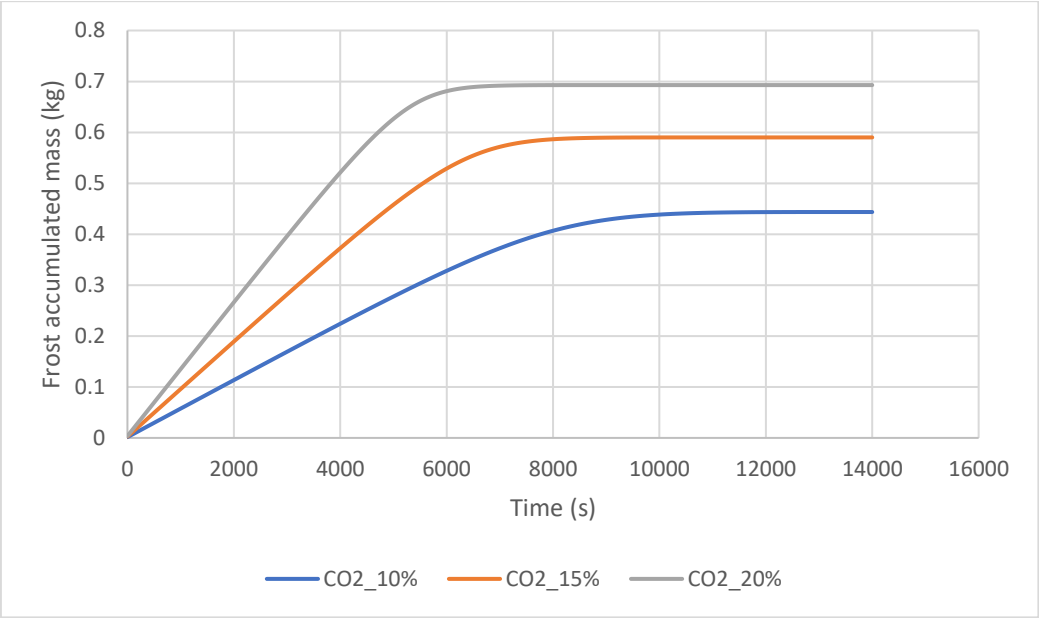

Figure 89: Accumulated CO_2 frost mass along the tube for different CO_2 concentrations in inlet biogas

Case 1:

Considering $y_{co2} = 10\%$ in the inlet biogas, the frosting time is t=5880s before reaching the condition $y_{ch4} < 97.5\%$ (Figure 88). The biomethane flow at the outlet of the system is kept at $\dot{V}_{ch4,outlet} = 250\ Nm^3/h$. Considering the same conditions leading to $\dot{m}_{n2} = 552\ kg/h = 0.000638 kg/s\ (per\ tube)$, the defrosting is completed in t=5638s. Figure 90 shows the frost thickness and mass decrease at x=3*L/10 where the last part of the frost is sublimated.

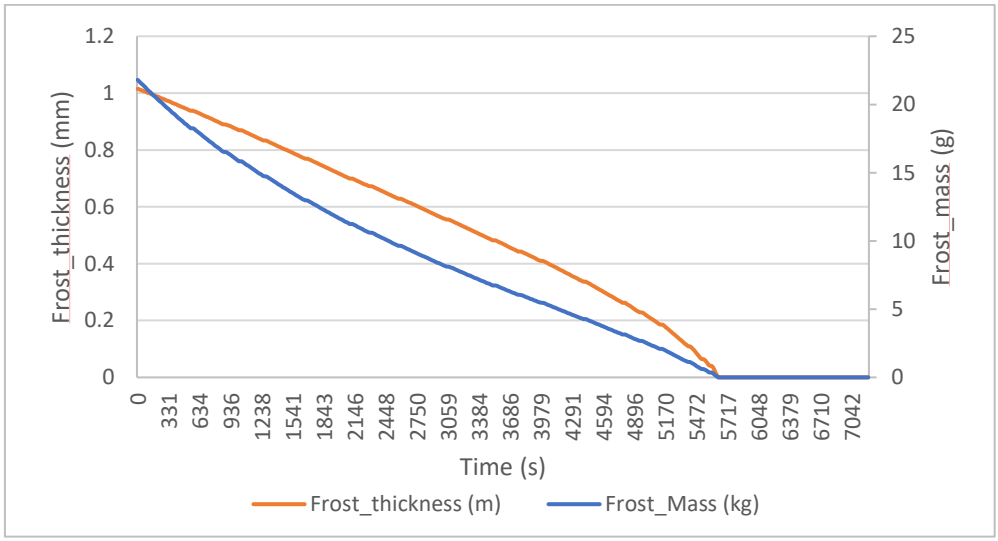

Figure 90: Evolution of frost mass and thickness during the defrosting phase for Case 1

The N_2 flow considered has liquefied biomethane and entered the defrosting HX and defrosting was completed in a time interval below the frosting time. Figure 91 shows the tube temperature evolution during the defrosting phase. At the end of the defrosting phase, the temperature gradient between the two extremities of the tube is of 11°C and the initial tube temperature of -120°C is not achieved. The low N_2 flow results in low convective heat transfer therefore less cooling of the tube near x=0 where the tube temperature is around -90°C. Also, the low amount of CO_2 frost results in lower cold recovery compared to the previous case of $y_{co2} = 26\%$ and $\dot{m}_{n2} = 1.66 \times 10^{-3} kg/s\ (per\ tube)$.

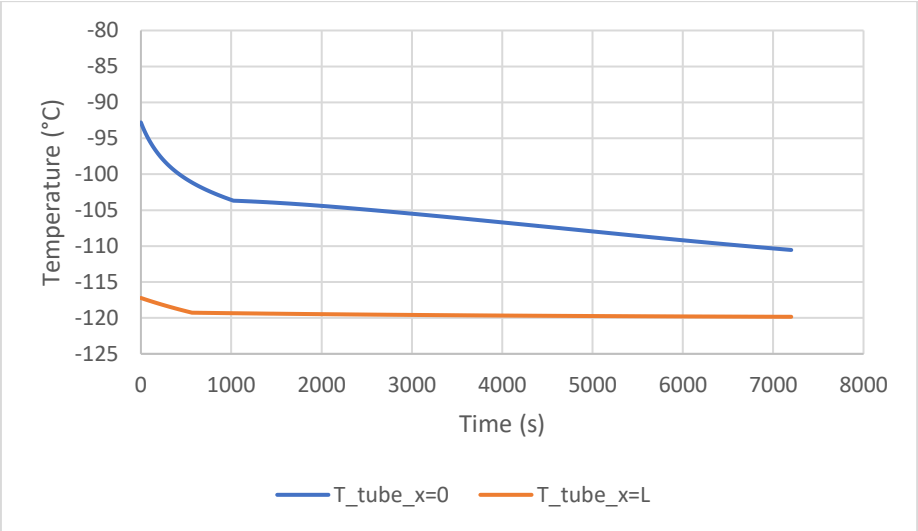

Figure 91: Tube temperature evolution at its extremities during CO_2 defrosting in Case 1

Case 2:

Table 9 shows that the temperature of the defrosting phase has a limited effect on the defrosting time and a major effect on the tube temperature considering the convective heat transfer between the N_2 flow and the "frost+tube". The N_2 flow will enter the defrosting HX at -135°C. Its mass flowrate is still considered $\dot{m}_{n2} = 552\ kg/h = 0.000638 kg/s\ (per\ tube)$ even though it can be slightly higher. The defrosting is completed in t=5860s. Figure 92 shows the evolution of the tube temperature; even though the temperature gradient is still 21.6°C, the tube average temperature is -120.7°C. Since the tube thermal conductivity is high, it can be kept homogenising until the frosting phase is completed.

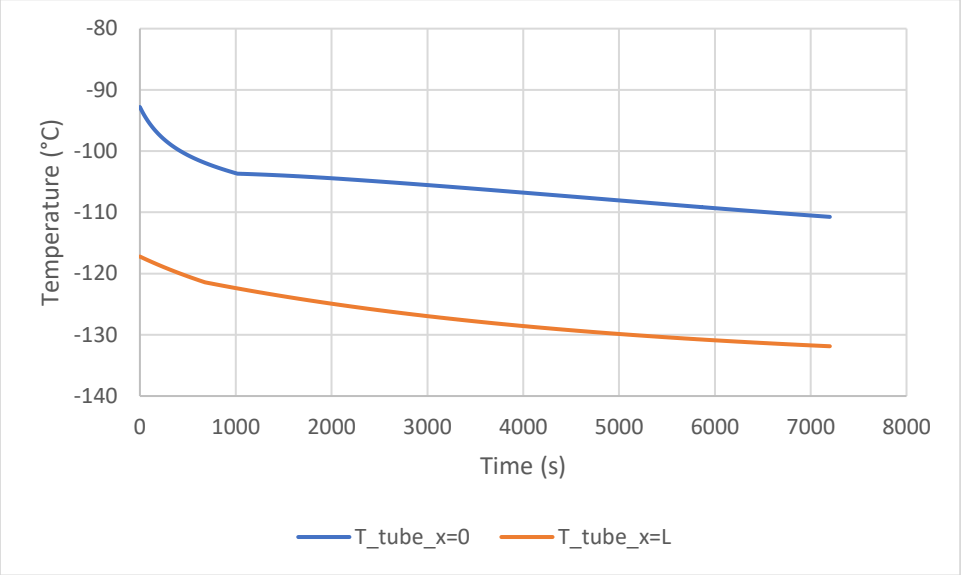

Figure 92: Tube temperature evolution at its extremities during CO_2 defrosting in Case 2

Although $y_{co2} = 26\%$ in inlet biogas was set to be in a more realistic case, the system might be more efficient for lower CO_2 concentrations in the inlet biogas since the available defrosting time will be longer for less CO_2 frost deposited. The system can become part of a hybrid system using a low-cost biogas upgrading system to get to low but not optimal CO_2 concentrations, e.g. $y_{co2} = 10\%$, and the system presented in this paper could come as a second step to complete the biogas upgrading in order to obtain $y_{ch4} > 97.5\%$.

Case 3:

Another case is considered with $\dot{V}_{ch4,outlet} = 500\ Nm^3/h$ and $y_{co2} = 10\%$. In the same considered before, the N_2 flow needed for biomethane liquefaction becomes $\dot{m}_{n2} = 1058\ kg/h = 0.0012245 kg/s\ (per\ tube)$ which is almost the double as the case before with a small difference depending on the amount of CO_2 frosted. Compared to the case with $\dot{V}_{ch4,outlet} = 250\ Nm^3/h$, frosting time t=2690s is shorter until $y_{ch4} < 97.5\%$.is reached and the amount of CO_2 frosted is higher since more CO_2 is available in the biogas.

Since the N_2 flow is low and is at -120°C, the tube will be at a temperature higher than what is needed for the next frosting phase similarly to the previous case. Therefore, inlet N_2 at -135°C will be directly sent for CO_2 sublimation. Defrosting time is t=2520s (Figure 93) which is below the frosting time therefore acceptable. The tube overall temperature will be distributed

between -110.8°C and -130.5°C. Its final average temperature is -121.4°C and it has a spare time of t=170s to homogenise before the next frosting phase starts (Figure 94).

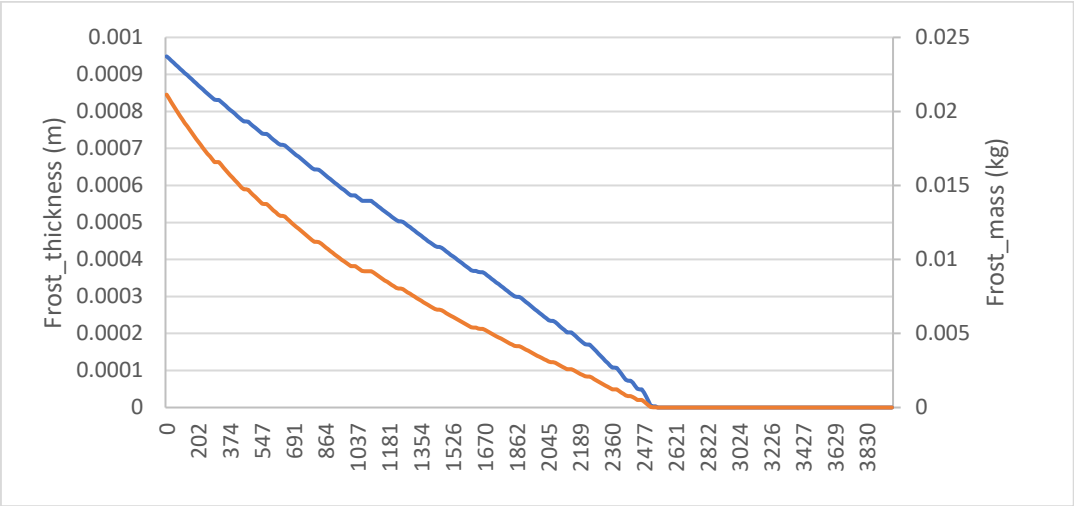

Figure 93: Evolution of frost mass and thickness during the defrosting phase in Case 3

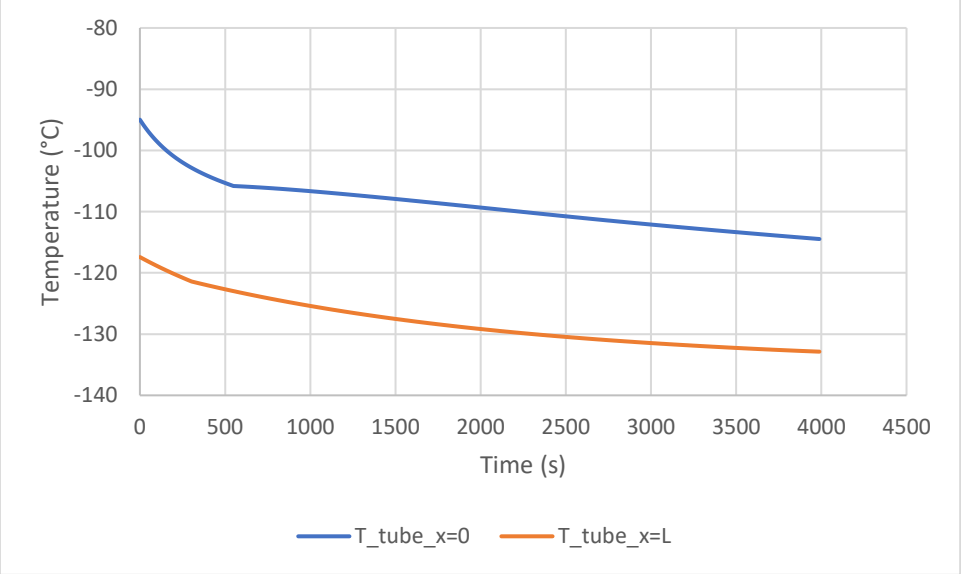

Figure 94: Tube temperature evolution at its extremities during CO_2 defrosting in Case 3

Lowering the tube initial temperature increases the outlet y_{ch4} as shown in Figure 55 where 100% pure methane is produced during the first hour. If the system is to be integrated with another one that produces biomethane at 85-90% CH_4, it would be more interesting to use this added system to obtain pure methane. The same work done in the previous part should be repeated to see if the system can accomplish defrosting at the same time interval set for frosting while recovering cold stored in the frost and returning the tube to its initial temperature of -120°C.

Conclusion

In this chapter, a literature review of the different defrosting systems was presented. The concept of controlled sublimation was further detailed. The frost sublimation will be caused by

a concentration gradient between a gas flow coming into contact with the frost and the frost itself. The gas flow will be cooler than the frost not to sublimate by convective heat transfer thus losing its cold potential. As CO_2 gets defrosted it drains heat from the HX to compensate its pressure loss. This will allow the cold recovery with a minor effect of convective heat transfer.

A model of controlled sublimation was presented and a sensitivity study was conducted to study the effect of the mass flowrate and the temperature of the defrosting gas on the defrosting time and the final temperature of the HX. The objective was to return the tube to its initial temperature (-120°C) before the frosting phase and for the defrosting to be completed in a time interval equal to the time of frosting in the second HX. The simulation results showed that, indeed the tube can be cooled to temperatures even below its initial temperature which is impossible by convective heat transfer alone. The main issue was the excessive defrosting time. The N_2 flow that will be used to liquefy the biomethane will be later used for defrosting. A high CO_2 concentration was chosen for the inlet biogas before the frosting phase. It was found that in order to end the frosting and defrosting phase at the same time, the N_2 flowrate that should be used for defrosting is 4 times higher than that used for methane liquefaction.

Solutions were presented in order to render the system more efficient. Stopping the frosting was the simplest solution but biomethane production will be stopped. Since a surplus of cooling load is available, it is possible to use it in another system for biomethane liquefaction or other cooling needs. It was found that lower CO_2 concentrations in the inlet biogas will result in better operation of the system. It is possible to end the frosting and defrosting at the same time with the amount of N_2 used for biomethane liquefaction. Since the amount of CO_2 frosted will be less than that for high CO_2 concentrations in inlet biogas, cold recovery will need to be supported by a cooler N_2 flow which will slightly increase the defrosting time but will return the HX to its initial temperature for the frosting phase.

Chapitre 4: Sublimation contrôlée du givre de CO_2 et récupération du froid

Introduction

De nombreuses méthodes de dégivrage peuvent être trouvées dans la littérature. Cependant, contrairement au phénomène de givrage, peu de modèles de dégivrage ont été développés, même dans le cas de la glace d'eau. Habituellement, il n'est pas très intéressant d'étudier le processus de décongélation autant que de se débarrasser du dépôt solide qui affecte généralement le système négativement.

Dans ce chapitre, le changement de phase du CO_2 solide vers sa phase gazeuse est étudié et modélisé. Contrairement aux méthodes de dégivrage classiques, le CO_2 sera sublimé par sublimation contrôlée par contact avec un troisième gaz froid. Cette méthode permet de récupérer le froid stocké dans le givre de CO_2 afin de l'utiliser pour épuré plus de biogaz. Les résultats du dégivrage du CO_2 et de la récupération de froid seront présentés et intégrés dans l'ensemble du procédé d'épuration et de liquéfaction du biogaz.

4.1. Méthodes de dégivrage

La séparation cryogénique du CO_2 aboutit à un échangeur de chaleur contenant du givre de CO_2 qui doit être éliminé. Le givre de CO_2 est éliminé en introduisant un gaz froid tertiaire qui dégivrera le CO_2 tout en refroidissant le système selon le même principe que le refroidissement par évaporation. Les deux principaux défis des cycles de dégivrage consistent à définir le temps de dégivrage et la chaleur transmise au réfrigérant pendant la phase de dégivrage [110]. Les méthodes de dégivrage les plus utilisées sont :

- Le cycle On-Off : lorsque le givre doit être éliminé, le système de réfrigération est arrêté et aucun réfrigérant ne passe dans l'évaporateur. Lorsque tout le givre est retiré, le système est remis en marche.
- Le dégivrage électrique peut être utilisé dans les applications à moyenne et basses températures. Des tiges chauffantes à résistance électrique sont incorporées dans les évaporateurs et lorsque l'accumulation du givre commence à affecter le bon fonctionnement de l'échangeur, un courant électrique traverse la résistance. La chaleur ajoutée augmente la température de l'échangeur de chaleur, ce qui conduit au dégivrage. Les réchauffeurs sont mis hors tension lorsque le dégivrage est terminé. Cette méthode présente un temps de dégivrage plus court que le cycle On-Off mais nécessite une source d'énergie externe. Un autre inconvénient de ce type de dégivrage est le coût des résistances électriques et leur installation.
- Le dégivrage au gaz est le plus utilisé pour le dégivrage dans les systèmes de réfrigération industriels[112]. Le dégivrage au gaz utilise la chaleur contenue dans les vapeurs à la sortie du compresseur pour effectuer le dégivrage. Plus aucun fluide frigorigène ne passe à travers l'évaporateur, une partie (ou la totalité) de la vapeur chaude est redirigée dans l'évaporateur pour éliminer le givre. L'air présent dans le milieu réfrigéré est chauffé et peut provoquer des fluctuations de température réduisant l'efficacité du système[107].

4.2. Le modèle de dégivrage du CO_2

La séparation cryogénique du CO_2 contenu dans le biogaz aboutit à un dépôt solide froid qui doit être éliminé pour permettre de givrer à nouveau sur la surface froide. Si le volume contenant le givre CO_2 est scellé, sa pression augmente et il est possible d'obtenir du dioxyde de carbone liquide. Une autre option de décongélation se présente dans ce que l'on peut appeler la « sublimation contrôlée ». Elle suit le même principe que l'évaporation contrôlée qui a été détaillé au chapitre 1, mais au lieu d'avoir un liquide en train de se vaporiser, un dépôt de givre va se sublimer. Ce n'est pas un phénomène physique commun à la pression atmosphérique mais c'est l'une des caractéristiques du CO_2. La sublimation contrôlée nécessite un gaz extérieur qui vient en contact avec le givre. Si le gaz de dégivrage est chaud, sa chaleur sensible augmente la température du givre jusqu'au point de sublimation. Cependant, le mélange final ne sera pas suffisamment froid pour être réutilisé pour une élimination cryogénique supplémentaire du CO_2 contenu dans le biogaz. Un des points importants du dégivrage par sublimation contrôlée est que le gaz utilisé pour dégivrer peut être plus froid que le givre. Lorsque le gaz de dégivrage froid passe à travers le volume de contrôle contenant le givre, la vapeur saturante du CO_2 s'y diffuse et sera transportée à la sortie de l'échangeur de chaleur. Le givre de CO_2 doit récupérer la perte de pression de vapeur et se sublime, ce qui permet à plus de vapeur de CO_2 d'être diffusée dans le gaz de dégivrage et d'être éliminée de l'échangeur de chaleur. Le gradient de concentration de CO_2 entre la surface de givre et le gaz de dégivrage entrant devient la force motrice qui sublimera le givre de CO_2. Lorsque le CO_2 se sublime, il faudra une source de chaleur pour maintenir sa pression de saturation à sa température de surface. Par conséquent, le givre CO_2 ainsi que la surface sur laquelle il s'est déposé vont se refroidir, récupérant ainsi le froid stocké dans le givre CO_2. La figure F20 montre les transferts de chaleur et de masse de la couche de givre vers le gaz de dégivrage. Elle est similaire à la figure D décrivant le givrage, mais les flèches sont inversées, puisque le CO_2 dégivré quitte la masse solide vers le gaz de dégivrage.

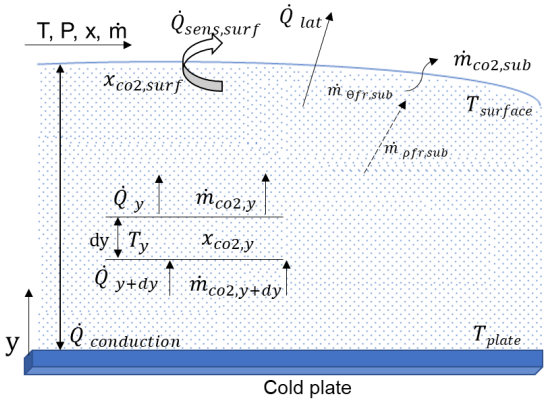

Figure F20: Bilan énergétique et massique à la surface et à l'intérieur du givre lors de la sublimation contrôlée

Comme dans le cas de givrage de CO_2 présenté au chapitre 2, le modèle divise le système en 3 parties: le gaz de dégivrage, l'interface givre-gaz et l'intérieur de la couche de givre. On ajoute la récupération du froid. De l'azote liquide sert à liquéfier le biométhane issu de la phase de givrage, il peut être utilisé comme gaz de dégivrage puisqu'il est également à une température inférieure à celle du givre. Les conditions initiales de dégivrage seront équivalentes aux conditions finales du modèle de givrage. Le modèle est très similaire à ce qui a été présenté au

chapitre 2 pour le givrage du CO_2 ; pour ne pas répéter, les équations différentes seront présentées et bien expliquées.

i. Le gaz de dégivrage

Puisque la température du givre de CO_2 diminue, la température du gaz de dégivrage doit être inférieure à celle du givre. L'objectif est de réduire autant que possible le transfert de chaleur sensible. Il est possible que le transfert de chaleur par convection entre la surface du givre et le gaz de dégivrage change de signe lorsque la surface du givre devient plus froide que le gaz de dégivrage du fait de la sublimation du givre. Le débit massique de CO_2 sublimé de la couche de givre vers le gaz de dégivrage $\dot{m}_{co2,sub}$ peut être exprimé par l'analogie entre les transferts de chaleur et de masse:

$$\dot{m}_{co2,sub} = -h_m \times \rho_{defrosting\ gas} \times (x_{fr,surf} - x_{n2/co2}) \quad \text{(F.4.1)}$$

L'interface entre le gaz de dégivrage (N_2) et la surface du givre est considérée en équilibre thermodynamique.

ii. L'interfacce givre-gaz

Comme pour le dégivrage, la couche de givre étant considérée comme un milieu poreux, le débit massique de CO_2 sublimé est représenté par deux termes. Le premier $\dot{m}_{\rho,frost}$ prend en compte la sublimation à l'intérieur de la couche de givre. La seconde $\dot{m}_{\theta,frost}$ correspond à la sublimation à la surface. Les équations pour ces deux flux de masse sont les mêmes que celles utilisées dans le modèle de givrage, mais la direction du flux est inversée. Le gradient de concentration sera négatif lors du passage de l'interface givre-gaz vers les couches de givre. Tous les flux de masse sont négatifs car le CO_2 est en cours de sublimation.
À la surface du givre, même si le but est de l'éliminer, un transfert de chaleur sensible par convection a lieu à l'interface avec le N_2. La chaleur latente est responsable de la sublimation du CO_2. Lorsque le CO_2 se sublime à la surface, le givre est refroidi car il sert comme source de chaleur pour compenser la perte de pression de vapeur saturante. La surface de l'échangeur de chaleur sera refroidie par conduction à l'intérieur des couches de givre. Les mêmes équations de la phase de givrage du chapitre 2 peuvent être utilisées avec des modifications des signes.

iii. La couche de givre

La densification du givre correspond à un terme négatif car le givre est sublimé à l'intérieur des couches de givre et peut être exprimé par un terme de porosification β_{co2}:

$$\beta_{co2} = -\frac{d\dot{m}_{\rho frost}}{dy} \quad \text{(F.4.2)}$$

L'équilibre entre le transfert de chaleur par conduction et le taux de sublimation de CO_2 à l'intérieur de la couche de givre peut être écrit sous la forme :

$$\frac{d\dot{q}_{cond}}{dy} = -\beta_{co2} \times L_{sv} \quad \text{(F.4.3)}$$

Comme pour la surface du givre, l'équilibre thermodynamique entre le gaz de dégivrage et le givre de CO_2 est considéré à l'intérieur de la couche de givre.

iv. Récupération du froid

Lorsque le CO_2 se sublime, la température de la phase solide et du métal (plaque ou tube) diminue. La surface sur laquelle le givre est formé est refroidie par conduction à travers la

couche de givre. Cette diminution de température peut être utilisée pour récupérer le froid stocké dans le givre CO_2. Si l'échangeur de chaleur est utilisé comme inertie thermique, sa température augmente au cours de la phase de givrage, puis elle diminue théoriquement à sa même température initiale après le dégivrage complet. Le flux de chaleur de l'inertie thermique vers la couche de givre est exprimé par:

$$\dot{q} = -m_{heat\ capacitor} \times c_{heat\ capacitor} \times \frac{dT_{heat\ capacitor}}{dt} \quad \text{(F.4.4)}$$

4.3. Résultats de la sublimation contrôlée

Un flux de N_2 gaz est introduit à contre-courant dans le HX contenant le givre de CO_2. Dans cette partie, le gaz de dégivrage de référence est du N_2 avec $\dot{m}_{n2} = 1.66 \times 10^{-3} kg/s\ (per\ tube)$ et $T_{in,n2} = -120°C$. Une étude de sensibilité est réalisée pour optimiser la phase de dégivrage. Les conditions initiales de la phase de dégivrage sont les conditions finales de la phase de givrage à t = 2764s du Chapitre 3.

4.3.1. Diminution de l'épaisseur et de la masse de givre

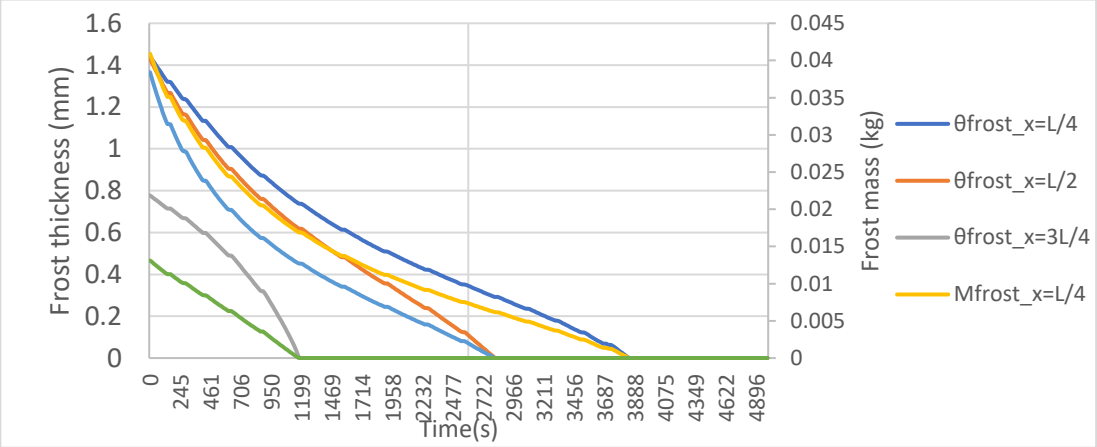

Figure F21: La diminution de l'épaisseur et de la masse du givre à diff. positions le long du tube en phase de dégivrage

La figure F21 montre différentes formes de diminution de l'épaisseur et de la masse du givre. Au centre du tube, le givre diminue presque linéairement. Dans les positions plus proches de l'entrée du N_2, la courbe de diminution de l'épaisseur devient convexe. Par contre, elle devient concave vers la sortie du N_2. Ces différents taux de sublimation sont dû à plusieurs facteurs :

- Lorsque le givre se refroidit, sa pression de vapeur diminue, ce qui entraîne une diminution du taux de sublimation. Le givre sublime encore mais en quantité plus faible.
- La masse volumique initiale à l'intérieur des couches de givre affecte son taux de sublimation. La masse volumique de givre proche de x = L est faible, ce qui permet une sublimation plus rapide, car plus de N_2 peut être diffusé dans le givre.

  Il est important de connaître le temps de dégivrage. Le flux de N_2 s'écoule jusqu'à ce que tout le givre soit sublimé. Dans ce cas, le temps de dégivrage est de t = 3885s.

4.3.2. Diminution de la température de l'échangeur

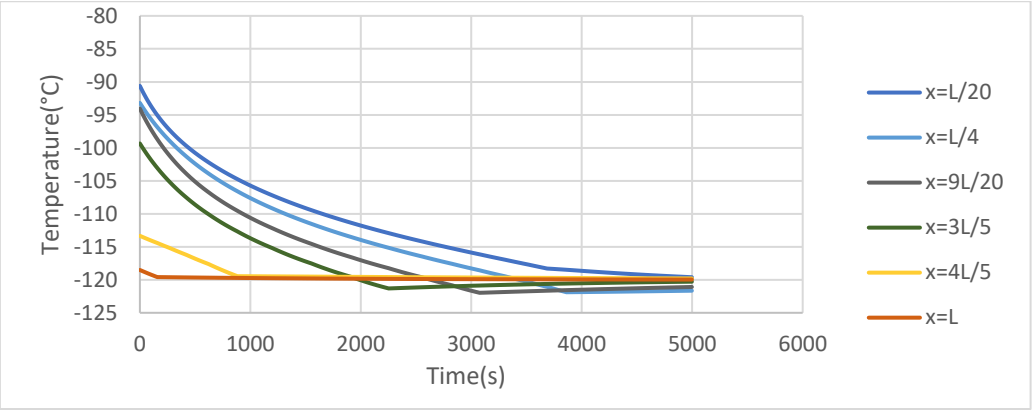

Figure F22: Température du tube à différentes positions le long du tube en phase de dégivrage du CO_2

La figure F22 montre la diminution de la température du tube lors du dégivrage. Le transfert de chaleur par convection avec N_2 refroidit le tube mais il n'est pas possible de baisser en dessous de la température d'entrée du N_2 par simple convection. Un autre phénomène entre en jeu : «la sublimation contrôlée ».

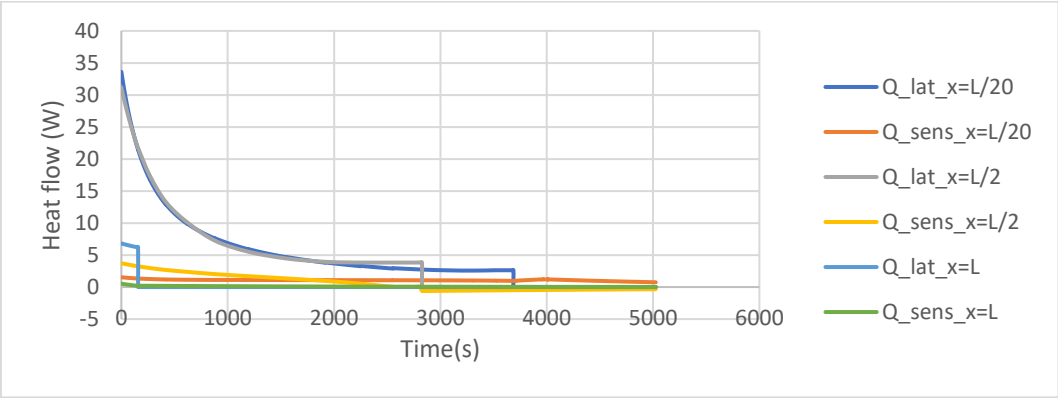

Figure F23: Flux de chaleur sensible et latente à différentes positions le long du tube en phase de dégivrage du CO_2

Figure F23 montre les flux de chaleur latente et sensible aux extrémités et au centre du tube. La convection entre le « givre+tube » et le flux de N_2 est représentée par la chaleur sensible. La chaleur latente est la chaleur extraite du « givre+tube » pour la sublimation du CO_2. Les résultats montrent que la chaleur latente est responsable de plus de 90% des flux de chaleur totaux dans le système. Puisque le transfert de chaleur par convection ne suffit pas pour couvrir les besoins calorifiques pour la sublimation du CO_2, la diminution de la température de la phase solide et du tube est le résultat du dégivrage. Le gradient de concentration entre le givre de CO_2 et le flux de N_2 provoque la sublimation. Comme le givre se sublime par la différence de pression entre sa surface et le débit de N_2, une source de chaleur est nécessaire pour compenser cette perte de charge. Dans ce cas, la source de chaleur est le tube qui se refroidit jusqu'une température inférieure à -120°C, qui est sa température initiale avant le début de la phase de givrage. Un gradient de température existe entre les deux extrémités du tube mais il est d'environ 3,5°C, la température maximale étant de -118,5°C et la basse température de -121,97°C. Afin d'optimiser l'ensemble de la phase de dégivrage, une étude de sensibilité est réalisée.

4.3.3. Etude de sensibilité de la phase de dégivrage

L'étude de sensibilité vise à mieux comprendre l'effet du débit massique de N_2 et de sa température d'entrée sur le dégivrage du CO_2. Deux résultats à optimiser:

- Le temps de dégivrage : comme indiqué précédemment, idéalement, il devrait être égal au temps de givrage. Si le temps de dégivrage est plus court, il y aura plus de temps pour l'homogénéisation de la température du HX, ce qui ne pose aucun problème. Si le temps de dégivrage est supérieur à celui du givrage, il faudra suspendre ce dernier et arrêter la production de méthane en attendant que le givre de CO_2 soit totalement sublimé et que le HX revienne à sa température cryogénique initiale.
- La température finale du tube : puisqu'il est impossible d'obtenir exactement la même température dans tout le tube, l'objectif est d'obtenir le moindre gradient de température entre les deux extrémités du tube et une température moyenne proche de la température initiale du tube pour la phase de givrage, dans ce cas -120°C.

Lorsque la température d'entrée du flux de N_2 augmente, le temps de dégivrage diminue puisque le transfert de chaleur convectif augmente. Lorsque tout le givre proche de l'entrée du N_2 est sublimé, il ne reste que le transfert convectif avec le tube. Pour des températures d'entrée élevées de N_2, le gradient de température augmente ainsi que la température moyenne dans le tube. Même pour les températures les plus élevées, il est encore possible de d'atteindre une température inférieure à la température initiale du tube grâce à la récupération du froid par sublimation contrôlée. Néanmoins, le temps de dégivrage reste très élevé comparé au temps de givrage qui est t = 2764s et constitue le problème principal.
Lorsque le débit massique de N_2 augmente tout en fixant la température d'entrée à -120°C, le temps de dégivrage diminue. Le débit d'azote étant à -120°C, il n'est pas possible de chauffer le givre par convection avec le débit de gaz. Le débit élevé de N_2 conduit à une augmentation des valeurs de coefficients de transfert de chaleur et de masse, mais l'impact sera plus important sur la chaleur latente puisqu'elle représente la partie majeure du flux de chaleur total. Le gradient de température dans le tube est compris entre 1 et 2°C et les températures moyennes et minimales sont proches de -120 ° C

Table F1: Temps de dégivrage et température du tube pour différents débits massiques de N_2 et températures d'entrée

Débit par tube (x10^{-3} kg/s)	Température (°C)	Temps de dégivrage (s)	Gradient de température(°C) $(T_{x=0} - T_{x=L})$	Température minimale(°C)	Température moyenne(°C)
1,667	-110	3820,1	-6,8	-120,9	-117,3
	-120	4010,9	1,3	-121,9	-120,6
	-130	4258,5	9,5	-128,8	-124,2
1,25	-120	5068,6	1,4	-121,8	-120.,5
1,667		4010,9	1,3	-121,9	-120,6
2,5		2870,6	1,1	122,1	-120,5

Bien que l'augmentation de la température semble une solution illogique si la température du HX doit être maintenue aussi homogène que possible, l'augmentation du débit de N_2 peut

présenter un coût plus élevé que le chauffage d'un faible débit de N_2. Les débits élevés de N_2 peuvent poser un problème s'ils sont destinés à liquéfier le méthane avant leur entrée dans le HX de dégivrage. Dans la prochaine partie, une étude sera menée pour déterminer les conditions optimales d'entrée de l'azote pour la liquéfaction du biométhane et le dégivrage complet. Des modifications pourraient être nécessaires pour couvrir toutes les conditions requises pour réussir la sublimation du CO_2, la récupération du froid et la liquéfaction du biométhane dans les délais impartis.

4.4. Dégivrage dans le système d'épuration

Le N_2 utilisé pour le dégivrage du CO_2 et la récupération du froid contenu dans le givre est utilisé pour liquéfier le biométhane. La figure F18 décrit le système d'épuration et de liquéfaction du biogaz. Les conditions d'entrée du biométhane dans l'échangeur de chaleur HX-03 dans lequel le biométhane se liquéfie sont spécifiées par le compresseur et HX-02. Ce dernier augmente la pression du biométhane, augmentant ainsi sa température de condensation, réduisant la puissance frigorifique nécessaire à sa liquéfaction. Diminuer la température du biométhane avant sa liquéfaction réduit la chaleur sensible nécessaire à son refroidissement jusqu'à la température de liquéfaction.

En considérant le biométhane à l'entrée de HX-03 à $P = 15bar$ et $T = -20°C$, le débit total d'azote liquide nécessaire à sa liquéfaction est de $\dot{m}_{n2} = 552\ kg/h = 0{,}000638kg/s\ (per\ tube)$ si les températures du biométhane et de N_2 sont respectivement fixées à $T_{biomethane,8} = -170°C$ et $T_{n2\_gas,10} = -120°C$. La phase de dégivrage devrait être terminée en t = 2764s, égal au temps de givrage. Selon Tableau A, le débit de N_2 requis pour le dégivrage dans cet intervalle de temps à $T_{n2\_gas,10} = -120°C$ est d'environ $\dot{m}_{n2} = 0{,}0025kg/s\ (per\ tube) = 2160\ kg/h$, soit quatre fois la quantité requise pour la liquéfaction du biométhane. Si le flux de N_2 entre à une température plus élevée, il réduit légèrement le temps de dégivrage mais augmente la température finale du tube.

4.4.1. Modifications et optimisation du système

Dans le cas étudié, le débit final de biométhane des gaz de sortie est fixé à $\dot{V}_{ch4,outlet} = 250\ Nm^3/h$, et la concentration de CO_2 à l'entrée est $y_{co2} = 26\%$. La récupération à froid par sublimation contrôlée est possible, mais si elle est contrainte par la condition de temps de dégivrage, elle nécessite des débits de N_2 élevés qui affecteront la liquéfaction du biométhane. Le système peut nécessiter des composants supplémentaires permettant un fonctionnement plus efficace pour différentes conditions d'entrée du biogaz. Il est possible d'éteindre le système en attendant la fin du dégivrage, de modifier les conditions dans HX-03, d'ajouter une source de chaleur externe (liquéfaction de biogaz provenant d'un système de valorisation différent) afin d'évaporer davantage de N_2, augmentant ainsi le débit de gaz de dégivrage.

4.4.2. Des concentrations plus basses de CO_2

Dans cette étude, la concentration molaire du CO_2 dans le biogaz en entrée est fixée à 26%. La figure F9 montre que le biogaz de plus faibles concentrations de CO_2 a un temps de givrage plus long avant d'atteindre $y_{ch4} < 97.5\%$ à la sortie de l'échangeur de chaleur en mode de givrage. Pour une concentration de CO_2 de $y_{co2} = 26\%$ dans le biogaz en entrée, le système de givrage et de dégivrage simultanés (par sublimation contrôlée) dans deux échangeurs de chaleur

différents, mais dans le même intervalle de temps, était limité par le flux de N_2 utilisé pour la liquéfaction du biométhane. Dans ce qui suit, une étude considérant des concentrations de CO_2 inférieures dans le biogaz en entrée est menée.

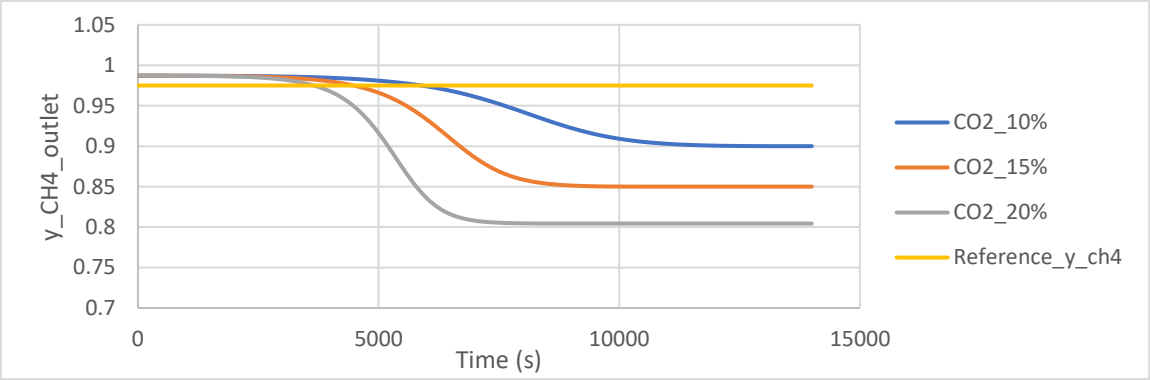

Figure F24: Concentration de CH_4 à la sortie du HX pour différentes concentrations de CO_2 dans le flux de biogaz en entrée

Figure F24 montre la concentration de CH_4 dans le flux de biométhane à la sortie de l'échangeur de chaleur en mode de givrage de CO_2. En effet, des concentrations de CO_2 plus faibles dans le biogaz d'entrée entraînent un temps de givrage plus long avant d'atteindre la condition $y_{ch4} < 97.5\%$. La formation du givre aboutit à une augmentation de la température du tube et le gradient de concentration de CO_2 entre le flux de biogaz et la surface du givre diminue au point où le CO_2 ne givre plus. Ceci explique la concentration constante de CH_4 à la sortie dans les courbes présentées dans la figure F24. La figure F25 montre la masse totale de givre de CO_2 accumulée le long du tube. Bien que le temps de givrage à des concentrations de CO_2 inférieures soit plus long, la quantité de givre est plus faible. Par conséquent, le temps de dégivrage sera plus court même pour les débits faibles de N_2.

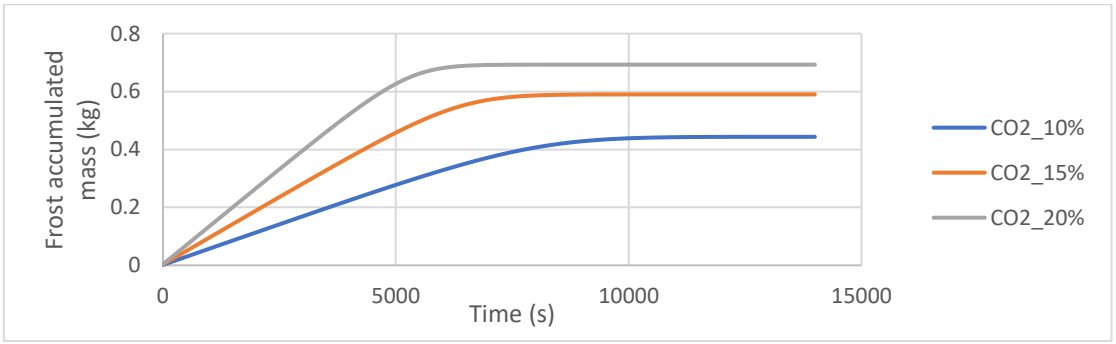

Figure F25: Masse de givre de CO_2 accumulé le long du tube pour diff. concentrations de CO_2 dans le biogaz en entrée

Cas 1 :

Considérant que $y_{co2} = 10\%$ dans le biogaz à l'entrée, le temps de givrage est de t=5880s avant que la condition $y_{ch4} < 97.5\%$ ne soit atteinte (Figure F24). Le débit de biométhane à la sortie du système est maintenu à $\dot{V}_{ch4,outlet} = 250\ Nm^3/h$. Considérant le même débit de N_2 que dans le cas précédent $\dot{m}_{n2} = 552\ kg/h = 0{,}000638 kg/s\ (per\ tube)$, le dégivrage est terminé en t=5638s. La figure F26 montre la diminution de l'épaisseur et de la masse du givre en x=3*L/10 où la dernière partie du givre est sublime

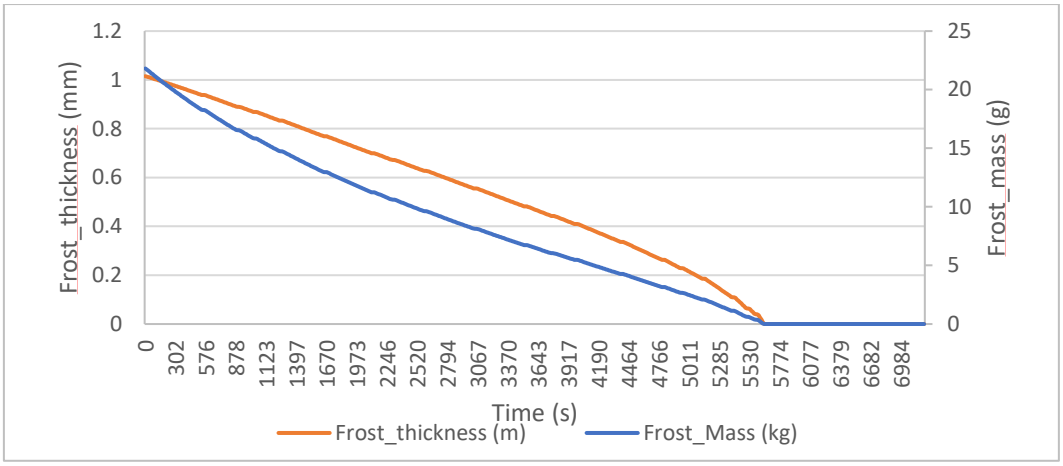

Figure F26: Evolution de la masse et de l'épaisseur du givre pendant la phase de dégivrage pour le Cas 1

Le flux de N_2 considéré liquéfie le biométhane avant d'entrer dans le HX en dégivrage. Le dégivrage était terminé dans un intervalle de temps inférieur au temps de givrage. La figure F27 montre l'évolution de la température du tube pendant la phase de dégivrage. À la fin de cette phase, le gradient de température entre les deux extrémités du tube est de 11°C et la température initiale du tube de -120°C n'est pas atteinte. Le faible débit de N_2 entraîne un faible transfert de chaleur par convection, d'où un refroidissement moins important du tube près de x=0 où la température du tube est d'environ -90°C. Aussi, la faible quantité de givre de CO_2 entraîne une récupération de froid inférieure à celle du cas précédent considérant $y_{co2} = 26\%$ et $\dot{m}_{n2} = 1{,}66 \times 10^{-3} kg/s\ (per\ tube)$.

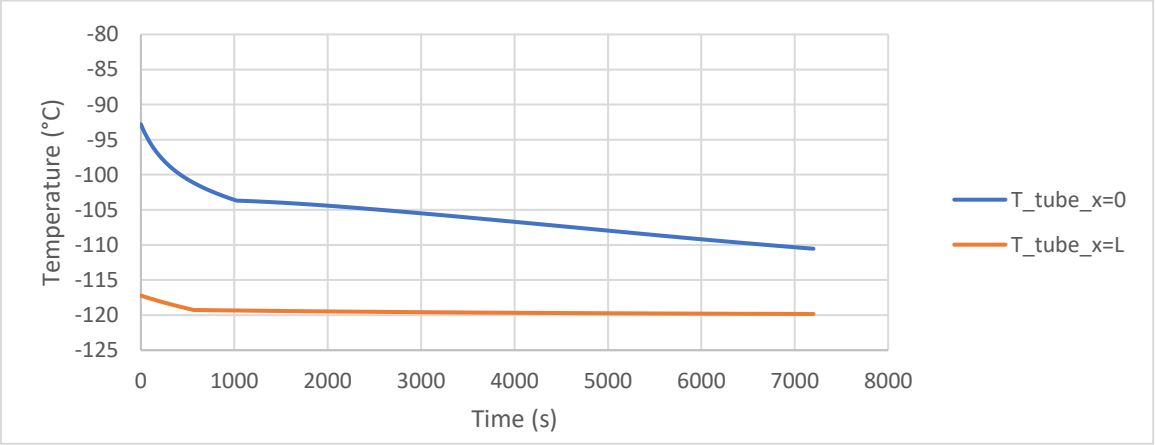

Figure F27: Evolution de la température du tube à ses extrémités lors du dégivrage du CO_2 dans le Cas 1

Cas 2 :

Le tableau F1 montre que la température du gaz de dégivrage a un effet limité sur le temps de dégivrage et un effet majeur sur la température du tube compte tenu du transfert de chaleur par convection entre le flux de N_2 et le « tube+givré ». Le flux de N_2 entre dans le HX de dégivrage à -135°C. Son débit massique est toujours considéré comme $\dot{m}_{n2} = 552\ kg/h = 0{,}000638 kg/s\ (per\ tube)$ même s'il peut être légèrement supérieur. Le dégivrage est terminé en t = 5860s. La figure F28 montre l'évolution de la température du tube; même si le gradient de température est toujours de 21,6°C, la température moyenne du tube est de -120,7°C. La conductivité thermique du tube étant élevée, il est possible d'homogénéiser la température dans tout le tube jusqu'à la fin de la phase de givrage.

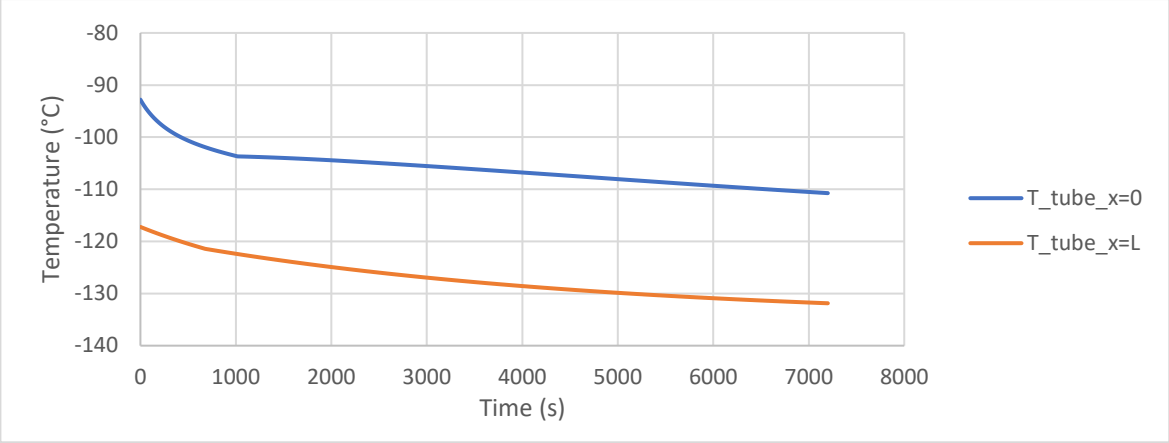

Figure F28: Evolution de la température du tube à ses extrémités lors du dégivrage du CO_2 dans le Cas 2

Même si $y_{co2} = 26\%$ dans le biogaz à l'entrée est considéré comme cas plus réaliste, le système pourrait être plus efficace pour des concentrations de CO_2 inférieures dans le biogaz à l'entrée, car le temps de dégivrage disponible sera plus long pour dégivrer moins de givre de CO_2. Le système peut devenir une partie d'un système hybride utilisant un procédé d'épuration de biogaz à faible coût pour atteindre des concentrations de CO_2 faibles mais non optimales, par ex. $y_{co2} = 10\%$, et le système présenté ici pourrait constituer une seconde étape pour compléter la valorisation du biogaz afin d'obtenir $y_{ch4} > 97{,}5\%$.

Cas 3:

Un autre cas est considéré avec $\dot{V}_{ch4,outlet} = 500\ Nm^3/h$ et $y_{co2} = 10\%$. Le débit de N_2 nécessaire pour la liquéfaction du biométhane devient $\dot{m}_{n2} = 1058\ kg/h = 0{,}0012245 kg/s\ (per\ tube)$, ce qui est presque le double du cas précédent, avec une petite différence en fonction de la quantité de CO_2 givré. En comparant avec le cas de $\dot{V}_{ch4,outlet} = 250\ Nm^3/h$, le temps de givrage est plus court (t=2690s) jusqu'à ce que $y_{ch4} < 97{,}5\%$ soit atteint et la quantité de CO_2 givré est plus importante car plus de CO_2 est disponible dans le biogaz.
Puisque le débit de N_2 est faible et est à -120°C, le tube est à une température supérieure à celle requise pour la prochaine phase de givrage, de la même manière que dans le cas précédent. Par conséquent, du N_2 à -135°C est envoyée pour la sublimation du CO_2. Le temps de dégivrage est t = 2520s (Figure F29), inférieur au temps de givrage alors acceptable. La température globale du tube est répartie entre -110,8°C et -130,5°C. Sa température moyenne finale est de -121,4°C et il dispose d'un temps d'homogénéisation de température t=170s avant le début de la prochaine phase de givrage (Figure F30).

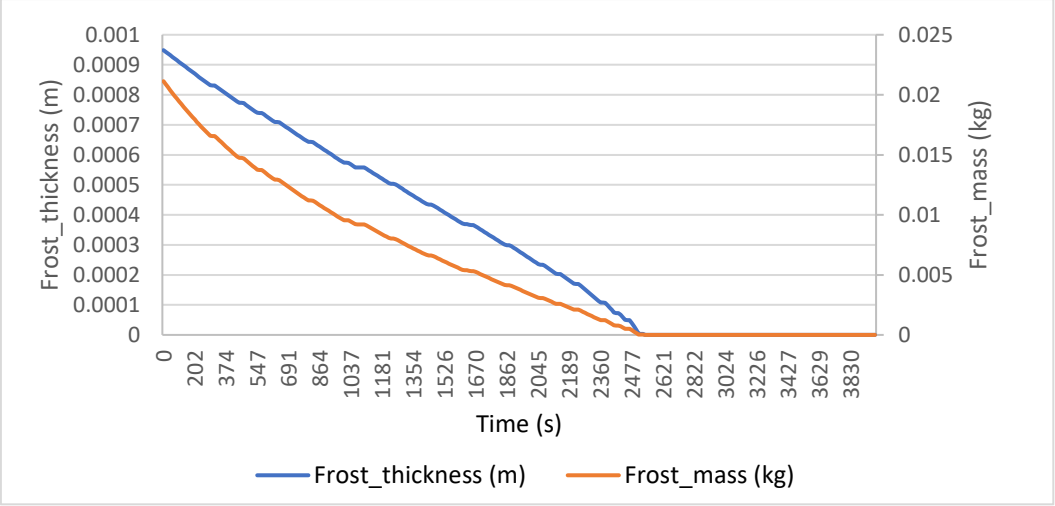

Figure F29: Evolution de la masse et de l'épaisseur du givre pendant la phase de dégivrage dans le Cas 3

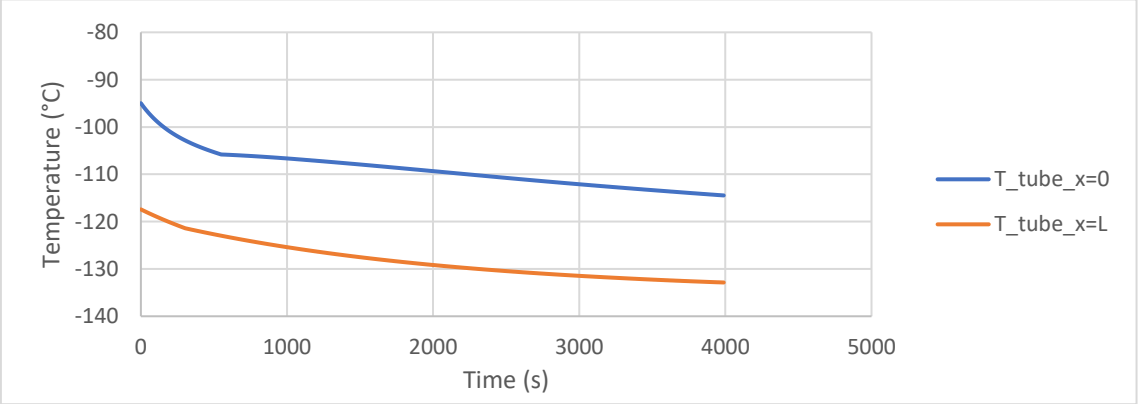

Figure F30: Evolution de la température du tube à ses extrémités lors du dégivrage du CO_2 dans le Cas 3

La diminution de la température initiale du tube augmente y_{ch4} à la sortie, comme illustré à la figure F13, où du méthane pur à 100% est produit au cours de la première heure. Si le système doit être intégré à un autre système produisant du biométhane à 85-90% de CH_4, il serait plus intéressant d'ajouter un tel système plus froid pour obtenir du méthane pur. Le même travail effectué dans la partie précédente doit être répété pour voir si le système peut effectuer le dégivrage à la même période de temps définie pour le givrage tout en récupérant le froid stocké dans le givre et en ramenant le tube à sa température initiale.

Conclusion

Dans ce chapitre, le concept de sublimation contrôlée a été détaillé. La sublimation du givre est induite par un gradient de concentration entre un flux de gaz se mettant en contact avec le givre et le givre lui-même. Le flux de gaz est plus froid que le givre pour ne pas se sublimer par transfert de chaleur convectif perdant ainsi son potentiel froid. Lorsque le CO_2 est dégivré, il draine la chaleur du HX pour compenser la perte de pression. Cela permettra la récupération du froid avec un effet mineur du transfert de chaleur par convection. Un modèle de sublimation contrôlée a été présenté et une étude de sensibilité a été réalisée pour étudier l'effet du débit massique et de la température du gaz de dégivrage sur le temps de dégivrage et la température finale du HX. L'objectif était de ramener le tube à sa température initiale (-120°C) avant la phase de givrage et de terminer le dégivrage dans un intervalle de temps égal à celui du givrage dans

le second HX. Les résultats de la simulation ont montré que le tube peut en effet être refroidi à des températures inférieures à sa température initiale, ce qui est impossible par la convection seule. Le problème était le temps de dégivrage. La concentration choisie pour CO_2 dans le biogaz en entrée avant la phase de givrage était élevée. On a constaté que pour mettre fin à la phase de givrage et de dégivrage en même temps, le débit de N_2 nécessaire pour le dégivrage est 4 fois supérieur à celui utilisé pour la liquéfaction du méthane. Plusieurs solutions ont été présentées afin de rendre le système plus efficace. L'arrêt du givrage est la solution la plus simple, mais la production de biométhane doit être arrêtée. Une étude sur les concentrations plus faibles de CO_2 dans le biogaz en entrée montre qu'une telle condition améliore le fonctionnement du système. Il est possible de mettre fin au givrage et au dégivrage en même temps avec la quantité de N_2 utilisée pour la liquéfaction du biométhane. Étant donné que la quantité de CO_2 givré sera inférieure à celle des concentrations élevées de CO_2 dans le biogaz entrant, la récupération du froid devra être soutenue par un flux de N_2 plus froid, ce qui augmenterait légèrement le temps de dégivrage mais ramènerait le HX à sa température initiale avant la prochaine phase de givrage.

Chapter 5: Experimental procedure

5.1. Global description of the experimental setup

The experimental apparatus known as "GPA" was constructed as part of the "Cryocap H_2" project and was used for many research studies concerning CO_2 condensation and deposition.

5.1.1. Objectives

Although this experiment was not designed specifically to fit in the operating conditions of CO_2 deposition and controlled sublimation that were presented in this thesis, many interesting results are expected from the tests that will be conducted in this experiment. The main objective of the experiment is to conduct an observational study on CO_2 frost formation and defrosting by controlled sublimation. If the results are to be compared with simulation results, the focus will be on the cold recovery instead of the frost formation and sublimation. The system can operate at a wide range of pressure (up to 40 bar), it uses pure CO_2 or a mixture of CO_2+N_2 for the study of frost formation. The experiment will be divided into two parts: frosting and defrosting. Each part has its own objectives and its own operating procedure that will be later detailed. Since the test bench was not specifically constructed for this thesis, the objectives foreseen for the frosting part will be limited to the observation of CO_2 frost formation and growth. Also, frost deposited will serve as initial operating conditions for the controlled sublimation phase which is the main part of this thesis.

The objectives of the defrosting part are the observation of the CO_2 defrost phenomena. It is very particular since phase change is from solid to gas without passing through a liquid phase. Since CO_2 frost will be formed from liquid CO_2, it will not have any pores and it will be all solid therefore the assumption of defrosting at the surface can be used since no fluid will infiltrate the frost. The second objective and most important is validating the principle of cold recovery by controlled sublimation as it was thoroughly detailed in chapters 1 and 4.

5.1.2. Overview of the experimental bench

The purpose of the GPA test bench is to observe and understand the process of forming CO_2 crystals from a pure liquid flow. The operating conditions of the system are temperatures below room temperature down to – 130°C and atmospheric pressure up to 40 bar.

Before going into detail about the operation of the experiment, the whole process can be briefly summarized in this simple explication: the system is mainly composed of two coaxial tubes and CO_2 crystallization takes place in between the two tubes. A coolant fluid is pumped into the inner tube after being cooled to a cryogenic temperature; a CO_2 flow passes inside the outer tube coming into contact with the outside of the inner tube. It is cooled due to the heat exchange with the coolant. The CO_2 outlet is closed and the system goes under pressure which liquefies the CO_2. The system is quickly depressurized and the liquid CO_2 solidifies. Then it can be sublimated by the heat infiltrated into the system or by introducing a gas flow that induces sublimation due to sensible heat and CO_2 concentration gradient between the frost surface and the gas flow. This was previously explained in chapter 2 and will be detailed later in this chapter. The 2D diagram in Figure 95 shows the main components of the test bench.

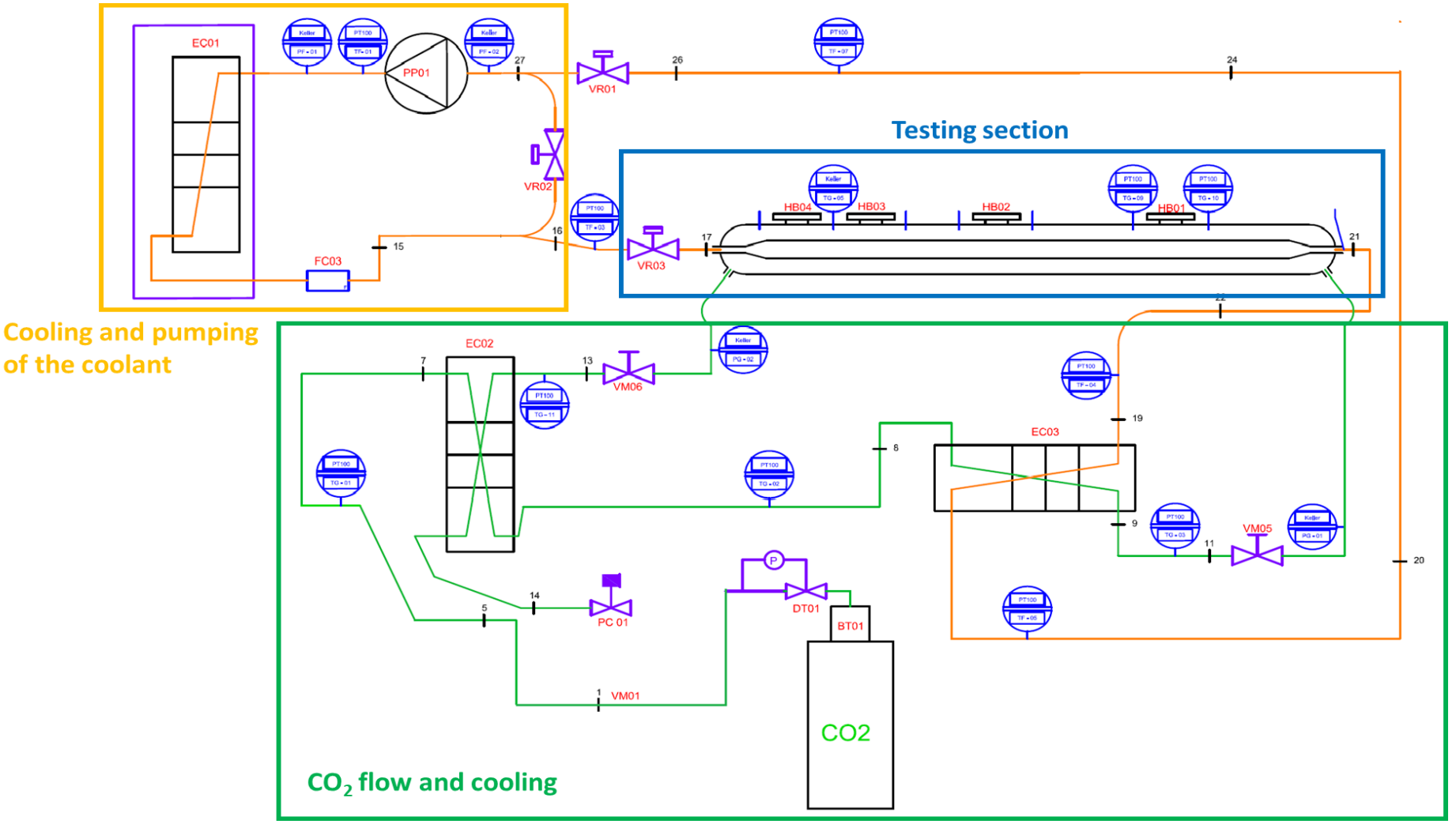

Figure 95: Flow diagram of the GPA test bench

It can be separated into 3 major parts:

1- Cooling and pumping of the coolant
2- CO_2 flow and cooling
3- Testing section

The coolant passes through a refrigeration cycle that reduces its temperature before entering the test section where a counter-current flow of CO_2 will cool, liquefy under pressure and eventually solidify when depressurization occurs. CO_2 entering the test section will be cooled by the CO_2 coming out of the test section and the coolant also exiting the test section. In the following, each part will be detailed with all its components and operating conditions.

5.2. Test bench operation

5.2.1. Data acquisition

In order to observe the CO_2 phase changes inside the outer tube, a digital microscope VHX-1000 is installed above the porthole HB-03. It is possible to observe the CO_2 liquefaction, solidification and sublimation. The VHX-1000 gives high resolution photos by using a 54-million pixels 3CCD handheld camera. It is equipped with an objective allowing a zoom up to 200x, a light source and a step-by-step motor that reduces vibrations of the equipment. The image can be visualized on the screen of a computer particular for VHX-1000.

Temperature sensors of type PT-100 are used to measure the gas and the coolant temperatures at different points in the test bench. They cover a wide temperature range going down to -200°C. Pressure was measured using KELLER pressure sensors.

The sensors are all connected to modules “Field Point” by “National Instrument”. For the temperature sensors FP-RTD-124, for the pressure and mass flowrate FP-AI-110 was used. This module allows the transformation of an electrical current to the real value corresponding to the entity measured.

For the gas pressures (in bar) the current “I” (in Amp) is transformed following the equation:

$$P = 6250 \times i - 25 \quad (5.1)$$

For the liquid coolant, two different pressure sensors were used before and after the pump:

$$P_{before} = 1875 \times i - 7.5 \quad (5.2)$$

$$P_{after} = 3125 \times i - 12.5 \quad (5.3)$$

The flowmeters were calibrated for methane and a transformation using the gas density at the given pressure must be used in order to obtain the final mass flowrate of CO_2 and N_2. The current “I” transmitted from the flowmeter gives the equivalent CH_4 mass flowrate. At the given pressure, the volumetric flowrate is calculated for CH_4. From this value it is possible to calculate the mass flowrate of CO_2 and N_2 passing through the flowmeter at the given pressure.

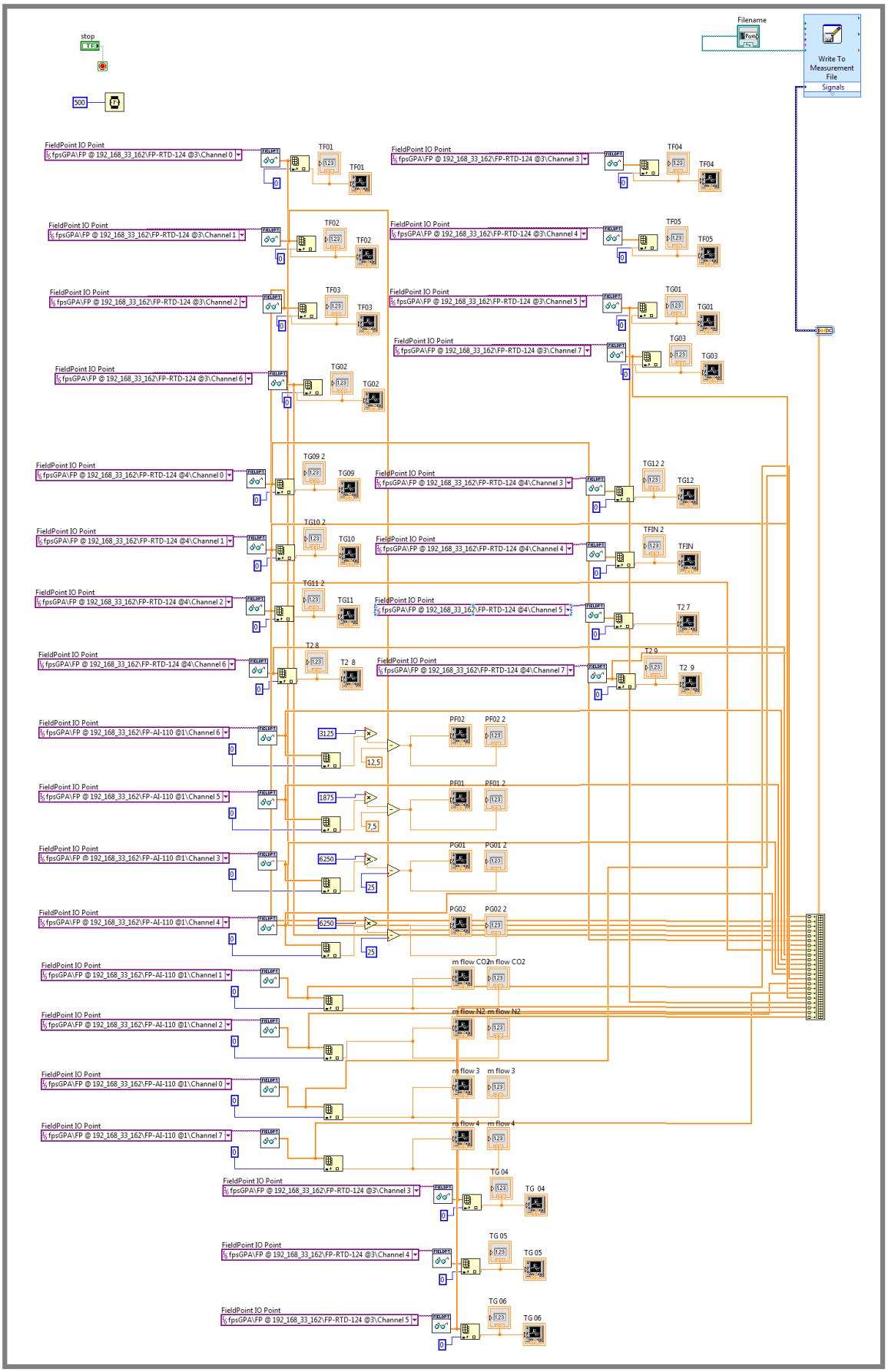

Figure 96: Labview data aquisition diagram for the test-bench

5.2.2. Experimental procedure

i. Cooling and pumping of the coolant

In the inner tube, a non-flammable refrigerant circulates at a low temperature using a special pump (AB pumps) which circulates a liquid at a minimum temperature of -130°C (Figure 97). It is a circuit that operates in a closed loop and transfers the cold available in the cooling system (Figure 98) to the liquid circulating in the other tube. The refrigerant fluid circuit is instrumented with temperature and pressure probes, as well as an Emerson ATEX Coriolis flowmeter, which measures fluid flow rates up to an operating temperature of -200°C (Figure 4). All these components are permanently connected to the computer. The maximum pressure in the refrigerant circuit is 5 bar. A safety valve is calibrated at 7bar (Figure 99). The fluid is NOVEC 7100, the technical data sheet of which is attached. The minimum operating temperature of the NOVEC 7100 fluid, and therefore that of the refrigerator, is -125°C. Below this temperature, the fluid passes in solid phase, which causes clogging of the tubes.

Figure 97: Refrigerant pump Brand AB (PP01) for flow rates up to 250 g / s NOVEC 7100 refrigerant

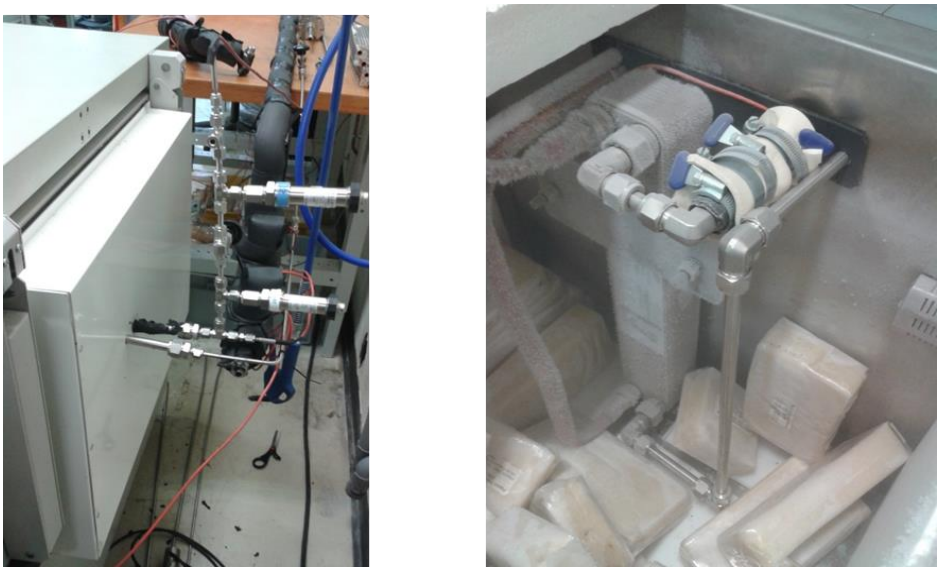

Figure 98: Cooling system (ECO1), minimum temperature of -164 ° C (LABOLOGIC Model LA - ZW128)

Figure 99: Safety valve for NOVEC 7100 non-flammable refrigerant (SP02).

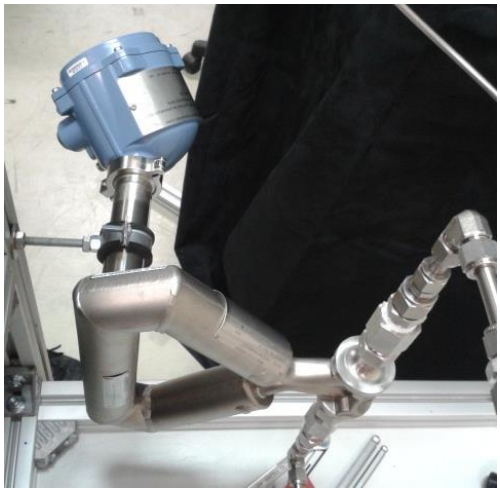

Figure 100: Emerson Coriolis refrigerant flowmeter -200 ° C

The coolant circuit followed leak tests for 36 hours of static test at ambient temperature and 7 bar of pressure under nitrogen, without leakage or loss of pressure. A second test with NOVEC 7100 was performed and proved a tightness tested for 6 weeks.

ii. CO_2 flow and cooling

The "green" lines in figure 95 represent the circuit where the pure CO_2 flows. A CO_2 container is firmly attached to the test bench and CO_2 flow is monitored by a system of calibrated Brooks flowmeters (Figure 101). At the outlet of the flowmeters, the gas is cooled down to a minimum temperature of -58°C and enters the outer tube in a liquid-gas mixture. When pressure is increased, it will be completely liquefied over its course. Depending on the flow rate, the cooling eventually leads to the formation of solid CO_2 on the wall of the coolant tube.

Figure 101: Brooks flow meters for each gas with inerting zone (FC01, FC02)

Figure 102: Observation windows of the CO_2 condensation phenomenon (HB01, HB02, HB03, HB04).

Figure 103: Portholes, seals and inerting / dehumidifying system

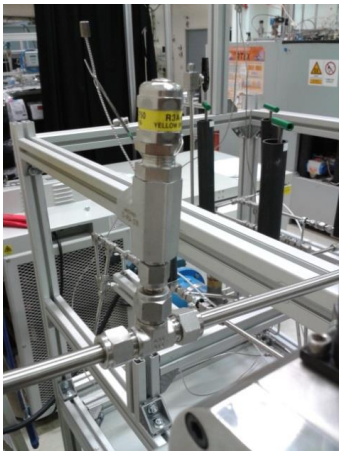

Figure 104: Safety valve calibrated at 50 bar for the gas circuit (SP01).

The system includes the following auxiliary components:

- Heat recovery exchanger (ECO2): This compact plate heat exchanger allows the cold recovery of the gases leaving the test section either it is pure CO_2 or a mixture of N_2+CO_2 when N_2 is added to accelerate the defrosting mecanism and achieve “controlled sublimation”. Thus, it is possible pre-cool the CO_2 entering the outer tube. The exchanger carries no other components than two temperature sensors (Figure 105). It is a gas-gas heat exchange but it can still operate if a portion of liquid CO_2 infiltrates inside it.

- Heat exchanger (ECO3): In this plate heat exchanger, the liquid coolant exiting the test section cools down the CO_2 flow exiting ECO2. It is then possible for the CO_2 flow to reach a temperature close to that of the coaxial tubes. The heat exchanger has two temperature sensors (Figure 105). This is a liquid-gas heat exchange (Figure 106).

- Heat resistance: This component is located on the outer wall of the coolant tube entering the cooling system. Perfectly insulated, either thermally and electrically, this resistance allows to vary the temperature of the coolant to accelerate the sublimation of CO_2 crystals in the concentric tubes at the end of the frosting phase in case the defrosting part isn’t being studied.

- Chromatograph: Gas composition measurements at the inlet and at the outlet of the concentric tubes are carried out using a chromatograph. The equipment is placed as far as possible from the test bench and communicates via two capillary tubes controlled by gas regulators. At the top of the chromatograph, a suction system has been put in place.

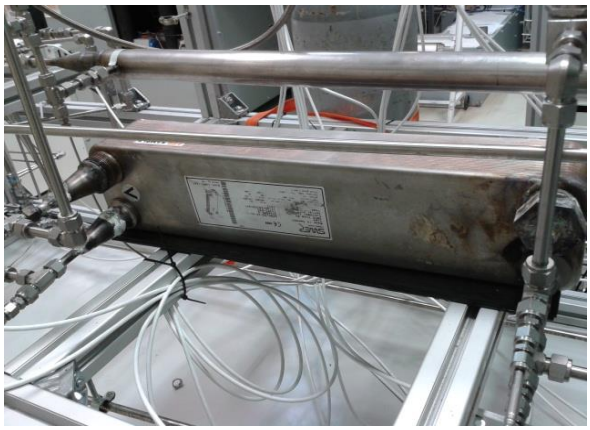

Figure 105: Heat recovery exchanger (ECO2).

Figure 106: Heat exchanger (ECO3).

iii. Test section

In the test section, it will be possible to observe the frost formation and its sublimation all while monitoring the temperature changes in the gas flow passing through the outer tube and the liquid coolant flow inside the inner tube. Each test will include three major parts and can be divided as follows: cooling of the CO_2 gas, pressurisation of cold CO_2 available in outer tube until liquefaction occurs, depressurisation and solidification of liquid CO_2 and finally CO_2 defrosting.

A) Cooling of CO_2 gas

Before injecting CO_2 into the system, some steps should be followed and some measures taken in order to guarantee the well-functioning of the experiment.

Start-up

The start-up is done following several steps:

- Checking the tightness of the gas circuit (see the last handling during the system shutdown phase - § Shutdown)
- Check the oxymeter (oxygen in atmosphere to avoid suffocation)
- Starting ventilation of the room to provide sufficient air renewal
- Start the pump (PP-01) on the refrigerant circuit until the CO_2 frosting temperature is reached (different for each test). The circuits 26 and 27 are connected during this phase, as well as the circuits 16 and 17.
- Getting the camera started and set the lenses to the observation porthole.
- Bottle BT01 and pressure regulator DT01 is open at test pressure +1 bar.
- The pressure at point P-01 (function of the test) is adjusted using the SP02 controller.

Filling of the coolant circuit

The filling of the coolant circuit is carried out via the reservoir RES1 and its circulation is guaranteed using a pump. It only takes place if the measured pressure in the cooling circuit shows values below atmospheric (vacuum). This means that the fluid density has changed and the amount in the circuit has been reduced (leakage). In order to expel the air present in the circuit, a second valve will be open until the first overflow drop. This valve will be placed at the high point and the delivery of the pump. The filling pressure will be checked using the P-03 pressure sensor. The three-way valves will be handled during filling to ensure that the entire circuit is filled.

CO_2 circulation and cooling

Now that the coolant and the CO_2 are circulating, it is possible to monitor the pressure of the CO_2 flow during the cooling phase, at the inlet and outlet of the test section. The cooling phase is carried out for about 4 hours, until the test bench reaches the operating temperature.

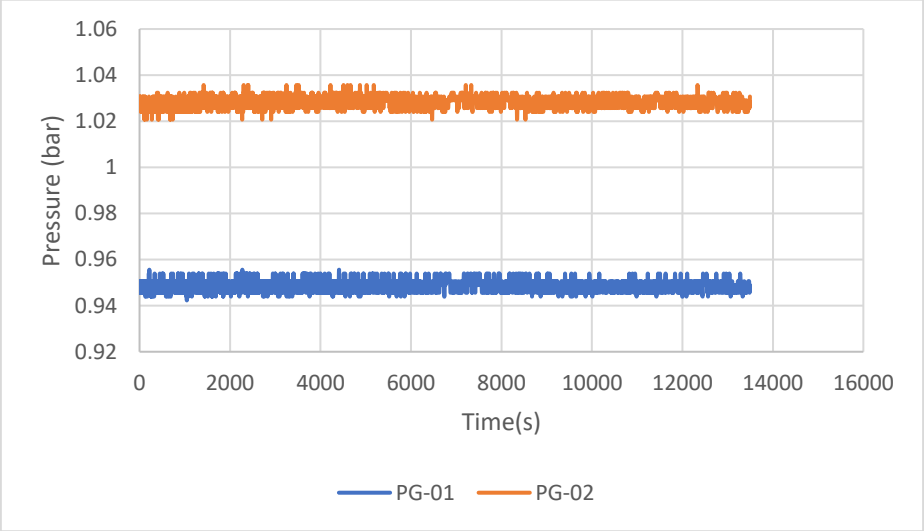

Figure 107: Pressure of the CO_2 gas at the inlet (PG-01) and outlet (PG-02) of the test section

Figure 107 shows that PG-01 is the pressure at the inlet of the test section and PG-02 the pressure at the outlet of the test section.

CO_2 passing through the test section is cooled by the coolant flow inside the inner tube of the coaxial heat exchanger. The cold CO_2 exiting the test section via VM-06 can be used to cool down the CO_2 flow from the heat exchanger (ECO02). Also, the coolant exiting the test section can be used to further cool the CO_2 before entering into the heat exchanger (ECO03).

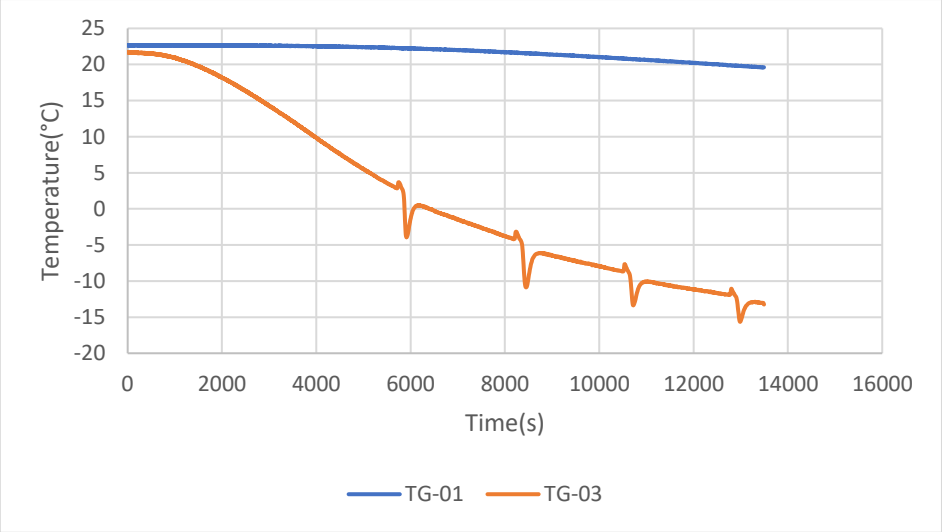

Figure 108: CO_2 gas temperature at the container outlet and at the inlet of the test section

The temperature of the CO_2 exiting the container (blue line in Figure 108) remains at room temperature at around 23°C. As the pressure of the bottle decreases, its temperature slightly decreases; also, the coolant flow reduces the temperature of the whole system. At the outlet of the second heat exchanger and just before entering the test section TG-03 (orange line) decreases as the CO_2 flow is mainly cooled by the coolant exiting the test section.

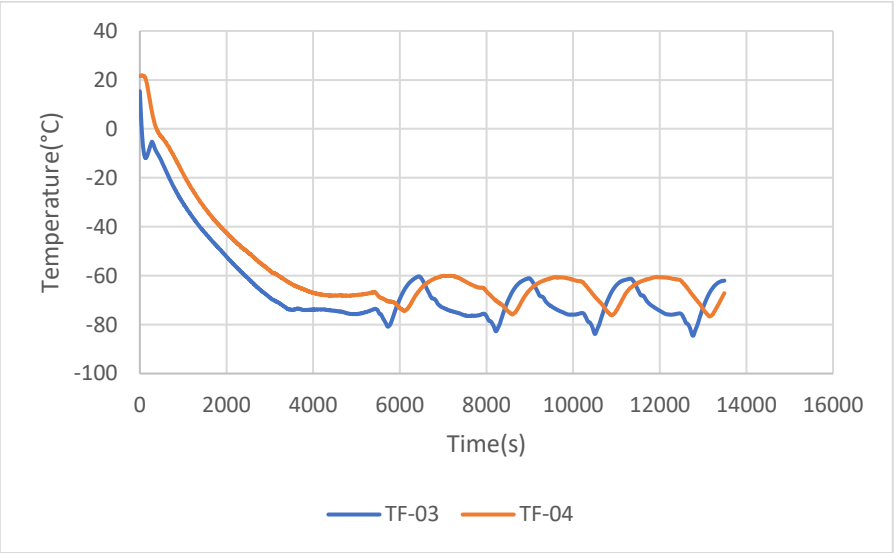

Figure 109: Temperature of the coolant fluid gas at the inlet (TF-03) and outlet (TF-04) of the test section

During the CO_2 cooling phase, the liquid coolant is also passing through the refrigeration unit where its temperature decreases (Figure 109). The jumpy cyclic behaviour is due to the refrigeration unit turning on and off automatically. The coolant heats up in the heat exchanger ECO03 where CO_2 gets cooled down before entering the test section.

In the co-axial tubes, the coolant passes inside the inner tube as the CO_2 passes in counter-current inside the outer tube and gets cooled down by convective heat transfer. The temperature along the CO_2 gas inside the test section can be found by monitoring TG-10 and TG-09 near the CO_2 inlet to the test section (Figure 95).

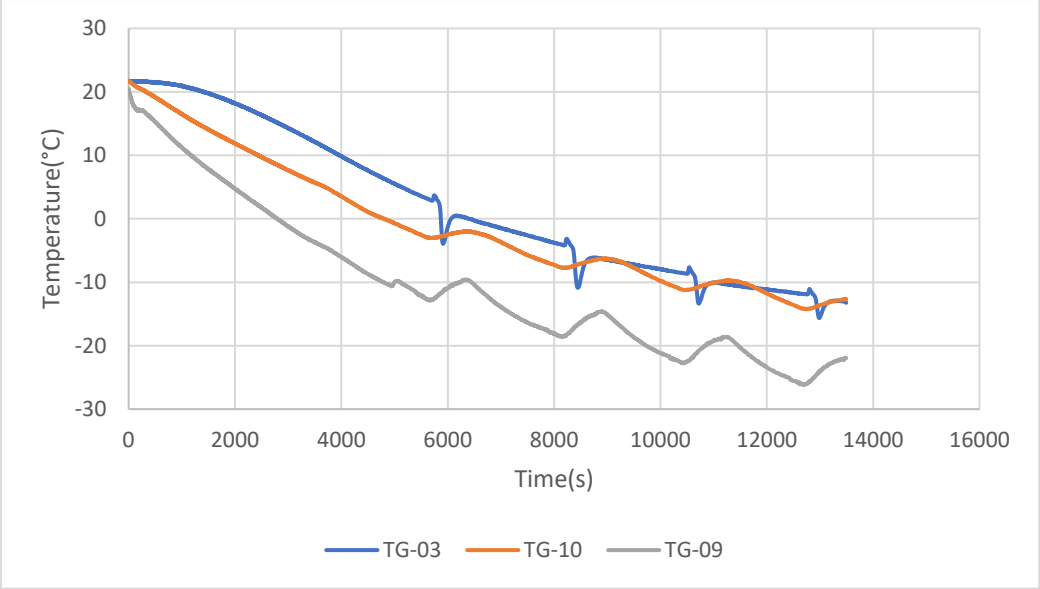

Figure 110: CO_2 gas temperature at different positions in the coaxial heat exchanger

B) Pressurisation and liquefaction of CO_2

In order to liquefy the cold CO_2 available in the test section, its pressure is increased. The liquefaction targets a formation of consistent solid phase without pores that will enable to assess the behaviour of controlled sublimation defrosting by simultaneously reducing the number of variables impacting the physical phenomenon. This pressure increase will be limited to 7bar. The CO_2 phase diagram presented in Figure 7 shows that a minimal temperature of ~-49°C is required to achieve liquefaction. The CO_2 valve at the outlet of the test section VM-06 is closed and pressure of the CO_2 flow from the container is increased. Pressure begins to rise in the system.

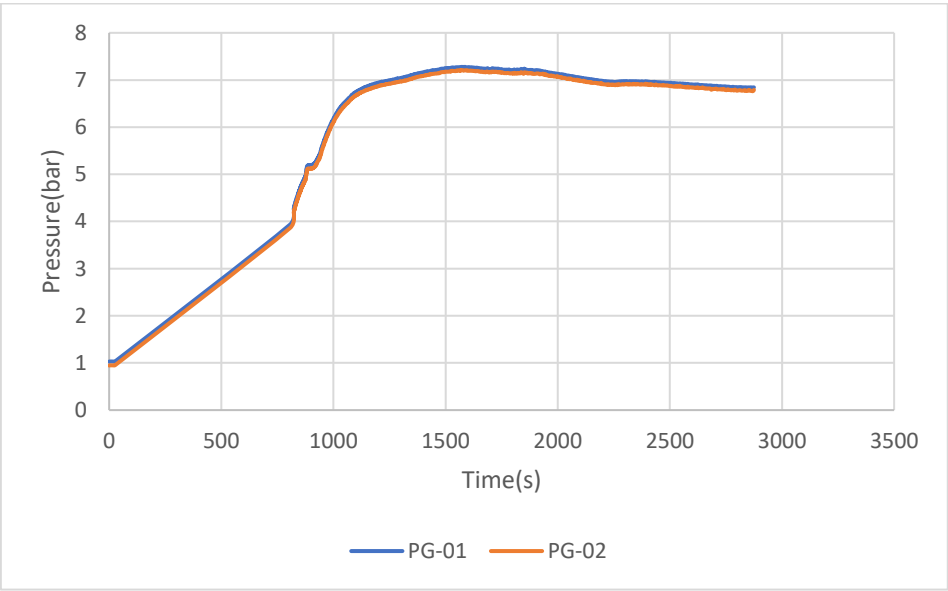

Figure 111: Pressure of the CO_2 gas at the inlet (PG-01) and outlet (PG-02) of the test section

When P=5.6bar is reached, it becomes possible to liquefy CO_2 as the triple point is passed on the phase diagram. Figure 112 shows the liquefaction starts as droplets of CO_2 start to form

on the outer surface of the inner tube. As pressure increases, more CO_2 is liquefied until the outer tube is filled with liquid CO_2.

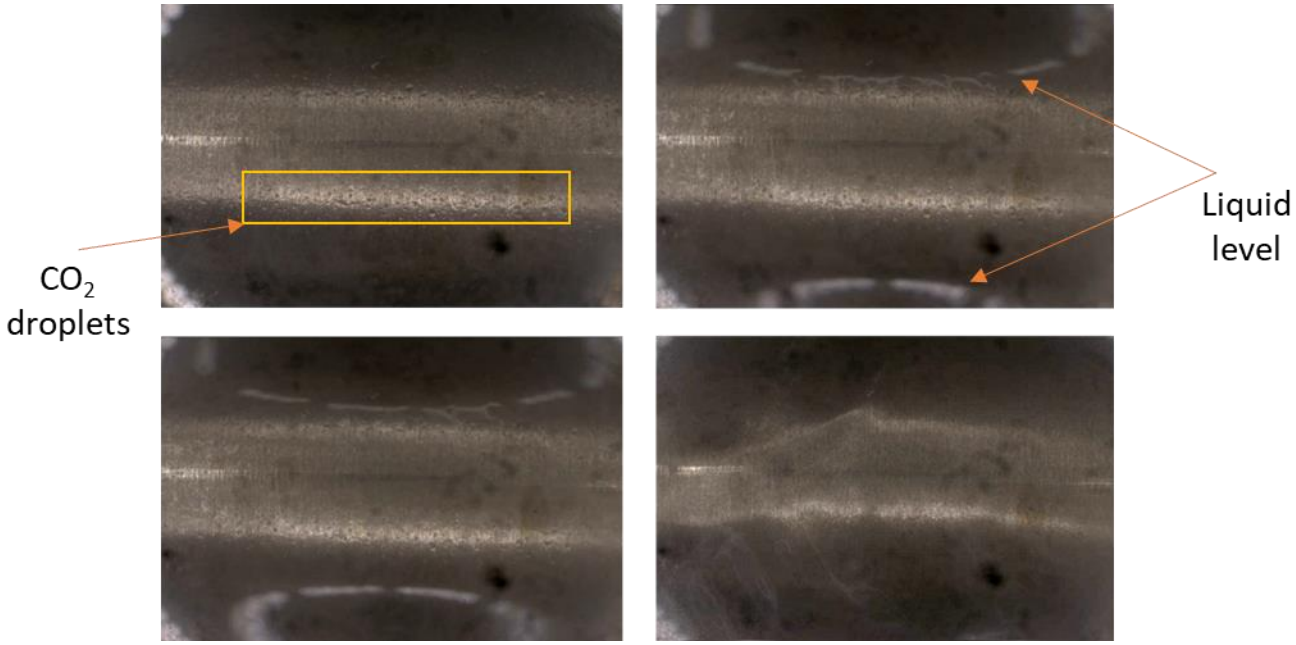

Figure 112: Local visualisation of CO_2 liquefaction in the coaxial tube

Before this phase, all the heat exchange between the coolant and the CO_2 flow is convective heat transfer through the inner tube. When CO_2 starts to liquify, its phase change requires more cooling load and the temperature of the coolant increases much more than in convective cooling phase. This allows the exact setting of the liquefaction time interval. Compared to the temperature gradient in Figure 109 where only CO_2 cooling by convection occurs, the effect of the latent heat transfer during the liquefaction phase can be observed in Figure 113 which shows a temperature gradient of the coolant between the outlet and the inlet of the test section of about 40°C.

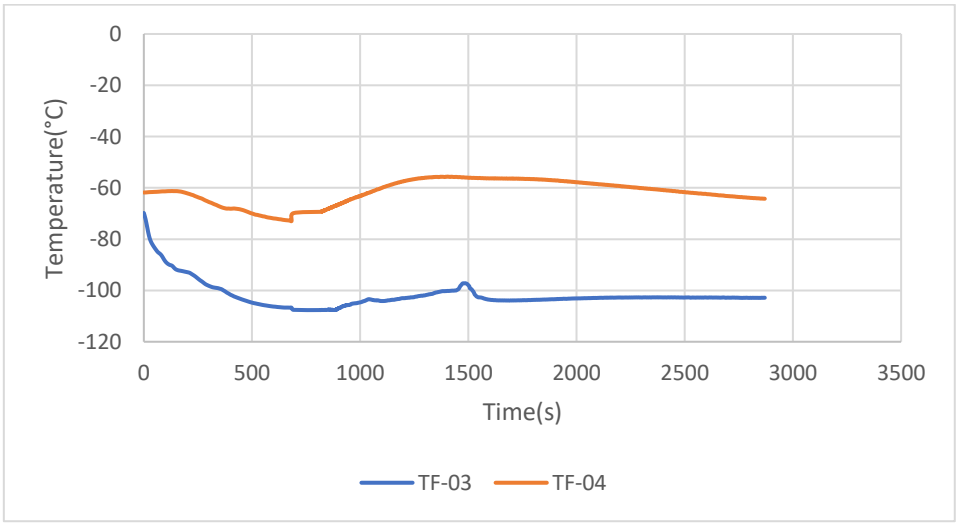

Figure 113: Temperature of the coolant fluid gas at the inlet (TF-03) and outlet (TF-04) of the test section

C) Depressurisation and solidification of liquid CO_2

The space between the inner and outer tubes of the test section is at low temperature and high pressure, it now contains liquid CO_2. The pressure of the CO_2 flow from the container is decreased and VM-06 (the valve at the CO_2 outlet of the test section) is opened. The pressure in the system quickly decreases and so does its temperature. CO_2 pressure at the outlet of the test section might have a delay in depressurisation caused by frost formation in the exhaust tube resulting in its blockage. In Figure 114, the blue line represents the inlet pressure which decreases almost instantaneously to atmospheric pressure as the valve VM-06 is opened. The orange line representing the gas pressure at the outlet of the test section shows a delay of about t=300s before reaching atmospheric pressure.

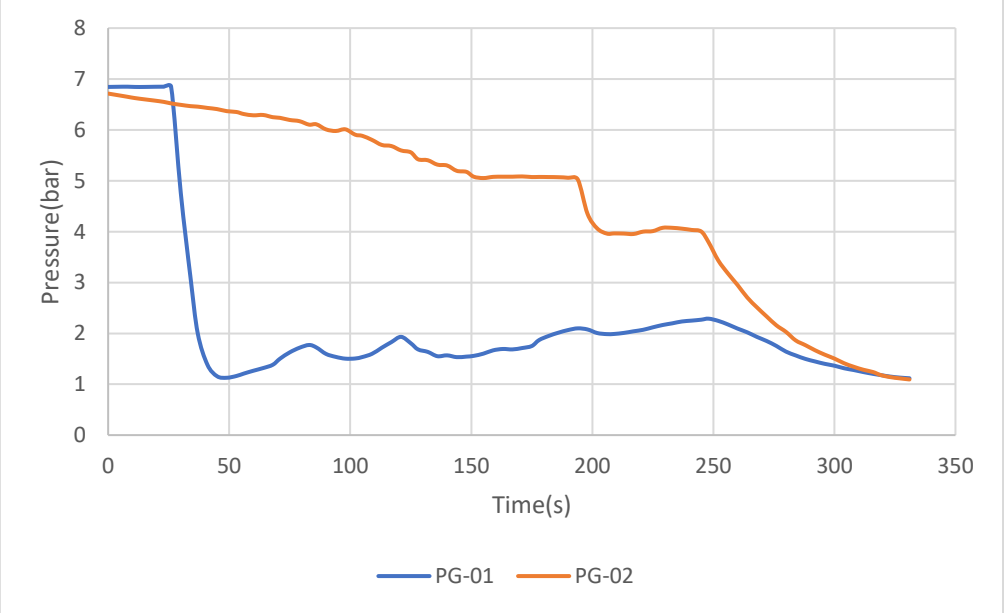

Figure 114: Pressure of the CO_2 gas at the inlet (PG-01) and outlet (PG-02) of the test section

The conditions at which depressurization is launched affects the CO_2 solid formation. If the liquid CO_2 has filled the outer tube, frost formation will cover the whole space between the inner and outer tube as it is shown in Figure 115. The frost is observed through the porthole HB-03. Water vapour contained in humid air surrounding the test bench might cause some ice formation on the outside of the porthole glass and it should be continuously scraped off.

The refrigerator that keeps the coolant fluid at a low temperature is turned off. The coolant flow heats up quickly before entering the test section but it cools down inside the test section by convection with the CO_2 frost formed. This causes more sublimation to occur.

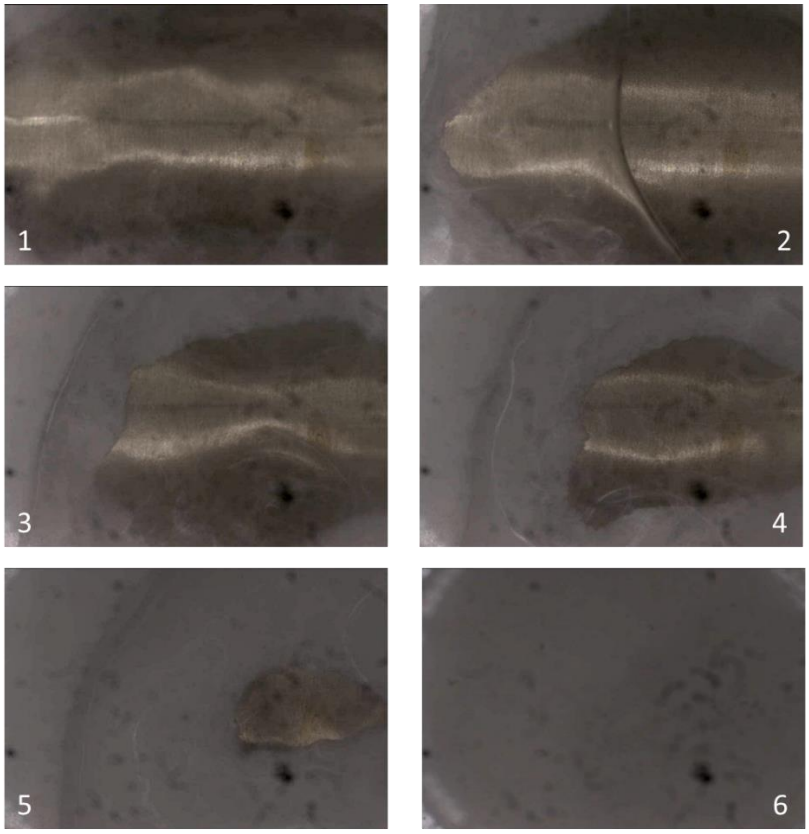

Figure 115: Local visualisation of CO_2 solidification from its liquid phase

D) Defrosting the CO_2 frost

This part covers the most important objective of this experiment: **validating cold recovery by controlled sublimation.** The system is at atmospheric pressure, CO_2 frost is accumulated in the space between the inner and outer tube. A small flow of N_2 is introduced to the system, its circulation is blocked the first few moments before it finds its path inside the frost.

The refrigerator remains turned off. The temperature of the cooling fluid at the inlet of the test section increases (blue line in Figure 116). Nevertheless, its temperature at the outlet of the test section (orange line) continues to decrease.

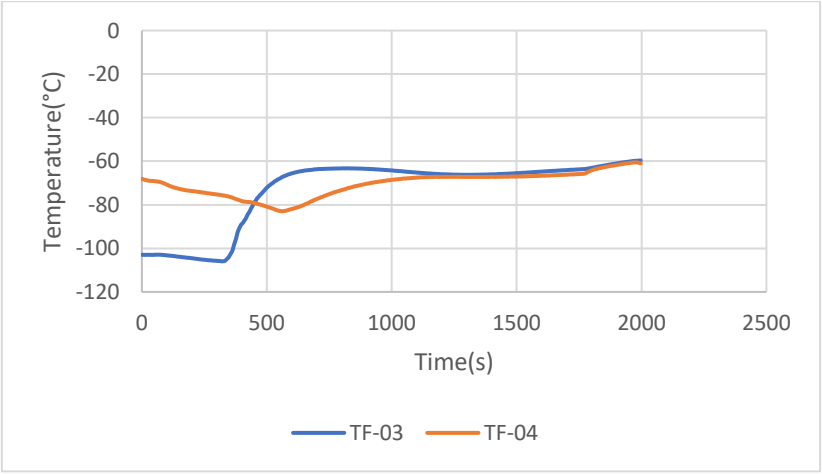

Figure 116: Temperature of the coolant fluid gas at the inlet (TF-03) and outlet (TF-04) of the test section

A small portion of the defrosting phenomenon was captured. If compared with the images taken for the frosting, it can be deduced that the first part to undergo defrosting is the last part to have witnessed CO_2 deposition.

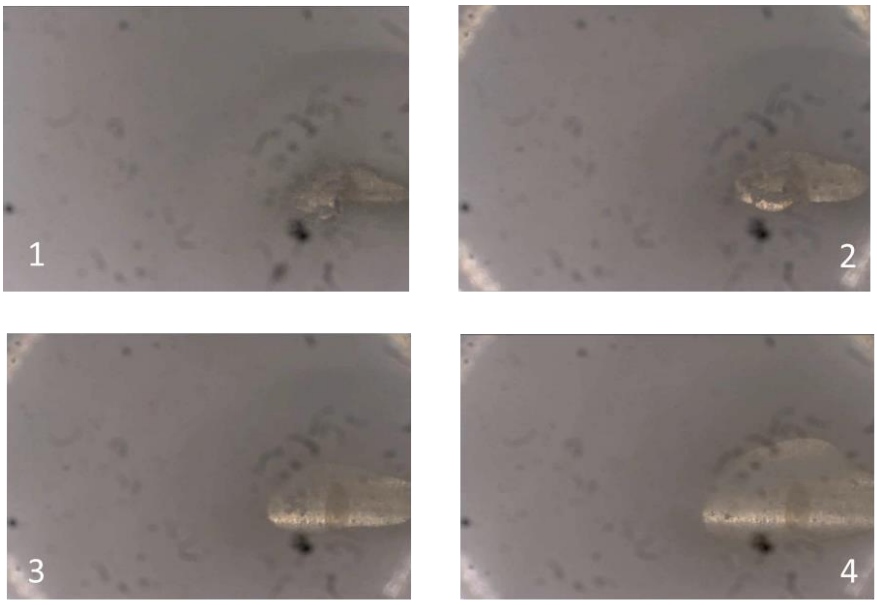

Figure 117: Defrosting of CO_2 frost by a N_2 flow at several stages (Δt (s) from start of defrost = 420, 700, 905, 1165)

The frost sublimates for four reasons: heat infiltrated from the outside, convective heat transfer with N_2 flow, convective heat transfer with the coolant flow when it reaches a temperature higher than that of the frost and the controlled sublimation caused by the CO_2 concentration (or vapour pressure) gradient between the surface of the CO_2 frost and the N_2 flow. The cooling of the N_2 flow will not result in a temperature decrease of the coolant flow, on the contrary it will heat up the frost thus decreasing the heat transfer from the coolant towards the CO_2 frost.

In order to better understand if the controlled sublimation is actually cooling down the coolant fluid, the three graphs of pressure, CO_2 and N_2 mass flowrate and the temperature of the coolant fluid at the inlet and the outlet of the test section will be merged and represented in Figure 118 which will be divided into 3 time sections for every part of the experimental procedure.

In the first time section from 0 to 2875 s, the pressure is increased in the system (Figure 118.b). The temperature of the coolant at the outlet (TF-04) increases as the CO_2 liquefies (orange line in Figure 118.a). At t=2850s, VM-06 is opened and depressurization starts. CO_2 frost begins to form and TF-04 continues to decrease by convection with the frost. The CO_2 flow is stopped and the N_2 container is connected to the system instead of CO_2. When the N_2 flow is introduced to the system at t=3206s (grey line in Figure 118.c), the outlet temperature of the coolant shows a higher slope of decrease (green line in Figure 120.a) than that without N_2 flow. At the point A, the refrigerant unit is stopped and the inlet temperature of the coolant fluid starts increasing but the temperature of the outlet coolant continues to decrease due to the “controlled sublimation” and the convection with the frost. Finally, the two temperatures meet as the system comes to equilibrium.

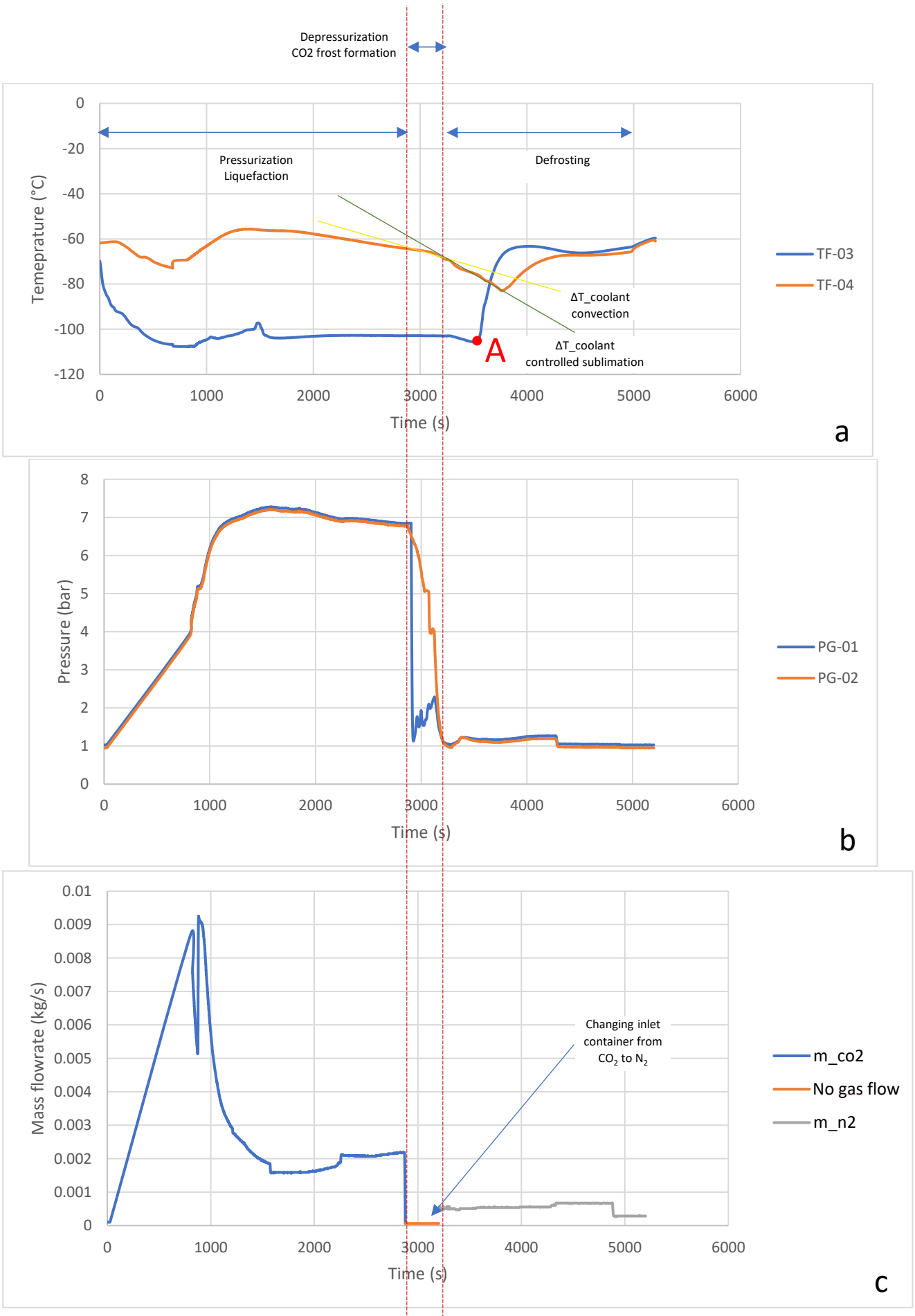

Figure 118: (a) Evolution of coolant temeprature, (b) CO_2 gas pressure and (c) mass flow of CO_2 and N_2 during CO_2 liquefaction and solidifaction phases

Another test was conducted where CO_2 follows all the previous steps consecutively: cooling, pressurisation, liquefaction, depressurization then solidification. The defrost phase starts with a low stream of CO_2. The refrigerator that keeps the coolant at low temperature is turned off and the temperature of the whole system starts increasing (Figure 119.a). At time t=592s, a high flow of N_2 (grey line in Figure 119.b) is introduced to the system even though not much solid CO_2 was still available. No cooling load was added to the system and yet, the temperature of the coolant at the outlet of the test section (orange line in Figure 119.a) starts decreasing even though it had been constantly increasing. The N_2 introduced served as defrosting gas in controlled sublimation and heat was recovered from the coolant fluid leading to a decrease in its outlet temperature.

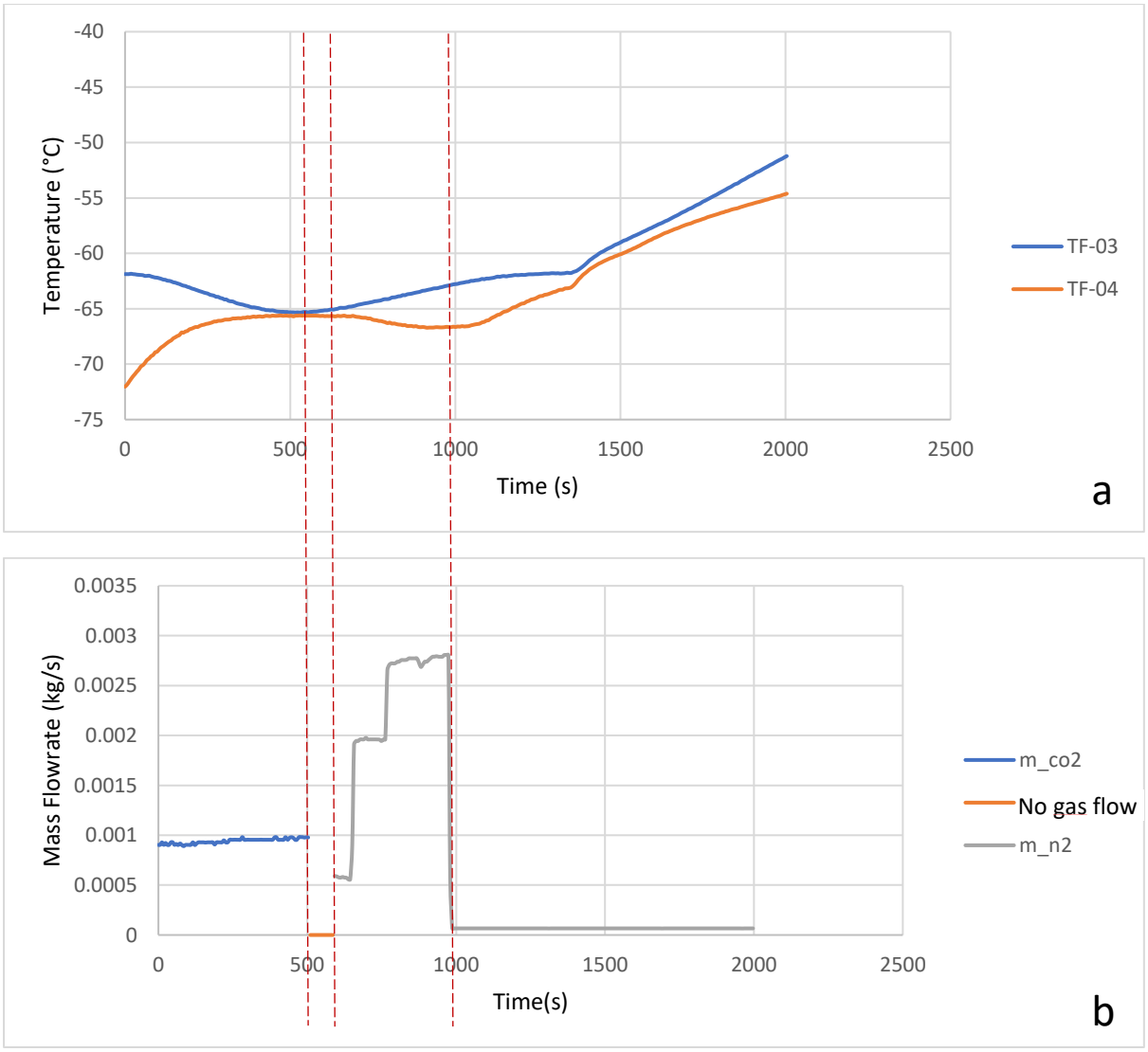

Figure 119: Evolution of coolant temperature and mass flow of CO_2 and N_2 during CO_2 defrosting phase

As CO_2 gets transported by the N_2 flow due to the CO_2 concentration gradient at the frost/N_2 interface, the vapour pressure at the surface of the frost decreases and heat is pumped from the coolant to compensate the pressure loss leading to a decrease in the coolant's outlet temperature. That is the principle of "cold recovery by controlled sublimation".

5.3. Validation of the defrosting model

As it was mentioned before, the conditions of the experiment and its original objectives do not correspond to those of the defrosting model developed in this thesis. Nevertheless, it is possible to use the results found to validate the defrosting model presented in chapter 4. The case scenario used to validate the model is the one shown in figure 116.

The following assumptions should be considered:

- The CO_2 frost formed is a solid medium and not porous, its density is equal to that of solid CO_2 found in Figure 28.
- The frost deposition is homogenous in both thickness and mass distribution along the outside surface of the inner tube. This will serve as the frost initial conditions at the beginning of the defrosting phase.
- The temperature at the surface of the frost is equal to that of the gas passing above it
- The temperature of the frost near the tube surface is equal to that of the coolant. Thus, all initial and boundary conditions are set.

The geometry and conditions of the model are changed in Dymola to fit those of the experiment. However, results found from modelling differ from experiment results and observation. One of the major contributions of the work on this thesis, besides the proposal of the controlled sublimation, is that solid generates preferential flow channels. As it can be observed in Figure 117, the sublimation of CO_2 shows to be heterogeneously driven. There is a point in which the removal of the solid phase is successful, while the rest of the tube remains completely covered by solid. The latter indicates that the flow of gas in contact with the solid phase will find the less pressure drop pathway and hence, the area of interface in which the gas and the solid are in contact is dramatically reduced compared to the theoretical one. Moreover, this preferential pathway means that the gas flow will show speeds and transfer coefficients that completely differ from theoretical ones. The arguments mentioned here above are the reason why the modelling results are not fit to the observations. A perspective for this work is to consider the use of controlled shapes on the plates which will enable the homogeneous distribution of solid and gas flow (avoid preferential pathways), and, potentially, the use of shorter frost/defrost cycles to generate only thin layer of solid phase that will render the gas flow during the defrost phase to be homogeneously spread in the system.

Chapitre 5: Procédure expérimentale

5.1. Présentation du banc d'essai

Le banc d'essai appelé «GPA» a été construit dans le cadre du projet «Cryocap H2» et a été utilisé pour de nombreuses études concernant la condensation et le givrage du CO_2.

5.1.1. Objectifs

Bien que cette expérience n'ait pas été conçue spécifiquement pour s'adapter aux conditions de fonctionnement du givrage de CO_2 et de la sublimation contrôlée présentées dans cette thèse, de nombreux résultats intéressants sont attendus. Le protocole expérimental du banc a été modifié pour servir les objectifs de cette thèse. Cette expérience vise principalement de mener une étude qualitative de la formation du givre et du dégivrage de CO_2 par sublimation contrôlée. Si les résultats doivent être comparés aux résultats de la simulation, l'accent sera mis sur la récupération du froid au lieu de la formation de givre et de la sublimation. Le système peut fonctionner dans une large plage de pression (jusqu'à 40 bars). Il utilise du CO_2 pur ou un mélange de CO_2+N_2 pour l'étude de la formation de givre. L'expérience est divisée en deux parties : le givrage et le dégivrage. Chaque partie a ses propres objectifs et son propre mode opératoire qui sera détaillé ultérieurement. Les objectifs prévus pour la partie de givrage se limiteront à l'observation de la formation et de la croissance du givre de CO_2. Aussi, le givre déposé servira comme état de fonctionnement initial pour la phase de sublimation contrôlée qui constitue la partie principale de cette thèse.

Les objectifs de la partie « dégivrage » sont l'observation des phénomènes de dégivrage du CO_2. Il s'agit d'un cas particulier, car le changement de phase s'opère directement du solide au gaz sans transiter par une phase liquide. Étant donné que le givre CO_2 se forme à partir de CO_2 liquide, il n'y aura pas de pores et il sera complétement solide. Le deuxième objectif et le plus important est de valider le principe de la récupération à froid par sublimation contrôlée tel qu'il a été détaillé aux chapitres 1 et 4.

5.1.2. Vue d'ensemble du banc d'eesai

Le banc d'essai GPA a pour but d'observer et de comprendre le processus de formation de cristaux de CO_2 à partir d'un écoulement de liquide pur. Les conditions de fonctionnement du système sont des températures inférieures à - 130°C et une pression entre 1 à 40 bars.

Le système est principalement composé de deux tubes coaxiaux et la cristallisation du CO_2 a lieu entre les deux tubes. Un fluide caloporteur est pompé dans le tube interne après avoir été refroidi à une température cryogénique ; un flux de CO_2 passe à l'intérieur du tube externe et entre en contact avec la surface externe du tube interne. Il est refroidi par échange de chaleur avec le liquide de refroidissement. La sortie de CO_2 est fermée et le système est mis sous pression, ce qui liquéfie le CO_2. Le système est dépressurisé rapidement et le CO_2 liquide se solidifie. Ensuite, il peut être sublimé par la chaleur infiltrée dans le système ou par l'introduction d'un flux de gaz qui induit une sublimation due à un gradient de concentration de CO_2 et de chaleur sensible entre la surface de givre et le flux de gaz. Ce phénomène a déjà été expliqué au chapitre 2 et sera détaillé plus tard dans ce chapitre. Le diagramme 2D de la Figure F31 montre les principaux composants du banc d'essai.

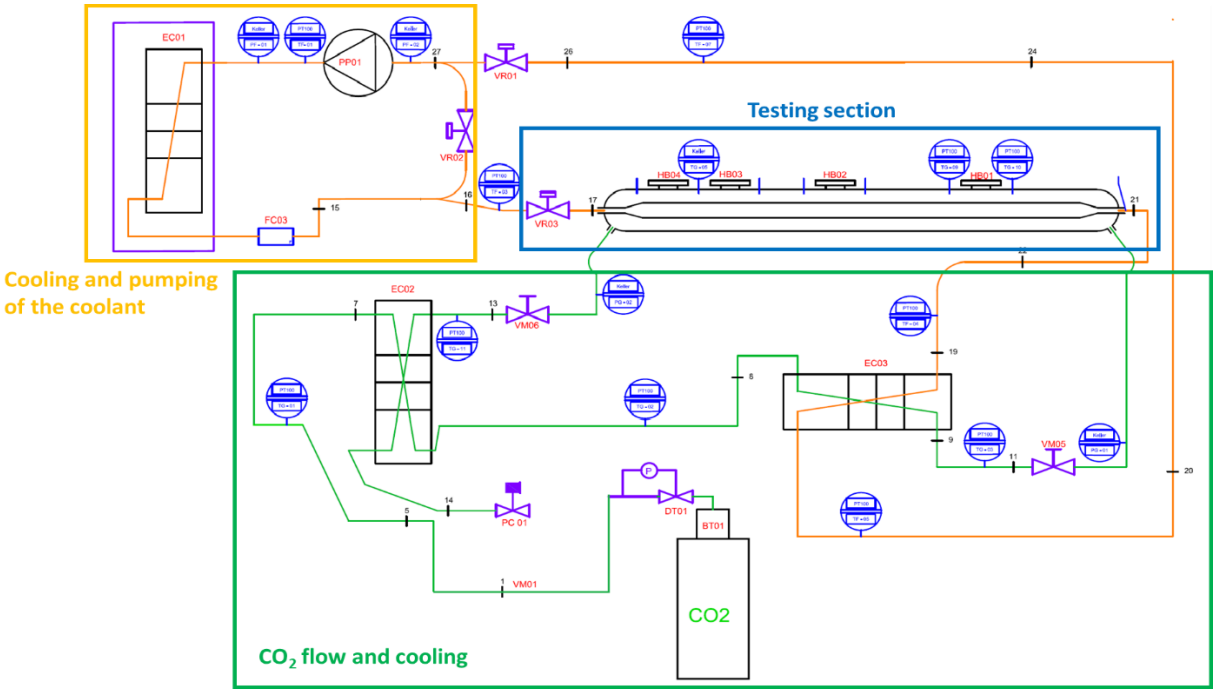

Figure F31: Le banc d'essai GPA

Le liquide de refroidissement passe par un cycle de réfrigération qui réduit sa température avant d'entrer dans la section de test où un flux de CO_2 en contre-courant se refroidit, se liquéfiera sous pression et se solidifie éventuellement par dépressurisation du système. Le CO_2 entrant dans la section de test est refroidi par le retour du flux de CO_2 ainsi que le réfrigérant sortants de cette section. Dans la suite, chaque partie sera détaillée avec tous ses composants et conditions de fonctionnement.

5.2. Fonctionnement du banc d'essai

5.2.1. L'acquisition des données

Afin d'observer les changements de phase du CO_2 à l'intérieur du tube externe, un microscope numérique VHX-1000 est installé au-dessus du hublot HB-03. Il est possible d'observer la liquéfaction, la solidification et la sublimation du CO_2. Le VHX-1000 offre des photos de haute résolution en utilisant une caméra portable 3CCD de 54 millions pixels. Il est équipé d'un objectif permettant un zoom jusqu'à 200x, d'une source de lumière et d'un moteur qui réduit les vibrations de l'équipement. L'image peut être visualisée sur l'écran d'un ordinateur particulier pour le VHX-1000. Les capteurs de température de type PT-100 sont utilisés pour mesurer les températures du gaz et du liquide de refroidissement à différentes positions du banc d'essai. Ils couvrent une large plage de température allant jusqu'à -200 ° C. La pression a été mesurée à l'aide de capteurs de pression KELLER.

5.2.2. Procédure expérimentale

i. Refroidissement du fluide caloporteur

Dans le tube interne, un réfrigérant (fluide caloporteur) non inflammable circule à basse température à l'aide d'une pompe spéciale qui peut faire circuler le liquide à température minimale de -130°C. Le fluide caloporteur est refroidi dans un circuit fermé de réfrigération. Le circuit du fluide frigorigène est équipé de sondes de température et de pression, ainsi que

d'un débitmètre Emerson ATEX Coriolis, qui mesure les débits de fluide jusqu'à une température de fonctionnement de -200°C. Tous ces composants sont connectés en permanence à l'ordinateur. La pression maximale dans le circuit de réfrigérant est de 5 bars. Une soupape de sécurité est calibrée à 7 bars. La température minimale de fonctionnement du fluide NOVEC 7100 (réfrigérateur), est de -125°C. En dessous de cette température, le fluide passe en phase solide, ce qui provoque le blocage des tubes.

ii. La circulation et le refroidissement du CO_2

Les lignes « vertes » sur la Figure F31 représentent le circuit dans lequel le CO_2 pur circule. Une bouteille de CO_2 est fermement attachée au banc d'essai et le débit de CO_2 est contrôlé par un débitmètre Brooks. À la sortie du débitmètre, le gaz est refroidi à une température minimale de -58°C et entre dans le tube externe. Lorsque la pression augmente, il est complètement liquéfié au cours de son parcours. En fonction du débit, le refroidissement conduit finalement à la formation de CO_2 solide sur la paroi du tube de refroidissement

- Échangeur de chaleur (ECO2): Cet échangeur de chaleur à plaques compact permet la récupération du froid des gaz quittant la section d'essai. Ainsi, il est possible de pré-refroidir le CO_2 entrant à la section de test. Il s'agit d'un échange de chaleur gaz-gaz, mais il peut toujours fonctionner si une partie du CO_2 liquide s'infiltre à l'intérieur.

- Échangeur de chaleur (ECO3): dans cet échangeur à plaques, le liquide de refroidissement sortant de la section d'essai refroidit le flux de CO_2 sortant d'ECO2. Il est alors possible que le débit de CO_2 atteigne une température proche de celle des tubes coaxiaux. Il s'agit d'un échange thermique gaz-liquide.

iii. Section de test

Dans la section d'essai, il est possible d'observer la formation du givre et sa sublimation tout en surveillant les variations de température dans le flux de gaz traversant le tube externe et le flux de liquide de refroidissement dans le tube interne. Chaque essai peut être divisé en trois parties principales : refroidissement du gaz CO_2, pressurisation du CO_2 froid disponible dans le tube extérieur jusqu'à sa liquéfaction, dépressurisation et solidification du CO_2 liquide et enfin dégivrage du givre de CO_2.

A) Refroidissement du flux de CO_2 gaz

Le CO_2 qui traverse la section d'essai est refroidi par le flux de liquide de refroidissement traversant le tube interne de l'échangeur de chaleur coaxial. Le CO_2 froid sortant de la zone de test via VM-06 peut être utilisé pour refroidir le flux de CO_2 provenant de la bouteille (ECO2). Aussi, le liquide de refroidissement sortant de la section d'essai peut être utilisé pour refroidir davantage le CO_2 avant d'entrer dans la section de test (ECO3).
Dans les tubes coaxiaux, le liquide de refroidissement passe à travers le tube interne, tandis que le CO_2 passe en contre-courant à travers le tube externe et est refroidi par convection. La température du CO_2 tout au long de la section de test peut être enregistrée en surveillant les TG-10 et TG-09 près de l'entrée de CO_2 à la section d'essai (Figure F32)

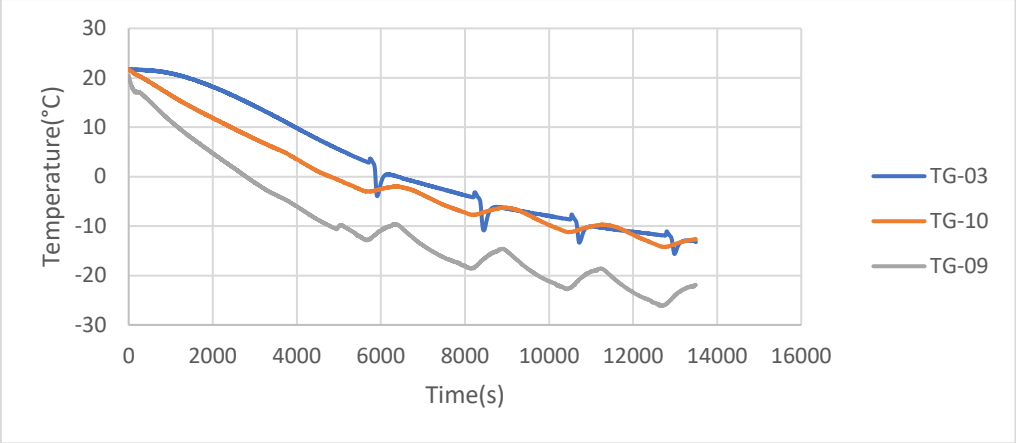

Figure F32: Température du CO_2 gaz à differentes positions dans l'échangeur co-axial

B) Pressurisation et liquéfaction du CO_2

Afin de liquéfier le CO_2 froid disponible dans la section d'essai, sa pression est augmentée. La liquéfaction vise une formation de phase solide cohérente sans pores qui permet d'évaluer le comportement du dégivrage contrôlé par sublimation en réduisant simultanément le nombre de variables ayant un impact sur le phénomène physique. Cette augmentation de pression est limitée à 7 bars. La vanne de CO_2 à la sortie de la section de test VM-06 est fermée et la pression du débit de CO_2 provenant de la bouteille est augmentée. La pression commence à monter dans le système.

Lorsque P=5,6 bars est atteinte, il devient possible de liquéfier le CO_2 puisque le point triple est dépassé sur le diagramme de phases. La Figure F33 montre le début de la liquéfaction lorsque des gouttelettes de CO_2 commencent à se former sur la surface externe du tube interne. Plus la pression augmente, plus de CO_2 se liquéfie jusqu'à ce que le tube externe soit rempli de CO_2 liquide

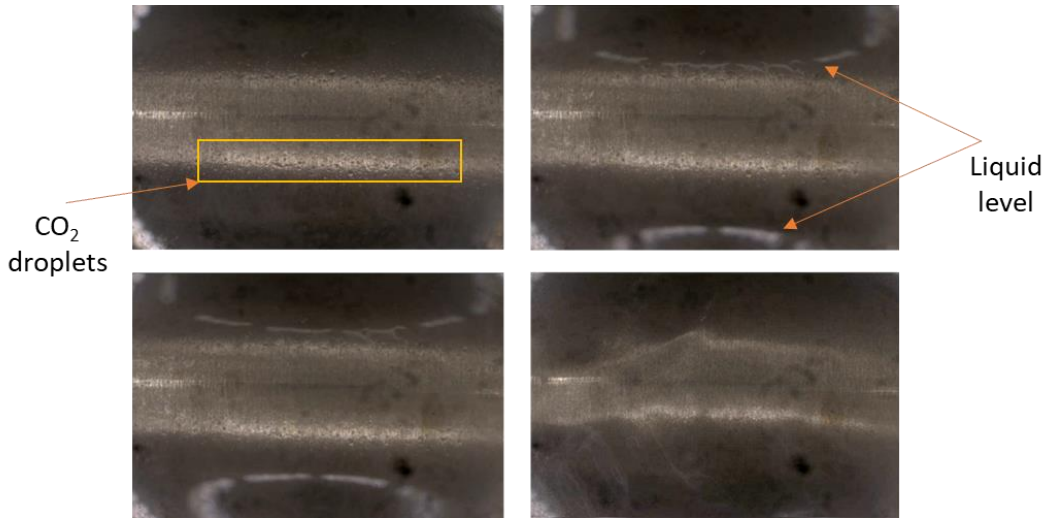

Figure F33: Visualisation locale de la liquéfaction du CO_2 dans le tube coaxial

Avant cette phase, seul un flux de chaleur sensible par convection existe entre le fluide caloporteur et le flux de CO_2 à travers le tube intérieur. Lorsque le CO_2 commence à se liquéfier, son changement de phase nécessite plus de puissance frigorifique et la température du liquide de refroidissement augmente beaucoup plus rapidement qu'en phase de refroidissement du CO_2. Cela permet le réglage exact de l'intervalle de temps de liquéfaction.

C) Dépressurisation et solidification du CO_2 liquide

L'espace entre le tube interne et externe de la section de test est à basse température et à haute pression. Il contient maintenant du CO_2 liquide. La pression du débit de CO_2 provenant de la bouteille est réduite et VM-06 (la vanne de CO_2 à la sortie de la section de test) est ouverte. La pression dans le système diminue rapidement, de même que sa température. La pression de CO_2 à la sortie de la section d'essai pourrait diminuer lentement en raison de formation de givre dans le tube d'échappement, provoquant un blocage (Figure F36).

Les conditions dans lesquelles la dépressurisation est déclenchée affectent la formation du CO_2 solide. Lorsque le CO_2 liquide remplit le tube externe, la formation de givre couvre tout l'espace entre les tubes interne et externe, comme illustré à la Figure F34. Le givre est observé à travers le hublot HB-03. La vapeur d'eau contenue dans l'air humide entourant le banc d'essai peut provoquer une formation de glace à l'extérieur du hublot en verre et il faut le nettoyer en permanence.

Le réfrigérateur qui maintient le liquide de refroidissement à basse température est arrêté. Le flux de liquide de refroidissement se réchauffe rapidement avant d'entrer dans la section de test, mais il se refroidit à l'intérieur de la section de test par convection avec le givre de CO_2 formé.

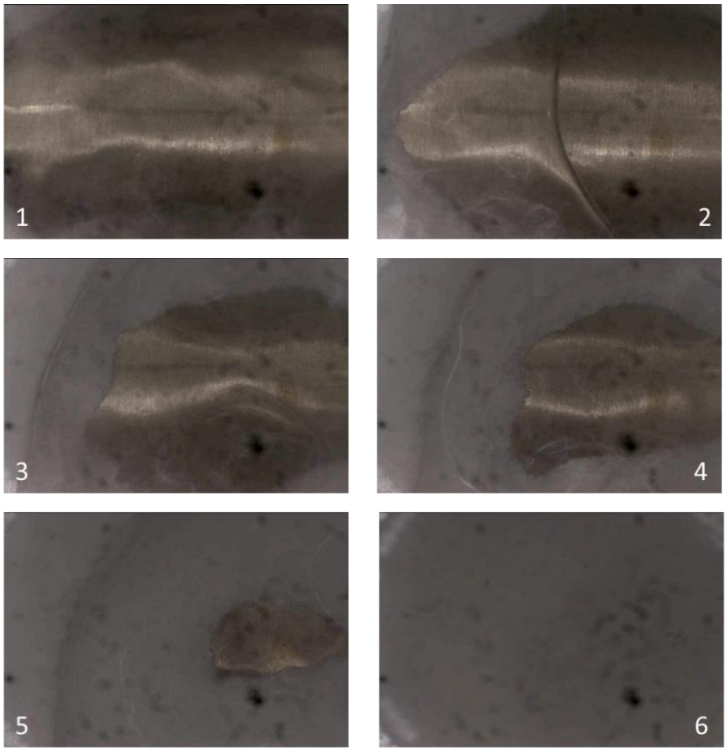

Figure F34 : Visualisation locale de la solidification du CO_2 de sa phase liquide

D) Dégivrage du givre de CO_2

Cette partie couvre l'objectif le plus important de cette expérience : « **valider la récupération à froid par sublimation contrôlée »**. Le système est à pression atmosphérique, le givre de CO_2 s'accumule entre le tube intérieur et extérieur. Un faible flux de N_2 est introduit dans le système, sa circulation est d'abord bloquée avant de trouver son chemin à l'intérieur du givre. Le système de réfrigération du fluide caloporteur reste en arrêt. La température du fluide de refroidissement à l'entrée de la section d'essai augmente (trait bleu sur la Figure F36.a).

Néanmoins, sa température à la sortie de la section d'essai (trait orange) continue à diminuer. Une petite partie du phénomène de dégivrage a été capturée. Si on les compare aux images prises en phase de givrage, on peut déduire que la première partie à subir le dégivrage est la dernière à avoir subi le givrage.

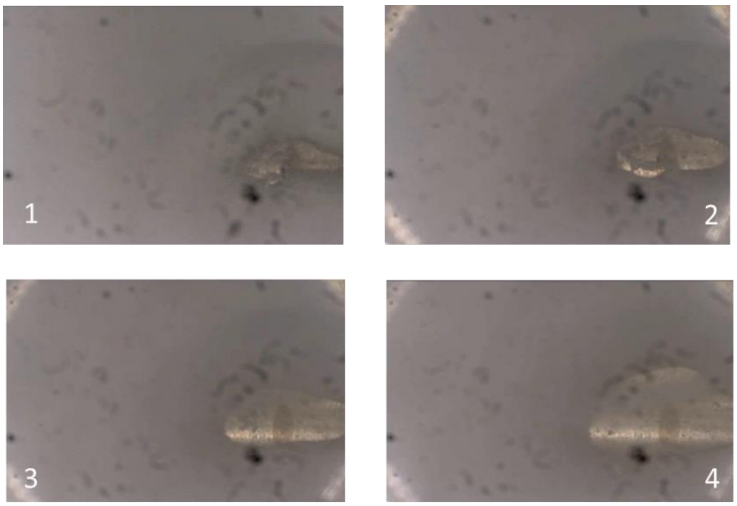

Figure F35: Dégivrage du CO_2 par un flux de N_2 (Δt (s) du début de dégivrage = 420, 700, 905, 1165)

Le givre se sublime pour quatre raisons : chaleur infiltrée de l'extérieur, transfert de chaleur par convection avec le flux de N_2, transfert de chaleur par convection avec le flux de liquide de refroidissement lorsqu'il atteint une température supérieure à celle du givre et par la sublimation contrôlée causée par le gradient de concentration de CO_2 entre la surface du givre et le flux de N_2. Le refroidissement du débit de N_2 n'entraîne pas de diminution de la température du débit de liquide de refroidissement, mais au contraire, il réchauffe le givre, réduisant ainsi le transfert de chaleur du liquide de refroidissement vers le givre de CO_2.

Afin de mieux comprendre si la sublimation contrôlée refroidit réellement le fluide caloporteur, les trois graphiques de pression, débits massiques de CO_2 et de N_2 et la température du fluide caloporteur à l'entrée et à la sortie de la section de test sont fusionnés et représentés dans la Figure F36 qui est divisée en 3 sections temporelles pour chaque partie de la procédure expérimentale.

Dans la première section de 0 à 2875s, la pression augmente dans le système (Figure F36.b). La température du liquide de refroidissement à la sortie (TF-04) augmente pendant que le CO_2 se liquéfie (trait orange sur la Figure F36.a). À t=2850s, VM-06 est ouvert et la dépressurisation commence. Le givre de CO_2 commence à se former et TF-04 continue à diminuer par convection avec le givre. Le flux de CO_2 est arrêté et la bouteille de N_2 est connecté au système au lieu du CO_2. Lorsque le flux de N_2 est introduit dans le système à t=3206s (ligne grise dans la Figure F36.c), la température de sortie du liquide de refroidissement présente une pente de décroissance supérieure (ligne verte dans la Figure F36.a) à celle sans le flux de N_2. Au point A, le système de réfrigération du fluide caloporteur est arrêté et sa température d'entrée commence à augmenter, mais sa température à la sortie continue à diminuer en raison de la «sublimation contrôlée» et de la convection avec le givre. Enfin, les deux températures se rencontrent lorsque le système s'équilibre

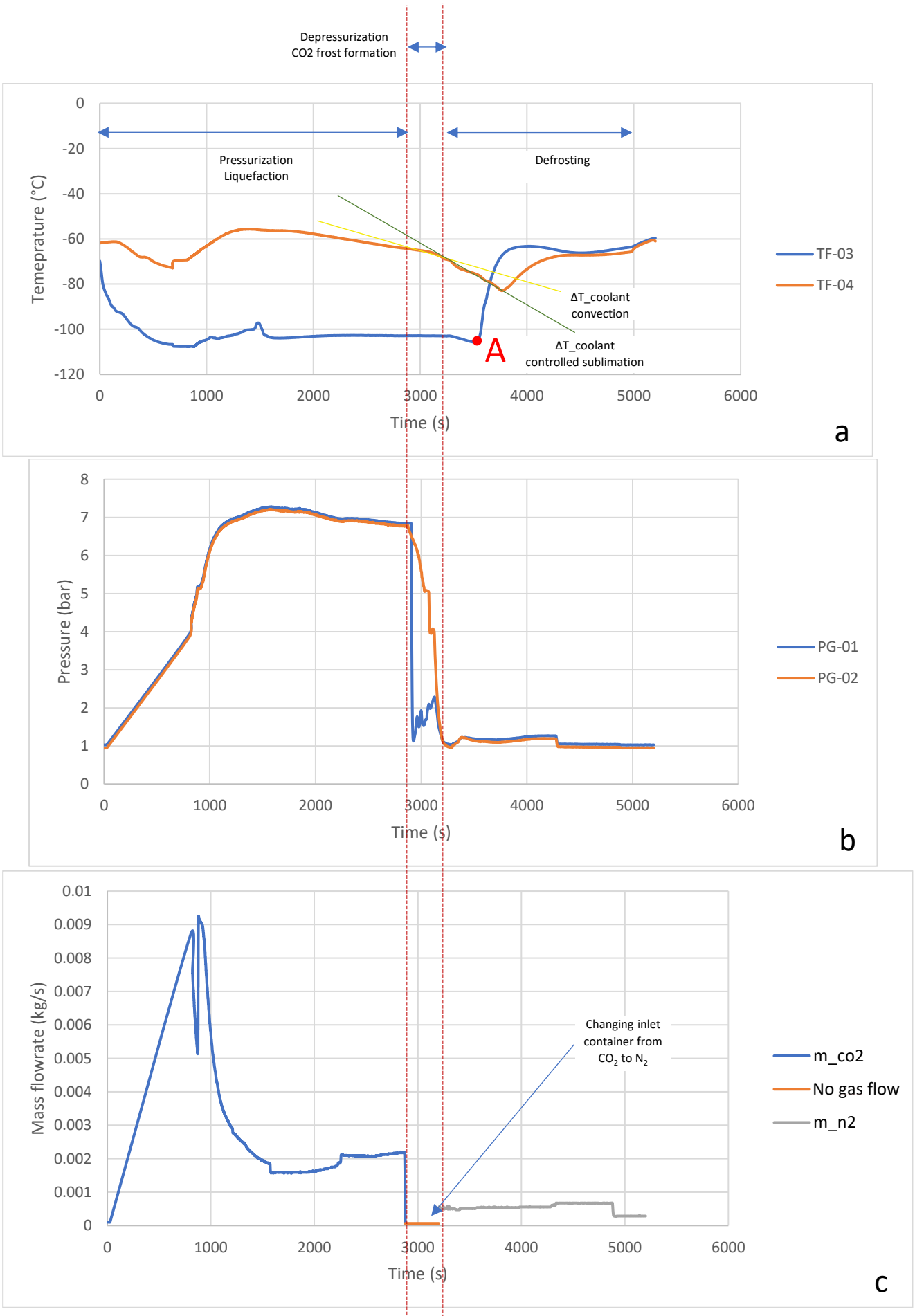

Figure F36: (a) Évolution de la température du liquide de refroidissement, (b) pression du CO_2 et (c) débit massique de CO_2 et de N_2 pendant les phases de liquéfaction, solidification et dégivrage du CO_2

Un autre test a été réalisé où le CO_2 suit toutes les étapes précédentes consécutivement : refroidissement, pressurisation, liquéfaction, dépressurisation puis solidification. La phase de dégivrage commence avec un faible flux de CO_2. Le système de réfrigération qui maintient le liquide de refroidissement à basse température est arrêté et la température de tout le système commence à augmenter (Figure F37.a). À l'instant t=592s, un débit élevé de N_2 (ligne grise dans la Figure F37.b) est introduit dans le système alors que peu de CO_2 solide était encore disponible. Aucune charge de refroidissement n'a été ajoutée au système et pourtant, la température du liquide de refroidissement à la sortie de la section d'essai (trait orange de la Figure F37.a) commence à diminuer tandis qu'elle augmentait avant. Le N_2 introduit sert comme gaz de dégivrage en sublimation contrôlée et la chaleur du fluide caloporteur est récupérée, ce qui entraîne une diminution de la température de sortie.

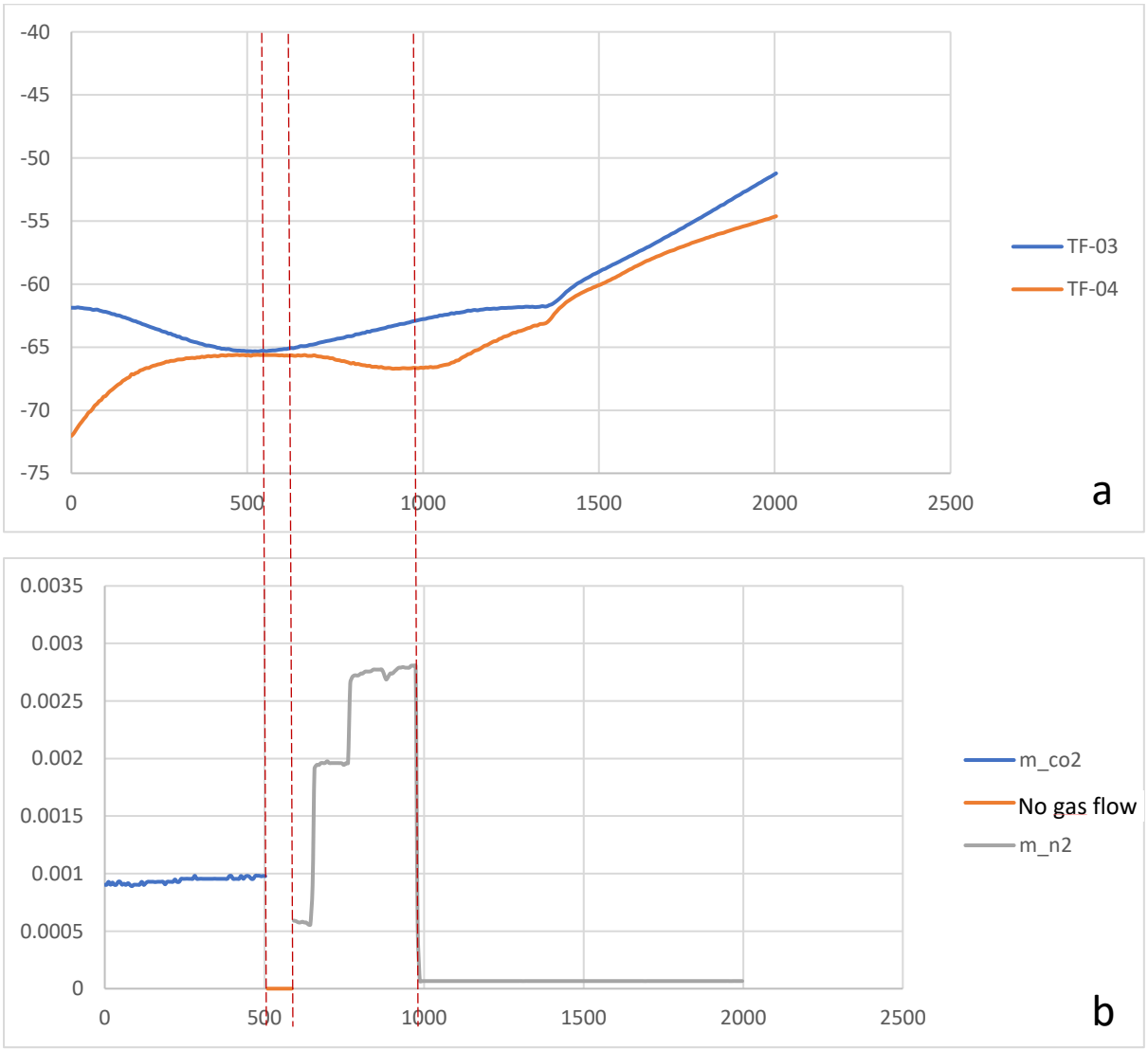

Figure F37: Evolution de la température du refrigérant et du débit de CO_2 et de N_2 pendant la phase de dégivrage

Lorsque le CO_2 est transporté par le flux de N_2 en raison du gradient de concentration de CO_2 à l'interface givre/N_2, la pression de vapeur à la surface du givre diminue et la chaleur est pompée du liquide de refroidissement pour compenser la perte de pression entraînant une diminution de sa température de sortie. C'est le principe de la « récupération à froid par sublimation contrôlée ».

Conclusions

As energy consumption increases daily and the environmental risks become more imminent, the need for renewable energies has become a necessity. Biogas is one of the solutions presented to the problem. Before its use, biogas must be upgraded and its CO_2 content reduced. Cryogenic separation is one of the most promising technologies for this application. Its main deployment challenge relies in the high cooling load and electricity consumption. In this thesis a new concept of cold recovery by controlled sublimation is proposed where cold is recovered from the CO_2 frost without the need for an additional cooling load.

In the first chapter, the frost formation and growth was detailed using what was found in the literature on ice formation by deposition of water vapour on a cold surface. A model of the CO_2 deposition was proposed and detailed calculations of the properties of the flows and the frost were presented. Shchelkunov et al. conducted experiments of CO_2 frost deposition on a cold surface from a binary mixture of N_2+CO_2. Simulation results show good agreement when compared to experimental results. The thermal conductivity of CO_2 frost was calculated using the experimental results of Shchelkunov et al.. Results show the importance of taking frost presence when considering the choice of the heat transfer correlation. A correlation proposed by Dietenberger et al. was used for the choice of the heat transfer coefficient which will be used to calculate the mass transfer coefficient and eventually the mass flow of CO_2 frosted.

A sensitivity study was led to better understand the effect of the inlet biogas flow conditions on the frosting phenomenon. The results show that for higher CO_2 concentrations, frost grows faster and more in terms of thickness and density. When the plate temperature was reduced, thickness increased because of the decrease of CO_2 saturation vapour concentration at the frost surface but density decreased because of CO_2 concentration decrease in the frost layer. Also, the increase of the biogas inlet temperature will reduce slightly the frost thickness while almost not affecting the density. Also, results for CO_2 frosting from biogas showed how higher relative concentrations of CO_2 increase heat transfer, in particular at the surface of the frost. The cold surface temperature has a very mild effect on heat transfer and inlet temperature has the opposite effect from concentration. Considering a plate as a heat capacitor (variable temperature) results in a quick decrease of sensible and latent heat transfer either on the surface or in the frost caused by the plate's temperature increase as CO_2 frosts.

Two different configurations of HX were compared: the flat plate and the tube. Simulation showed that the tube presents a better configuration in terms of heat and mass transfer for a given time but for longer frosting periods the plate is the better choice since its exchange surface remains constant as CO_2 deposits. The CO_2 frost formation along the tube was studied and compared with the literature for validation. The results show that frost deposition present a certain delay along the tube because of the concentration gradient decrease as frost deposits at earlier positions in the tube.

A system of biogas upgrading and biomethane liquefaction was presented and all its components and flow calculations were detailed. The process uses two heat exchangers operating simultaneously and alternatively as frosting and defrosting. The N_2 flow that will be

used for biomethane liquefaction will be later used for “controlled sublimation” and cold recovery.

In the concept of controlled sublimation, the frost sublimation will be caused by a concentration gradient between a gas flow coming into contact with the frost and the frost itself. The gas flow will be cooler than the frost not to sublimate by convective heat transfer thus losing its cold potential. As CO_2 gets defrosted, it will use the HX as a heat source thus cooling it. This will allow the cold recovery with a minor effect of convective heat transfer.

The controlled sublimation was modelled and a sensitivity study was conducted to study the effect of the mass flowrate and the temperature of the defrosting gas on the defrosting time and the final temperature of the HX. The objective was for the defrosting to be completed in a time interval equal to the time of frosting in the second HX and to return the tube to its initial temperature (-120°C) before the frosting phase. The simulation results showed that, indeed the tube can be cooled to temperatures even below its initial temperature which is impossible by convective heat transfer alone. The main challenge to tackle was the long defrosting time. It was found that in order to end the frosting and defrosting phase at the same time, the N_2 flowrate that should be used for defrosting is 4 times higher than that used for methane liquefaction.

Several solutions were presented in order to increase the system’s efficiency. The frosting can be stopped while the defrosting is completed but this will decrease the biomethane production. It was found that lower CO_2 concentrations in the inlet biogas will result in better operation of the system. It is possible to end the frosting and defrosting at the same time with the amount of N_2 used for biomethane liquefaction. Since the amount of CO_2 frosted will be less than that for high CO_2 concentrations in inlet biogas, cold recovery will need to be supported by a cooler N_2 flow which will slightly increase the defrosting time but will return the HX to its initial temperature for the frosting phase.

Experiment results have qualitatively confirmed that controlled sublimation enables cold recovery without setting a cold utility. Frost layer formed sublimates when nitrogen is injected into the system and the temperature of the solid phase and the heat transfer fluid used in the test-bench is cooled down. As perspective, the study of preferential gas flow pathways shall be studied, as nitrogen tends to generate channels in the solid phase. This leads to an improper sublimation rate and modelling becomes inaccurate. The use of short time frost/defrost cycles could be one solution to avoid preferential pathways for Nitrogen flow (thin layer).

Conclusions

Plus la consommation d'énergie augmente et que les risques environnementaux deviennent plus imminents, les énergies renouvelables sont devenues une nécessité. Le biogaz est l'une des solutions proposées à ce problème. Avant son utilisation, le biogaz doit être épuré et sa teneur en CO_2 réduite. La séparation cryogénique est l'une des technologies les plus prometteuses pour cette application. Son défi principal est la charge de refroidissement et la consommation d'électricité élevées. Dans cette thèse, un nouveau concept de récupération du froid par sublimation contrôlée est proposé, dans lequel le froid est récupéré en éliminant le givre de CO_2 sans nécessiter une puissance frigorifique supplémentaire.

La formation du givre et sa croissance ont été décrits en se basant sur le givrage de la vapeur d'eau sur une surface froide dans la littérature. Un modèle de givrage de CO_2 a été proposé et des calculs détaillés des propriétés des flux et du givre ont été présentés. Shchelkunov et al. ont mené des expériences sur le dépôt du CO_2 sur une surface froide à partir d'un mélange de N_2+CO_2. Les résultats de la simulation montrent un bon accord par rapport à ceux obtenus expérimentalement. Ces derniers ont permis le calcul de la conductivité thermique du givre de CO_2. Les résultats de l'etude montrent l'importance de la prise en compte de la présence de givre lorsque l'on considère le choix de la corrélation du coefficient de transfert de chaleur. Une corrélation proposée par Dietenberger et al. a été utilisée pour le choix du coefficient de transfert de chaleur qui sera utilisé pour calculer le coefficient de transfert de masse et éventuellement le débit massique de CO_2 givré.

Une étude de sensibilité a été menée pour mieux comprendre l'effet des conditions du flux de biogaz en entrée sur le phénomène de givrage. Les résultats montrent que pour des concentrations plus élevées de CO_2 (0.6>0.5>0.4 conc. massqiue) , le givre croit plus rapidement en épaisseur et en densité. Lorsque la température de la plaque a été réduite, l'épaisseur a augmenté à cause de la diminution de la concentration de vapeur saturante en CO_2 à la surface du givre, mais la densité a diminué en raison de la diminution de la concentration en CO_2 à l'intérieur de la couche de givre. En outre, l'augmentation de la température d'entrée du biogaz réduit légèrement l'épaisseur de givre presque sans affecter la densité. Les résultats concernant le givrage du CO_2 à partir du biogaz ont montré comment les concentrations élevées en CO_2 dans le biogaz en entrée augmentent le transfert de chaleur, en particulier à la surface du givre. La température de la surface froide a un effet « de variation proportionnelle » sur le transfert de chaleur et la température d'entrée a un effet opposé à celui de la concentration. Considérer une plaque comme inertie thermique entraîne une diminution rapide du transfert de chaleur sensible et latent, en surface ou dans le givre, provoqué par l'augmentation de la température de la plaque quand plus de givre se forme.

Deux configurations différentes de HX ont été comparées : la plaque plane et le tube. Les simulations montrent que le tube constitue un meilleur choix en termes de transfert de chaleur et de masse pour un temps donné, mais pour des périodes de givrage prolongées, la plaque est le meilleur choix puisque sa surface d'échange reste constante durant la phase de givrage de CO_2. La formation du givre de CO_2 le long du tube a été étudiée, comparée et validée par comparaison à des résultats dans la littérature. Les résultats montrent que les dépôts de givre

présentent un certain retard Δt le long du tube à cause de la diminution du gradient de concentration quand le givre se forme sur les positions antérieures du tube.

Un système d'épuration de biogaz et de liquéfaction de biométhane a été présenté avec les explications et les calculs concernant chaque composant. Le procédé utilise deux échangeurs de chaleur fonctionnant simultanément et alternativement en givrage et en dégivrage. Le flux de N_2 qui est utilisé pour la liquéfaction du biométhane sera ultérieurement utilisé pour la « sublimation contrôlée» et la récupération du froid.

Dans le concept de sublimation contrôlée, la sublimation du givre est due au gradient de concentration entre le flux de gaz entrant en contact avec le givre et le givre lui-même. Le flux de gaz sera plus froid que le givre pour que ce dernier ne se sublime pas par convection perdant ainsi son potentiel froid. Pour que le CO_2 puisse se dégivrer, il utilise le HX comme source de chaleur et ainsi le refroidira. Ce qui permet la récupération du froid avec un effet mineur du transfert de chaleur par convection

La sublimation contrôlée a été modélisée et une étude de sensibilité a été menée pour étudier l'effet du débit massique et de la température du gaz de dégivrage sur le temps de dégivrage et la température finale du HX. L'objectif était de terminer le dégivrage dans un intervalle de temps égal au temps de givrage dans le deuxième HX et de ramener le tube à sa température initiale (-120°C) avant la phase de givrage. Les résultats de la simulation ont montré que le tube peut en effet être refroidi à des températures inférieures à sa température initiale, ce qui est impossible par un simple transfert de chaleur par convection. Le défi principal à surmonter concernait le temps de dégivrage très long. Pour mettre fin à la phase de givrage et de dégivrage en même temps, le débit de N_2 utilisé pour le dégivrage est 4 fois supérieur à celui utilisé pour la liquéfaction du biométhane.

Plusieurs solutions ont été présentées afin d'augmenter l'efficacité du système. Le givrage peut être mis en arrêt pendant que le dégivrage soit terminé, mais cela réduira la production de biométhane. On a constaté que des concentrations de CO_2 plus faibles (<15%) dans le biogaz en entrée amélioreraient le fonctionnement du système. Il est possible de mettre fin au givrage et au dégivrage en même temps avec la même quantité de N_2 utilisée pour la liquéfaction du biométhane. Étant donné que la quantité de CO_2 givré sera inférieure à celle des concentrations élevées de CO_2 dans le biogaz entrant, la récupération du froid doit être soutenue par un flux de N_2 plus froid, ce qui augmente légèrement le temps de dégivrage mais ramène le HX à sa température initiale avant la phase de givrage.

Les résultats de l'expérience ont confirmé qualitativement que la sublimation contrôlée permet la récupération du froid. La couche de givre formée se sublime lorsque l'azote est injecté dans le système et que la température de la phase solide et du fluide caloporteur utilisé dans le banc d'essai diminue. En perspective, l'étude des voies préférentielles d'écoulement des gaz doit être étudiée car l'azote tend à générer des canaux dans le givre ; cela conduit à un taux de sublimation incorrect et la modélisation devient imprécise. L'utilisation de cycles de givrage/dégivrage de courte durée pourrait être une solution pour éviter les voies préférentielles pour le flux d'azote (couche mince).

References

[1] Working Group III Technical Unit, *Climate change 2014: Mitigation of Climate Change.* New York, NY: Cambridge University Press, 2014.

[2] International Energy Agency, “Global energy and CO2 status report 2018.” 2019.

[3] U.S. Energy Information Administration, “International Energy Outlook 2017.” 2017.

[4] PikeResearch, “Worldwide power generation from biogas will double by 2022.” 2012.

[5] Sundicat des énergies renouvelables, “Le biogaz.” Jun. 2017, [Online]. Available: www.enr.fr/le-biogaz.

[6] J. B. Holm-Nielsen, T. Al Seadi, and P. Oleskowicz-Popiel, “The future of anaerobic digestion and biogas utilization,” *Bioresource Technology*, vol. 100, no. 22, pp. 5478–5484, 2009, doi: 10.1016/j.biortech.2008.12.046.

[7] “Global Biogas Market Professional Survey Report 2018.” 2018, [Online]. Available: https://www.htfmarketreport.com/reports/1070428-global-biogas-market-6.

[8] M. Raboni, P. Viotti, and A. G. Capodaglio, “A comprehensive analysis of the current and future role of biofuels for transport in the European Union (EU),” *Ambiente e Agua - An Interdisciplinary Journal of Applied Science*, vol. 10, no. 1, pp. 9–21, 2015, doi: 10.4136/ambi-agua.1492.

[9] S. Chaemchuen, N. A. Kabir, K. Zhou, and F. Verpoort, “Metal–organic frameworks for upgrading biogas via CO2 adsorption to biogas green energy,” *Chemical Society Reviews*, vol. 42, no. 24, p. 9304, 2013, doi: 10.1039/c3cs60244c.

[10] P. Jean-Philippe, “La filière biométhane fait le plein d’optimisme.” Feb. 2017, [Online]. Available: https://www.greenunivers.com/2017/02/la-filiere-biomethane-fait-le-plein-doptimisme-157993/.

[11] Mnistère de la Transition Ecologique et Solidaire, “Stratégie Française pour l’Energie et le Climat, Programmation Pluriannuelle de l’Energie.” 2019, [Online]. Available: https://www.ecologique-solidaire.gouv.fr/sites/default/files/Synth%C3%A8se%20finale%20Projet%20de%20PPE.pdf.

[12] GRDF, “Contrat relatif à l’injection de biométhane dans le réseau de distribution de gaz naturel.” Gaz Réseau Distribution France, Oct. 14, 2016.

[13] R. Kadam and N. L. Panwar, “Recent advancement in biogas enrichment and its applications,” *Renewable and Sustainable Energy Reviews*, vol. 73, pp. 892–903, 2017, doi: 10.1016/j.rser.2017.01.167.

[14] X. Y. Chen, H. Vinh-Thang, A. A. Ramirez, D. Rodrigue, and S. Kaliaguine, “Membrane gas separation technologies for biogas upgrading,” *RSC Advances*, vol. 5, no. 31, pp. 24399–24448, 2015, doi: 10.1039/C5RA00666J.

[15] J. Markõs, “Mass Transfer in Chemical Engineering Processes.” INTECH Open Access Publisher, 2011.

[16] W. Edelmann, A. Joss, and H. Engeli, “Two step anaerobic digestion of organic solid wastes,” *Proceedings of the second international symposium on anaerobic digestion of solid wastes*, vol. 1, pp. 153–160, 1996.

[17] S. R. Qasim, *Wastewater treatment plants: planning, design and operation*, 2nd Edition. CRC Press, 1999.

[18] W. Ghyoot and W. Verstraete, “Anaerobic digestion of primary sludge from chemical pre-precipitation,” *Wat. Sci. Tech.*, vol. 36, no. 6–7, pp. 257–365, 1997.

[19] M. H. Gerardi, *The microbiology of anaerobic digesters*. Hoboken, N.J: Wiley-Interscience, 2003.
[20] D. Deublein and A. Steinhauser, *Biogas from waste and renewable resources*, 1st ed. Wiley-VCH, Weinhem, 2008.
[21] B. Schink, "Energetics of Syntrophic Cooperation in Methanogenic Degradation," *Microbiology and Molecular Biology Reviews*, vol. 61, pp. 262–280, 1997.
[22] D. Wilken *et al.*, "Biogas to biomethane." Fachverband Biogas e. V., 2017.
[23] O. W. Awe, Y. Zhao, A. Nzihou, D. P. Minh, and N. Lyczko, "A Review of Biogas Utilisation, Purification and Upgrading Technologies," *Waste and Biomass Valorization*, vol. 8, no. 2, pp. 267–283, 2017, doi: 10.1007/s12649-016-9826-4.
[24] A. Noyola, J. M. Morgan-Sagastume, and J. E. López-Hernández, "Treatment of Biogas Produced in Anaerobic Reactors for Domestic Wastewater: Odor Control and Energy/Resource Recovery," *Reviews in Environmental Science and Bio/Technology*, vol. 5, no. 1, pp. 93–114, 2006, doi: 10.1007/s11157-005-2754-6.
[25] A. Sugiharto, M. Hidayat, S. Sutijan, and S. Sarto, "Sensitivity Analysis of Water Scrubbing Process for Biogas Purification," *The 2nd International Conference on Engineering Technologi and Industrial Application*, vol. 2, pp. 35–39, 2015.
[26] D. Schüwer, K. Arnold, K. Bienge, D. S. Bringezu, L. Echternacht, and A. Esken, "CO2 ReUse NRW-Evaluating gas sources, demand and utilization for CO2 and H2 within the North RhineWestphalia area with respect to gas qualities," *Wuppertal Institute for Cliamte, Environment and Energy*, 2015.
[27] W. L. Theo, J. S. Lim, H. Hashim, A. A. Mustaffa, and W. S. Ho, "Review of pre-combustion capture and ionic liquid in carbon capture and storage," *Applied Energy*, vol. 183, pp. 1633–1663, 2016, doi: 10.1016/j.apenergy.2016.09.103.
[28] H. Li, Y. Tan, M. Ditaranto, J. Yan, and Z. Yu, "Capturing CO2 from Biogas Plants," *Energy Procedia*, vol. 114, pp. 6030–6035, 2017, doi: 10.1016/j.egypro.2017.03.1738.
[29] K. Thambimuthu, M. Soltanieh, J. C. Abanades, R. Allam, O. Bolland, *et al.*, "Capture of CO2." New York (United States): Cambridge University Press, 2005, [Online]. Available: IPCC special report on carbon dioxide capture and storage.
[30] S. D. Kenarsari *et al.*, "Review of recent advances in carbon dioxide separation and capture," *RSC Advances*, vol. 3, no. 45, 2013, doi: 10.1039/c3ra43965h.
[31] D. Thrän *et al.*, *Biomethane status and factors affecting market development and trade: a joint study*. 2014.
[32] G. P. Towler and R. K. Sinnott, *Chemical engineering design: principles, practice and economics of plant and process design*. Amsterdam ; Boston: Elsevier/Butterworth-Heinemann, 2008.
[33] J. Läntelä, S. Rasi, J. Lehtinen, and J. Rintala, "Landfill gas upgrading with pilot-scale water scrubber: Performance assessment with absorption water recycling," *Applied Energy*, vol. 92, pp. 307–314, 2012, doi: 10.1016/j.apenergy.2011.10.011.
[34] M. Arnold, "Reduction and monitoring of biogas trace compounds," *Espoo 2009. VTT Tiedotteita*, vol. Research Notes 2496, p. 84, 2009.
[35] R. Muñoz, L. Meier, I. Diaz, and D. Jeison, "A review on the state-of-the-art of physucal/chemical and biological technologies for biogas upgrading," *Reviews in Environmental Science and Bio/Technology*, no. 14, pp. 727–759, 2015.
[36] F. Bauer, T. Persson, C. Hulteberg, and D. Tamm, "Biogas upgrading—technology overview, comparison and perspectives for the future," *Biofuels Bioproduction and Biorefining*, vol. 7, no. 5, pp. 499–511, 2013.

[37] L. Yang and X. Ge, “Biogas and Syngas Upgrading,” in *Advances in Bioenergy*, vol. 1, Elsevier, 2016, pp. 125–188.
[38] K. Hoyer, C. Hulteberg, M. Svensson, J. Jernberg, and Ø. Nørregård, “Biogas upgrading - Technical Review,” *ENERGIFORSK*, 2016.
[39] J. Lasocki, K. Kołodziejczyk, and A. Matuszewska, “Laboratory-Scale Investigation of Biogas Treatment by Removal of Hydrogen Sulfide and Carbon Dioxide,” *Polish Journal of Environmental Studies*, vol. 24, pp. 1427–1434, 2015, doi: 10.15244/pjoes/35283.
[40] T. D. Biswas, A. R. S. Kartha, and R. Pundarikakhadu, “Removal of carbon dioxide from biogas.” The Indian Agricultural Research Institute, New Delhi, India, 1977.
[41] M. Beil, “Overview on biogas upgrading technologies.” European Biomethane Fuel Conference, Goteberg, Sweden, 2009.
[42] S. Kim, H.-T. Kim, and B.-C. Choi, “Optimization of CO2 Absorption Process with MEA Solution,” in *Studies in Surface Science and Catalysis*, vol. 153, Elsevier, 2004, pp. 429–434.
[43] E. Ryckebosch, M. Drouillon, and H. Vervaeren, “Techniques for transformation of biogas to biomethane,” *Biomass and Bioenergy*, vol. 35, no. 5, pp. 1633–1645, 2011, doi: 10.1016/j.biombioe.2011.02.033.
[44] S. Atchariyawut, R. Jiraratananon, and R. Wang, “Separation of CO2 from CH4 by using gas–liquid membrane contacting process,” *Journal of Membrane Science*, vol. 304, no. 1–2, pp. 163–172, 2007, doi: 10.1016/j.memsci.2007.07.030.
[45] F. Bauer, C. Hulteberg, T. Persson, and D. Tamm, “Biogas upgrading - Review of commercial technologies,” *SGC Rapport-Svenskt Gastekniskt Center AB*, vol. Vol. 270, 2013.
[46] L. Deng and M.-B. Hägg, “Techno-economic evaluation of biogas upgrading process using CO2 facilitated transport membrane,” *International Journal of Greenhouse Gas Control*, vol. 4, no. 4, pp. 638–646, 2010, doi: 10.1016/j.ijggc.2009.12.013.
[47] M. Scholz, T. Melin, and M. Wessling, “Transforming biogas into biomethane using membrane technology,” *Renewable and Sustainable Energy Reviews*, vol. 17, pp. 199–212, 2013, doi: 10.1016/j.rser.2012.08.009.
[48] L. B. Allegue and J. Hinge, “Report: Biogas and bio-syngas upgrading.” Danish Technology Institute, 2012.
[49] M. Persson, “Biogas upgrading and utilization as vehicle fuel,” presented at the European Biogas Workshop. The future of biogas in Europe III, SGC, 2007.
[50] C. A. Grande and A. E. Rodrigues, “Biogas to Fuel by Vacuum Pressure Swing Adsorption I. Behavior of Equilibrium and Kinetic-Based Adsorbents,” *Industrial & Engineering Chemistry Research*, vol. 46, no. 13, pp. 4595–4605, 2007.
[51] K. Maqsood, A. Mullick, A. Ali, K. Kargupta, and S. Ganguly, “Cryogenic carbon dioxide separation from natural gas: a review based on conventional and novel emerging technologies,” *Reviews in Chemical Engineering*, vol. 30, no. 5, Jan. 2014, doi: 10.1515/revce-2014-0009.
[52] I. P. Suarsana, “Producing High CO2 Gas Content Reservoirs in Pertamina Indonesia Using Multi Stage Cryogenic Process,” in *SPE Asia Pacific Oil and Gas Conference and Exhibition*, Brisbane, Queensland, Australia, 2010, doi: 10.2118/134278-MS.
[53] G. Xu, L. Li, Y. Yang, L. Tian, T. Liu, and K. Zhang, “A novel CO2 cryogenic liquefaction and separation system,” *Energy*, vol. 42, no. 1, pp. 522–529, 2012, doi: 10.1016/j.energy.2012.02.048.

[54] D. Thrän *et al.*, *Biomethane status and factors affecting market development and trade: a joint study*. 2014.
[55] D. Clodic and M. Younes, “A new Method for CO2 CaptureFrosting CO2 at Atmospheric Pressure,” in *Greenhouse Gas Control Technologies - 6th International Conference*, vol. I, Elsevier, 2003, pp. 155–160.
[56] M. J. Tuinier, M. van Sint Annaland, G. J. Kramer, and J. A. M. Kuipers, “Cryogenic CO2 capture using dynamically operated packed beds,” *Chemical Engineering Science*, vol. 65, no. 1, pp. 114–119, Jan. 2010, doi: 10.1016/j.ces.2009.01.055.
[57] M. J. Tuinier, M. van Sint Annaland, and J. A. M. Kuipers, “A novel process for cryogenic CO2 capture using dynamically operated packed beds—An experimental and numerical study,” *International Journal of Greenhouse Gas Control*, vol. 5, no. 4, pp. 694–701, Jul. 2011, doi: 10.1016/j.ijggc.2010.11.011.
[58] M. J. Tuinier, H. P. Hamers, and M. van Sint Annaland, “Techno-economic evaluation of cryogenic CO2 capture—A comparison with absorption and membrane technology,” *International Journal of Greenhouse Gas Control*, vol. 5, no. 6, pp. 1559–1565, Nov. 2011, doi: 10.1016/j.ijggc.2011.08.013.
[59] T. C. Merkel, H. Lin, X. Wei, and R. Baker, “Power plant post-combustion carbon dioxide capture: An opportunity for membranes,” *Journal of Membrane Science*, vol. 359, no. 1–2, pp. 126–139, Sep. 2010, doi: 10.1016/j.memsci.2009.10.041.
[60] M. B. Berkenpas, C. H. Frey, J. J. Fry, J. Kalagnanam, and E. S. Rubin, “Integrated Environmental Control Model-Technical Documentation,” *Center for Energy and Environmental Studies*, 1999.
[61] C. F. Song, Y. Kitamura, and S. H. Li, “Evaluation of Stirling cooler system for cryogenic CO2 capture,” *Applied Energy*, vol. 98, pp. 491–501, Oct. 2012, doi: 10.1016/j.apenergy.2012.04.013.
[62] J. Y. Hu, W. Dai, E. C. Luo, X. T. Wang, and Y. Huang, “Development of high efficiency Stirling-type pulse tube cryocoolers,” *Cryogenics*, vol. 50, no. 9, pp. 603–607, Sep. 2010, doi: 10.1016/j.cryogenics.2010.02.015.
[63] S. N. Kondepudi and D. L. O’Neal, “Performance of finned-tube heat exchangers under frosting conditions: II. Comparison of experimental data with model,” *International Journal of Refrigeration*, vol. 16, no. 3, pp. 181–184, Jan. 1993, doi: 10.1016/0140-7007(93)90046-B.
[64] S. Jonsson and J. Westman, “Cryogenic biogas upgrading using plate heat exchangers,” *Departement of Energy and Environment*, vol. Division of Energy Technology, 2011.
[65] A. Petersson and A. Wellinger, “Biogas upgrading technologies – developments and innovations,” *IEA Bioenergy-Task37*, 2009.
[66] D. Pandelidis, A. Pacak, and S. Anisimov, “Energy Saving Potential by Using Maisotsenko-Cycle in Different Applications,” *International Journal of Earth & Environmental Sciences*, vol. 3, no. 2, Nov. 2018, doi: 10.15344/2456-351X/2018/159.
[67] P. M. Cuce and S. Riffat, “A state of the art review of evaporative cooling systems for building applications,” *Renewable and Sustainable Energy Reviews*, vol. 54, pp. 1240–1249, Feb. 2016, doi: 10.1016/j.rser.2015.10.066.
[68] B. Porumb, P. Ungureşan, L. F. Tutunaru, A. Şerban, and M. Bălan, “A Review of Indirect Evaporative Cooling Technology,” *Energy Procedia*, vol. 85, pp. 461–471, Jan. 2016, doi: 10.1016/j.egypro.2015.12.228.

[69] C. Wani, S. Ghodke, and C. Shrivastava, “A Review on Potential of Maisotsenko Cycle in Energy Saving Applications Using Evaporative Cooling,” no. 01, p. 6, 2012.
[70] T. Muangnoi, W. Asvapoositkul, and S. Wongwises, “An exergy analysis on the performance of a counterflow wet cooling tower,” *Applied Thermal Engineering*, vol. 27, no. 5–6, pp. 910–917, 2007.
[71] L. D. Berman, *Evaporative cooling of circulating water*. Michigan University: Pergamon Press, 1961.
[72] D. G. Kröger, “Air-Cooled Heat Exchangers and Cooling Towers,” *THERMAL POWER PLANTS*, vol. 3, no. Air-Cooled Heat Exchnagers and Colling Towers, 1998.
[73] D. R. Baker and H. A. Shryock, “A Comprehensive Approach to the Analysis of Cooling Tower Performance,” *J. Heat Transfer*, vol. 83, no. 3, p. 339, 1961, doi: 10.1115/1.3682276.
[74] U.S. Department of Energy, “Cooling Towers: Understanding Key Components of Cooling Towers and How to Improve Water Efficiency.” Federal Energy Management Program, Feb. 2011.
[75] S. S. Kachhwaha and S. Prabhakar, “Heat and mass transfer study in a direct evaporative cooler,” *Journal of scientific and industrial research*, vol. 69, pp. 705–710, 2010.
[76] U. E. Gross and A. I. Weinstein, “A cryogenic-solid cooling system,” *Infrared Physics*, vol. 4, no. 3, pp. 161–169, Oct. 1964, doi: 10.1016/0020-0891(64)90022-3.
[77] “CO2 Transcritical Systems Training Manual.” Hussmann Corporation, 2018.
[78] M. R. O. Panão, J. J. Costa, and M. R. F. Bernardo, “Thermal assessment of sublimation cooling with dry-ice sprays,” *International Journal of Heat and Mass Transfer*, vol. 118, pp. 518–526, Mar. 2018, doi: 10.1016/j.ijheatmasstransfer.2017.11.015.
[79] R. Sherman, “Dry surface cleaning using CO2 snow,” *Journal of Vacuum Science & Technology B: Microelectronics and Nanometer Structures*, vol. 9, no. 4, p. 1970, Jul. 1991, doi: 10.1116/1.585390.
[80] C. J. L. Hermes, F. R. Loyola, and V. S. Nascimento, “A semi-empirical correlation for the frost density,” *International Journal of Refrigeration*, vol. 46, pp. 100–104, Oct. 2014, doi: 10.1016/j.ijrefrig.2014.02.008.
[81] H. W. Schneider, “Equation of the growth rate of frost forming on cooled surfaces,” *International Journal of Heat and Mass Transfer*, vol. 21, no. 8, pp. 1019–1024, Aug. 1978, doi: 10.1016/0017-9310(78)90098-4.
[82] J. Cui, W. Z. Li, Y. Liu, and Z. Y. Jiang, “A new time- and space-dependent model for predicting frost formation,” *Applied Thermal Engineering*, vol. 31, no. 4, pp. 447–457, Mar. 2011, doi: 10.1016/j.applthermaleng.2010.09.022.
[83] B. Na and R. L. Webb, “New model for frost growth rate,” *International Journal of Heat and Mass Transfer*, vol. 47, no. 5, pp. 925–936, Feb. 2004, doi: 10.1016/j.ijheatmasstransfer.2003.09.001.
[84] K.-S. Lee, S. Jhee, and D.-K. Yang, “Prediction of the frost formation on a cold flat surface,” *International Journal of Heat and Mass Transfer*, vol. 46, no. 20, pp. 3789–3796, Sep. 2003, doi: 10.1016/S0017-9310(03)00195-9.
[85] R. Le Gall, J. M. Grillot, and C. Jallut, “Modelling of frost growth and densification,” *International Journal of Heat and Mass Transfer*, vol. 40, no. 13, pp. 3177–3187, Sep. 1997, doi: 10.1016/S0017-9310(96)00359-6.
[86] A. N. Ogunbameru, P. L. T. Brian, and R. C. Reid, “On Carbon Dioxide Frost Formation,” *Industrial and Engineering Chemistry Fundamentals*, vol. 12, no. 3, pp. 385–387, 1973.

[87] V. N. Shchelkunov, N. Z. Rudenko, Y. V. Shostak, and V. I. Dolganin, “Surface desublimation of carbon dioxide from binary gas mixtures,” *Journal of Engineering Physics*, vol. 51, no. 6, 1986.
[88] F. Brèque and M. Nemer, “Frosting modeling on a cold flat plate: Comparison of the different assumptions and impacts on frost growth predictions,” *International Journal of Refrigeration*, vol. 69, pp. 340–360, Sep. 2016, doi: 10.1016/j.ijrefrig.2016.06.010.
[89] B. W. Jones and J. D. Parker, “Frost formation with varying environmental parameters,” *Journal of Heat Transfer*, vol. 97, no. 2, pp. 255–259, 1975.
[90] Y. Hayashi, A. Aoiki, A. Adachi, and K. Hori, “Study of frost formation based on a theoretical model of the frost layer,” *Journal of Heat Transfer*, vol. 99, pp. 239–245, 1977.
[91] B. Na and R. L. Webb, “A fundamental understanding of factors affecting frost nucleation,” *International Journal of Heat and Mass Transfer*, vol. 46, no. 20, pp. 3797–3808, Sep. 2003, doi: 10.1016/S0017-9310(03)00194-7.
[92] Y. B. Lee and S. T. Ro, “Analysis of the frost growth on a flat plate by simple models of saturation and supersaturation,” *Experimental Thermal and Fluid Science*, vol. 29, no. 6, pp. 685–696, Jul. 2005, doi: 10.1016/j.expthermflusci.2004.11.001.
[93] K.-S. Lee, W.-S. Kim, and T.-H. Lee, “A one-dimensional model for frost formation on a cold flat surface,” *International Journal of Heat and Mass Transfer*, vol. 40, no. 18, pp. 4359–4365, Nov. 1997, doi: 10.1016/S0017-9310(97)00074-4.
[94] O. Maass and W. H. Barnes, “Some thermal constants of solid and liquid carbon dioxide,” *Proceedings of the Royal Society of London series A*, vol. 111, pp. 224–244.
[95] V. V. Sumarokov, P. Stachowiak, and A. Jeżowski, “Low-temperature thermal conductivity of solid carbon dioxide,” *Low Temperature Physics*, vol. 29, no. 5, pp. 449–450, May 2003, doi: 10.1063/1.1542510.
[96] M. Azreg-Aïnou, “Low-temperature data for carbon dioxide,” *Monatshefte für Chemie - Chemical Monthly*, vol. 136, no. 12, pp. 2017–2027, Dec. 2005, doi: 10.1007/s00706-005-0370-3.
[97] W. F. Giauque and C. J. Egan, “Carbon Dioxide. The Heat Capacity and Vapor Pressure of the Solid. The Heat of Sublimation. Thermodynamic and Spectroscopic Values of the Entropy,” *The Journal of Chemical Physics*, vol. 5, no. 1, pp. 45–54, Jan. 1937, doi: 10.1063/1.1749929.
[98] P. L. T. Brian, R. C. Reid, and Y. T. Shah, “Frost Deposition on Cold Surfaces,” *Ind. Eng. Chem. Fund.*, vol. 9, no. 3, pp. 375–380, Aug. 1970, doi: 10.1021/i160035a013.
[99] B. E. Poling, J. M. Prausnitz, and J. P. O’Connell, *Properties of Gases and Liquids*, McGraww Hill. New York, 2000.
[100] C. L. Yaws, *Chemical Properties Handbook: physical, thermodynamic, environmental, transport, safety, and health related properties for organic and inorganic chemicals*. McGraw-Hill, 1999.
[101] Y. A. Cengel, *Heat transfer: a practical approach*, 2nd edition. Magraw-Hill, 2002.
[102] N. Yamakawa, N. Takahashi, and S. Ohtani, “Forced convection heat and mass transfer under frost condition,” vol. 1, pp. 155–165, 1972.
[103] M. Dietenberger, P. Kumar, and J. Luers, “Frost Formation on an Airfoil:A Mathematical Model I.” NASA Contractor Report 3129.
[104] T. L. Bergman, A. S. Lavine, F. P. Incropera, and D. P. Dewitt, *Fundementals of Heat and Mass Transfer*, John Wiley and Sons. 2011.

[105] C.-F. Song, Y. Kitamura, S.-H. Li, and W.-Z. Jiang, “Analysis of CO2 frost formation properties in cryogenic capture process,” *International Journal of Greenhouse Gas Control*, vol. 13, pp. 26–33, Mar. 2013, doi: 10.1016/j.ijggc.2012.12.011.
[106] S. Mokhatab, J. Y. Mak, J. V. Valappil, and D. A. Wood, *Handbook of liquefied natural gas*, 1st Edition. Gulf Professional Publishing, 2013.
[107] J. A. Dopazo, J. Fernandez-Seara, F. J. Uhía, and R. Diz, “Modelling and experimental validation of the hot-gas defrost process of an air-cooled evaporator,” *International Journal of Refrigeration*, vol. 33, no. 4, pp. 829–839, Jun. 2010, doi: 10.1016/j.ijrefrig.2009.12.027.
[108] H. Cho, Y. Kim, and I. Jang, “Performance of a showcase refrigeration system with multi-evaporator during on–off cycling and hot-gas bypass defrost,” *Energy*, vol. 30, no. 10, pp. 1915–1930, Jul. 2005, doi: 10.1016/j.energy.2004.11.006.
[109] M. Amer and C.-C. Wang, “Review of defrosting methods,” *Renewable and Sustainable Energy Reviews*, vol. 73, pp. 53–74, Jun. 2017, doi: 10.1016/j.rser.2017.01.120.
[110] S. A. Sherif and M. G. Hertz, “A semi-empirical model for electric defrosting of a cylindrical coil cooler,” *International Journal of Energy Research*, vol. 22, no. 1, pp. 85–92, 1998.
[111] S. Kenneth and C. M. Franklin, “Defrosting Methods.” RSES. The HVACR Training Authority, 2001.
[112] N. Hoffenbecker, S. A. Klein, and D. T. Reindl, “Hot gas defrost model development and validation,” *International Journal of Refrigeration*, vol. 28, no. 4, pp. 605–615, 2005, doi: 10.1016/j.ijrefrig.2004.08.016.
[113] D. Demma, “Introduction to refrigeration defrost methods-Part II.” Heating Plumbing Air Conditioning, 2017.
[114] C. Ratti, “Hot air and freeze-drying of high-value foods: a review,” *Journal of Food Engineering*, vol. 49, no. 4, pp. 311–319, 2001, doi: 10.1016/S0260-8774(00)00228-4.
[115] S. Lin, “An Exact Solution of the Sublimation Problem in a Porous Medium,” *Journal of Heat Transfer*, vol. 103, no. 1, pp. 165–168, 1981, doi: 10.1115/1.3244413.
[116] A. V. Luikov, “Systems of differential equations of heat and mass transfer in capillary-porous bodies (review),” *International Journal of Heat and Mass Transfer*, vol. 18, no. 1, pp. 1–14, 1975, doi: 10.1016/0017-9310(75)90002-2.
[117] H. Inaba and S. Imai, “Study on Sublimation Phenomenon of Horizontal Frost Layer Exposed to Forced Convection Air Flow and Radiant Heat,” *Journal of Heat Transfer*, vol. 118, no. 3, pp. 694–701, 1996, doi: 10.1115/1.2822688.
[118] V. Vionnet *et al.*, “Simulation of wind-induced snow transport and sublimation in alpine terrain using a fully coupled snowpack/atmosphere model,” *The Cryosphere*, vol. 8, no. 2, pp. 395–415, 2014, doi: 10.5194/tc-8-395-2014.
[119] J. W. Pomeroy’, “Coupled Modelling of Forest Snow Interception and Sublimation,” *55th Eastern Snow Conference-Jackson, New Hampshire*, 1998.
[120] Y. B. Lee and S. T. Ro, “Frost formation on a vertical plate in simultaneously developing flow,” *Experimental Thermal and Fluid Science*, vol. 26, pp. 939–945, 2002.
[121] Y. Mao, R. W. Besant, and K. S. Rezkallah, “Measurement and correlations of frost properties with airflow over a flat plate,” *ASHRAE Transactions*, vol. 98, no. 2, pp. 65–77, 1992.

[122] Y. Mao, R. W. Besant, and H. Chen, “Frost characteristics and heat transfer on a flat plate under freezer operating conditions: Part I, Experimentation and correlations,” *ASHRAE Transactions*, vol. 105, no. 2, pp. 231–251, 1999.
[123] C. J. L. Hermes, R. O. Piucco, J. R. Barbosa, and C. Melo, “A study of frost growth and densification on flat surfaces,” *Experimental Thermal and Fluid Science*, vol. 33, no. 2, pp. 371–379, 2009, doi: 10.1016/j.expthermflusci.2008.10.006.
[124] W. Wang, “A generalized simple model for predicting frost growth on cold flat plate,” *International Journal of Refrigeration*, vol. 35, pp. 475–486, 2012.
[125] T. Benítez and S. S.A., “Modeling spatial and temporal frost formation with distributed properties on a flat plate using the orthogonal collocation method,” *International Journal of Refrigeration*, vol. 76, pp. 193–205, 2017.
[126] C. Kim, J. Shin, and A. V. Tikhonov, “Experimental study on frost structure on surfaces with different hydrophilicity: Density and thermal conductivity,” *Journal of Heat Transfer*, vol. 125, no. 1, pp. 84–94, 2003.
[127] D.-K. Yang and K.-S. Lee, “Dimensionless correlations of frost properties on a cold plate,” *International Journal of Refrigeration*, vol. 27, no. 1, pp. 89–96, 2004, doi: 10.1016/S0140-7007(03)00118-X.
[128] M. Kandula, “Frost growth and densification in laminar flow over flat surfaces,” *International Journal of Heat and Mass Transfer*, vol. 54, no. 15–16, pp. 3719–3731, 2011, doi: 10.1016/j.ijheatmasstransfer.2011.02.056.
[129] P. L. Brian, R. C. Reid, and I. Brazinsky, “Cryogenic frost properties,” *Cryogenic Technology*, vol. 5, no. 5, pp. 205–212, 1969.
[130] Z. Hadid, A. Zoughaib, N. Bariteau, and H. Robidou, “Modeling Ice Formation On Heat Exchnagers Fins.” Congres International de Refrigeration-CDI-ROM EDITION, 2011.
[131] F. R. Loyola, V. S. Nascimento, and C. J. L. Hermes, “Modeling of frost build-up on parallel-plate channels under supersaturated air-frost interface conditions,” *International Journal of Heat and Mass Transfer*, vol. 79, pp. 790–795, 2014, doi: 10.1016/j.ijheatmasstransfer.2014.08.055.
[132] R. He-Sheng, “Construction of a generalized psychrometric chart for different pressures,” *International Journal of Mechanical Engineering Education*, 2004.

ANNEX A: Different correlations for frost growth

Table 10: Frost layer thickness correlations

Equation	*Range of application*	*Ref.*
$\theta_{frost} = 0.1083(W)^{1.704}(T^*)^{3.177}(Re_D)^{0.1424}(D^*)^{13.36}(X^*)^{-0.1488}(Fo)^{0.6724}$	AHR (10^{-3} kg/kgDA)= 3 to 5.5 $T_{cooling\ surface}$(°C)= -20 to -10 T_{air}(°C)= 5 to 20 Reynolds= 1000 to 3000	[120]
$\theta_{frost} = 0.156(X^*)^{-0.098}(W)^{1.723}\left(\frac{T_{tp}-T_w}{T_a-T_w}\right)^{1.10} Re^{0.343} Fo^{0.655}$	$T_{cooling\ surface}$(°C)= -15 to -5 T_{air}(°C)= 15 to 23	[121]
$\theta_{frost} = 9.183\times10^{-5}(X^*)^{-0.085}(W)^{0.4}\left(\frac{T_{tp}-T_w}{T_a-T_w}\right)^{-1.712} Re_D^{0.449} Fo^{0.699}$	$T_{cooling\ surface}$(°C)= -41 to -20.5 T_{air}(°C)= -25.8 to -10.1	[122]
$\theta_{frost}(t+\Delta t) = \theta_{frost}(t) + \Delta t \times \left.\frac{m_g}{\rho_{frost}}\right\|_t$	RH (%)= 50 to 80 $T_{cooling\ surface}$(°C)= -16 to -4 T_{air}(°C)= 16 to 22 Reynolds= 6000 to 50000	[123]
$\theta_{frost}(t+\Delta t) = \theta_{frost}(t) + \Delta t \times \left.\frac{m_g}{\rho_{frost}}\right\|_t$	RH (%)= 30 to 80 $T_{cooling\ surface}$(°C)= -16 to -4 T_{air}(°C)= -8 to 25 v (m/s)= 0.7 to 5	[124]
$\frac{d\theta_{frost}}{dt} = \frac{h_m(\rho_{v,\infty} - \rho_v\|_{\eta=1})}{\rho_f\|_{\eta=1}} - \frac{D_{eff,s}}{\theta_{frost}\,\rho_f\|_{\eta=1}} \left.\frac{\partial \rho v}{\partial \eta}\right\|_{\eta=1}$	RH (%)= 40 to 70 $T_{cooling\ surface}$(°C)= -15 to -10 T_{air}(°C)= 20 to 27 v (m/s)= 1.8 to 4.2	[125]
$\theta_{frost} = (0.0852 + 0.00134DCA)t^{0.6954-0.00154DCA}$	AHR (10^{-3} kg/kgDA)= 4.2 $T_{cooling\ surface}$(°C)= -22 T_{air}(°C)= 12 Reynolds= 9000 DCA (°)=23;55;88	[126]
$\theta_{frost}(t+\Delta t) = \theta_{frost}(t) + \Delta t \times \left.\frac{m_g}{\rho_{frost}}\right\|_t$	AHR(10^{-3} kg/kgDA)=3.2 to 8.5 $T_{cooling\ surface}$(°C)= -35 to -15 T_{air}(°C)= -5 to 15 v (m/s)= 1 to 2.5	[127]

Table 11: Frost layer density correlations

Equation	Range of application	Ref.
$\rho_{frost} = 0.2416(W)^{-0.5011}(T)^{-1.827}(Re_D)^{0.0413}(D)^{-5.591}(X)^{-0.1819}(Fo)^{0.251}$	AHR (10^{-3} kg/kgDA)= 3 to 5.5 $T_{cooling\ surface}$(°C)= -20 to -10 T_{air}(°C)= 5 to 20 Reynolds= 1000 to 3000	[120]
$\rho_{frost} = 650 \times e^{(0.277 \times T_{fs})}$	AHR (10^{-3} kg/kgDA)= 7.5 $T_{cooling\ surface}$(°C)= -18.6 to -5 v(m/s)= 2 to 6	[90]
$\rho^*_{frost} = 5.559 \times 10^{-5}(\frac{\delta}{L})^{-0.137} Re^{0.715} {\omega_a}^{-0.413} Fo^{0.252} \left(\frac{T_{tp}-T_w}{T_a-T_w}\right)^{-0.997}$	$T_{cooling\ surface}$(°C)= -15 to -5 T_{air}(°C)= 15 to 23	[121]
$\rho^*_{frost} = 1.714 \times 10^{-4}(\frac{\delta}{L})^{-0.056} {Re_D}^{0.463} {\omega_a}^{-0.011} Fo^{0.217} \left(\frac{T_{tp}-T_w}{T_a-T_w}\right)^{0.845}$	$T_{cooling\ surface}$(°C)= -41 to -20.5 T_{air}(°C)= -25.8 to -10.1	[122]
$\rho_{frost} = 207 \times e^{(0.266 \times T_f - 0.0615 \times T_w)}$	RH (%)= 50 to 80 $T_{cooling\ surface}$(°C)= -16 to -4 T_{air}(°C)= 16 to 22 Reynolds= 6000 to 50000	[123]
$\frac{\rho_{frost}}{\rho_i} = 0.5 \times \left(\frac{T_f-T_w}{T_m-T_w}\right) \times e^{-\left(0.376+1.5\times\left(\frac{T_f-T_w}{T_m-T_w}\right)\right)\left(1-\sqrt{\frac{Re}{Re_c}}\right)}$	RH (%)= 50 to 80 $T_{cooling\ surface}$(°C)= -20 to -5 T_{air}(°C)= 10 to 22 v(m/s)= 0.7 to 2.5	[128]
$\rho_{frost} = \frac{M}{z_f \times l^2}$	RH (%)= 30 to 80 $T_{cooling\ surface}$(°C)= -16 to -4 T_{air}(°C)= -8 to 25 v (m/s)= 0.7 to 5	[124]
$\bar{\rho}_{frost}(t) = \frac{1}{\delta_f}\int_0^{\delta_f} \rho_f(t,z)dz = \int_0^1 \rho_f(t,\eta)d\eta \approx \sum_{j=1}^{N+2} w_j \rho_f(t,\eta_j)$	RH (%)= 40 to 70 $T_{cooling\ surface}$(°C)= -15 to -10 T_{air}(°C)= 20 to 27 v (m/s)= 1.8 to 4.2	[125]
$\rho_{frost} = (109.53 - 45.541\log(DCA))t^{0.0479 DCA^{0.4357}}$	AHR (10^{-3} kg/kgDA)= 4.2 $T_{cooling\ surface}$(°C)= -22 T_{air}(°C)= 12 Reynolds= 9000 DCA (°)=23;55;88	[126]
$\frac{\rho_{frost}}{\rho_i} = 1.54 \times 10^{-4} \times Re^{0.351} {\omega_a}^{-0.368} Fo^{0.311} \times (e^{\left(\frac{T_f-T_w}{T_m-T_w}\right)})^{2.4}$	AHR(10^{-3}kg/kgDA)=3.2 to 8.5 $T_{cooling\ surface}$(°C)= -35 to -15 T_{air}(°C)= -5 to 15 v (m/s)= 1 to 2.5	[127]

Table 12: CO_2 frost thermal conductivity correlations

Equation	Range of application	Ref.
$k_{frost} = 0.011 \times X^{-0.375}\ W^{2.044} \left(\frac{T_{tp} - T_w}{T_a - T_w}\right)^{-0.216} Re^{1.093} Fo^{0.699}$	$T_{cooling\ surface}$(°C)= -15 to -5 T_{air}(°C)= 15 to 23	[121]
$k_{frost} = k_{solid,co2} \times 6.534 \times 10^{-4} (X)^{-0.056} Re_D^{0.375} W^{0.004} Fo^{0.18} \left(\frac{T_{tp} - T_w}{T_a - T_w}\right)^{0.737}$	$T_{cooling\ surface}$(°C)= -41 to -20.5 T_{air}(°C)= -25.8 to -10.1	[122]
$k_{frost} = 0.132 + 3.13 \times 10^{-4} \rho_f + 1.6 \times 10^{-7} \rho_f^2$	RH (%)= 50 to 80 $T_{cooling\ surface}$(°C)= -16 to -4 T_{air}(°C)= 16 to 22 Reynolds= 6000 to 50000	[123]
$\frac{k_{frost}}{k_{eff}} = 1 - \sqrt{1-\varepsilon} + \frac{2\sqrt{1-\varepsilon}}{1-\varsigma B} + \left[\frac{(1-\varsigma)B}{(1-\varsigma B)^2} \ln\left(\frac{1}{\varsigma B}\right) - \left(\frac{B+1}{2}\right) - \left(\frac{B-1}{1-\varsigma B}\right)\right]$	RH (%)= 50 to 80 $T_{cooling\ surface}$(°C)= -20 to -5 T_{air}(°C)= 10 to 22 v(m/s)= 0.7 to 2.5	[128]
$k_{frost} = C_{DCD}(0.0448 + 4.42 \times 10^{-8} \rho_f^3$	AHR (10^{-3} kg/kgDA)= 4.2 $T_{cooling\ surface}$(°C)= -22 T_{air}(°C)= 12 Reynolds= 9000 DCA (°)=23;55;88	[126]
$\frac{k_{frost}}{k_i} = 1.184 \times 10^{-2} \times (lnRe)^{0.619} \omega_a^{-0.086} Fo^{0.084} \times \left(e^{\left(\frac{T_a - T_{tp}}{T_a - T_w}\right)}\right)^{0.512}$	AHR(10^{-3} kg/kgDA)=3.2 to 8.5 $T_{cooling\ surface}$(°C)= -35 to -15 T_{air}(°C)= -5 to 15 v (m/s)= 1 to 2.5	[127]

Table 13: Mass transfer coefficient correlations as function of the heat transfer coefficient

Equation	Range of application	Ref.
$h_m = \frac{h_c}{\rho_{air} \times c_{p,air} \times 1}$	RH (%)= 50 to 80 $T_{cooling\ surface}$(°C)= -20 to -5 T_{air}(°C)= 10 to 22 v(m/s)= 0.7 to 2.5	[128]
$h_m = \frac{Sh_L \times D_{AB}}{L};\ Sh_L = 0.664\ Re_L^{0.5} Sc^{1/3};\ Sc = \frac{\mu}{\rho_a \times D_{AB}}$	RH (%)= 40 to 70 $T_{cooling\ surface}$(°C)= -15 to -10 T_{air}(°C)= 20 to 27 v (m/s)= 1.8 to 4.2	[125]

ANNEX B: Other models of frost formation in the literature

Several studies have been conducted to study frost formation, the simplest models are those using empirical correlations. They aim in principle to calculate the evolution of the density and the thickness of the frost but they are limited to the case of a flat plate [123] [81].

To better predict the results and improve the model, many studies consider frost as porous media and develop a model based on mass and heat transfer equations [84] [85] [89] [129]. These models take into account hypotheses to reduce the complexity of the simulations and the computation time but they explain well the deposition phenomenon and give results in coherence with the experiments. Since the studies carried out on CO_2 deposition, theoretical or experimental remain very limited, modelling the CO_2 deposition will be based on the mass and heat transfer equations. Different hypotheses were made in different research to try to better predict frost formation, either by changing the correlations used for the various frost characteristics (conductivity, porosity, diffusion ...) or by simplifying the model by taking a mean density [130] or constant densification [131]... Although none of these hypotheses will be applied to the model developed in this thesis, they still are interesting to briefly mention for future studies for comparing the effect of each hypothesis on the results obtained:

First hypothesis: average density

The nature of frost texture (porosity, density, temperature...) depends on the frosting time, typical correlations used for mass and heat transfers can no longer be used. It is necessary to use a diffusion model in which frost is considered as a porous medium [98]. Mass transfer from the flue gases to the frost surface takes place, increasing the thickness of the frost. Also, some of the CO_2 contained in the flue gases diffuses into the frost layer and solidifies to increase the density. In the model using this hypothesis, a homogeneous density throughout the frost layer is considered. This hypothesis is not theoretically valid, but several studies validated it by comparing it to experimental results. In this case, it is no longer necessary to take a density for each frost layer of thickness dy but an average density for all the frost.

Second hypothesis: absorption rate proportional to the density

In the model using this hypothesis[93], it is considered that the diffusion of the CO_2 into the frost takes place in a direction normal to the cold surface. It is also considered that the amount of CO_2 that is diffused into the frost is proportional to the frost density. The diffusion mechanism is then expressed as follows:

$$D_{eff}\frac{d^2\,\rho_{frost}}{dy^2} = \alpha_{co2} \times \rho_{frost}$$

With α_{co2} the absorption rate coefficient per unit volume. By specifying the boundary conditions, the frost density and the absorption coefficient can be calculated. The mass

transfer equations are similar to the classical case as two types of mass transfer take place: one that affects frost thickness and one that affects frost density.

Third hypothesis: Constant absorption rate

In other studies, constant absorption rate is considered (Lee and Ro [92], Loyola et al. [131] ...) and the differential equation shown below is solved in order to calculate the relative humidity:

$$\frac{d^2x}{dy^2} = \frac{\dot{m}\rho_{frost}}{\theta_{frost} \times D_{eff} \times \rho_{flue\ gases}}$$

As already mentioned, the work found on frost formation in the literature is almost exclusively applied to the case of water vapour deposition. The assumptions made are then compared with many experimental results to calculate the error margin. Since the work done on the CO_2 deposition is very little and studies found in literature show mainly experimental results, the model chosen for the rest of this thesis will be a model based on the equations of mass and heat transfer without modifications.

ANNEX C: Frost growth for different frost initial conditions

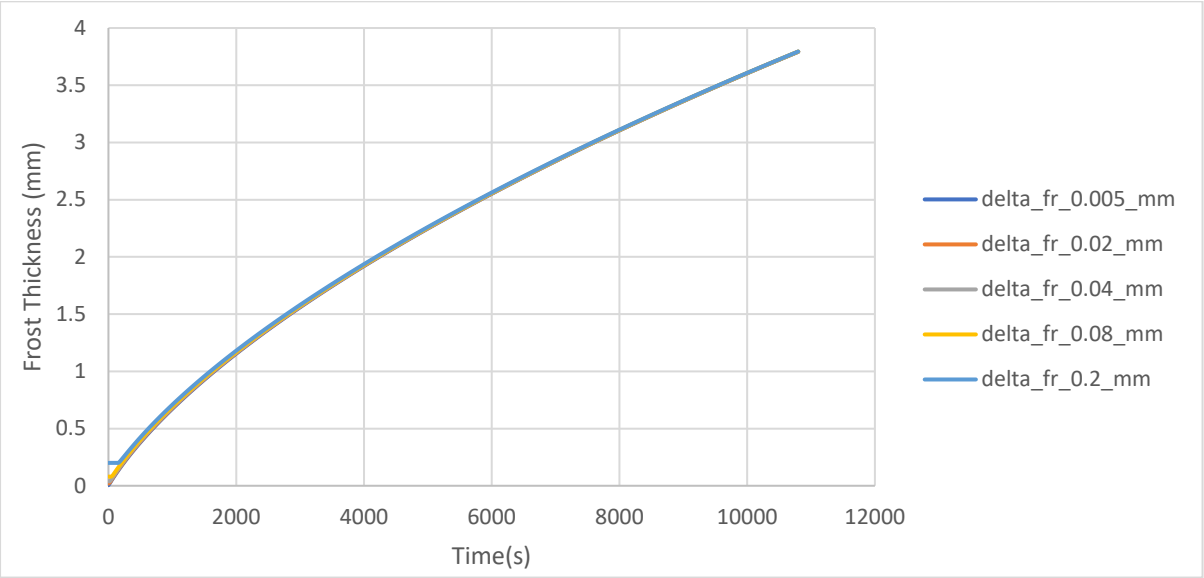

Figure 120: Frost thickness growth for different initial thickness of pre-existing frost layer

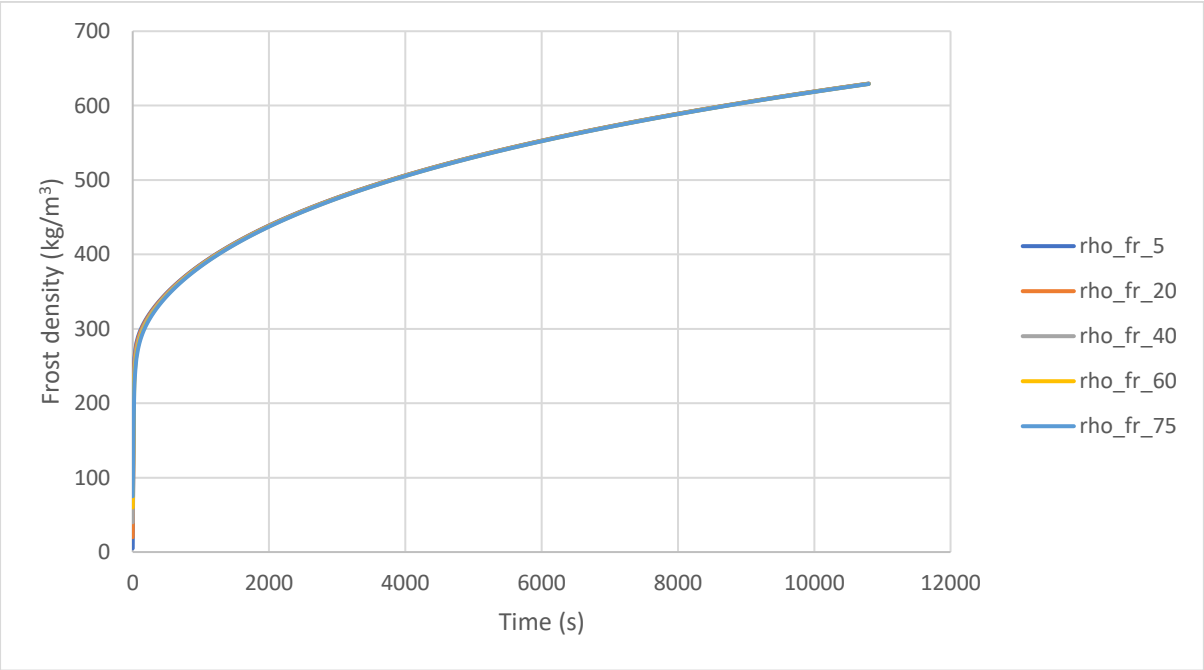

Figure 121: Frost density growth for different initial density of pre-existing frost layer

Since the study of the nucleation phase is hard task to complete, a thin and light pre-existing frost layer is considered present on the cold surface. This initial frost layer serves as the base of all the frost formed upon the cold surface. Figure 122 and figure 123 show the frost growth in terms of thickness and density for different initial pre-existing frost layer. The figures show that, as mentioned in chapter 2, the initial values of frost thickness and density will not affect the frost growth as long as they have low initial values.

ANNEX D: Psychrometric chart construction

Balance between Solid-Steam phase and psychrometric diagrams

Since the flow is a binary CH_4 / CO_2 mixture with phase change, consider the state of these chemical compounds at the phase equilibrium conditions on the frost surface and in the volume where it circulates. The CO_2 concentration in the near-surface gas stream is related to the surface temperature (the boundary layer temperature) by the psychrometric diagram.

Specific psychrometric diagrams for CH_4 / CO_2 were constructed. Similarly, for the defrosting step, conducted by sublimation, the psychrometric diagrams for N_2 / CO_2 were constructed.

The construction methodology of these psychrometric diagrams is based on that of He Sheng Ren [132], for the classical psychrometric air / water diagram. Humid air is replaced with biogas, CH_4 represents the dry air and CO_2 the water vapour.

D'après la loi des gaz parfaits :

Pour le CO_2 : $P_{CO2}.V = n_{CO2}.R.T = m_{CO2}.R_{CO2}.T$

Pour le CH_4 : $P_{CH4}.V = n_{CH4}.R.T = m_{CH4}.R_{CH4}.T$

Pour le biogaz (mélange) : $P.V = n.R.T$

Avec $P = P_{CO2} + P_{CH4}$ the total pressure of the mixture and $n = n_{CO2} + n_{CH4}$ the total number of moles of the mixture. The mole fractions of each component are equal to the ratio of partial fractions to the total pressure:

$$y_{CO2} = n_{CO2}/n = P_{CO2}/P$$

$$y_{CH4} = n_{CH4}/n = P_{CH4}/P$$

In our case, the moisture content of the classical diagram will be replaced by the "concentration ratio ($kgCO_2$ / $kgCH_4$)" which is the mass ratio of CO_2 (solid-vapor phase) relative to the mass of methane CH_4:

$$X = \frac{m_{CO2}}{m_{CH4}} = (\frac{R_{CH4}}{R_{CO2}})/(\frac{P_{CO2}}{P - P_{CO2}}) = (\frac{R_{CH4}}{R_{CO2}})/(\frac{y_{CO2}}{1 - y_{CO2}})$$

The absolute density (kg/m^3) (density of the solid-vapor mixture of CO_2):

$$\rho_{CO2} = m_{CO2}/V$$

The relative concentration (as relative humidity), is the ratio of the absolute concentration to the absolute concentration of saturated CO_2 at this temperature:

$$\varphi = \frac{\rho_{CO2}}{\rho_{CO2S}} = \frac{y_{CO2}}{y_{CO2S}} = \frac{P_{CO2}}{P_{CO2S}}$$

with P_{CO2S} the saturating vapour pressure of CO_2 at T.

Using Refprop V9.1, the saturation P-T values are obtained and using a curve fitting program, the relation between the sublimation pressure (saturating vapour-solid pressure) and the temperature can be found:

$$P_{CO2S} = 6 \times 10^{-38}.T^{18.444}$$

Specific volume ($m^3/kgCH_4$) of the mixture per unit mass CH_4:

$$v = V/m_{CH4} = \frac{R_{CH4}.T}{P-P_{CO2}} = [(R_{CH4}.T)/P][1 + \{x.(R_{CO2}/R_{CH4})\}]$$

The calculation of enthalpy is made with respect to the mass of CH_4 (kJ / $kgCH_4$):

$$h = h_{CH4} + x.h_{CO2}$$

ANNEX E : The model in Dymola

All the equations in the model presented above and all the CO_2 properties were to be coded in order to simulate the frost growth. The software used for these simulations is called Dymola and it uses the Modelica coding language. The model is divided into 4 parts: the inlet (source), the outlet (reservoir), the heat exchanger which is the control volume containing all the heat and mass transfers and the cold source conditions.

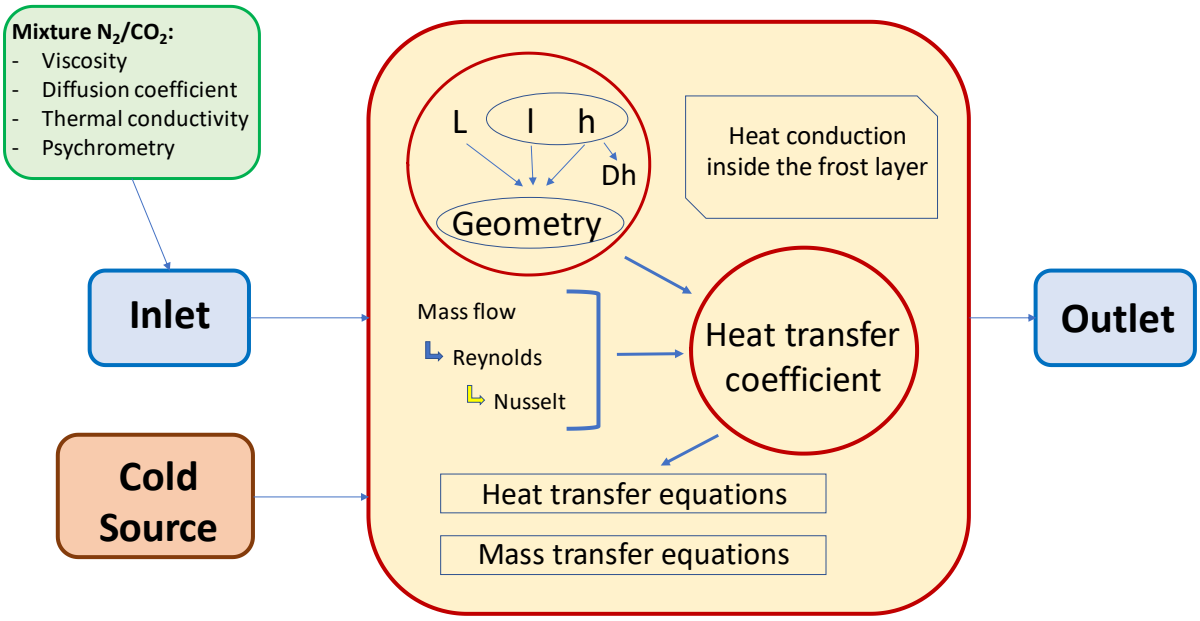

1. The source (inlet)

In the model, inlet gases are flue gases, a mixture of nitrogen and carbon dioxide. All the other components (O_2, H_2O ...) are not taken into. A library of the mixture was created in which all parameters and equations were modified to match the properties of flue gases described in the part above. From a psychrometric point of view, instead of working with air and water vapour, they are replaced by nitrogen and carbon dioxide respectively. The concentration of CO_2 in the flue gases is equivalent to the humidity of the air and the frost formed is equivalent to the water droplets formed when the saturation temperature is reached with appropriate concentration and pressure conditions.

The correlation proposed by Azreg-Aïnou for sublimation pressure as a function of the flue gases temperature is introduced in the code. It was compared to data gathered from REFPROP and showed good agreement. The specific heat capacity of the mixture was calculated depending on the concentration of each component in the mixture. Enthalpy and entropy of the mixture can be calculated using the heat capacity previously calculated. Dynamic viscosity, thermal conductivity and the diffusion coefficient were calculated using the references found in “Properties of Gases and Liquids” which were discussed before.

The fluid leaving the source represents the inlet to the heat exchanger where the deposition occurs. It sets a temperature, a concentration and a mass flow. The temperature specifies the

thermodynamic conditions at the entrance (enthalpy, entropy ...), the concentration represents the mixture composition at the entrance and the mass flow is equivalent to the flow's velocity depending on the inlet section.

2. The reservoir (outlet)

The flue gases now with less CO_2 concentration will be collected at the exit of the exchanger. Exit conditions must be specified even if in the code it will not really affect the results but a good initialization of the outlet parameters can improve the resolution speed. A temperature at the outlet, a concentration of CO_2 in the biogas and the pressure of the system are given.

3. The cold source

This component is the source of low temperature that will frost the CO_2. Frost forms on the surface of the heat exchanger (plate/tube/ring). The cold source can be a constant temperature which in real life can be represented by a fluid during phase change. Also, the cold source can be a heat capacitor preferably with high inertia to store as much cold as possible. Its initial low temperature is given. When using a heat capacitor instead of constant temperature, the cold source's temperature will increase as flue gases pass over it and frost deposits. The increase of the cold source's temperature limits the frosting capacity.

4. The heat exchanger (control volume for all heat and mass transfers)

In the "heat exchanger" component there are several external functions that are used to connect the whole system in a single compact component. CO_2 deposition is done in the exchanger in order to the thickness, the mass, the density, the temperature of the frost and all the heat transfers at the surface and inside the frost layer. Its input is the flue gases issued from the "inlet" component and verifying the conditions and thermodynamic characteristics given to it. The temperature of the cold source responsible for the cooling leading to deposition is also an input of the heat exchanger. The fluid that enters and leaves this exchanger is the mixture of nitrogen and carbon dioxide. Physical constants, geometry, initial conditions of frost, heat and mass transfer correlations... are all set directly in the heat exchanger depending on the conditions of the flue gases. Every correlation used, conditions chosen, parameter set can be easily changed to fit the conditions required for the simulation.

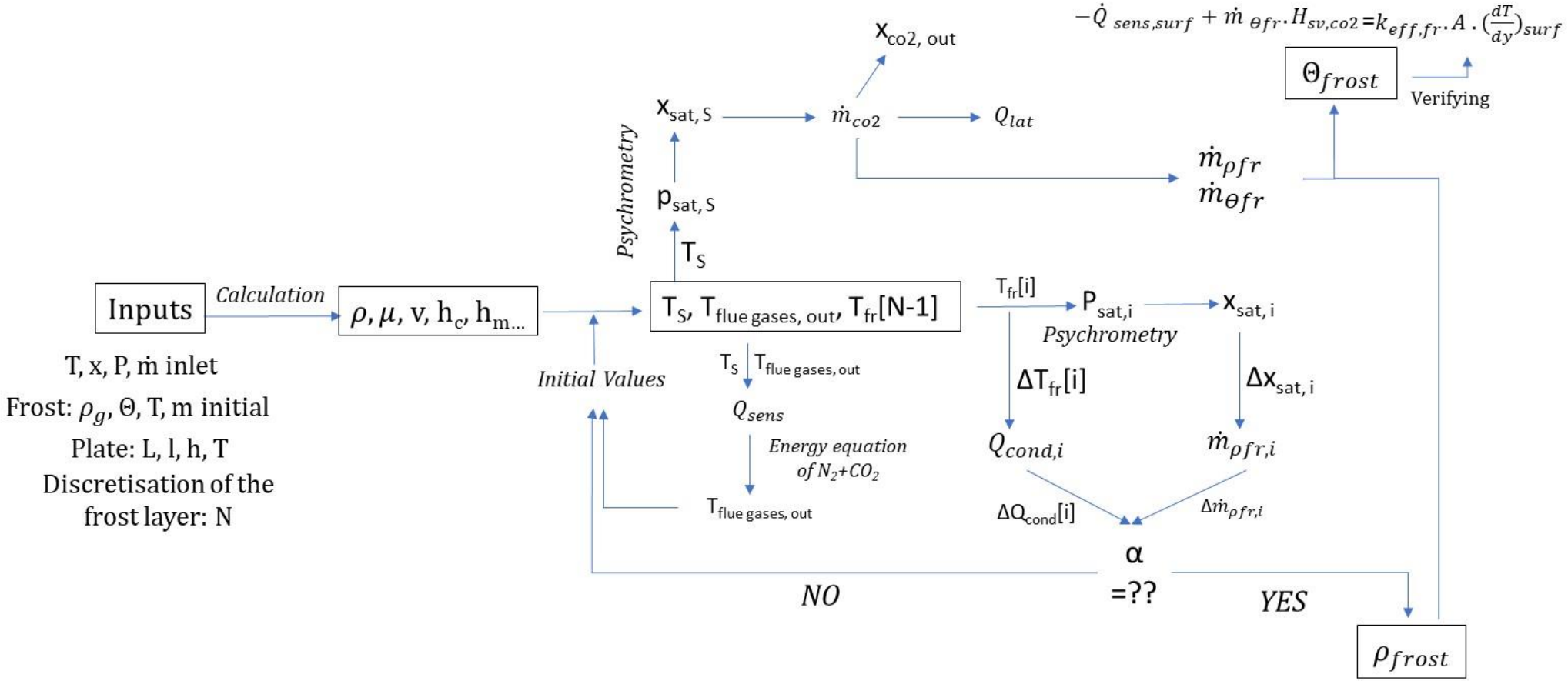
$-\dot{Q}_{sens,surf} + \dot{m}_{\theta fr} . H_{sv,co2} = k_{eff,fr} . A . (\frac{dT}{dy})_{surf}$
Θ_{frost}
Verifying
$x_{co2,\ out}$
$x_{sat,\ S}$
$\dot{m}_{co2}$
Q_{lat}
Psychrometry
$\dot{m}_{\rho fr}$
$\dot{m}_{\theta fr}$
$p_{sat,\ S}$
T_S
Inputs
Calculation
$\rho, \mu, v, h_c, h_{m...}$
$T_S, T_{flue\ gases,\ out}, T_{fr}[N-1]$
$T_{fr}[i]$
$P_{sat,i}$
$x_{sat,\ i}$
Psychrometry
T, x, P, ṁ inlet
Frost: ρ_g, Θ, T, m initial
Plate: L, l, h, T
Discretisation of the frost layer: N
Initial Values
T_S | $T_{flue\ gases,\ out}$
Q_{sens}
Energy equation of N_2+CO_2
$T_{flue\ gases,\ out}$
$\Delta T_{fr}[i]$
$\Delta x_{sat,\ i}$
$Q_{cond,i}$
$\dot{m}_{\rho fr,i}$
$\Delta Q_{cond}[i]$
$\Delta \dot{m}_{\rho fr,i}$
α
=??
NO
YES
ρ_{frost}

RÉSUMÉ

Les systèmes cryogéniques sont l'une des technologies les plus prometteuses et toujours en progrès pour valoriser le biogaz, car elles permettent son épuration sans solvants et possiblement à pression atmosphérique. Dans ce travail, un nouveau concept de récupération de froid par sublimation contrôlée est présenté. Un gaz froid est utilisé en tant que gaz de dégivrage. Il sublimera le givre en utilisant le gradient de pressions partielles entre le givre et la teneur de CO_2 dans le gaz au lieu de gaspiller le froid par transfert de chaleur par convection. Avant cette étape, les dépôts de CO_2 doivent être étudiés. La formation et la croissance de givre de CO_2 sont détaillées et un modèle est présenté pour mieux expliquer comment le CO_2 est séparé du biogaz et des dépôts sur une surface froide. Une comparaison entre les configurations de plaque plane et de tube a montré que cette dernière était meilleure pour la capture de CO_2 dans un système cryogénique en termes de transfert de chaleur et de masse. Cependant, elle pose un problème de colmatage lorsque le givre augmente à l'intérieur du tube. L'étude de la formation de givre le long du tube a montré un décalage de temps pour le dépôt de givre le long du tube. Un processus d'épuration cryogénique du biogaz et de liquéfaction de biométhane a été présenté avec des calculs pour tous les composants inclus dans le système. Les résultats de la simulation montrent que la récupération de froid est possible par sublimation contrôlée et que la température du tube a atteint des valeurs inférieures à la température initiale, ce qui n'est pas possible par le simple transfert de chaleur par convection. Le concept de vaporisation contrôlée fonctionne mieux pour les faibles concentrations de CO_2 dans le biogaz si les phases de givrage et de dégivrage doivent être terminées à durée égale. Enfin, une expérience a été menée pour valider le concept de récupération à froid par sublimation contrôlée. Les résultats montrent que cette technique a le potentiel d'éliminer complètement les utilités froides de certains procédés cryogéniques d'élimination de CO_2.

MOTS CLÉS

Cryogénie, épuration biogaz, captage CO_2, sublimation contrôlée, récupération du froid, formation du givre, croissance du givre.

ABSTRACT

Cryogenic systems are one of the most promising and still rising technologies for upgrading biogas as it is solvent free and can operate at atmospheric pressure. In this work a new concept for cold recovery by controlled sublimation is presented. A cold gas flow is used as a defrosting gas that will sublimate the frost using the partial pressure gradient between the frost and the gas flow instead of wasting the cold by convective heat transfer. Prior to this step, CO_2 deposition should be studied. CO_2 frost formation and growth is thoroughly detailed and a model is presented to better explain how CO_2 is separated from biogas and deposits on a cold surface. A comparison between the flat plate and the tube configurations showed that the latter was better for CO_2 capture in a cryogenic system in terms of heat and mass transfer but it presents a problem of clogging as frost increases inside the tube. The study of frost formation along the tube showed a delay in the starting time of deposition at position further from the biogas inlet. A process for biogas cryogenic upgrading and biomethane liquefaction was presented with calculations for all the components included in the system. Simulation results show that cold recovery is possible by controlled sublimation and the tube temperature reached values lower to the gas flow temperature which is not possible by single convective heat transfer. The concept works best for lower CO_2 concentrations in the inlet biogas if the frosting and defrosting phases are to be completed at the same time. Finally, an experiment was conducted to validate the concept of cold recovery by controlled sublimation, for which results have shown the potential to totally avoid cold utilities use in the cryogenic capture of CO_2.

KEYWORDS

Cryogenics, biogas upgrading, CO_2 capture, controlled sublimation, cold recovery, frost formation, frost growth.